



HAL
open science

Study of the mechanisms of oxide-ion diffusion in $\text{Nd}_2\text{NiO}_{4+d}$ oxides

Adrien Perrichon

► **To cite this version:**

Adrien Perrichon. Study of the mechanisms of oxide-ion diffusion in $\text{Nd}_2\text{NiO}_{4+d}$ oxides. Material chemistry. Université de Montpellier, 2015. English. NNT : . tel-02147882

HAL Id: tel-02147882

<https://theses.hal.science/tel-02147882>

Submitted on 5 Jun 2019

HAL is a multi-disciplinary open access archive for the deposit and dissemination of scientific research documents, whether they are published or not. The documents may come from teaching and research institutions in France or abroad, or from public or private research centers.

L'archive ouverte pluridisciplinaire **HAL**, est destinée au dépôt et à la diffusion de documents scientifiques de niveau recherche, publiés ou non, émanant des établissements d'enseignement et de recherche français ou étrangers, des laboratoires publics ou privés.

THÈSE

Pour obtenir le grade de
Docteur

Délivré par **UNIVERSITE DE MONTPELLIER**

Préparée au sein de l'école doctorale
Sciences Chimiques Balard
Et de l'unité de recherche
Chimie et Cristallochimie des Matériaux
de l'**Institut Charles Gerhardt de Montpellier**

Spécialité : **Chimie**

Présentée par **Adrien Perrichon**

**Etude des mécanismes de diffusion des
ions oxydes à température ambiante dans
 $\text{Nd}_2\text{NiO}_{4+d}$**

Soutenue le 28 septembre 2015 devant le jury composé de

M. Antoine VILLESUZANNE

ICMCB, Bordeaux

Rapporteur

M. Jürg SCHEFER

Paul Scherrer Institut, Villigen

Rapporteur

M. Martin BOEHM

Institut Laue-Langevin, Grenoble

Examineur

M. Andrea PIOVANO

Institut Laue-Langevin, Grenoble

Co-Encadrant

M. Werner PAULUS

C2M-ICGM, Montpellier

Directeur de thèse



Remerciements

Ce travail de recherche a été effectué dans le groupe *Chimie et Cristallochimie des Matériaux* de l'Institut Charles Gerhardt de Montpellier. Mes remerciements s'adressent tout d'abord aux directeurs de l'Institut, Dr. François Fajula puis Pr. Jean-Marie Devoisselle, au directeur du groupe *C2M*, Pr. Philippe Papet, et au directeur de l'école doctorale Sciences Chimiques Balard, Dr. Jean-Jacques Vasseur, pour m'avoir accueilli pendant ces quatre années.

Je souhaite remercier en priorité mon superviseur Pr. Werner Paulus, pour m'avoir donné l'opportunité de m'investir dans ce projet de recherche, m'avoir laissé l'autonomie de diriger mes travaux, et pour ses conseils et son soutien tout au long de ma thèse. Je tiens également et particulièrement à remercier mes co-encadrants à l'Institut Laue Langevin, Dr. Andrea Piovano et Dr. Martin Boehm, pour leur aide précieuse autant dans la recherche que dans la rédaction de cette thèse, et pour l'expérience de la diffusion neutronique qu'ils m'ont fait partager. Merci à vous pour votre patience, votre disponibilité et votre investissement, qui ont fait de cette thèse une expérience enrichissante autant scientifiquement qu'humainement.

Je tiens à remercier Dr. Monica Ceretti, du groupe *C2M*, pour m'avoir initié aux méthodes de synthèse et fourni les monocristaux étudiés pendant cette thèse. Je souhaite également remercier M. Bernard Fraisse, M. Julien Fullenwarth, Mme. Dominique Granier et M. David Bourgogne de leur support technique pour les expériences de diffraction des rayons X et de spectroscopie RAMAN.

Mes remerciements s'adressent également aux responsables des grands instruments, à l'ILL et à l'ESRF, avec qui j'ai eu le plaisir de travailler, Dr. Andrea Piovano et Dr. Martin Boehm sur IN8, Dr. Mohamed Zbiri sur IN6, Dr. Marie-Hélène Lemée-Cailleau sur D19 et Vivaldi, et Dr. Dmitry Chernyshov sur BM01A. Je tiens également à remercier Dr. Mark Johnson, du groupe *CS* de l'ILL, pour m'avoir enseigné les bases des calculs *ab initio*, permis d'utiliser le cluster de l'ILL, et pour ses réponses à mes nombreuses questions.

Je tiens enfin à remercier les membres du groupe *C2M* de l'ICGM à Montpellier, et des groupes *TAS*, *TOF*, *DIF* et *CS* de l'ILL à Grenoble, avec qui j'ai pu travailler ou simplement avoir des discussions fructueuses. Je tiens spécifiquement à remercier Dr. Jiri Kulda, chef du groupe *TAS* à l'ILL, pour m'avoir permis de participer à la vie du groupe, notamment *via* les mémorables *TAS Outing*.

Je voudrais remercier ma famille, et en particulier mes parents, pour leur soutien inconditionnel pendant ces quatre années inoubliables.

Je termine en remerciant mes collègues et amis, Serena, Laetitia, Kinga, Bartek, Avishek et Rajesh, pour les nombreux souvenirs et histoires improbables qui me suivront encore longtemps.

Résumé

Le développement de systèmes pour la conversion d'énergie, comme les piles à combustibles à oxydes solides, est lié à la disponibilité de matériaux montrant une forte conductivité ionique à des températures de fonctionnement réduites. De plus, pour assurer la durabilité des dispositifs, ces matériaux, qu'ils soient purs conducteurs ioniques ou conducteurs mixtes ioniques-électroniques, doivent présenter de bonnes propriétés structurales et thermochimiques en terme de stabilité et d'interface. A cet égard, le système $\text{Nd}_2\text{NiO}_{4+d}$ est un bon candidat en tant qu'électrode stable à température modérée pour piles à combustibles à oxydes solides.

De façon surprenante, le système $\text{Nd}_2\text{NiO}_{4+d}$, ainsi que quelques autres oxydes non-stœchiométriques comme les Brownmillerites $\text{Sr}(\text{Fe},\text{Co})\text{O}_{2.5}$ ou les phases $\text{RE}_2\text{MO}_{4+d}$ type K_2NiF_4 (avec $\text{RE} = \text{La}, \text{Pr}$ et $\text{M} = \text{Ni}, \text{Cu}, \text{Co}$), montrent une mobilité ionique à température ambiante sous potentiel électrochimique. Ce comportement soulève des questions quant au mécanisme microscopique réel de transport ionique dans ces familles de matériaux pour des températures aussi basses que $T=300\text{K}$.

Un mécanisme de « diffusion assistée par les phonons », impliquant la présence d'excitations de réseau à basse énergie, a été développé dans les phases Brownmillerites pour décrire, à l'échelle atomique, comment la diffusion des ions oxydes peut être déclenchée à température ambiante. Dans le cas des phases $\text{RE}_2\text{MO}_{4+d}$, les conducteurs ioniques $\text{La}_2\text{CuO}_{4.07}$, $\text{Pr}_2\text{NiO}_{4.25}$, et $\text{Nd}_2\text{NiO}_{4.25}$ montrent une délocalisation dynamique des oxygènes apicaux des octaèdres MO_6 , sur un cercle de 1Å de diamètre. Cette instabilité structurale, activée par la présence d'oxygènes excédentaires, induit des déplacements importants des oxygènes apicaux vers les sites interstitiels vacants, et donc est supposée jouer un rôle majeur sur la mobilité non-classique de l'oxygène à température ambiante.

A travers l'examen des phases $\text{Nd}_2\text{NiO}_{4+d}$, nous avons étudié les corrélations entre les instabilités structurales induites par l'hyper-stœchiométrie en oxygène et ses effets sur la dynamique de réseau et leur rôle dans la diffusion des ions oxydes à température modérée. En particulier, nous avons développé des approches innovantes pour l'étude de la dynamique de réseau dans les systèmes désordonnés et fortement corrélés. Les résultats issus de diffraction sur monocristal, de diffusion inélastique des neutrons et des simulations *ab initio*, ont montré que la diffusion non-classique des ions oxydes à température ambiante est liée à la fois à des mouvements spécifiques activés par le réseau et des mouvements de particules isolées, tout deux directement induits par la présence d'oxygènes excédentaires. Le mécanisme proposé, étroitement associé à celui de « diffusion assistée par les phonons », propose un cadre conceptuel permettant la description à l'échelle atomique de la diffusion non-classique des oxygènes dans les oxydes non-stœchiométriques.

Abstract

The development of devices for energy conversion, such as solid state fuel cells, depends on the availability of materials showing high oxygen ion conduction together with low operating temperatures. Moreover, adequate structural and thermochemical stability of the pure ionic conductor membrane and the mixed ionic electronic electrodes as well as their matching at the interface are essential for the durability of the device. In this regard, the $\text{Nd}_2\text{NiO}_{4+d}$ system proved to be a good candidate as a stable electrode for intermediate temperature solid state fuel cells.

More intriguing is the fact that $\text{Nd}_2\text{NiO}_{4+d}$, like a few other nonstoichiometric oxides derived from the perovskite framework like the Brownmillerite-type $\text{Sr}(\text{Fe},\text{Co})\text{O}_{2.5}$ and K_2NiF_4 -type $\text{RE}_2\text{MO}_{4+d}$ ($\text{RE} = \text{La}, \text{Pr}$ and $\text{M} = \text{Ni}, \text{Cu}, \text{Co}$), shows oxygen ionic mobility in an electrochemical reaction at room temperature. This surprising behavior raises questions about the real microscopic transport mechanisms in these classes of materials when the temperature is as low as $T=300\text{K}$.

A « phonon assisted diffusion » mechanism, based on the presence of a low-lying phonon modes, has been developed in Brownmillerites to describe on an atomic scale how oxygen ion diffusion can be triggered in solid oxides down to ambient temperature. Concerning the $\text{RE}_2\text{MO}_{4+d}$ systems, oxygen conductors $\text{La}_2\text{CuO}_{4.07}$, $\text{Pr}_2\text{NiO}_{4.25}$, and $\text{Nd}_2\text{NiO}_{4.25}$ have been reported to show a dynamical delocalization of apical oxygen atoms of the MO_6 octahedra on a circle of at least 1\AA diameter. This structural instability, activated by the presence of excess oxygen, implies important shifts of apical oxygen atoms closer to vacant interstitial sites, and is thus believed to play a major role on the non-classical oxygen mobility at ambient temperature.

Through this work, we have investigated, in the $\text{Nd}_2\text{NiO}_{4+d}$ phases, the correlations between structural instabilities induced by the oxygen hyper-stoichiometry and their subsequent effects on the lattice dynamics and role in promoting oxygen diffusion in the moderate-temperature regime. We have, in particular, developed innovative approaches to investigate lattice-dynamics of highly-correlated and disordered systems. Results from single-crystal diffraction, inelastic neutron scattering and first-principle simulations have evidenced that indeed the non-classical oxygen diffusion at ambient temperature can be depicted as an interplay of specific lattice-activated and single-particle motions, both directly correlated to the oxygen hyper-stoichiometry. The subsequent mechanism, closely related to the “phonon assisted diffusion mechanism”, provides a comprehensive framework to describe on an atomic scale the non-classical oxygen diffusion in non-stoichiometric oxides.

Table of content

Chapter 1. Introduction	1
Chapter 2. State-of-the-art & Outline. Nd₂NiO_{4+d} and related RE₂MO_{4+d} materials	11
<u>2.1. Phase diagram, structure and magnetism of Nd₂NiO_{4+d} and related RE₂MO_{4+d} materials</u>	12
2.1.1. <i>The Ruddlesden-Popper phases</i>	12
2.1.2. <i>La₂NiO_{4+d}: the system of reference for single-phase structures of the RE₂MO_{4+d} family</i>	13
2.1.3. <i>Structural complexity: the case of La₂CoO_{4+d}</i>	15
2.1.4. <i>Further complexity: stripe-phases in RE₂NiO_{4+d} nickelates</i>	16
2.1.5. <i>Crystalline and magnetic structures of the Nd₂NiO_{4+d} single-phases</i>	17
<u>2.2. Atomistic simulations of RE₂MO_{4+d} ionic conductors</u>	20
2.2.1. <i>Simulation methods and models of RE₂MO_{4+d} materials</i>	20
2.2.2. <i>The interstitialcy mechanism as dominant process in the high-temperature regime</i>	21
<u>2.3. Oxide ion diffusion at moderate-temperature: the concept of lattice activated diffusion</u>	23
2.3.1. <i>Phonon assisted diffusion mechanism: the case of (Sr,Ca)FeO_{2.5} brownmillerites</i>	23
2.3.2. <i>Mobility and structural instability: the case of La₂CuO_{4+d}</i>	26
<u>2.4. Choice of investigation methods of Nd₂NiO_{4+d} in the moderate-temperature regime & Outline of the thesis</u>	28
<u>2.5. Bibliography</u>	30
Chapter 3. Synthesis, Theory & Experimental methods	33
<u>3.1. Synthesis of Nd₂NiO_{4+d} phases</u>	33
3.1.1. <i>Solid-state synthesis</i>	33
3.1.2. <i>Control over excess oxygen d</i>	34
3.1.3. <i>Single-crystal growth</i>	36
<u>3.2. Powder and single-crystal diffraction – Theory & Instrumentation</u>	38
3.2.1. <i>Basis of X-ray and neutron diffraction</i>	38
3.2.2. <i>Twinning in Nd₂NiO_{4+d} single-cristals</i>	39
3.2.3. <i>Neutron diffractometer D19</i>	40
3.2.4. <i>Synchrotron radiation on BM01A</i>	41
<u>3.3. Density-functional theory</u>	42
3.3.1. <i>HK and KS theorems</i>	42
3.3.2. <i>Exchange-correlation energy</i>	44
3.3.3. <i>Direct method for phonon calculations</i>	45
3.3.4. <i>MD & VACF</i>	46
<u>3.4. Positional recurrence maps</u>	48
<u>3.5. Inelastic neutron scattering – Theory</u>	50
3.5.1. <i>Inelastic scattering cross section</i>	50
3.5.2. <i>Scattering by nuclei</i>	51
3.5.3. <i>Scattering by phonons</i>	52
3.5.4. <i>Calculations of the dynamic structure factor from molecular dynamics</i>	55
<u>3.6. Inelastic neutron scattering – Instrumentation</u>	56
3.6.1. <i>The ILL reactor</i>	56
3.6.2. <i>Time-of-flight IN6 spectrometer</i>	56
3.6.3. <i>Three-axis IN8 spectrometer</i>	59
<u>3.7. Bibliography</u>	62

Chapter 4. Diffraction on the Nd₂NiO_{4.25} single-crystal	65
4.1. Neutron single-crystal diffraction at low-temperature on Nd ₂ NiO _{4.25}	65
4.2. X-ray single-crystal diffraction at high-temperature on Nd ₂ NiO _{4.25}	68
4.3. Conclusion.....	72
4.4. Bibliography.....	73
Chapter 5. First-principle DFT calculations	75
5.1. Models and optimized geometries of the Nd ₂ NiO _{4+d} phases.....	76
5.1.1. Stoichiometric Nd ₂ NiO _{4.0}	76
5.1.2. Intermediate Nd ₂ NiO _{4.10}	80
5.1.3. Further discussion about the defect localization.....	82
5.1.4. Fully-oxidized Nd ₂ NiO _{4.25}	83
5.2. Phonon calculations.....	85
5.2.1. Parameters for Nd ₂ NiO _{4.0}	85
5.2.2. Phonon dispersion curves and DOS of Nd ₂ NiO _{4.0}	86
5.2.3. Eigenvectors for Nd ₂ NiO _{4.0}	93
5.2.4. Overstoichiometric Nd ₂ NiO _{4.125} & Nd ₂ NiO _{4.25}	96
5.3. Molecular dynamics of the Nd ₂ NiO _{4+d} phases.....	99
5.3.1. Parameters.....	99
5.3.2. Diffusion events: pathway & MSD.....	101
5.3.3. Phonon density of states.....	104
5.4. Positional recurrence maps.....	106
5.4.1. d-dependent PRM.....	106
5.4.2. T-dependent PRM.....	109
5.4.3. About the interstitial site.....	111
5.4.4. About the nickel, equatorial oxygen, and neodymium sites.....	113
5.5. Conclusion.....	114
5.6. Bibliography.....	115
Chapter 6. INS-TOF. Lattice dynamics on Nd₂NiO_{4+d} powders	117
6.1. Experiments on the IN6 spectrometer.....	117
6.1.1. The high-temperature experiment.....	118
6.1.2. The low-temperature experiment.....	118
6.2. Generalized phonon density of states.....	119
6.2.1. Measured gDOS.....	119
6.2.2. Attribution of modes.....	121
6.3. Comparison with calculations.....	123
6.4. Analogy with RAMAN spectra.....	127
6.5. Conclusion.....	129
6.6. Bibliography.....	130
Chapter 7. INS-TAS. Lattice dynamics on Nd₂NiO_{4.25} single-crystal	131
7.1. Dispersion curves of Nd ₂ NiO _{4.25} measured on the IN8 spectrometer.....	131
7.2. Comparison of phonon modes with dynamic structure factors from MD.....	135
7.3. Conclusion.....	140
7.4. Bibliography.....	141
Chapter 8. General conclusion	143
Appendix	147

Chapter 1. Introduction.

In the fascinating and interdisciplinary field of ionic conductors, and driven by a need for cleaner and more efficient energy sources, oxygen ion conducting materials have been the object of thorough investigation in the past decade. The property of oxygen ion conduction, meaning the current flow induced by the diffusion of oxide ions through the crystal, is of particular interest for technological devices as oxygen sensors, oxygen separation membranes, catalysis, and electrolytes for solid oxide fuel cell (SOFC).

In the specific case of SOFC, which is a promising technology in the domain of energy conversion, the challenge is to reach high efficiency energy conversion from chemical energy to electricity, yet with the less environment-noxious byproducts. Most cells are operating in the high temperature range (up to 1300K), which lead to issues in term of chemical stability, microstructural degradation and cracking of the membranes. Since the operating temperature is dictated by the cathode and electrolyte conducting properties, *i.e.* the oxygen conducting material itself, there is a need for new materials with high oxygen conductivity in the moderate-temperature range.

In order to design oxygen conducting materials, one has to describe the microscopic mechanism of diffusion, meaning the movements of an oxide ion from one site of the crystal lattice to another. A first obvious statement concerning the material structures has to be made: the crystal shall contain connected and partially-occupied oxygen sites. Such restrictions limit the potential materials to a few families of structures: the fluorite-type oxides with the well-known ceria-based materials or yttria-stabilized zirconia, the perovskites and perovskite-related oxides with lanthanum gallate-based materials, the LAMOX family, apatites and BIMEVOX-type oxides, and the K_2NiF_4 -type oxides. In **Figure 1.1** is reported a comparison of the ionic conductivity of several ionic conductors in the moderate temperature range.

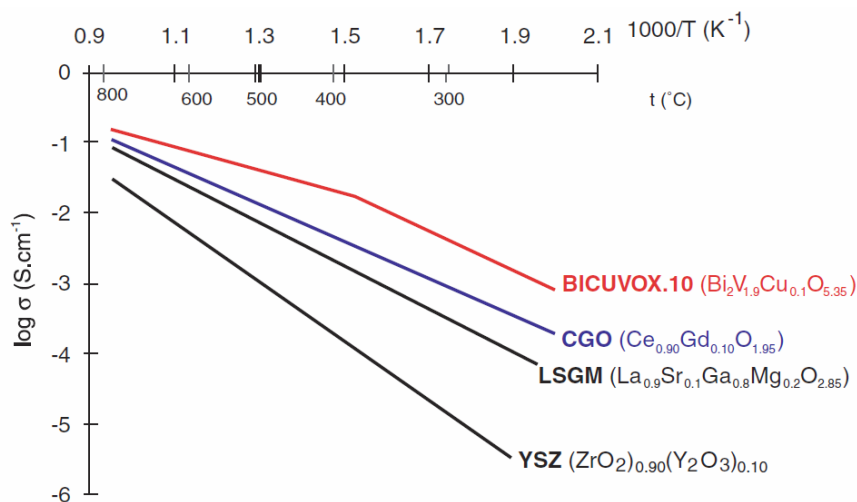


Figure 1.1 – Ionic conductivity as a function of the inverse temperature of several ionic conductors considered for moderate temperature applications. Figure from reference [1].

Prior to describe in details oxygen conducting materials, their structures and associated diffusion mechanisms, one has to consider a few general considerations about diffusion in oxide materials.

Diffusion is a fundamental and physically complex phenomenon. The main difference between bulk diffusion in oxides compared to other materials, as metals, is that the existence of the anion and cation sublattice restricts ionic diffusion to its own sublattice, while the diffusion is still influenced by the behavior of the cation sublattice. In oxides the anion and cation sublattices are commonly considered separately, and this approximation is justified since in most technologically interesting oxide materials, oxygen self-diffusion is significantly faster than cation diffusion.

Applied to crystalline materials, diffusion requires the migration of atoms away from their equilibrium positions and, thus, diffusion mechanisms describe the way an atom can move from one equilibrium position to the neighboring one. Consequently, and since oxygen conducting materials show generally defective structures with partially filled oxygen sites, the role of point defects in enabling diffusion is fundamental. For the oxide materials considered in this study, there are three generally accepted mechanisms associated with point defects, known as vacancy mechanism, interstitial mechanism, and interstitialcy mechanism.

In the vacancy mechanism, host ion diffuses by jumping to a neighboring vacancy. In the interstitial mechanism, ions positioned at interstitial sites in the lattice migrate by jumping from one interstitial site to a neighboring interstitial site. And in the interstitialcy mechanism, the interstitial ion displaces an ion from its equilibrium lattice site in the host lattice to a neighboring vacant interstitial site. The difference between interstitial and interstitialcy is that the interstitial mechanism does not require the presence of other defects except from the interstitial ions themselves, while the interstitialcy mechanism implies permanent displacements of both defect and host ions. These three mechanisms are schematized in **Figure 1.2**.

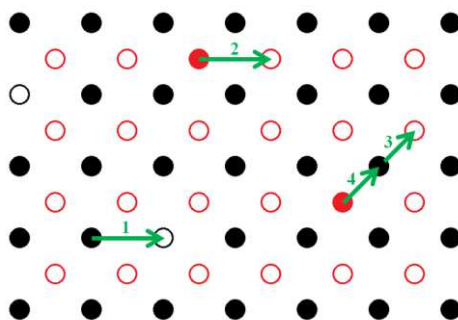


Figure 1.2 – Scheme of mechanisms of diffusion on a 2D grid of ‘host’ atomic sites in black, and ‘interstitial’ atomic sites in red. Occupied sites are filled circle and vacancies empty circles. The vacancy mechanism (1) consists of a direct hopping, from an oxygen atom of the host lattice to a vacant oxygen site of the host lattice. The interstitial mechanism (2) is also a direct hopping, from an oxygen atom in interstitial site to another vacant interstitial site. And the interstitialcy mechanism (3 then 4) is a two-step process, where the interstitial oxygen pushes its neighbor on the host lattice to a vacant interstitial site, then recombine in the newly vacant site of the host lattice.

Besides the diffusion pathway, diffusion mechanisms are to describe the energy required of an ion to migrate in the crystal, which is a microscopic-scale description, to macroscopic diffusion coefficients. In this respect, due to their double negative charges and large ionic radius of 1.4\AA , the mobility of oxide ion seems, at first sight, difficult to apprehend. The migration of an oxide ion is generally attributed to the sole thermally-activated hopping, with a typical energy of migration lower than 1eV . And as such, in order to reach suitable values of ionic conductivity, relatively high temperatures had to be considered.

However, recent studies have proven that a few materials of the Brownmillerite-type and of the K_2NiF_4 -type, in particular $\text{RE}_2\text{NiO}_{4+d}$ ($\text{RE}=\text{Nd},\text{Pr}$) and $\text{La}_2\text{MO}_{4+d}$ ($\text{M}=\text{Ni},\text{Cu},\text{Co}$), show significant and highly anisotropic oxygen mobility under potential at room-temperature^[2-8]. We remark that, even in the high-temperature regime, the oxygen diffusion in $\text{RE}_2\text{MO}_{4+d}$ phases is highly anisotropic, as shown for $\text{Nd}_2\text{NiO}_{4+d}$ in **Figure 1.3**, with about three orders of magnitude between oxygen diffusion in the (a,b) plane and along the c -axis^[9].

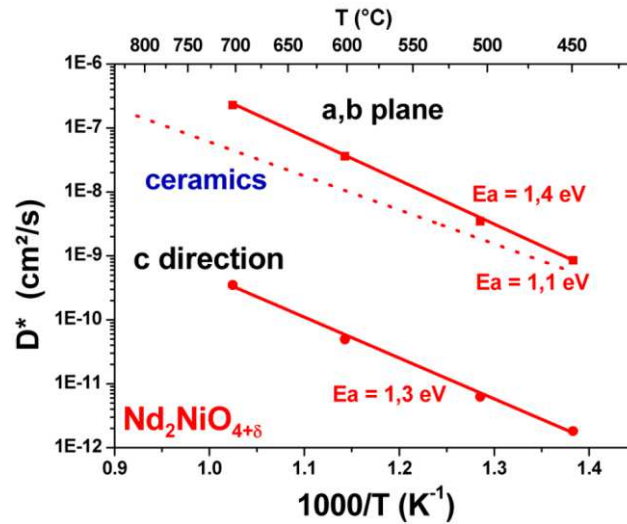


Figure 1.3 – Diffusivities vs $1000/T$ for $\text{Nd}_2\text{NiO}_{4+d}$ single-crystal (solid lines) and comparison with polycrystalline ceramics^[10] (dotted line). Figure from reference [9].

In the high-temperature regime, the classical diffusion is usually described with an Arrhenius law, shown in **equation 1.1**, where D is the diffusion coefficient, D_0 a prefactor representing the maximum diffusion at infinite temperature, E_A the activation energy, k_B the Boltzmann constant and T the temperature. However, in the low-temperature regime, the diffusion is non-classical and cannot be explained in the framework of classic thermally-activated stochastic oxygen hopping.

$$D = D_0 e^{\frac{-E_A}{k_B T}} \quad (\text{Eq. 1.1})$$

Deviation of ion conductivity from the pure Arrhenius behavior have already been described by the Vogel-Tam-Fucher (VTF)^[11-13] and Williams-Lander-Ferry (WLF)^[14] equations. These descriptions, based on phenomenological approaches, assume faster relaxation processes induced by thermal motion, without providing a microscopic interpretation of enhanced low-

temperature ion conductivity. Anomalies have been reported for polymer electrolytes^[15], silver conducting AgI composite glasses^[16], and crystallized chalcogenides^[17]. Ionic transport described by the VTF equation is much less common in oxides, but it has already been reported for lithium diffusion in $\text{La}_{2/3-x}\text{Li}_{3x}\text{TiO}_3$ solid solutions^[18] and for oxygen diffusion in $\text{La}_2\text{Mo}_{2-y}\text{W}_y\text{O}_9$ ^[19].

In the case of the Brownmillerite system, a phonon-assisted diffusion mechanism^[20] was proposed to describe the non-classical oxygen diffusion at low-temperature at a microscopic scale, relying on the concept that specific low-lying lattice excitations are promoting diffusion events. This mechanism will be described in detail in **chapter 2**. Concerning the case of the K_2NiF_4 -type materials, there aren't, yet, any explanations for the room-temperature oxygen mobility. However numerous studies, mostly focused on crystalline structures, phase transitions and associated dynamics, and electronic properties, reveal both low-lying excitations and strong and complex structural and electronic correlations. While the structural study of these high complexity systems is of fundamental interest by itself, our aim is to investigate how the correlation of point defects with the lattice may play a role on the non-classical oxide ion diffusion at moderate-temperature. As such, we have to wonder if a similar coupling between diffusion and lattice dynamics, as shown for the Brownmillerite, could describe, at least qualitatively, the specific diffusion properties of the K_2NiF_4 -type materials in the moderate-temperature range.

In any case, diffusion mechanisms for bulk mobility are dependent on average structures, organizations of defects, and local deformations. Prior to be able to quantify, or even qualitatively describe, the oxygen diffusion linked to these mechanisms, one has to know in details the material structures and associated diffusion pathways.

The K_2NiF_4 -type $(\text{Nd,Pr})_2\text{NiO}_{4+d}$ and $\text{La}_2(\text{Ni,Cu,Co})\text{O}_{4+d}$, besides their oxide ion conducting properties, are highly anisotropic materials showing a complex phase diagram as a function of temperature and oxygen excess d . While the phases will be described in details in the following chapters, they display a similar set of structures, with variations depending on the collective tilting pattern of MO_6 octahedra, and the long-range ordering of excess oxygen atoms in interstitial sites and their associated defective clusters. The main phases are schematized in **Figure 1.4**. The high-temperature tetragonal (HTT) phase is observed at high-temperature for all compositions. The low-temperature orthorhombic (LTO) and low-temperature tetragonal (LTT), with tilting pattern respectively in the [100] and [110] direction, are observed for the stoichiometric $d=0$ phase at room- and low-temperature. In the case of $(\text{Nd,Pr})_2\text{NiO}_{4.10}$ intermediate phase, a tetragonal phase analogue to the LTT is also observed at room-temperature. Also, for compositions that can adapt a huge amount of excess oxygen atoms, an incommensurate phase can be observed, often described in an average orthorhombic $Fmmm$ space-group. At last, for $d>0$ compositions, we remark that the incorporation of excess oxygen atoms in interstitial sites will strain the tilting pattern around the interstitial oxygen.

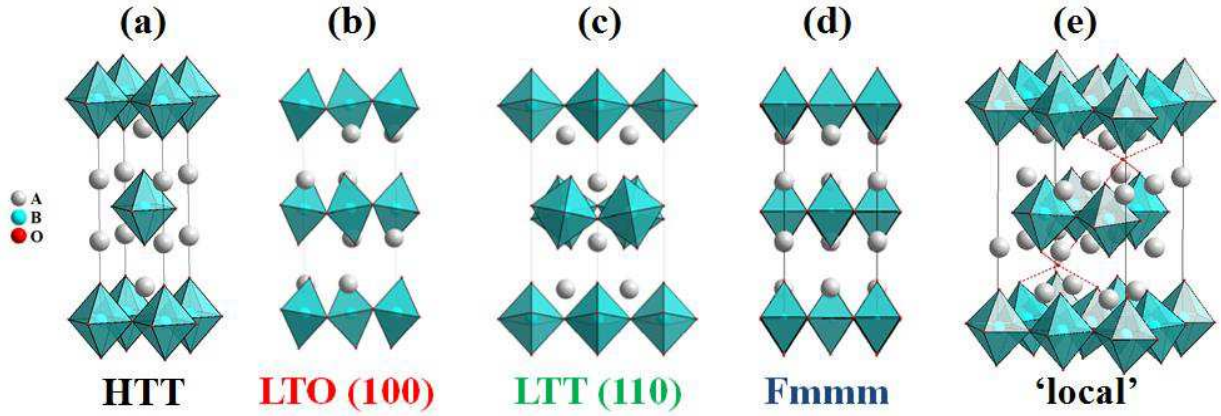


Figure 1.4 – Schemes of the most common structures of the Re_2MO_{4+d} phases. (a) The high-temperature tetragonal (HTT) phase is observed for all compositions at high-temperature, and is referred as the high-symmetry parent phase. (b) The low-temperature orthorhombic (LTO) phase is observed for most compositions with $d=0$ at room-temperature, and shows a long-range ordered tilting pattern of MO_6 octahedra along the $[100]$ direction. (c) The low-temperature tetragonal (LTT) phase is observed for some compositions with $d=0$ at low-temperature, and can also be observed for intermediate $d=0.05-0.10$ compositions at room-temperature, as in the case of $(Pr,Nd)_2NiO_{4.10}$. (d) For compositions incorporating a huge amount of excess oxygen atoms, about $d=0.25$, complex incommensurate structures are observed, often described in an average orthorhombic $Fmmm$ structure. (e) Besides the natural ordering of MO_6 octahedra tilts, the presence of excess oxygen atoms in interstitial site will strain its surrounding and modify the tilt of the neighboring MO_6 octahedra.

Besides incommensurate structures of the most oxidized $d=0.25$ phases, numerous evidences have been found of the structural and associated electronic and magnetic complexity in the RE_2MO_{4+d} family, including high-temperature superconductivity, incommensurate magnetic correlations, stripe phases, charge ordering and even phase separations^[21-28]. While most of these effects only appears at low-temperature, the structural incommensurability persists in the room-temperature regime, for which non-classical oxygen mobility have been observed in $(Nd,Pr)_2NiO_{4+d}$ and $La_2(Ni,Cu,Co)O_{4+d}$ materials.

A remarkable behavior observed for these materials is the shallow potential on which sits regular oxygen atoms on apex on MO_6 octahedra, referred as apical oxygen atoms, evidenced by their disc-shaped delocalization as shown in **Figure 1.5**. The width of the delocalization depends on the composition and the excess oxygen content, as shown for $La_2CuO_{4.07}$ ^[29] and $Nd_2NiO_{4.25}$ ^[30]. The delocalization is partly static, corresponding to the tilting angle of the MO_6 octahedra, and is partly dynamical, as the shift in the delocalization shape with temperature evidence for $La_2CuO_{4.07}$. In the series of composition of RE_2MO_{4+d} with $RE=La,Nd,Pr$ and $M=Ni,Cu,Co$, the Nd_2NiO_{4+d} and Pr_2NiO_{4+d} systems have the advantage of being able to adapt the largest amount of excess oxygen atoms, up to $d=0.25$, and show the largest delocalization of apical oxygen atoms, on a disc of 2\AA diameter (**Figure 1.5**). The delocalization of apical oxygen atoms is, *a priori*, directly correlated with the room-temperature oxygen mobility since it draws the apical oxygen atom closer to empty interstitial

sites, thus reducing the diffusion pathway and lowering the energy required to activate a diffusion hopping event.

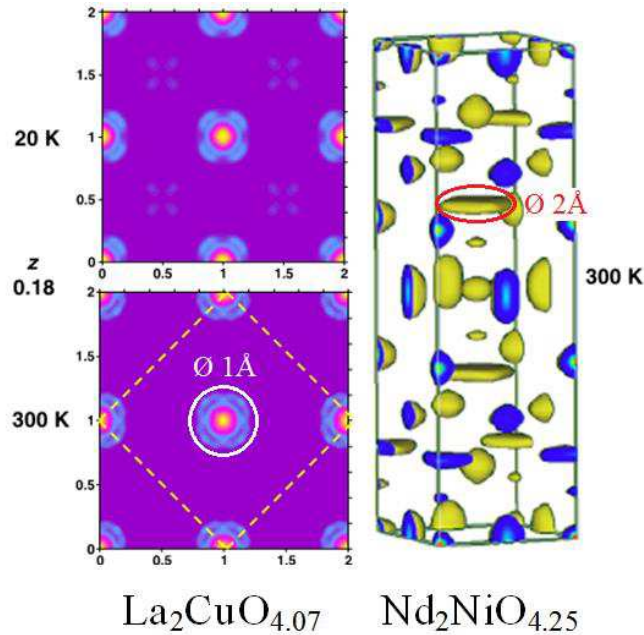


Figure 1.5 – Nuclear density maps calculated using the maximum entropy method (MEM) on single-crystal neutron diffraction data on (left) $\text{La}_2\text{CuO}_{4.07}$ ^[29] and (right) $\text{Nd}_2\text{NiO}_{4.25}$ ^[30]. For $\text{La}_2\text{CuO}_{4.07}$, the nuclear density maps is projected on the (ab) plan at $z=0.18$ corresponding to the apical oxygen positions $(0\ 0\ z)$. The dotted box represent the F -cell. We observe at $T=20\text{K}$ a cross-shape delocalization in the directions $[100]$ and $[010]$ with respect to the F -cell, corresponding to static CuO_6 tilts, while at $T=300\text{K}$ the delocalization is a 1\AA diameter circle, thus showing activated dynamics in the $[110]$ direction – toward interstitial sites – with respect to the F -cell. In the $\text{Nd}_2\text{NiO}_{4.25}$ system at $T=300\text{K}$, the delocalization is even more pronounced on a circle of 2\AA diameter.

In order to unveil the microscopic oxygen diffusion mechanism, extensive theoretical studies have been performed on the $\text{RE}_2\text{MO}_{4+d}$ phases^[31-35]. However, in most cases, only the high-temperature regime have been investigated, which involve the high-temperature high-symmetry parent tetragonal phase common to all K_2NiF_4 -type materials for which no correlations of point defects with the lattice have been observed. In the high-temperature regime, it has been shown both through diffraction experiments and theoretical calculations that the dominant microscopic diffusion mechanism is the interstitialcy mechanism^[31, 33, 35-37], as shown in **Figure 1.6**, involving both excess oxygen atoms in interstitial sites and apical oxygen atoms. This high-temperature diffusion mechanism have been shown to be a thermally activated stochastic hopping process, that can be macroscopically describe by Arrhenius law.

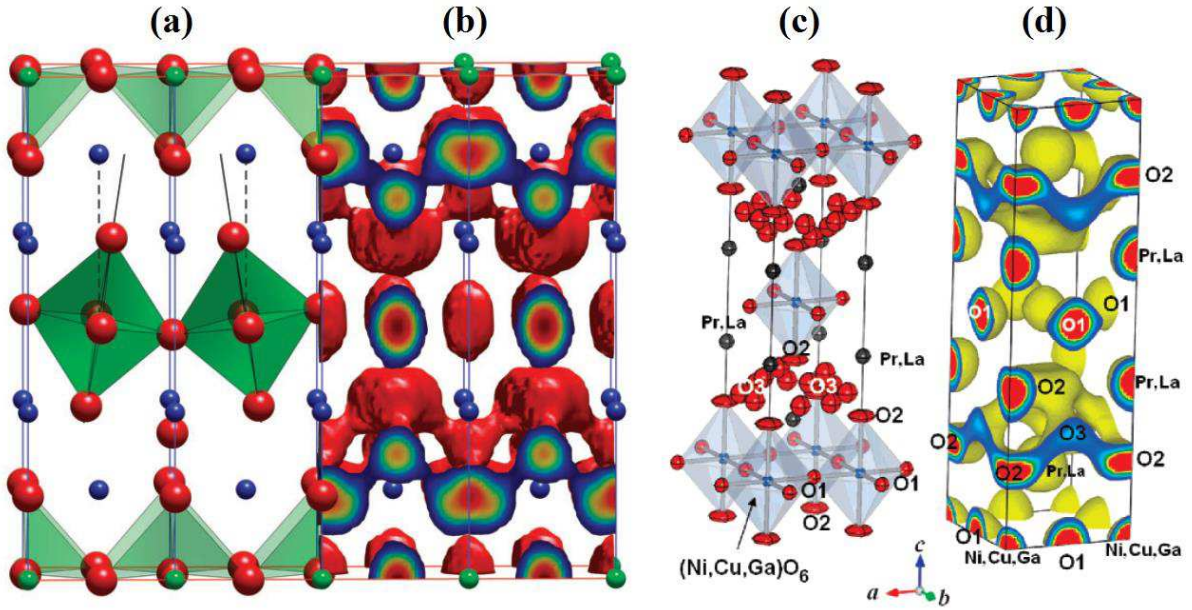


Figure 1.6 – (a) Crystal structure of $\text{La}_2\text{NiO}_{4+d}$ (O ions in red, NiO_6 octahedra in green and La ions in blue), showing the characteristic tilting of the NiO_6 octahedra caused by the introduction of the oxygen interstitial; along with (b) the calculated isosurface connecting the oxygen conduction sites in $\text{La}_2\text{CoO}_{4.125}$ from MD calculations at $T=1500\text{K}$ ^[33]. (c) Refined crystal structure and (d) isosurface of nuclear density at $0.05 \text{ fm}\cdot\text{\AA}^{-3}$ of the mixed oxide-ion and electronic conductor $(\text{Pr}_{0.9}\text{La}_{0.1})_2(\text{Ni}_{0.74}\text{Cu}_{0.21}\text{Ga}_{0.05})\text{O}_{4+d}$ determined in situ at $T=1015.6^\circ\text{C}$ in the tetragonal $I4/mmm$ unit cell^[36]. For both system, the merging of occupancy clouds of interstitial and apical oxygen sites evidence that the interstitialcy mechanism is the dominant diffusing process in the high-temperature regime.

However, as already mentioned, these compounds also show non-classical diffusion at moderate-temperature, down to even room-temperature under potential^[5-7]. While the conceptual framework of lattice-activated diffusion, with in particular the phonon assisted diffusion mechanism, provide an explanation at the microscopical scale of enhanced oxygen mobility by low-lying phonon modes, many uncertainties concerning its application in the $\text{RE}_2\text{NiO}_{4+d}$ phases are to be elucidated. In particular, the following interrogations arise:

In a temperature regime where the defective clusters, formed by the adaptation of excess oxygen atoms on interstitial sites, are long-range ordered, hence correlated with the crystal structure and its subsequent dynamics, we wonder how single-particle hopping process can take place. How does the excess oxygen atom impact on the lattice dynamics? Similarly, how does the shallow potential of the apical oxygen atom contribute? And more generally, is the phonon-assisted diffusion effective to describe the non-classical oxygen diffusion in the $\text{RE}_2\text{NiO}_{4+d}$ phases? If so, what would be the signature on lattice dynamics of such a contribution? Also, is the high-temperature diffusion pathway associated with the interstitialcy mechanism valid at moderate temperature?

In order to address these issues, we have performed an extensive investigation of the $\text{Nd}_2\text{NiO}_{4+d}$ phases both in the moderate- and in the high-temperature regime, using a synergetic approach involving both diffraction and spectroscopic experiments and first-principle theoretical calculations. Our aim being the unveiling of the microscopic mechanism of oxygen diffusion in the moderate temperature regime, and specifically the role of lattice dynamics to promote the diffusion, the present study is focused on the effect of excess oxygen content on the lattice dynamics of $\text{Nd}_2\text{NiO}_{4+d}$, using complementary tools of inelastic neutron scattering techniques, both on powders and single-crystals, and *ab initio* phonon calculations and molecular dynamics simulations.

Bibliography

1. Vannier, R.N. (2002). Paper presented at the Proc. Europ. Mat. Res. Soc. Symp.
2. Alonso, J.A., Martínez-Lope, M.J., García-Muñoz, J.L., and Fernández-Díaz, M.T. (1997). *Journal of Physics: Condensed Matter*, 9(30), 6417.
3. Le Toquin, R., Paulus, W., Cousson, A., Prestipino, C., and Lamberti, C. (2006). *Journal of the American Chemical Society*, 128(40), 13161-13174.
4. Nemudry, A., Rudolf, P., and Schöllhorn, R. (1996). *Chemistry of Materials*, 8(9), 2232-2238.
5. Paulus, W., Cousson, A., Dhalenne, G., Berthon, J., Revcolevschi, A., Hosoya, S., Treutmann, W., Heger, G., and Le Toquin, R. (2002). *Solid State Sciences*, 4(5), 565-573.
6. Paulus, W., Heger, G., Rudolf, P., and Schöllhorn, R. (1994). *Physica C: Superconductivity*, 235–240, Part 2(0), 861-862.
7. Rudolf, P., Paulus, W., and Schöllhorn, R. (1991). *Advanced Materials*, 3(9), 438-440.
8. Takeda, Y., Kanno, R., Takada, T., Yamamoto, O., Takano, M., and Bando, Y. (1986). *Zeitschrift für anorganische und allgemeine Chemie*, 540(9-10), 259-270.
9. Bassat, J.M., Burriel, M., Wahyudi, O., Castaing, R., Ceretti, M., Veber, P., Weill, I., Villesuzanne, A., Grenier, J.C., Paulus, W., and Kilner, J.A. (2013). *The Journal of Physical Chemistry C*, 117(50), 26466-26472.
10. Boehm, E., Bassat, J.M., Dordor, P., Mauvy, F., Grenier, J.C., and Stevens, P. (2005). *Solid State Ionics*, 176(37–38), 2717-2725.
11. Fulcher, G.S. (1925). *J. Am. Ceram. Soc.*, 8, 339-355.
12. Tammann, G. and Hesse, W. (1926). *Z. Anorg. Allg. Chem.*, 156, 245-257.
13. Vogel, H. (1921). *Phys. Z.*, 22, 645-646.
14. Williams, M.L., Landel, R.F., and Ferry, J.D. (1955). *J. Am. Chem. Soc.*, 77, 3701-3707.
15. Gray, F. and Arnaud, M. (1999). Polymer Electrolytes *Handbook of Battery Materials* (pp. 499-523).
16. Kuwata, N., Saito, T., Tatsumisago, M., Minami, T., and Kawamura, J. (2004). *Solid State Ionics*, 175, 679-682.
17. Ribes, M., Taillades, G., and Pradel, A. (1998). *Solid State Ionics*, 105, 159-165.
18. Bohnke, O., Bohnke, C., and Fourquet, J.L. (1996). *Solid State Ionics*, 91, 21-31.
19. Georges, S., Bohnke, O., Goutenoire, F., Laligant, Y., Fouletier, J., and Lacorre, P. (2006). *Solid State Ionics*, 177, 1715-1720.

20. Paulus, W., Schober, H., Eibl, S., Johnson, M., Berthier, T., Hernandez, O., Ceretti, M., Plazanet, M., Conder, K., and Lamberti, C. (2008). *Journal of the American Chemical Society*, 130(47), 16080-16085.
21. Anissimova, S., Parshall, D., Gu, G.D., Marty, K., Lumsden, M.D., Chi, S., Fernandez-Baca, J.A., Abernathy, D.L., Lamago, D., Tranquada, J.M., and Reznik, D. (2014). *Nature Communications*, 5, 3467.
22. Wochner, P., Tranquada, J.M., Buttrey, D.J., and Sachan, V. (1998). *Physical Review B*, 57(2), 1066-1078.
23. Yoshizawa, H., Kakeshita, T., Kajimoto, R., Tanabe, T., Katsufuji, T., and Tokura, Y. (2000). *Physical Review B*, 61(2), R854-R857.
24. Hayden, S.M., Lander, G.H., Zarestky, J., Brown, P.J., Stassis, C., Metcalf, P., and Honig, J.M. (1992). *Physical Review Letters*, 68(7), 1061-1064.
25. Yamada, K., Omata, T., Nakajima, K., Endoh, Y., and Hosoya, S. (1994). *Physica C: Superconductivity*, 221(3-4), 355-362.
26. Tranquada, J.M., Lorenzo, J.E., Buttrey, D.J., and Sachan, V. (1995). *Physical Review B*, 52(5), 3581-3595.
27. Tranquada, J.M., Buttrey, D.J., Sachan, V., and Lorenzo, J.E. (1994). *Physical Review Letters*, 73(7), 1003-1006.
28. Tranquada, J.M., Kong, Y., Lorenzo, J.E., Buttrey, D.J., Rice, D.E., and Sachan, V. (1994). *Physical Review B*, 50(9), 6340-6351.
29. Villesuzanne, A., Paulus, W., Cousson, A., Hosoya, S., Le Dréau, L., Hernandez, O., Prestipino, C., Ikbel Houchati, M., and Schefer, J. (2012). *Journal of Solid State Electrochemistry*, 15(2), 357.
30. Wahyudi, O. (2011). *Université de Rennes 1, PhD thesis 4468*.
31. Chroneos, A., Parfitt, D., Kilner, J.A., and Grimes, R.W. (2010). *Journal of Materials Chemistry*, 20(2), 266-270.
32. Frayret, C., Villesuzanne, A., and Pouchard, M. (2005). *Chemistry of Materials*, 17(26), 6538-6544.
33. Kushima, A., Parfitt, D., Chroneos, A., Yildiz, B., Kilner, J.A., and Grimes, R.W. (2011). *Physical Chemistry Chemical Physics*, 13(6), 2242-2249.
34. Minervini, L., Grimes, R.W., Kilner, J.A., and Sickafus, K.E. (2000). *Journal of Materials Chemistry*, 10(10), 2349-2354.
35. Parfitt, D., Chroneos, A., Kilner, J.A., and Grimes, R.W. (2010). *Physical Chemistry Chemical Physics*, 12(25), 6834-6836.
36. Yashima, M., Enoki, M., Wakita, T., Ali, R., Matsushita, Y., Izumi, F., and Ishihara, T. (2008). *Journal of the American Chemical Society*, 130(9), 2762-2763.
37. Yashima, M., Sirikanda, N., and Ishihara, T. (2010). *Journal of the American Chemical Society*, 132(7), 2385-2392.

Chapter 2. State-of-the-art & Outline.

$\text{Nd}_2\text{NiO}_{4+d}$ and related $\text{RE}_2\text{MO}_{4+d}$ materials.

As introduced in **chapter 1**, $\text{RE}_2\text{MO}_{4+d}$ compositions have a rich phase diagram as a function of excess oxygen content d and temperature, showing complex long-range ordering in over-stoichiometric phases, interesting electronic and magnetic properties and, for some compositions, non-classical oxygen mobility in the room- and moderate-temperature regimes. In this chapter, we will summarize the state-of-the-art knowledge, relevant to the aim of our work, concerning the $\text{RE}_2\text{MO}_{4+d}$ materials, and in particular the $\text{Nd}_2\text{NiO}_{4+d}$ composition.

In **section 2.1** we will focus on phase diagrams, crystalline structures of single-phases, and magnetic ordering found for $\text{Nd}_2\text{NiO}_{4+d}$ and other materials of the $\text{RE}_2\text{MO}_{4+d}$ family. We will also briefly summarize the numerous signatures of the high structural, magnetic and electronic complexity found in these systems.

The **section 2.2** is dedicated to theoretical calculations of $\text{RE}_2\text{MO}_{4+d}$ oxide ion conductors. We will summarize calculation methods, specify their strength and limitations in the simulation of such complex systems, and present diffusion mechanism, pathway, and coefficients found in the high-temperature regime.

In **section 2.3** we will introduce the concepts of non-classical diffusion in the moderate-temperature regime, with the example of the phonon assisted diffusion mechanism, combining structural instabilities with generation of soft modes and related changes in lattice dynamics, as evidenced for Brownmillerites $(\text{Sr,Ca})\text{FeO}_{2.5}$ and $\text{La}_2\text{CuO}_{4.07}$. We will also show that the $\text{Nd}_2\text{NiO}_{4+d}$ system is closely related to the $\text{La}_2\text{CuO}_{4.07}$ system, showing the same type of structural instability, which suggest that the non-classical diffusing behavior may be explained in the framework of the phonon assisted diffusion mechanism.

At last, in **section 2.4**, we will summarize the behaviors of interest that will be investigated through the next chapters, and especially define the approximations and methods we used to simulate the $\text{Nd}_2\text{NiO}_{4+d}$ material in the moderate-temperature range. We will also present the outline of the thesis.

2.1. Phase diagram, structure and magnetism of $\text{Nd}_2\text{NiO}_{4+d}$ and related $\text{RE}_2\text{MO}_{4+d}$ materials

The first step in the understanding of the diffusing behavior of $\text{RE}_2\text{MO}_{4+d}$ is the description of the structure, hence the electronic structure, which define the physical properties of any system. In this section we will introduce crystalline and related magnetic structures, starting from the Ruddlesden-Popper phases, to $\text{RE}_2\text{MO}_{4+d}$ phases, and then specifically the $\text{Nd}_2\text{NiO}_{4+d}$ composition.

2.1.1. The Ruddlesden-Popper phases

The Ruddlesden-Popper (RP) phases are intergrowth phases of n perovskite layers ABO_3 separated by one rock-salt AO layer (i.e. NaCl-type). Thus, while the general formula is $\text{A}_{n+1}\text{B}_n\text{O}_{3n+1}$, a more meaningful description would be $(\text{AO})(\text{ABO}_3)_n$. Ideal structures are schematized in **Figure 2.1**. Concerning the local environment, B cations are 6-coordinated similarly to the perovskite, while A-cation can be either 9- or 12-coordinated, depending on they are bridging (AO) and (ABO_3) layers, or two (ABO_3) layers, respectively. We also note that two consecutive stacks of perovskite layers are shifted by $(\frac{1}{2}\frac{1}{2}0)$ in the convention where the c-axis is the stacking axis.

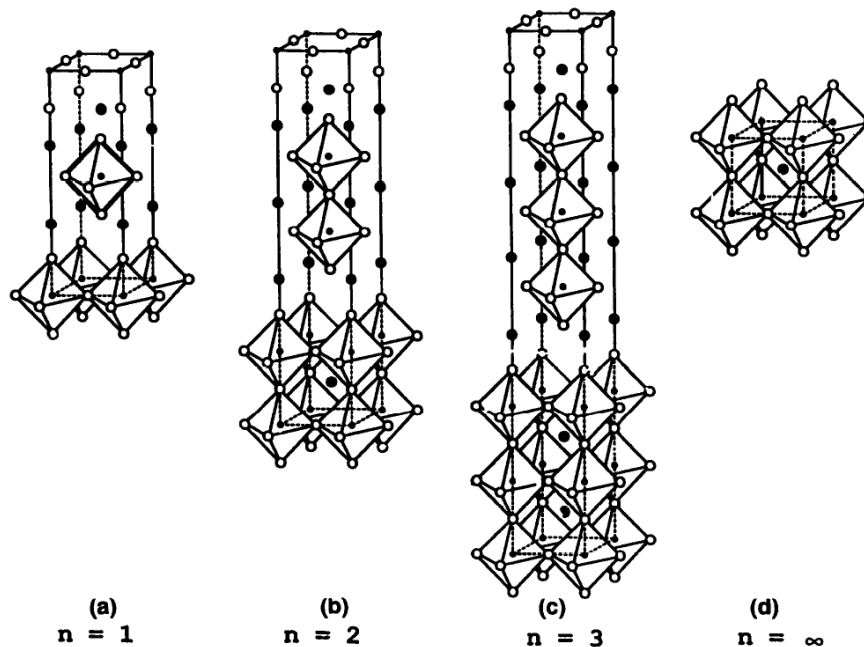


Figure 2.1 – Schemes of ideal structures of Ruddlesden-Popper phases for (a) $n=1$, (b) $n=2$, (c) $n=3$, and the limit case (d) of $n=\infty$ equivalent to an ideal perovskite. The space-group describing such structures for $n \in]0; \infty[$ would be the tetragonal $I4/mmm$, generally found for the high-temperature phases, and thus known as high-temperature tetragonal (HTT) phase. Figure from reference [1].

As for the perovskite system, A-sites are generally occupied by alkaline metal or rare earth elements and B-site by transition metals. The stoichiometry is quite flexible in term on oxygen hypo- or hyper-stoichiometry, which allows various geometries of MO_x polyhedra (down to 4-coordinated B cations in the case of lack of oxygen^[2]) and complex tilting schemes. Such flexibility allows for a wide range of composition, doping, and associated physical properties to gather, which led to a strong interest in the phase transitions and defective structures of the Ruddlesden-Popper phases, and in particular for the $n=1$ family where high-temperature superconductivity was discovered for $\text{La}_{2-x}\text{Sr}_x\text{CuO}_{4+d}$ compounds.

2.1.2. $\text{La}_2\text{NiO}_{4+d}$: the system of reference for single-phase structures of the $\text{RE}_2\text{MO}_{4+d}$ family

The K_2NiF_4 -type oxides, with $\text{A}_2\text{BO}_{4+d}$ stoichiometries, are the $n=1$ subgroup of the Ruddlesden-Popper family, described above, and basically an intergrowth of one perovskite ABO_3 and one rock-salt AO_{1+d} layers. As for the other compounds of the RP family, the ideal structure would be described in the tetragonal space-group $I4/mmm$, which is indeed found at high-temperature (e.g. at 423K for $\text{La}_2\text{NiO}_{4.0}$ ^[3]). Since La_2NiO_4 was one of the most extensively studied system, its phase diagrams and structures are considered as references for most Re_2MO_4 compounds. We remark that phases can be obtained through two types of doping of La_2NiO_4 : cation doping which leads to well controlled phases, stable with temperature, as strontium-doped $\text{La}_{2-x}\text{Sr}_x\text{NiO}_4$; and oxygen doping, which leads to $\text{La}_2\text{NiO}_{4+d}$ phases with adjustable stoichiometry even at low-temperature. The schematic phase diagram of $\text{La}_2\text{NiO}_{4+d}$ as a function of d and T is shown in **Figure 2.2**. To further justify its description hereafter, in the context of oxide ion conductivity, the $\text{La}_2\text{NiO}_{4+d}$ system have shown promising results with oxygen mobility for temperatures ranging from $T=750$ to 1050K ^[4-9], which is competitive with perovskite-based materials. However, since further investigations on the Ni-based conductors have shown that the diffusing properties can be enhanced when considering alternative rare-earth elements, $\text{Re}_2\text{NiO}_{4+d}$ ($\text{Re}=\text{Nd}, \text{Sm}, \text{Pr}$)^[10, 11], specificities of the $(\text{Nd},\text{Pr})_2\text{NiO}_{4+d}$ will then be described.

While phase diagrams vary strongly depending on the composition and excess oxygen content of the $\text{RE}_2\text{MO}_{4+d}$ materials, most of the phases observed at room-temperature and in the low-temperature regime are subgroups of the parent phase $I4/mmm$, referred as high-temperature tetragonal structure (HTT). Variation from this ideal structure are linked to the long-range arrangement of MO_6 octahedra tilting pattern. The tilting pattern of the most common single-phase structure are schemed in **Figure 2.16**, where the low-temperature orthorhombic (LTO) shows MO_6 tilt toward the $[010]$ direction, the low-temperature tetragonal (LTT) toward the $[110]$ direction, and the low-temperature less orthorhombic (LTLO) shows tilt toward a direction inbetween $[010]$ and $[110]$.

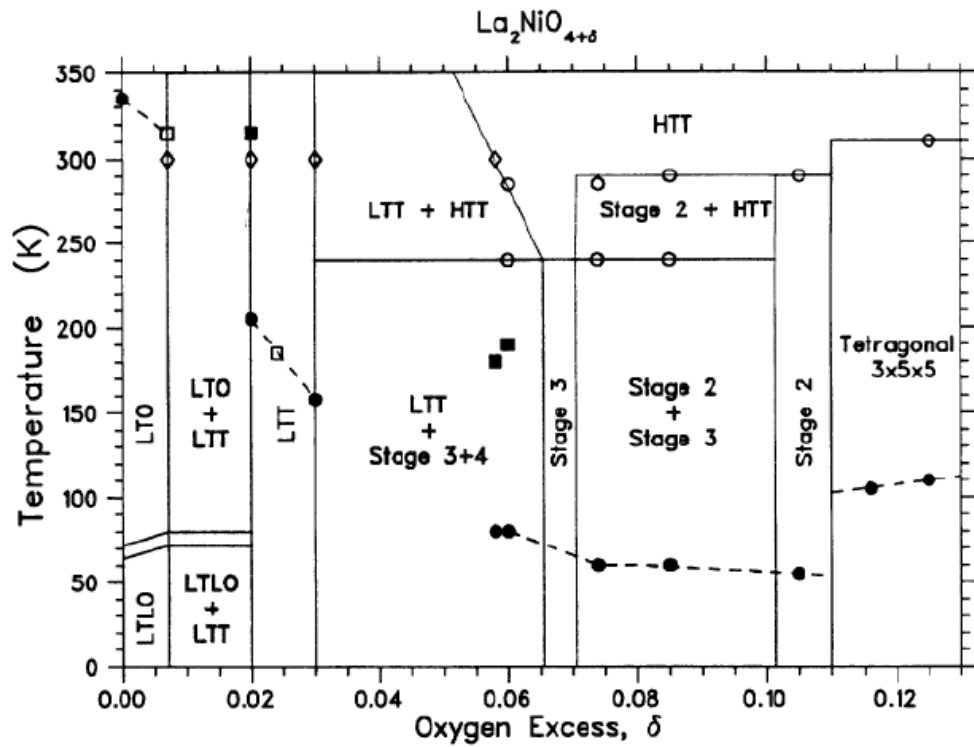


Figure 2.2 – Schematic phase diagram of $\text{La}_2\text{NiO}_{4+d}$ by Tranquada *et al.*^[12]. Straight lines are estimation of phase transitions and phase stability domains from models and experimental values (circles), while dotted lines correspond to magnetic transitions from para- to antiferromagnetism. Phases acronyms are described in text below.

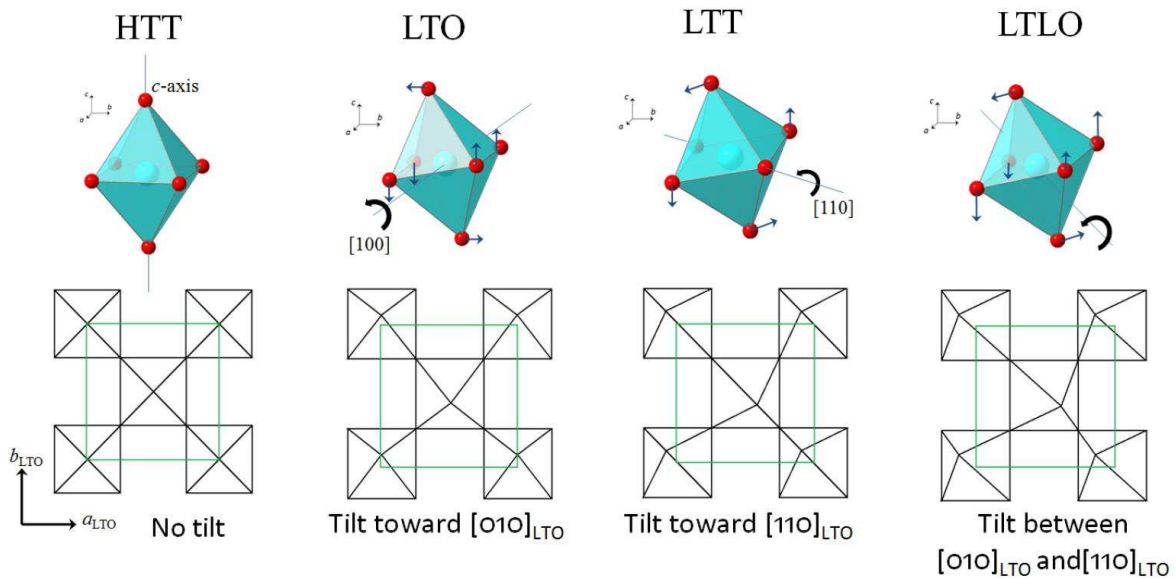


Figure 2.3 – Tilting pattern of MO_6 octahedra for the single-phases HTT, LTO, LTT and LTLO commonly found in $\text{RE}_2\text{MO}_{4+d}$ materials at room- and low-temperature. For each tilting pattern, the lower figure is a projection on the (ab) plan of the upper figure, where the green box represents the F-cell ($Z=4$) and the five black boxes the side and upper edges of the MO_6 octahedra. Figure from reference [13].

2.1.3. Structural complexity: the case of $\text{La}_2\text{CoO}_{4+d}$

While some compositions of the $\text{RE}_2\text{MO}_{4+d}$ family, such as $\text{La}_2\text{NiO}_{4+d}$ or $\text{La}_2\text{CuO}_{4+d}$ can incorporate only a limited amount of excess oxygen d , some other, as $(\text{Nd,Pr})_2\text{NiO}_{4+d}$ or $\text{La}_2\text{CoO}_{4+d}$ can adapt up to $d=0.25$ excess oxygen. Neutron and synchrotron diffraction experiments have evidenced that the diffraction pattern of these high- d phase show numerous incommensurate or commensurate satellite peaks, corresponding to the complex long-range ordering of the defective clusters formed around excess oxygen atoms in interstitial sites. The case of $\text{La}_2\text{CoO}_{4+d}$ is of particular interest since an incommensurate structure is found for $\text{La}_2\text{CoO}_{4.14}$ ^[14], while the structure turns commensurate for $\text{La}_2\text{CoO}_{4.25}$ ^[13]. As an example, reciprocal space maps of $\text{La}_2\text{CoO}_{4.14}$ at RT, $T=423\text{K}$ and $T=473\text{K}$, reconstructed from synchrotron X-ray diffraction data, from the work of Le Dréau et al.^[13, 14], are shown in **Figure 2.5**. The incommensurate modulation is stable in temperature and last up to $T=433\text{K}$. We also remark that, besides the incommensurate satellites, the single-crystal shows a pseudo-merohedral twinning – this specific twinning is systematically present for $\text{RE}_2\text{MO}_{4+d}$ crystals grown from floating zone method, and will be described in detail in **chapter 3**. Without the need of describing in details the structures found for $\text{La}_2\text{CoO}_{4+d}$, their study have evidenced that the incommensurability depends both on the exact excess oxygen content and the temperature, and represent the long-range ordering of the tilting pattern of MO_6 octahedra and the 3-dimensional ordering of excess oxygen atoms in interstitial sites and their associated defective clusters.

Furthermore, nuclear intensity profiles of CoO_6 octahedra of $\text{La}_2\text{CoO}_{4.14}$ have been calculated by maximum entropy method (MEM) on the main reflections of single-crystal neutron diffraction data^[14], as shown in **Figure 2.4**. Significant temperature-dependent displacive motions of apical oxygen atoms have been evidenced, associated with CoO_6 tilting, and will be furtherly discussed in **section 2.3.2**.

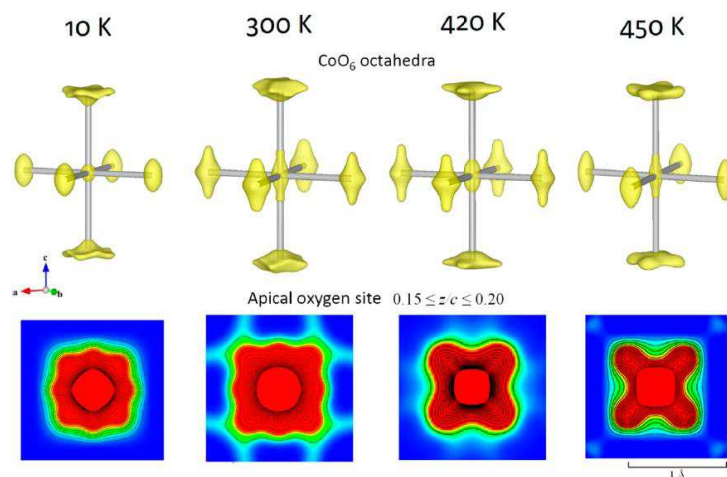


Figure 2.4 – (top) 3D nuclear intensity profiles of CoO_6 octahedra of $\text{La}_2\text{CoO}_{4.14}$, calculated by MEM using single-crystal diffraction data (main reflections only). (bottom) 2D maps for apical oxygen atoms. Figure from reference [14].

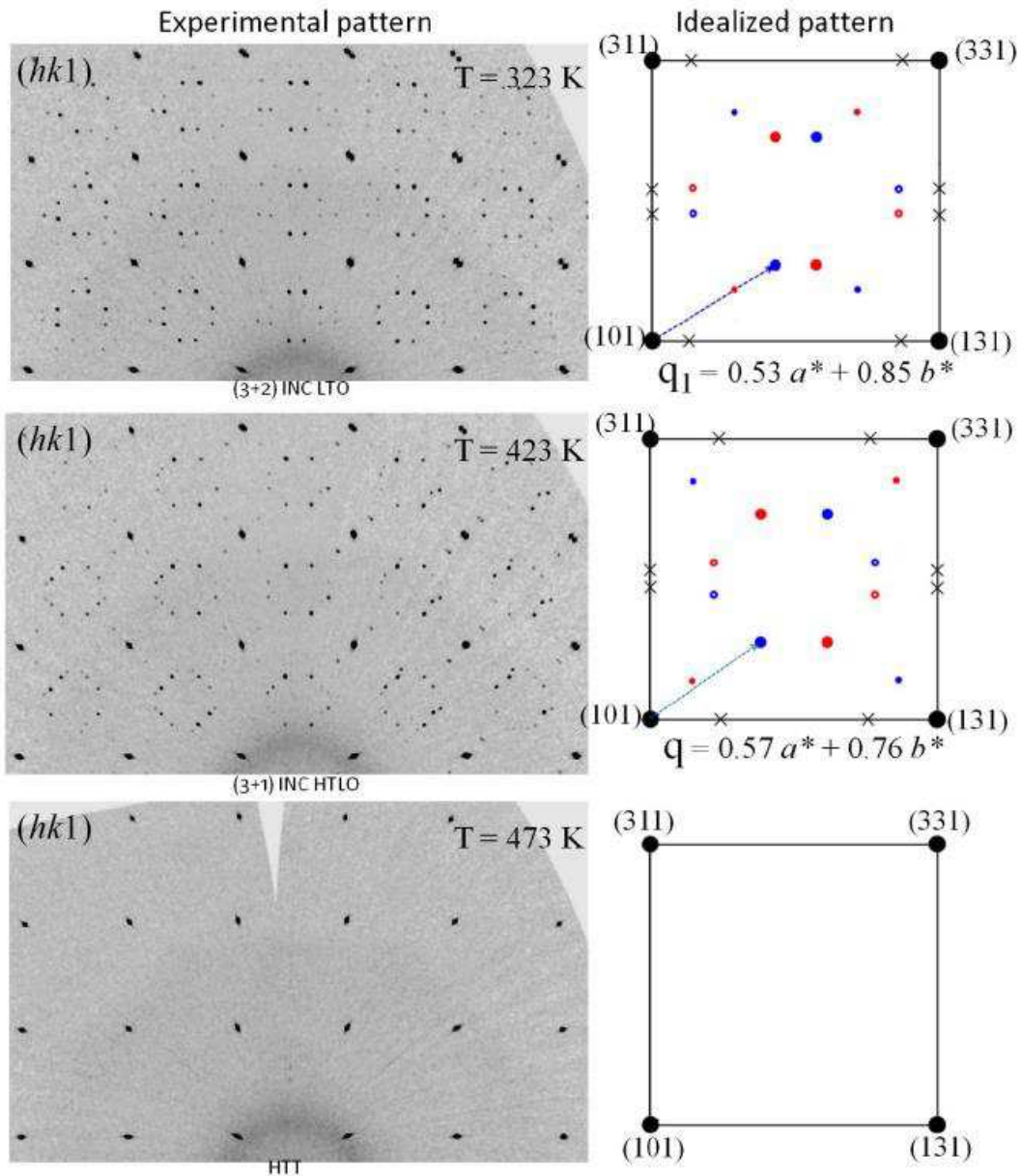


Figure 2.5 – $(hk1)$ reciprocal space maps of $\text{La}_2\text{CoO}_{4.14}$ reconstructed from synchrotron X-ray diffraction data, in the three different phases LTO, HTLO and HTT, respectively at RT, $T=423\text{K}$ and $T=473\text{K}$, together with the corresponding idealized reciprocal pattern for one pseudo-merohedral twin individual. Figure from reference [13].

2.1.4. Further complexity: stripe-phases in $\text{RE}_2\text{NiO}_{4+d}$ nickelates

Besides the incommensurate structures found in high- d compositions of the $\text{RE}_2\text{MO}_{4+d}$ family, another kind of complexity, involving charge and magnetic ordering, have been evidenced for, in particular, the strontium doped $\text{La}_{2-x}\text{Sr}_x\text{NiO}_4$ system. For the composition $\text{La}_{1.67}\text{Sr}_{0.33}\text{NiO}_4$ at $T=240\text{K}$, charge and magnetic stripe have been evidenced by inelastic neutron scattering^[15], as shown in **Figure 2.6**.

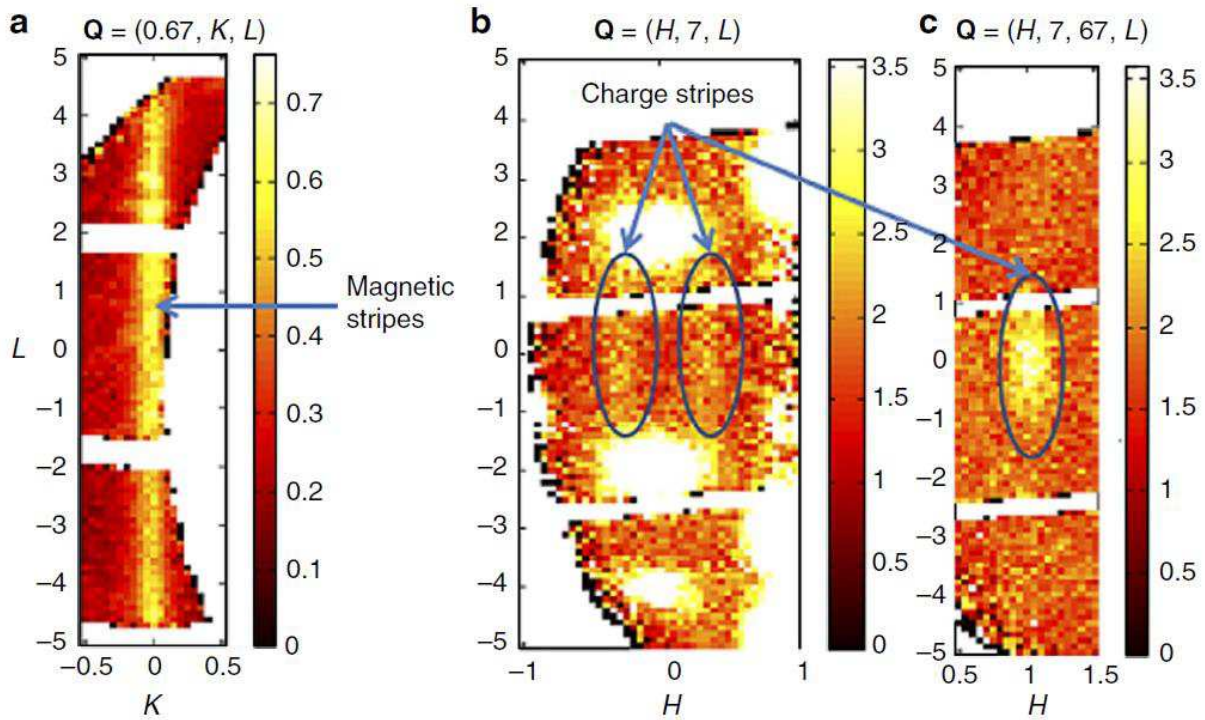


Figure 2.6 – Distinct L dependence of spin- and charge-stripe fluctuations, measured on $\text{La}_{1.67}\text{Sr}_{0.33}\text{NiO}_4$ at $T=240\text{K}$ and $E=5.5\pm 1.5\text{meV}$ with three-axis inelastic neutron scattering. (a) Magnetic scattering at $\mathbf{Q}=(0.67,0,L)$. Charge-stripe fluctuations at (b) $\mathbf{Q}=(\pm 0.33,7,L)$ and (c) $\mathbf{Q}=(1,7.67,L)$, as indicated by ovals. Figure from reference [15].

While these behaviors are not of direct interest in the study of room- and moderate-temperature oxygen mobility, we have to remind that – and as opposed to the high-temperature regime – some of the complexity is still observed at room-temperature, and may play indirectly on lattice dynamics, hence on the non-classical diffusion of oxygen atoms.

2.1.5. Crystalline and magnetic structures of the $\text{Nd}_2\text{NiO}_{4+d}$ single-phases

Now that we have introduced the most commonly found phases of the $\text{RE}_2\text{MO}_{4+d}$ family, and shown some examples of the complexity inherent to these systems, we will introduce the $\text{Nd}_2\text{NiO}_{4+d}$ composition.

The phase diagram of the $\text{Nd}_2\text{NiO}_{4+d}$ system have been determined at RT via *in situ* electrochemical intercalation reaction followed with powder neutron diffraction^[16]; the refined scale factor as a function of charge transfer, hence excess oxygen content, is shown in **Figure 2.7.a**. While this phase diagram represent out-of-equilibrium phases of $\text{Nd}_2\text{NiO}_{4+d}$, it is of fundamental interest when considering the oxygen diffusion instead of isolated structures of well defined stoichiometries. The starting point of this experiment is the $\text{Nd}_2\text{NiO}_{4.25}$ stoichiometry described in an average $Fmmm$ structure, which is evidenced in the range $d=0.22-0.25$. Upon reduction, a tetragonal phase is found in the range $d=0.05-0.10$, described

in the space-group $P4_2/ncm$ (equivalent to the low-temperature tetragonal (LTT) phase described in **section 2.1.2**). With further reduction, the stoichiometric $Bmab$ (LTO) structure is found. Interestingly, upon re-oxidation, the material reaches and stays in the tetragonal intermediate phase but does not recover the orthorhombic symmetry observed for $Nd_2NiO_{4.25}$. A contrario, the phase diagram at equilibrium^[17] is shown in the range $d=0.05-0.25$ in **Figure 2.7.b**. The tetragonal intermediate phase is found for $d=0.05-0.10$, as in the out-of-equilibrium phase diagram yet, from the evolution of cell parameters with the excess oxygen content, several orthorhombic phase are proposed in the range $d=0.15-0.25$.

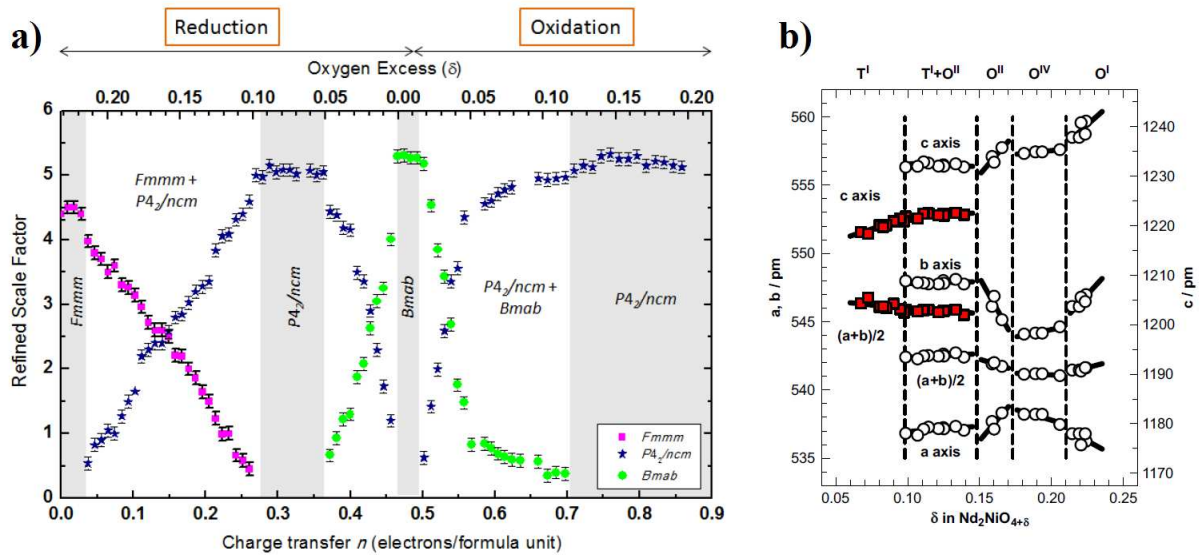


Figure 2.7 – (left) Refined scale factor as a function of charge transfer and oxygen excess, from the electrochemical intercalation experiment followed in situ by powder neutron diffraction^[16]. Regions in grey represent single-phase regions while white represent biphasic regions. (right) Variation of the lattice parameters at room-temperature of Nd_2NiO_{4+d} with the excess oxygen content d ^[17].

Similarly to the La_2CoO_{4+d} composition, an incommensurate structure is found for the most-oxidized $Nd_2NiO_{4.25}$ phase, as evidenced by single-crystal neutron diffraction. A reconstruction of the scattering plan ($hk4$) from the work of Wahyudi et al.^[16] is shown in **Figure 2.8**. The incommensurate modulation vector has been determined to be $q = 0.78 a^* + 0.56 b^*$, which is a value comparable with what have been found for incommensurate $La_2CoO_{4.14}$.

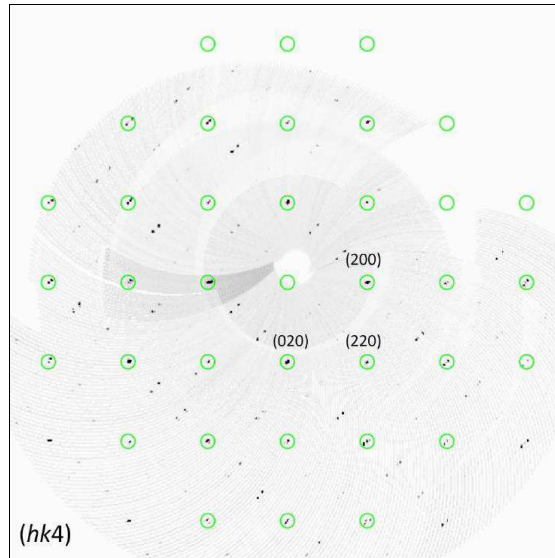


Figure 2.8 – Reconstructed $(hk4)$ scattering plan of $\text{Nd}_2\text{NiO}_{4.25}$ from single-crystal neutron diffraction data^[16]. Bragg peaks are marked with a green circle; other reflections are incommensurate satellites. The incommensurate modulation vector has been determined to be $q = 0.78 a^* + 0.56 b^*$.

Concerning the magnetic properties of the $\text{Nd}_2\text{NiO}_{4+d}$ phases, an antiferromagnetic ordering of the nickel sublattice has been found for stoichiometric $\text{Nd}_2\text{NiO}_{4.0}$ in the temperature range from $T=130\text{-}320\text{K}$, with magnetic moments toward the $[100]$ direction^[18-20]. At $T=130\text{K}$, the structure undertake a phase transition from the low-temperature orthorhombic (LTO) $Bmab$ structure to the low-temperature tetragonal (LTT) $P4_2/nm$ structure. Below $T=4\text{K}$, the neodymium sublattice becomes also antiferromagnetically ordered with moments toward the $[-110]$ direction, while magnetic moments of the nickel atoms are toward the $[110]$ direction. The magnetic structures in the ranges $T=130\text{-}320\text{K}$ and below $T=4\text{K}$ are shown in **Figure 2.9**. No evidence of magnetic ordering was found in the non-stoichiometric phases of $\text{Nd}_2\text{NiO}_{4+d}$ ^[21].

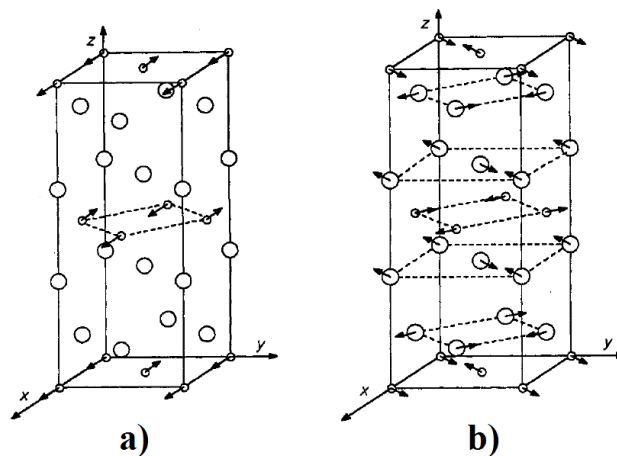


Figure 2.9 – Schematic representation of the magnetic structures of $\text{Nd}_2\text{NiO}_{4.0}$ (a) in the range $T=130\text{-}320\text{K}$ (nickel sublattice only) and (b) below $T=4\text{K}$ ^[20].

2.2. Atomistic simulations of $\text{RE}_2\text{MO}_{4+d}$ ionic conductors

After a structural overview of phases of the $\text{RE}_2\text{MO}_{4+d}$ family, we will shortly introduce the theoretical work undertaken to simulate their diffusing behavior, with a particular focus on atomistic simulations.

2.2.1. Simulation methods and models of $\text{RE}_2\text{MO}_{4+d}$ materials

A foreword. Properly simulating the physical properties of a system is directly dependent on properly simulating the electronic structure, hence the crystalline structure, of a system. Yet there is a fundamental difference between crystalline structures, as described in crystallography, and the structural models used in atomistic calculations. In the calculations, structures must be exact, meaning that there is no partial occupancy of a site by an atom – there is an atom, or there is not. As a consequence, and in particular for materials with defects as $\text{RE}_2\text{MO}_{4+d}$ phases, defect positions must be localized and the symmetry applied to the calculation, if any, is in general lower than the symmetry of the crystallographic average description from experiments. We also remark that, for *ab initio* calculations, due to limited computing power, only a few inequivalent atoms can be simulated – which means in the case of the $\text{RE}_2\text{MO}_{4+d}$ family that high- d incommensurate phases cannot be simulated. Considering these two major limitations – the full occupancy of sites and the limited number of inequivalent atoms –, the play in atomistic calculations is to find a relevant approximation of the real material structure to use as model structure. Hence all the results of a calculation are valid in the limit where the structural model is accurate enough to properly describe the real material.

In literature, there are two predominant approaches to simulate the diffusive properties of phases of the $\text{RE}_2\text{MO}_{4+d}$ family.

The first one is atomistic calculations of model structures to estimate the formation energy of defects involved in the diffusion process, and estimate the potential energy barrier on a known diffusion pathway, through calculation of saddle state structures, as for example the work of Minervini et al.^[22] and Frayret et al.^[23] on the $\text{La}_2\text{NiO}_{4+d}$ phases. Such calculations are generally performed in the DFT framework, on small structural models of a few hundred atoms, and at $T=0\text{K}$.

The second approach is molecular dynamics calculations, *i.e.* calculations of a structure evolution with time, in order to find diffusion pathways and estimate the macroscopic diffusion coefficients. These calculations are generally performed with classical mechanics using potential models to describe the electronic interactions between atoms, and involve extended structural models of several thousand atoms, at a set temperature. We quote as an example the work of Kilner et al. on numerous phases of the $\text{RE}_2\text{MO}_{4+d}$ family as $\text{La}_2\text{NiO}_{4+d}$ ^[24], $\text{Pr}_2\text{NiO}_{4+d}$ ^[25] and $\text{La}_2\text{CoO}_{4+d}$ ^[26]. We remark that, in classical molecular dynamics, the potential energy landscape is calculated only once at the initial step of the

simulation. Regardless, high-temperature classical molecular dynamics have been proven to be effective in the calculation of macroscopic diffusion coefficients and, as an example of the many results they yield, we show in **Figure 2.10** the evolution of the diffusion coefficients upon oxygen hyperstoichiometry in $\text{Pr}_2\text{NiO}_{4+d}$ simulated at $T=1100\text{K}$ ^[25].

We remark that most simulations performed on the $\text{RE}_2\text{MO}_{4+d}$ phases to calculate oxygen diffusion are designed for the high-temperature regime of diffusion, to get a direct correspondance with the operating temperature of fuel cells, and a direct comparison of calculated diffusion coefficients with experimental ones. In the high-temperature regime, phases of $\text{RE}_2\text{MO}_{4+d}$ are best described in the high-temperature tetragonal (HTT) parent phase, and so are the structural models used in calculations, with a random distribution of excess oxygen atoms on interstitial sites.

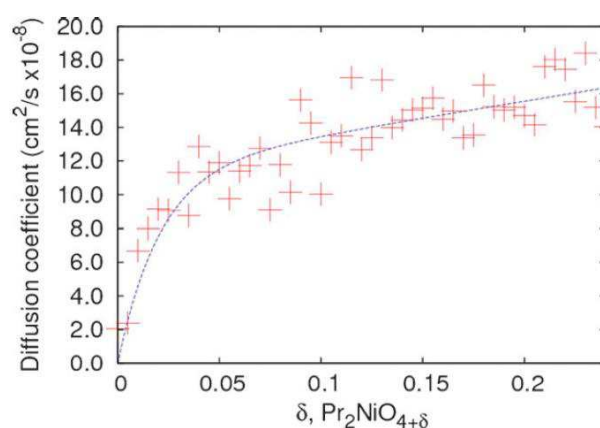


Figure 2.10 – Calculated diffusion coefficient with respect to the oxygen hyper-stoichiometry in $\text{Pr}_2\text{NiO}_{4+d}$, from classical molecular dynamics calculations at $T=1100\text{K}$. Figure from reference [25].

2.2.2. The interstitialcy mechanism as dominant process in the high-temperature regime

A fundamental result from classical molecular dynamics of $\text{RE}_2\text{MO}_{4+d}$ phases at high-temperature, which have been supported by atomistic calculations and diffraction experiments, is that the dominant process of diffusion in the high-temperature regime is the interstitialcy mechanism^[24-27]. The interstitialcy mechanism is a two-step diffusion process, schematized in **Figure 2.11**, where the interstitial oxygen atom pushes one of the four apical oxygen atoms in its vicinity to a neighboring vacant interstitial site, then recombine on the newly vacant apical oxygen site.

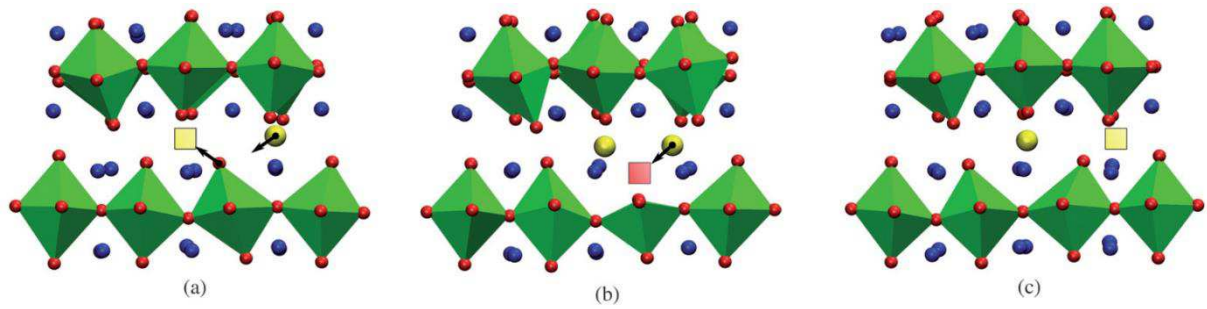


Figure 2.11 – Snapshot of a typical diffusion process occurring during a molecular dynamics simulation of $\text{La}_2\text{NiO}_{4+d}$ at $T=900\text{K}$ and $d=0.09$. Only a small subset of ions is plotted to aid visualization. Lanthanum ions are represented by blue spheres, nickel-oxygen polyhedra are plotted in green and individual oxygen ions represented by red spheres, or yellow in the case of interstitial ions. Vacant sites relevant to the diffusion process are indicated by red and yellow squares. Figure from reference [24]. (a) and (c) represent structure prior and after the diffusion event, and (b) represent the saddle state structure.

The diffusion pathway associated with the interstitialcy mechanism can be directly observed from the cumulative trajectory from molecular dynamics calculation, and is shown for $\text{Pr}_2\text{NiO}_{4+d}$ ^[25] in **Figure 2.12**, along with supporting diffraction data on Pr_2NiO_4 -based oxide^[28].

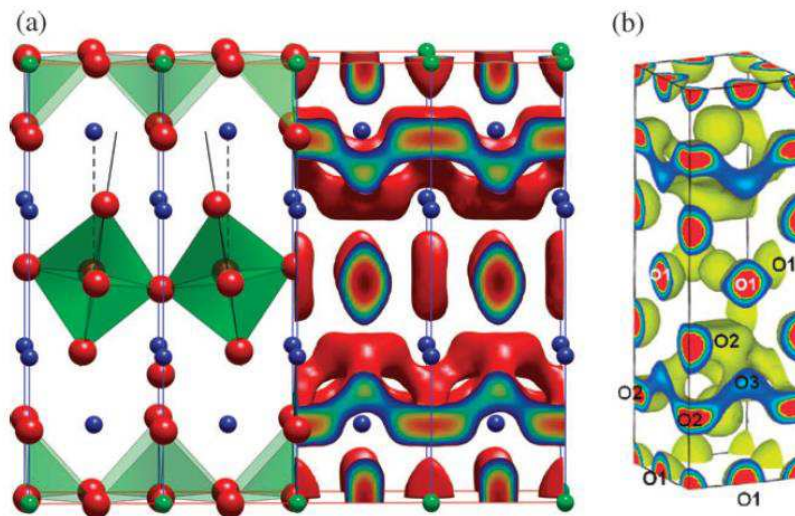


Figure 2.12 – (a) Crystal structure of $\text{Pr}_2\text{NiO}_{4+d}$ (O ions in red, NiO_6 octahedra in green and Ni ions in blue, the c-axis is the vertical axis) and the isosurface connecting the O diffusion sites in the a-b plan from MD at $T=1100\text{K}$ and $d=0.09875$. Figure from reference [25]. (b) Isosurface of nuclear density at $0.05 \text{ fm}\cdot\text{\AA}^{-3}$ of a Pr_2NiO_4 -based oxide at $T\approx 1280\text{K}$, reconstructed using the maximum entropy method on neutron powder diffraction data. Figure from reference [28].

2.3. Oxide ion diffusion at moderate-temperature: the concept of lattice activated diffusion

We have seen in **section 2.2** the theoretical description of oxygen diffusion in $\text{RE}_2\text{MO}_{4+d}$ in the high-temperature regime, and the relevance of the atomistic simulations in describing both the microscopic motion and the macroscopic diffusing behavior. However, most of calculations are performed on the high-temperature parent phase HTT, using a classical Newtonian approach to simulate the phases, hence with a framework that cannot take into account the structural complexity, thus are not fit to describe the room-temperature structures and their associated dynamical and diffusive properties.

In order to introduce theoretical concepts of oxygen mobility in $\text{RE}_2\text{MO}_{4+d}$ and related material, in the room- and moderate-temperature range, we will now describe the phonon-assisted diffusion, a microscopic mechanism where low-lying lattice dynamics promote diffusion events. This behavior have been evidenced by comparison of $\text{SrFeO}_{2.5}$ and $\text{CaFeO}_{2.5}$ brownmillerites, through a joint study with time-of-flight inelastic neutron scattering and first-principle DFT calculations. After a short introduction on the structure of brownmillerite phases, we will describe the phonon assisted diffusion mechanism, and present the analogy with the $\text{RE}_2\text{MO}_{4+d}$ materials, in particular with $\text{La}_2\text{CuO}_{4+d}$ and $\text{Nd}_2\text{NiO}_{4+d}$.

2.3.1. Phonon assisted diffusion mechanism: the case of $(\text{Sr,Ca})\text{FeO}_{2.5}$ brownmillerites

The Brownmillerite structure $\text{ABO}_{2.5}$, represented in **Figure 2.13**, can be described as a deficient perovskite with alternating octahedral and tetrahedral layers, in which the tetrahedra are corner-sharing and form a 1D ordered vacancy channels. While some materials such as $\text{SrFeO}_{2.5}$ or $\text{SrCoO}_{2.5}$ are mixed ionic-electronic conductors and can be obtained by room-temperature electrochemical red/ox reaction from perovskites^[29-31], some compounds as $\text{BaInO}_{2.5}$ or $\text{SrSc}_{0.5}\text{Ga}_{0.5}\text{O}_{2.5}$ show pure ionic conductivity.

Atoms of the tetrahedral chains are usually slightly shifted away from the ideal perovskite positions due to cooperative rotation of tetrahedra within the chains. Since these displacements are minor, the two possible rotation directions, arbitrarily called right (R) and left (L), lead to almost similar ground state energies, allowing an easy switch of the rotation and loose tetrahedra dynamics. Depending on the correlation length of the tetrahedra cooperative rotation and the organization of neighboring chains along the b-axis, the structure is best described in fully-ordered space-groups as $Pnma$ and $I2mb$, or in partially-disordered space-group $Imma$, as represented in **Figure 2.14**.

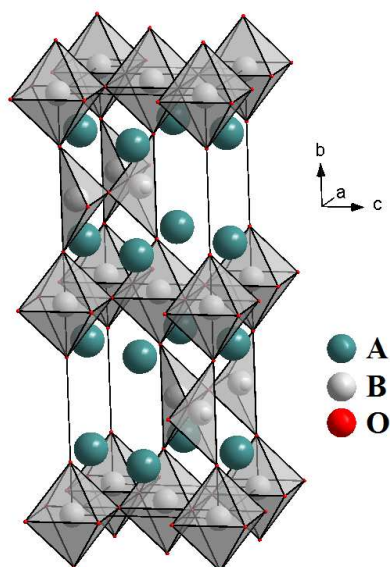


Figure 2.13 – Brownmillerite structure $ABO_{2.5}$, represented here the $Pnma$ space-group, in a $(2\sqrt{2}; 2\sqrt{2}; 2)$ representation in respect to the perovskite cell. The structure can be seen as a stacking of corner-sharing BO_6 tetrahedra layers and corner-sharing BO_4 tetrahedra layers. The 1D vacancy channels can be seen along the a direction.

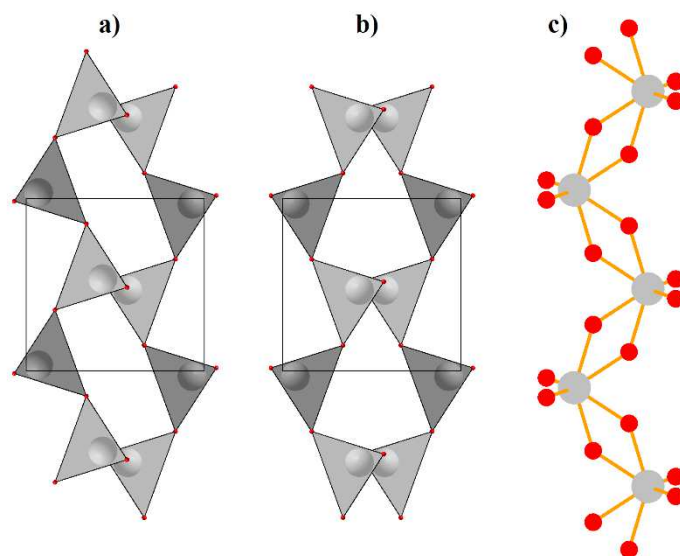


Figure 2.14 – Tetrahedra chain arrangements for the three space-groups describing the brownmillerite phases, projected along the b -axis. For figures (a) and (b), two chains respectively at $y=0.75$ and $y=0.25$ are represented. In the $Pnma$ space-group (a), all the chains have the same rotation (R-R or L-L). In the $I2mb$ space-group (b), neighboring chains along the b -axis show alternating rotation (R-L). In the average description of the $Imma$ space-group (c), oxygen sites along the tetrahedra chain are split.

While the high-temperature regime of oxygen diffusion in brownmillerites can be accurately described, as for the perovskites, with the vacancy mechanism, the highly anisotropic low-temperature counterpart cannot be described in this framework.

Paulus et al. have shown, from the compared study of the oxygen-conducting brownmillerite $\text{SrFeO}_{2.5}$ and non-conducting $\text{CaFeO}_{2.5}$, that a phonon-assisted diffusion is best to describe the unusual fast oxygen transport at low-temperature^[32]. Such results were drawn from joint inelastic neutron scattering and *ab initio* molecular dynamics. Indeed, the lattice dynamics, through generalized phonon densities of states, can be measured experimentally with time-of-flight neutron spectroscopy, and can be calculated from molecular dynamic trajectories, as shown in **Figure 2.15**. In this mechanism, lattice dynamics associated with the relaxation and cooperative motion of polyhedra locally assists the conduction of oxygen atoms.

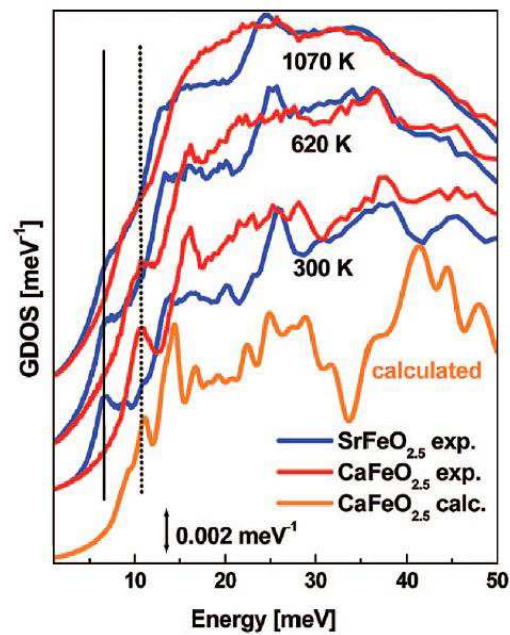


Figure 2.15 – Experimental generalized phonon densities of states (gDOS) of $\text{SrFeO}_{2.5}$ (blue) and $\text{CaFeO}_{2.5}$ (red) obtained from inelastic neutron scattering performed on the IN6 spectrometer at ILL (Grenoble, France) at different temperatures vertically shifted for clarity: 300K (bottom), 620K (middle), and 1070K (top). The orange spectrum reports the calculated DOS for $\text{CaFeO}_{2.5}$ at 0K. The low energy mode was found at 7 meV for $\text{SrFeO}_{2.5}$ independent of the temperature (vertical solid line); for $\text{CaFeO}_{2.5}$, below the $Pnma \rightarrow Imma$ phase transition (300 and 620 K), it appears at 12 meV (vertical dotted line), being softened to 9 meV above the transition (1070 K). Figure from reference [32].

The apical oxygen atoms (bridging octahedra and tetrahedra) exhibit large displacements and can eventually fall into vacancy channels of the tetrahedra layer, as schematized in **Figure 2.16**. The shallow potential allowing this displacement is determined by the Fe-O bond strength, directly linked to the length of the b-axis, and is reinforced by a low-lying breathing mode along the b-axis. The local arrangement is thus changed from a configuration octahedron-tetrahedron (**Figure 2.16.a**), to a configuration square pyramid-reoriented tetrahedron (**Figure 2.16.b**): the structure is able to dynamically accommodate multiple polyhedral configurations. A pronounced lattice dynamics is associated to the tetrahedra

chains, showing a marked switching behavior, which promotes the mobile oxygen from a tetrahedron to another along the chain. In comparison, the isostructural and non-conducting $\text{CaFeO}_{2.5}$, whose \mathbf{b} -axis is shorter than the one of $\text{SrFeO}_{2.5}$, shows slower dynamics with less active modes, and need higher temperatures to reach comparable diffusing ability.

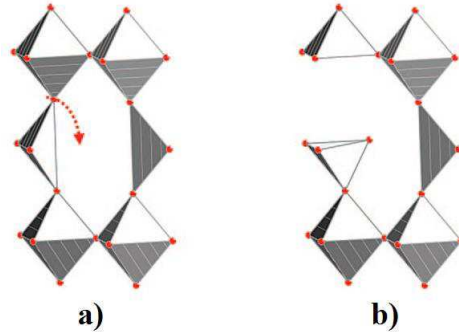


Figure 2.16 – Local rearrangement of the polyhedral configuration when the apical oxygen atom falls into the vacancy channel. Figure from reference [32].

In summary, the phonon assisted diffusion mechanism explain the enhanced mobility in a partially-filled lattice, through the coupling of low-lying phonon modes with single-particle atomic motions of the diffusive specie – these low-lying lattice dynamics being directly linked to structural instabilities.

2.3.2. Mobility and structural instability: the case of $\text{La}_2\text{CuO}_{4+d}$

A similar concept as the one of phonon assisted diffusion can be used to describe the non-classical room-temperature mobility observed in the $\text{La}_2(\text{Cu,Ni,Co})\text{O}_{4+d}$ ^[33-35] and, in particular, have been evidenced to take place in $\text{La}_2\text{CuO}_{4+d}$ system^[36].

As introduced in **chapter 1**, it has been shown that the apical oxygen atoms of the CuO_6 octahedra in the $\text{La}_2\text{CuO}_{4.07}$ phase are dynamically delocalized on a circle of 1\AA diameter. This structural instability is evidenced by the comparison of nuclear density maps at $T=20\text{K}$ and $T=300\text{K}$, reconstructed by maximum entropy method (MEM) from single-crystal neutron diffraction data, as shown in **Figure 2.17**. We can observe in the figure that the apical oxygen atom delocalization from its high-symmetry position is cross-shaped in the $[100]$ direction at $T=20\text{K}$ – with respect to the F-cell –, while the delocalization is circular at room-temperature, hence there is a dynamical $[110]$ delocalization growing with temperature. Similarly for the interstitial oxygen atom, its position is well defined at low-temperature while a cross-shape delocalization toward the $[110]$ direction is found at room-temperature. This structural instability brings, dynamically, the oxygen atom closer to empty interstitial sites, which reduce the length of the diffusion pathway and, *a priori*, promote diffusion hopping events.

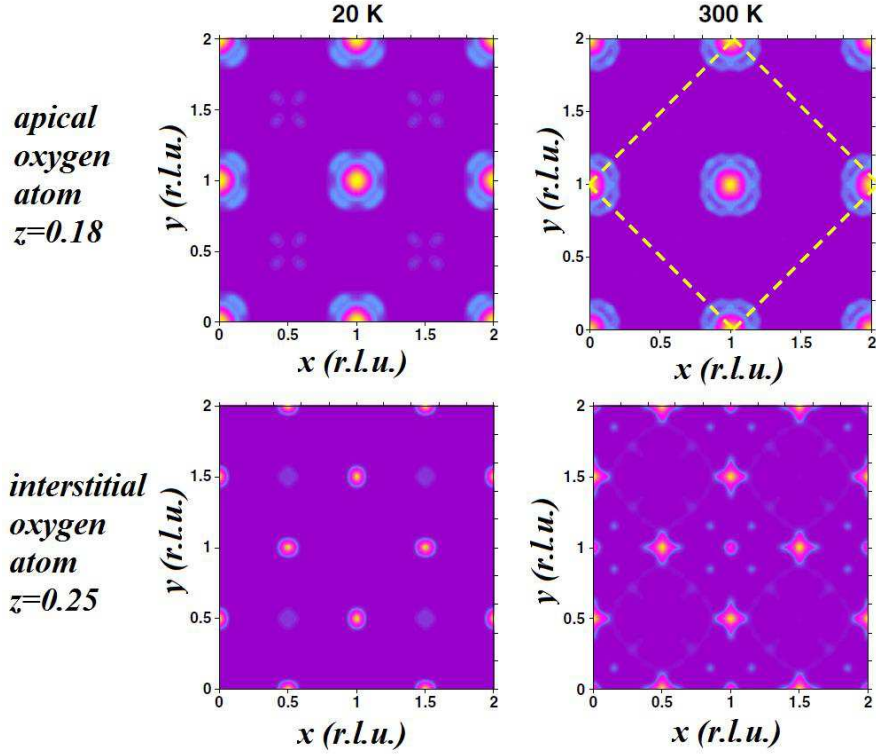


Figure 2.17 – Nuclear scattering densities obtained from $\text{La}_2\text{CuO}_{4.07}$ twinned single-crystal by neutron diffraction studies and subsequent reconstruction using the maximum entropy method at $T=20\text{K}$ and ambient temperature. Sections of the apical oxygen layer at $z=0.18$ and of the interstitial site layer at $z=0.25$. The F -cell is outlined for the figure at $z=0.18$ and $T=300\text{K}$. Figure from reference [36].

Ab initio phonon calculations have been performed on stoichiometric $\text{La}_2\text{CuO}_{4.0}$ and non-stoichiometric $\text{La}_2\text{CuO}_{4+d}$, showing that the presence of excess oxygen induces an overall stiffening of the lattice dynamics, yet with a significant activation of lanthanum and apical oxygen atom displacements toward the $[110]$ direction even at low-energy^[36]. Such results imply that excess oxygen atoms, through their impact on lattice dynamics and in particular the activation of vibrational modes with displacements toward the $[110]$ direction – hence toward the diffusion pathway – are promoting the mobility of apical oxygen atoms, and thus the diffusion. This microscopic model involves the same diffusion pathway as the one described in the interstitialcy mechanism in the high-temperature regime.

As mentioned in **chapter 1**, the analogy with the $\text{Nd}_2\text{NiO}_{4+d}$ composition is straightforward, since on one hand the $\text{Nd}_2\text{NiO}_{4+d}$ can adapt a greater amount of excess oxygen atoms, up to $d=0.25$, and on the other hand shows a larger delocalization of apical oxygen atoms at RT, on a circle with 2\AA diameter instead of 1\AA diameter for $\text{La}_2\text{CuO}_{4.07}$, as shown in **Figure 2.18**.

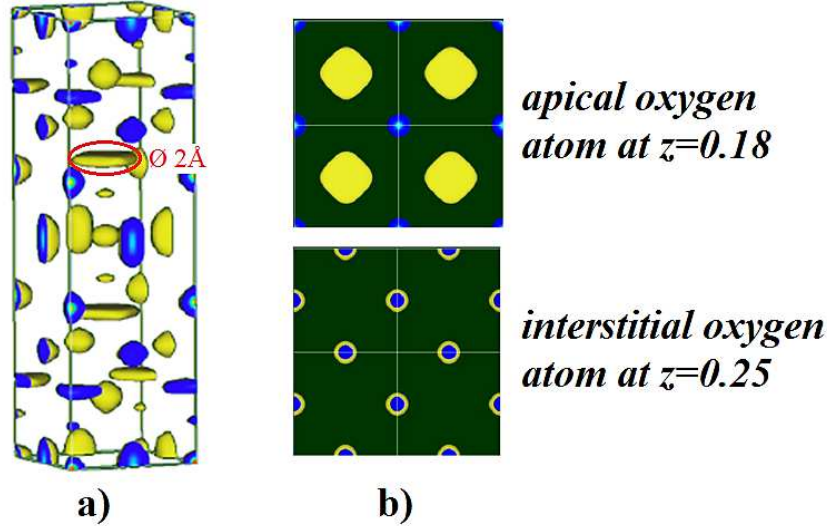


Figure 2.18 – Nuclear scattering densities obtained from $\text{Nd}_2\text{NiO}_{4.25}$ twinned single-crystal by neutron diffraction studies and subsequent reconstruction using MEM at room-temperature. a) 3D structure in the I-cell. b) Sections of the apical oxygen layer at $z=0.18$ and interstitial layer at $z=0.25$. Figure from reference [16].

2.4. Choice of investigation methods of $\text{Nd}_2\text{NiO}_{4+d}$ in the moderate-temperature regime & outline of the thesis

Through this chapter, we have provided an overview of structures of the $\text{RE}_2\text{MO}_{4+d}$ family, shown signatures of their complexity at room- and low-temperature, presented calculation methods to simulate the oxygen diffusion in the high-temperature regime, and introduced the concept of phonon assisted diffusion to describe the oxygen mobility in the room- to moderate-temperature regimes.

We remind that the aim of this work is the determination of the dominant mechanism of non-classical oxygen diffusion in the moderate-temperature regime, *i.e.* at temperatures where the phases of $\text{Nd}_2\text{NiO}_{4+d}$ cannot be describe in the high-temperature tetragonal (HTT) structure, where long-range structural correlations are still observed, and where, from analogy with the phonon-assisted diffusion, there is a strong assumption that structural instabilities and their impact on lattice dynamics play a role on the diffusion process.

As a consequence, the investigation of the $\text{Nd}_2\text{NiO}_{4+d}$ phases is focused on the correlations between structural instabilities induced by the oxygen hyper-stoichiometry and their subsequent effects on the lattice dynamics and role in promoting oxygen diffusion in the moderate-temperature regime.

From the phase diagram of $\text{Nd}_2\text{NiO}_{4+d}$, we have selected three stoichiometries corresponding to the three-single phases, respectively $\text{Nd}_2\text{NiO}_{4.0}$, $\text{Nd}_2\text{NiO}_{4.10}$ and $\text{Nd}_2\text{NiO}_{4.25}$, which will be the reference phases investigated throughout the following chapters. In particular, the high- d incommensurate $\text{Nd}_2\text{NiO}_{4.25}$ phase will be investigated as a function of temperature using single-crystal neutron and X-ray synchrotron diffraction.

Since atomistic simulations have been proven effective in the investigation of oxygen diffusion in $\text{RE}_2\text{MO}_{4+d}$ phases, we will use them extensively to characterize the $\text{Nd}_2\text{NiO}_{4+d}$ phases. However, due to the presumed importance of structural instabilities, we have chosen to perform all atomistic simulations in the framework of the density functional theory, including the molecular dynamics (MD) calculations, in order to properly simulate the competing interactions that may generate instabilities, and so despite the limitation of number of atoms. Indeed, the potential energy landscape is recalculated at each step of an *ab initio* molecular dynamics, *a contrario* from classical molecular dynamics where the potential is only calculated at the initial step. Thus *ab initio* molecular dynamics have the advantage of considering instantaneous structures, and include the effective variations of potential energy landscapes with atomic displacements.

Limited number of atoms implies questionable approximations on the structural models used in our calculations, especially as we are investigating a temperature regime where the statistic of diffusion events is too small to calculate diffusion coefficients. However, we will discuss other macroscopic values with experiments by comparing calculated inelastic structure factors and associated phonon densities of states with our experiments of inelastic neutron scattering.

Actually, inelastic neutron scattering is the method of choice to investigate lattice dynamics. We will thus perform time-of-flight and three-axis neutron spectroscopy to back-up our atomistic simulations and provide experimental evidences of the effect of oxygen hyperstoichiometry on the lattice dynamics of $\text{Nd}_2\text{NiO}_{4+d}$ phases.

Including the **chapter 1** of introduction, the thesis is composed of eight chapters. The **chapter 2** herebefore have presented the state of the art knowledge about the $\text{Nd}_2\text{NiO}_{4+d}$ material, in particular structures of the three single-phases $\text{Nd}_2\text{NiO}_{4.0}$, $\text{Nd}_2\text{NiO}_{4.10}$ and $\text{Nd}_2\text{NiO}_{4.25}$. We have summarized theoretical studies on oxygen ion conductors of the $\text{RE}_2\text{MO}_{4+d}$ family, with $\text{RE}=\text{La},\text{Nd},\text{Pr}$ and $\text{M}=\text{Ni},\text{Cu},\text{Co}$, and show their relevance and limitations for the study of moderate temperature diffusion. We have also introduced the concept of phonon assisted diffusion to describe non-classical oxygen diffusion at low-temperature. In the **chapter 3**, we will describe the synthesis of the $\text{Nd}_2\text{NiO}_{4+d}$ materials, introduce the prerequisite concepts and theories associated with the experiments and calculations we performed, and describe the instruments we used for diffraction and spectroscopic experiments. The **chapter 4** is dedicated to neutron and synchrotron diffraction experiments on fully oxidized $\text{Nd}_2\text{NiO}_{4.25}$ single-crystals, with a focus on phase transition and temperature dependence of incommensurate satellites. The **chapter 5** gathers the theoretical analysis we performed on the $\text{Nd}_2\text{NiO}_{4+d}$ system, explaining structural models we used to describe room-temperature structures, presenting the results of *ab initio* phonon calculations and molecular dynamics

simulations, as well as results from positional recurrence maps (PRM), a code we developed to post-process trajectories from MD. In the **chapter 6** we will present results from time-of-flight (TOF) inelastic neutron spectroscopy performed on powders of $\text{Nd}_2\text{NiO}_{4.0}$, $\text{Nd}_2\text{NiO}_{4.10}$ and $\text{Nd}_2\text{NiO}_{4.25}$, in particular the dependence of phonon density of states with oxygen hyperstoichiometry and temperature, and the comparison with theoretical results. The **chapter 7** is dedicated to neutron inelastic three-axis spectroscopy (TAS) experiments performed on a single-crystal of $\text{Nd}_2\text{NiO}_{4.25}$. We will present phonon dispersion curves, analysis of inelastic spectra and compare them with theoretical results. Finally the **chapter 8** will provide conclusions and perspectives on the results obtained during this thesis.

2.5. Bibliography

1. Greenblatt, M. (1997). *Current Opinion in Solid State and Materials Science*, 2(2), 174-183.
2. Houchati, M.I., Ceretti, M., Ritter, C., and Paulus, W. (2012). *Chemistry of Materials*, 24(19), 3811-3815.
3. Skinner, S.J. (2003). *Solid State Sciences*, 5(3), 419-426.
4. Kharton, V.V., Viskup, A.P., Kovalevsky, A.V., Naumovich, E.N., and Marques, F.M.B. (2001). *Solid State Ionics*, 143(3-4), 337-353.
5. Kilner, J.A. and Shaw, C.K.M. (2002). *Solid State Ionics*, 154-155(0), 523-527.
6. Skinner, S.J. and Kilner, J.A. (1999). *Ionics*, 5(3-4), 171-174.
7. Skinner, S.J. and Kilner, J.A. (2000). *Solid State Ionics*, 135(1-4), 709-712.
8. Kharton, V., Viskup, A.P., Naumovich, E.N., and Marques, F.M.B. (1999). *Journal of Materials Chemistry*, 9(10), 2623-2629.
9. Vashook, V.V., Tolochko, S.P., Yushkevich, I.I., Makhnach, L.V., Kononyuk, I.F., Altenburg, H., Hauck, J., and Ullmann, H. (1998). *Solid State Ionics*, 110(3-4), 245-253.
10. Bassat, J.M. (2002). Paper presented at the Fifth European Solid Oxide Fuel Cell Forum, Luzern, Switzerland.
11. Boehm, E. (2000). Paper presented at the Fourth European Solid Oxide Fuel Cell Forum, Luzern, Switzerland.
12. Tranquada, J.M., Kong, Y., Lorenzo, J.E., Buttrey, D.J., Rice, D.E., and Sachan, V. (1994). *Physical Review B*, 50(9), 6340-6351.
13. Le Dréau, L. (2011). *Université de Rennes 1, PhD thesis 4366*.
14. Le Dréau, L., Prestipino, C., Hernandez, O., Schefer, J., Vaughan, G., Paofai, S., Perez-Mato, J.M., Hosoya, S., and Paulus, W. (2012). *Inorganic Chemistry*, 51(18), 9789-9798.
15. Anissimova, S., Parshall, D., Gu, G.D., Marty, K., Lumsden, M.D., Chi, S., Fernandez-Baca, J.A., Abernathy, D.L., Lamago, D., Tranquada, J.M., and Reznik, D. (2014). *Nature Communications*, 5, 3467.
16. Wahyudi, O. (2011). *Université de Rennes 1, PhD thesis 4468*.
17. Ishikawa, K., Metoki, K., and Miyamoto, H. (2009). *Journal of Solid State Chemistry*, 182(8), 2096-2103.

18. Batlle, X., Martínez, B., Obradors, X., Pernet, M., Vallet, M., González-Calvet, J., and Alonso, J. (1992). *Journal of Magnetism and Magnetic Materials*, 104–107, Part 2(0), 918-920.
19. Batlle, X., Obradors, X., and Martnez, B. (1992). *Physical Review B*, 45(6), 2830-2843.
20. Rodríguez-Carvajal, J., Fernández-Díaz, M.T., Martínez, J.L., Fernández, F., and Saez-Puche, R. (1990). *Europhysics Letters*, 11(3), 261.
21. Buttrey, D.J. and Honig, J.M. (1988). *Journal of Solid State Chemistry*, 72(1), 38-41.
22. Minervini, L., Grimes, R.W., Kilner, J.A., and Sickafus, K.E. (2000). *Journal of Materials Chemistry*, 10(10), 2349-2354.
23. Frayret, C., Villesuzanne, A., and Pouchard, M. (2005). *Chemistry of Materials*, 17(26), 6538-6544.
24. Chroneos, A., Parfitt, D., Kilner, J.A., and Grimes, R.W. (2010). *Journal of Materials Chemistry*, 20(2), 266-270.
25. Parfitt, D., Chroneos, A., Kilner, J.A., and Grimes, R.W. (2010). *Physical Chemistry Chemical Physics*, 12(25), 6834-6836.
26. Kushima, A., Parfitt, D., Chroneos, A., Yildiz, B., Kilner, J.A., and Grimes, R.W. (2011). *Physical Chemistry Chemical Physics*, 13(6), 2242-2249.
27. Yashima, M., Sirikanda, N., and Ishihara, T. (2010). *Journal of the American Chemical Society*, 132(7), 2385-2392.
28. Yashima, M., Enoki, M., Wakita, T., Ali, R., Matsushita, Y., Izumi, F., and Ishihara, T. (2008). *Journal of the American Chemical Society*, 130(9), 2762-2763.
29. Le Toquin, R., Paulus, W., Cousson, A., Prestipino, C., and Lamberti, C. (2006). *Journal of the American Chemical Society*, 128(40), 13161-13174.
30. Nemudry, A., Rudolf, P., and Schöllhorn, R. (1996). *Chemistry of Materials*, 8(9), 2232-2238.
31. Takeda, Y., Kanno, R., Takada, T., Yamamoto, O., Takano, M., and Bando, Y. (1986). *Zeitschrift für anorganische und allgemeine Chemie*, 540(9-10), 259-270.
32. Paulus, W., Schober, H., Eibl, S., Johnson, M., Berthier, T., Hernandez, O., Ceretti, M., Plazanet, M., Conder, K., and Lamberti, C. (2008). *Journal of the American Chemical Society*, 130(47), 16080-16085.
33. Le Toquin, R., Paulus, W., Cousson, A., Dhahlenne, G., and Revcolevschi, A. (2004). *Physica B: Condensed Matter*, 350(1–3, Supplement), E269-E272.
34. Paulus, W., Cousson, A., Dhahlenne, G., Berthon, J., Revcolevschi, A., Hosoya, S., Treutmann, W., Heger, G., and Le Toquin, R. (2002). *Solid State Sciences*, 4(5), 565-573.
35. Paulus, W., Heger, G., Rudolf, P., and Schöllhorn, R. (1994). *Physica C: Superconductivity*, 235–240, Part 2(0), 861-862.
36. Villesuzanne, A., Paulus, W., Cousson, A., Hosoya, S., Le Dréau, L., Hernandez, O., Prestipino, C., Ikbel Houchati, M., and Schefer, J. (2012). *Journal of Solid State Electrochemistry*, 15(2), 357.

Chapter 3. Synthesis, Theory & Experimental methods.

The current chapter will gather every prerequisite concepts and explanations necessary to understand the experiments and results described in the following chapter.

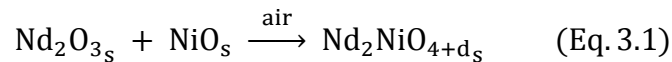
Firstly, in **section 3.1**, we address the synthesis routes to obtain powders and single-crystals of the $\text{Nd}_2\text{NiO}_{4+d}$ phases, and how to control the excess oxygen stoichiometry. In **section 3.2**, we introduce the basis of powder and single-crystal diffraction, and describe the diffractometer we used. In **section 3.3**, we refer to the founding principles involved in the density functional theory (DFT) based simulations we performed, and in **section 3.4** we describe in detail the positional recurrence map code we developed to post-process molecular dynamic calculations. Lastly, in **section 3.5**, we describe the theory of inelastic neutron scattering and detail the neutron spectrometers used for our experiments in **section 3.6**.

3.1. Synthesis of $\text{Nd}_2\text{NiO}_{4+d}$ phases

Synthesis routes, for both ceramics and crystal samples, were developed and optimized prior to the PhD work described here. Particularly, single-crystals of $\text{Nd}_2\text{NiO}_{4+d}$ used for diffraction and three-axis neutron spectroscopy experiments were grown and fully characterized in our lab and are described in literature^[1].

3.1.1. Solid-state synthesis

Polycrystalline $\text{Nd}_2\text{NiO}_{4+d}$ was prepared by conventional solid state method, from reactants Nd_2O_3 (Alfa Aesar, 0.99) and NiO (Alfa Aesar, 0.99) in stoichiometric proportions, according to the reaction:



Due to the hygroscopic nature of the reactants, the Nd_2O_3 powder was heated under dynamic primary vacuum at $T=1170\text{K}$ in a tubular furnace overnight, while the NiO powder was dried at $T=390\text{K}$ in an oven in the same time.

The stoichiometric amount of the reactants was first mixed in ethanol then grinded for 4 hours in an agate mechanical mill. The light-blue powder was heated in an alumina crucible under air at $T=1470\text{K}$ in a tubular furnace overnight, and afterwards furnace cooled to $T=350\text{K}$. The resulting black powder was grinded with an agate mechanical mill for 2 hours, pressed into pellets of about 2.0g, and sintered under air at $T=1470\text{K}$ overnight. This step was repeated

twice. In this way the black sintered powder of $\text{Nd}_2\text{NiO}_{4+d}$ (NNO4x) has an oxygen excess d of about $d=0.23-0.25$.

The purity of the NNO4x powder samples was confirmed by conventional X-ray diffraction. Data was collected with a powder diffractometer X-Pert Pro II Philips, using the copper K_α wavelength of $\lambda=1.54056\text{\AA}$ in a Bragg-Brentano geometry. Diffractogram is shown in **Figure 3.1**. The cell parameters obtained through fitting are $a=5.378(1)\text{\AA}$, $b=5.463(1)\text{\AA}$ and $c=12.385(1)\text{\AA}$, in the $Fmmm$ space-group, corresponding to the fully oxidized $\text{Nd}_2\text{NiO}_{4.25}$. No impurity phases are detected.

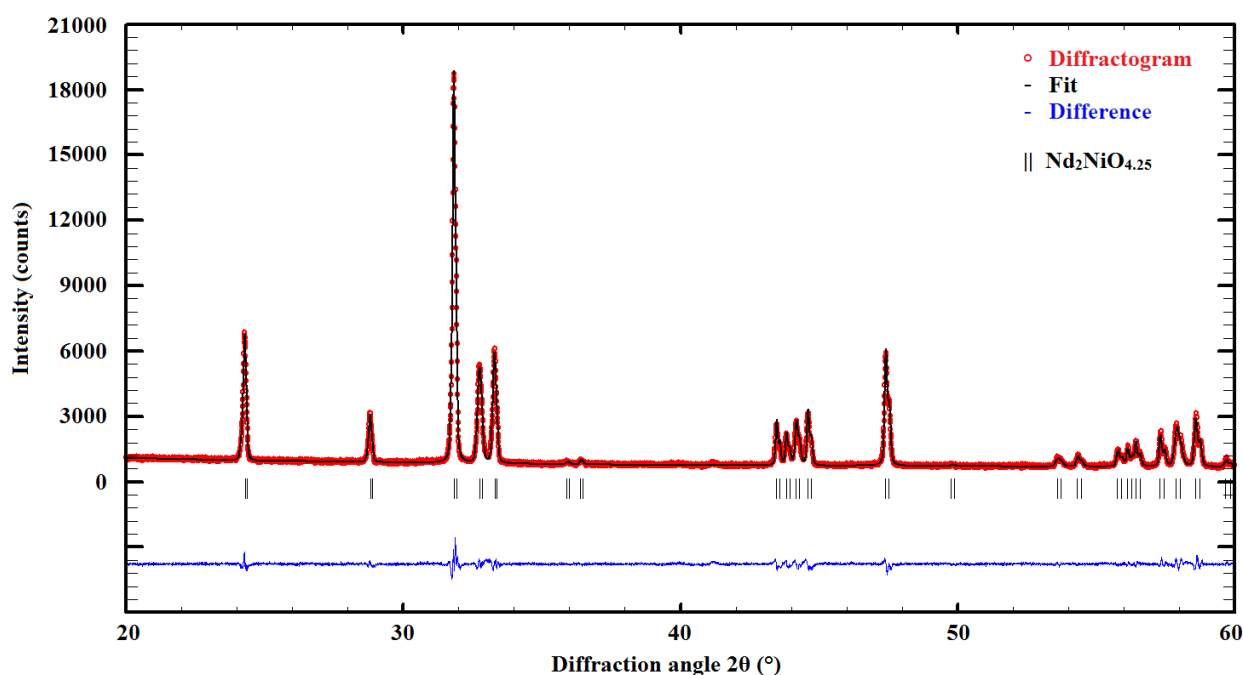


Figure 3.1 – Diffractogram of $\text{Nd}_2\text{NiO}_{4.25}$ powder, refined in the $Fmmm$ space-group, with fitted cell parameters $a=5.378(1)\text{\AA}$, $b=5.463(1)\text{\AA}$ and $c=12.385(1)\text{\AA}$.

3.1.2. Control over excess oxygen d

Since our interest goes on the three-single phases of $\text{Nd}_2\text{NiO}_{4+d}$, respectively $\text{Nd}_2\text{NiO}_{4.0}$, $\text{Nd}_2\text{NiO}_{4.10}$ and $\text{Nd}_2\text{NiO}_{4.25}$, we are interested in ways to reach these stoichiometries from the as-grown powder.

Let untreated in an uncontrolled environment, the as-grown powder shows a growing impurity phase of Nd_2O_3 after some time. In order to stabilize and fix the fully-oxidized $\text{Nd}_2\text{NiO}_{4.25}$, further thermic treatment are necessary: first a grinding and sintering at 1470K under air in a tubular furnace, then a sintering at 670K under flow of oxygen in a quartz reactor for 48h. The samples are then sealed in oxygen rich environment awaiting the experiments. After treatment, the diffractogram is the same as the one shown in **Figure 3.1**.

The $\text{Nd}_2\text{NiO}_{4.10}$ powder was obtained from grinding NNO_4x and sintering it at 1070K under dynamic primary vacuum in a quartz reactor for 48h. The samples are then sealed in oxygen-free environment. The diffractogram of $\text{Nd}_2\text{NiO}_{4.10}$ is shown in **Figure 3.2**, fitted in the $P4_2/nm$ space-group with cell parameters $a=b=5.465(1)\text{\AA}$ and $c=12.216(1)\text{\AA}$. In the neutron time-of-flight spectroscopy experiments, for the low temperature part of the experiment from $T=150\text{-}310\text{K}$, the $\text{Nd}_2\text{NiO}_{4.10}$ sample was prepared as previously described. However, for the high-temperature part from $T=310\text{-}1070\text{K}$, the $\text{Nd}_2\text{NiO}_{4.10}$ sample was made *in situ* during the experiments from reduction from the $\text{Nd}_2\text{NiO}_{4.25}$ sample (the sample holder being under dynamic secondary vacuum).

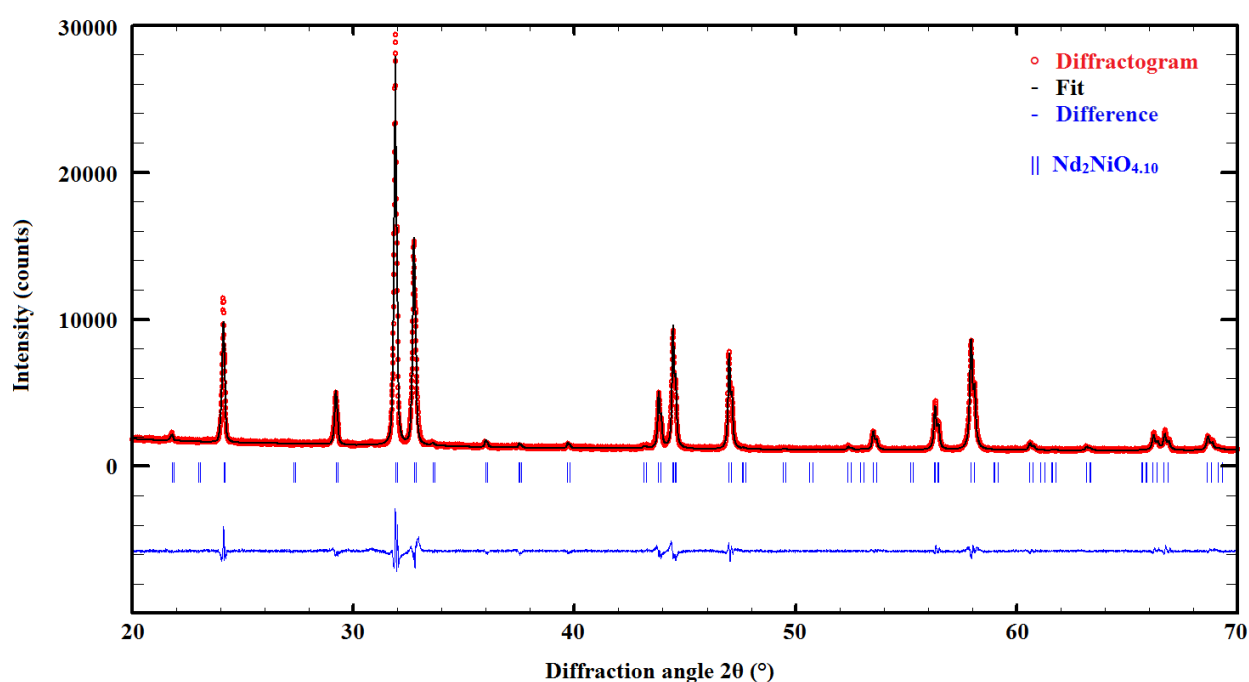


Figure 3.2 – Diffractogram of $\text{Nd}_2\text{NiO}_{4.10}$ powder, refined in the $P4_2/nm$ space-group, with fitted cell parameters $a=b=5.465(1)\text{\AA}$ and $c=12.216(1)\text{\AA}$.

The $\text{Nd}_2\text{NiO}_{4.0}$ powder was obtained from reduction of NNO_4x pellets at 670K under flow of CO/CO_2 with ratio 1/10 in a tubular furnace overnight. $\text{Nd}_2\text{NiO}_{4.0}$ was then grinded in a glove box and sealed in oxygen-free containers. The diffractogram of $\text{Nd}_2\text{NiO}_{4.0}$ is shown in **Figure 3.3**, fitted in the $Bmcb$ space-group with cell parameters $a=5.386(1)\text{\AA}$, $b=5.591(1)\text{\AA}$ and $c=12.124(1)\text{\AA}$. The diffractogram shows traces of NiO, meaning that the material is slightly over-reduced.

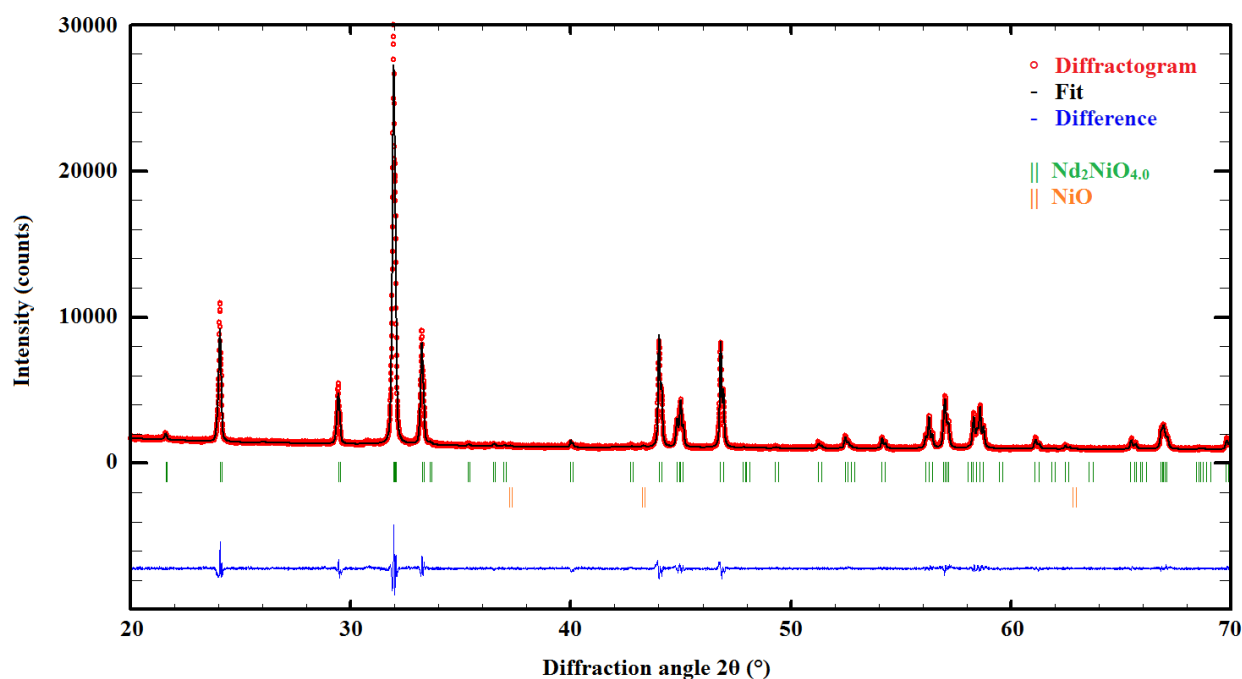


Figure 3.3 - Diffractogram of $\text{Nd}_2\text{NiO}_{4.0}$ powder, refined in the $Bmcb$ space-group, with fitted cell parameters $a=5.386(1)\text{\AA}$, $b=5.591(1)\text{\AA}$ and $c=12.124(1)\text{\AA}$.

3.1.3. Single-crystal growth

While a lot of useful information can be determined from scattering experiments on powders, single-crystal samples are needed to investigate accurately the long-range ordering through incommensurate reflexions, and the specific \mathbf{Q} -dependence of the dynamics.

Crystals were grown using the traveling solvent floating zone (TSFZ) technique, with a NEC SC3-MDH11020 mirror furnace in vertical configuration, as pictured in **Figure 3.4**, well adapted to the growth of oxides. The furnace is composed of two gold-coated ellipsoidal mirrors which focus the light on a millimetric spot of the feed rod, which reach temperatures higher than $T=3000\text{K}$ and melt. The melt crystallize epitaxially at the solid-liquid interface on a single-crystal seed, thus forming a growing single-crystal when the ceramics feed rod is shifted through the melting zone.

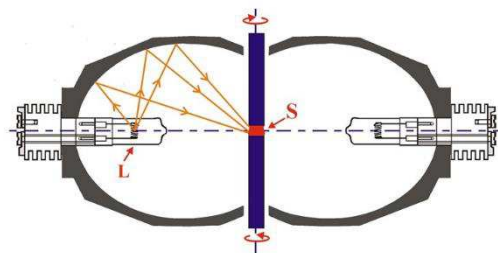
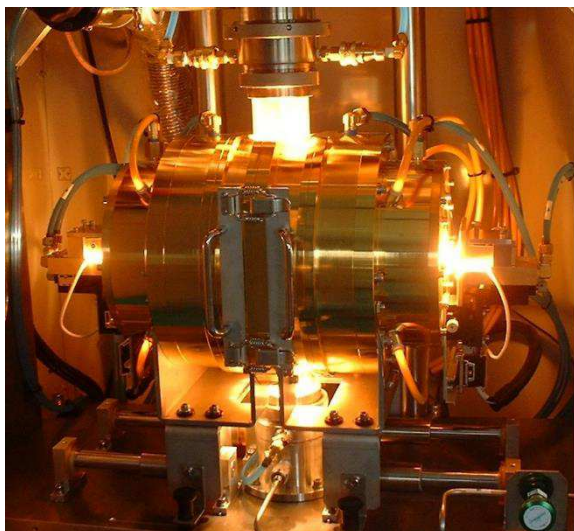


Figure 3.4 – (Left) Picture of the actual NEC SC3-MDH11020 mirror furnace used to grow the single-crystals of $\text{Nd}_2\text{NiO}_{4+d}$. (Right) Scheme of the mirror furnace, where *L* is the halogen lamps and *S* the melting zone. Figure from reference [1].

Stabilizing the melting zone and growing an homogeneous crystals of well-defined stoichiometry is a challenging task due to the number of, interfering, experimental parameters. In order to obtain single-crystals of $\text{Nd}_2\text{NiO}_{4+d}$ with $d=0.22-0.23$, with final length of 80-90mm and $\text{Ø}=6.5\text{mm}$, as pictured in **Figure 3.5**, the rotating speed of the feed and the seed rod were set to 30 rpm, with a growth speed of 2-3mm/h, and an oxygen rich atmosphere was applied. Ceramics composing the feed rod was prepared as described in **section 3.1.1**, with an extra step of grinding, compacting in a latex capillary with a 10Mpa hydrostatic pressure, and annealing.



Figure 3.5 – As-grown single-crystal of $\text{Nd}_2\text{NiO}_{4+d}$, with $d=0.22-0.25$, obtain through TSFZ growth on the NEC SC3-MDH11020 mirror furnace. The single-crystal is homogeneous and one-time twinned. Figure from reference [1].

Several trials to reduce the as-grown single-crystal from the (about) fully-oxidized state, to the single-phases $\text{Nd}_2\text{NiO}_{4.10}$ and $\text{Nd}_2\text{NiO}_{4.0}$ were performed by mean of electrochemistry, as it has been done on $\text{La}_2\text{CoO}_{4+d}$ single-crystals^[2]. However, due to time required for such reduction (about 5 months) to get single-crystal big enough to perform neutron spectroscopy, and due to the very easy and irreversible formation of Nd_2O_3 oxide, as well as the strong strain on the structure switching from orthorhombic to tetragonal, both making the cristal extremely brittle, we didn't manage to get single-crystals of $\text{Nd}_2\text{NiO}_{4.10}$ nor $\text{Nd}_2\text{NiO}_{4.0}$.

3.2. Powder and single-crystal diffraction – Theory & Instrumentation

3.2.1. Basis of X-ray and neutron diffraction

The analysis of crystalline materials by diffraction methods is based on the interaction of waves with a crystal particles – electromagnetic waves with electron clouds of atoms in the case of X-rays diffraction, and neutrons with atomic nuclei in the case of neutron diffraction. Due to the periodical ordering of the structure, the diffracted waves exhibit interference phenomena. From the geometric arrangement of coherently diffracted waves, structural informations can be obtained. The crystal structure can be described as a sum of lattice planes constituted by symmetrically ordered point-like particles, each plane being defined by their Miller indices (hkl) , representing their intersection with the crystallographic axis a , b and c . Diffraction phenomena, thus the coherent interference of waves with crystal planes, is observed when the geometric condition known as Bragg law is fulfilled, as shown in **equation 3.2** and **Figure 3.6**, where d_{hkl} is the distance between parallel lattice planes, θ the diffraction angle between the incident wave and lattice plane, n a natural integer and λ the wavelength. Thus, the spatial arrangement of diffracted waves give informations on the interplanar distance d_{hkl} , hence cell parameters of a crystal structure.

$$2 d_{hkl} \sin\theta = n\lambda \quad (\text{Eq. 3.2})$$

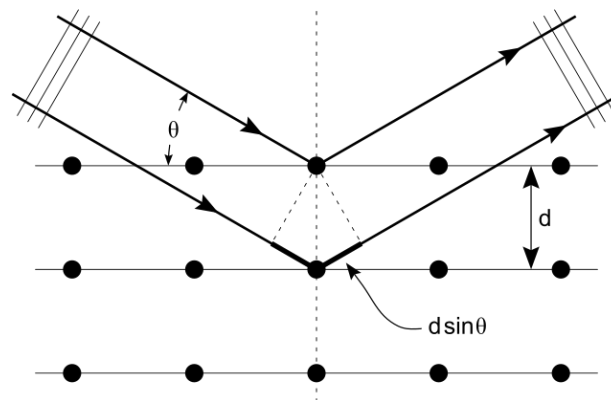


Figure 3.6 – Geometric representation of Bragg law, with d the interplanar distance and θ the diffraction angle.

Basically, the structure can be defined as its density $\rho(\mathbf{r})$ of electrons – or nuclei – throughout the crystal, with \mathbf{r} the three-dimensional position vector. Scattering intensities are related to the Fourier transform of the density $\rho(\mathbf{r})$, thus we define $F(\mathbf{q})$ the Fourier transform of $\rho(\mathbf{r})$ with $\mathbf{q} = \vec{k}_i - \vec{k}_f$ the three-dimensional position vector in reciprocal space. The relations between $\rho(\mathbf{r})$ and $F(\mathbf{q})$ are shown in **equation 3.3** and **equation 3.4**.

$$\rho(\mathbf{r}) = \frac{1}{V} \sum_{\mathbf{q}} F(\mathbf{q}) e^{-2\pi i \mathbf{q} \cdot \mathbf{r}} \quad (\text{Eq. 3.3})$$

$$F(\mathbf{q}) = \int \rho(\mathbf{r}) e^{2\pi i \mathbf{q} \cdot \mathbf{r}} d\mathbf{r} \quad (\text{Eq. 3.4})$$

Considering structures as three-dimensional arrangements of point-like particles, the scattering function $F(\mathbf{q})$ can be rewritten as shown in **equation 3.5**, where f_N is the form factor of atom N . Scattering intensities are proportional to the square modulus of the scattering function, as shown in **equation 3.6** – through diffraction, the information on atomic phases is lost.

$$F(\mathbf{q}) = \sum_N f_N e^{2\pi i \mathbf{q} \cdot \mathbf{r}_N} \quad (\text{Eq. 3.5})$$

$$I(\mathbf{q}) \propto |F(\mathbf{q})|^2 \quad (\text{Eq. 3.6})$$

In the case of X-ray diffraction, the spatial extension of electronic clouds is of similar order with the wavelength, hence the X-ray atomic form factor is dependent with the scattering angle θ . In the case of neutron scattering, the spatial extension of nuclei is several order of magnitude lower than the wavelength, hence the neutron atomic form factor is constant with the scattering angle θ . The scattering length of the ions constituting Nd_2NiO_4 , with respect to x-rays and neutrons, are shown in **Tableau 3.1**.

Tableau 3.1 – Scattering lengths in X-ray and neutron diffraction of O, Ni and Nd ions.

Element	Atomic number Z	X-rays (fm) $2\theta=0$	Neutrons (fm)
O^{2-}	8	28	5.803
Ni^{2+}	28	73	10.3
Nd^{3+}	60	160	7.69

3.2.2. Twinning in $\text{Nd}_2\text{NiO}_{4+d}$ single-crystals

As mentioned in **chapter 2**, the K_2NiF_4 -type oxides have the ideal $I4/mmm$ tetragonal symmetry, as observed for $\text{Nd}_2\text{NiO}_{4+d}$ in the high-temperature parent phase. Hence, during the growth of the single-crystal by travelling solvent floating zone method, as described in **section 3.1.3**, the crystal, upon cooling down, goes through a transition from tetragonal to orthorhombic. The lowering of the symmetry implies the loss of one or more symmetry elements, which will be the twinning law describing the orientation of each twin with respect to the others.

In the $\text{Nd}_2\text{NiO}_{4+d}$ case, the transition from tetragonal to orthorhombic comes from the long-range ordering of NiO_6 octahedra tilts upon cooling. Such ordering will slightly differentiate the \mathbf{a} and \mathbf{b} cell parameters ($\mathbf{a} < \mathbf{b}$), leading to the loss of the 4-fold axis and of the [110] mirror plans, the [110] mirror plan being the boundary between two twins and, thus, the twinning law. Since the twin law does not belong to the point group, the twinning is called non-merohedral. Yet, since the \mathbf{a} and \mathbf{b} cell parameters stay close, some Bragg reflexion are overlapping, and the

twinning is called pseudo-merohedral. If only one $[110]$ mirror plan is lost during the tetragonal to orthorhombic transition, the crystal is one-time twinned with two twin domains; if the two $[110]$ mirror plans are lost, the crystal is two-time twinned with four twin domains. A scheme of the $(hh0)$ scattering plan in the case of one- and two-time twinned $\text{Nd}_2\text{NiO}_{4+d}$ crystal is shown in **Figure 3.7**^[3].

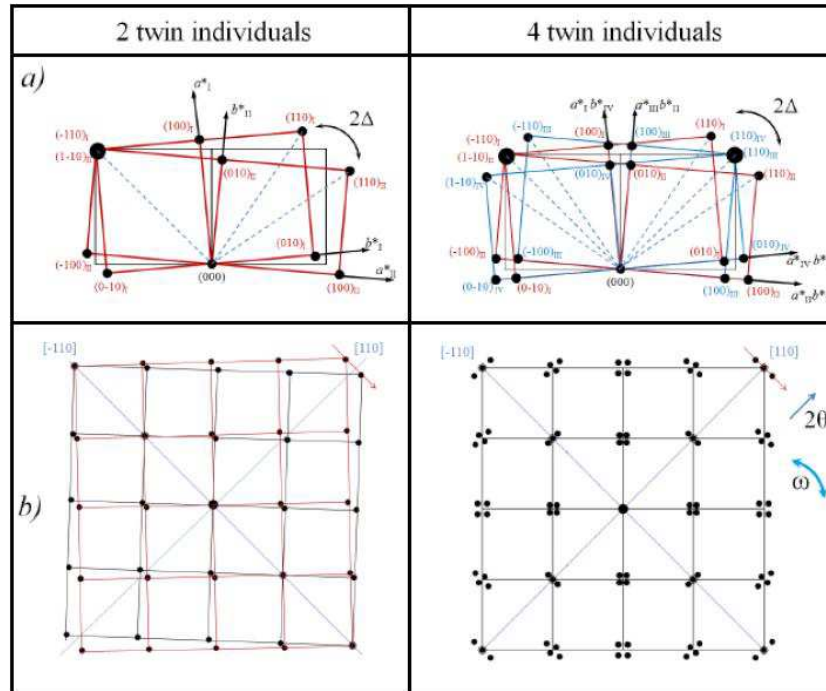


Figure 3.7 – Schematic representation of the twinning law in $\text{Nd}_2\text{NiO}_{4+d}$ in the case of (left) one-time twinned crystal, and (right) two-time twinned crystal^[3]. Figures (a) show the loss of the $[110]$ mirrors, and figures (b) show the corresponding $(hh0)$ scattering plans. We note that the splitting 2Δ is directly linked to the orthorhombicity, with $\Delta = \tan^{-1}(a/b) - \tan^{-1}(b/a)$, and can be directly measured by an ω -scan.

3.2.3. Neutron diffractometer D19

The large structures diffractometer D19 is a monochromatic thermal neutron single-crystal diffractometer at the Laue-Langevin Institute, optimized to measure crystals with unit cell edges ranging from 10 to 50Å. D19 is a high-flux high-resolution instrument, and incorporates a very large 2D banana position-sensitive detector (PSD), allowing resolution of 0.19° horizontally and 0.12° vertically. The sample is placed at the center of an Euler cradle, which can accommodate a compact cryostat to cool the sample down to $T=20\text{K}$. A scheme of the instrument is shown in **Figure 3.8**.

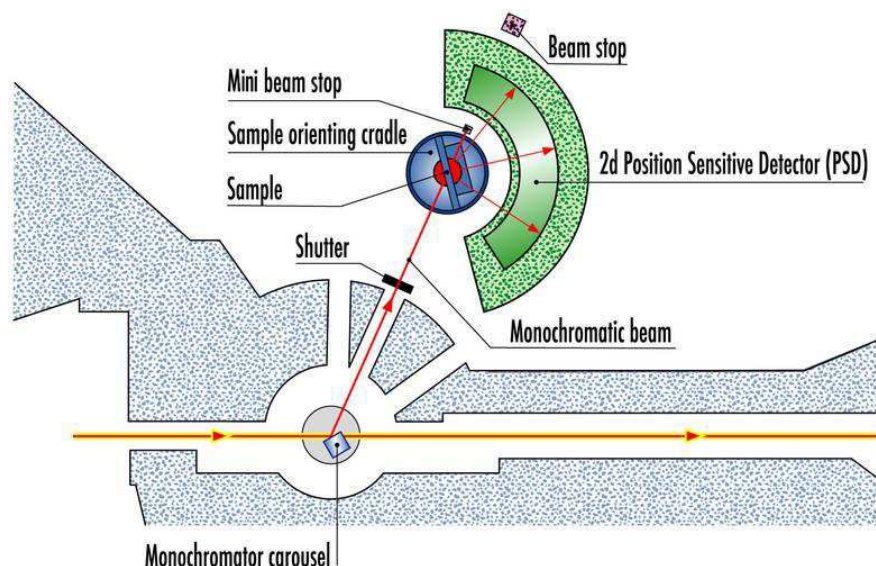


Figure 3.8 – Scheme of the thermal neutron single-crystal diffractometer D19 at the Laue-Langevin Institute^[4].

During our experiments, we used monochromatic wavelengths of $\lambda=1.46\text{\AA}$ and $\lambda=0.95\text{\AA}$, respectively with reflexion of the neutron beam on a Cu(220) monochromator with a takeoff angle of 70° , and with a Cu(331) monochromator and a takeoff angle of 90° .

The $\lambda=1.46\text{\AA}$ wavelength was chosen due to its subsequent high-flux, in order to get a good set of data on incommensurate satellites of $\text{Nd}_2\text{NiO}_{4.25}$, while the $\lambda=0.95\text{\AA}$ wavelength, with only half the maximum flux available, was chosen to collect the Bragg reflexions with lower resolution but higher momentum transfert.

3.2.4. Synchrotron radiation on BM01A

The station Bending Magnet 01A is the Swiss-Norwegian diffraction line at the European Synchrotron Radiation Facility (ESRF), optimized for high resolution single-crystal diffraction using the high-flux of the synchrotron radiation. Through a set of vertically focusing mirror and horizontally focusing monochromator, schemed in **Figure 3.9**, it achieves highly intense X-Ray beam of size $0.5 \times 0.5 \text{mm}^2$ on the sample, with spectral range from 6-22keV. The single-crystal diffractometer is based on the PILATUS2M detector, which combines the advantages of pixel area detector with flexible goniometry and easy re-positioning. The setup can accomodate an Oxford Cryostream700+ blower to reach temperatures on the sample of $T=80\text{-}500\text{K}$, a heat blower for $T=\text{RT}\text{-}1270\text{K}$, or a flow cryostat for $T=5\text{-}300\text{K}$.

During our experiments, in order to minimize the absorption of the sample, the wavelength was set to $\lambda=0.663055\text{\AA}$, corresponding to an energy of about $E=18.7\text{keV}$.

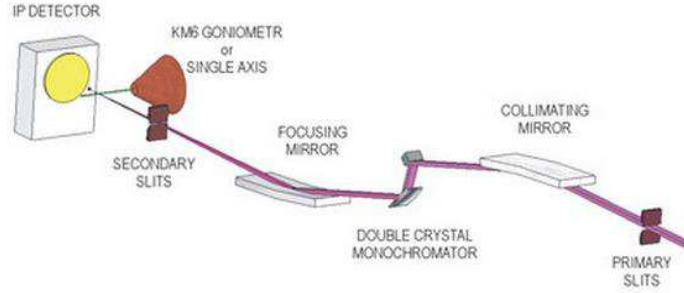
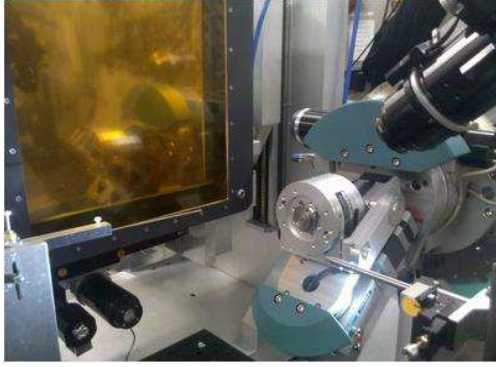


Figure 3.9 – (left) Picture of the sample environment, showing the PILATUS2M detector, the single-axis of the sample holder, the collimator nose and the beam stop. (right) Optics from the bending magnet to the detector.

3.3. Density-functional theory

All calculations described in **chapter 5** were performed in the framework of density functional theory (DFT), using the VASP code^[5, 6]. Post-processing of *ab initio* data were performed using the PHONON code^[7], the nMoldyn code^[8, 9], and Matlab^[10] for the codes we developed. Hereafter are summarized founding principles and final equations of the DFT, on which are based the calculations we performed.

3.3.1. HK and KS theorems

To understand a material's properties, in most of the case, one has to properly describe the electronic structure of the material. An exact description of the electronic structure is the non-relativistic Schrödinger equation, for multi-electron wavefonctions, reported in **equation 3.7** in the approximation of Born-Oppenheimer.

$$\left\{ -\frac{\hbar^2}{2m} \sum_j \nabla_j^2 - \sum_{j,l} \frac{Z_l e^2}{|r_j - R_l|} + \frac{1}{2} \sum_{j \neq j'} \frac{e^2}{|r_j - r_{j'}|} - E \right\} \Psi = 0, \quad (\text{Eq. 3.7})$$

Where r_j are the electron positions, R_l and Z_l the positions and atomic numbers of atoms, E the energy and Ψ the wavefunction.

While the equation's solutions are exact, the solving, in computing science, is limited by the number of electrons. Assuming N the number of electrons, and p the number of parameters per variables to reach the aimed accuracy, the number of parameters involved in the calculation is M , as reported in **equation 3.8**. The exponentially growing number of parameters limits the size of the system to a few effective electrons, which make this equation ineffective for an extended system such as crystalline solids.

$$M = p^{3N} \quad (\text{Eq. 3.8})$$

To reduce the number of parameters, methods considering the electronic density instead of the wavefunction were developed, in the 30s by Thomas-Fermi, and latter in the 60s with the Density Functional Theory (DFT).

The DFT is founded on three principles: the Hohenberg-Kohn theorem (HK1)^[11], the variational principle of Hohenberg-Kohn (HK2), and the Kohn-Sham auto-coherent equations (KS)^[12]. While HK1 and HK2 establish a direct link between the electronic density and the fundamental state of the system, an issue remains on the choice of the functional: the exact electronic kinetic energy is not known due to inter-electronic interactions. However, the solution proposed by Hartree, formerly for wavevectors, of considering a set of equations of single electron in effective potential^[13] can be applied. In this way, the HK1 theorem, described in **equation 3.9** is reformulated in **equation 3.10**.

$$E[n(\vec{r})] = T[n(\vec{r})] + \int n(\vec{r}) v_{ext}(\vec{r}) d^3r + U[n(\vec{r})] \quad (\text{Eq. 3.9})$$

$$E[n(\vec{r})] = T_S[n(\vec{r})] + \int n(\vec{r}) v_{eff}(\vec{r}) d^3r + E_{Hartree}[n(\vec{r})] + E_{XC}[n(\vec{r})] \quad (\text{Eq. 3.10})$$

Where $E[n(\vec{r})]$ is the total energy, $T[n(\vec{r})]$ and $T_S[n(\vec{r})]$ respectively the electronic kinetic energy with and without interaction, v_{ext} and v_{eff} the external potential and effective external potential as described in **equation 3.11**, and $U[n(\vec{r})]$ the total potential energy, separated in a mean field term $E_{Hartree}[n(\vec{r})]$ and an exchange-correlation term $E_{XC}[n(\vec{r})]$.

$$v_{eff}(\vec{r}) = v_{ext}(\vec{r}) + \int \frac{n(\vec{r}')}{|\vec{r} - \vec{r}'|} d^3r' + v_{xc}(\vec{r}) \quad (\text{Eq. 3.11})$$

Where $v_{xc}(\vec{r})$ the local potential of exchange-correlation, as described in **equation 3.12**, depending only on the density of distribution $\tilde{n}(\vec{r})$.

$$v_{xc}(\vec{r}) = \frac{\delta}{\delta \tilde{n}(\vec{r})} E_{xc}[\tilde{n}(\vec{r})] |_{\tilde{n}(\vec{r})=n(\vec{r})} \quad (\text{Eq. 3.12})$$

To solve the kinetic energy issue, the KS approach states that a system of non-interacting electrons can be exactly described by an antisymmetric wavefunction of the type of Slater determinant. This approach implies that the real system can be described by the Hamiltonian H_S of a system of free electrons in a local effective potential V_{KS} . The eigenvectors of the H_S Hamiltonian can be expressed as Kohn-Sham orbitals, as for the Hartree-Fock theory, in the form of Slater determinants, where the mono-electronic orbitals are linked to the electronic density. The variational principle HK2 is applied to the **equation 3.10**, which leads to the Kohn-Sham equations, reported in **equation 3.13**, which are basically a set of coupled partial differential equations. The effective potential of the poly-electronic system is thus directly linked the electronic density, which depends of Kohn-Sham orbitals $\varphi(\vec{r}_i)$, themselves depending on the potential V_{KS} .

$$\left[-\frac{1}{2}\nabla^2 + V_{KS} - \epsilon_i\right]\varphi(\vec{r}_i) = 0 \quad \equiv \quad [H_{KS} - \epsilon_i]\varphi(\vec{r}_i) = 0 \quad (\text{Eq. 3.13})$$

Thus the final form of the ground state energy is as reported in **equation 3.14**:

$$E[n(\vec{r})] = \sum_i \epsilon_i + E_{XC}[n(\vec{r})] - \int v_{xc}(\vec{r}) n(\vec{r}) d^3r - \frac{1}{2} \int \frac{n(\vec{r})n(\vec{r}')}{|\vec{r} - \vec{r}'|} \quad (\text{Eq. 3.14})$$

The Kohn-Sham formulation can be interpreted as the equivalent of the Hartree theory, where all the poly-electronic effect are included when v_{xc} and E_{XC} are exact. These two values being linked to the **equation 3.12**, the effectiveness of the DFT depends on the approximation of the exchange-correlation functional.

To summarize: from an approximate electronic density - i.e. a guess on the structure -, the potential V_{KS} is calculated and the differential equations for the wavefonctions $\varphi(\vec{r}_i)$ are solved. From these wavefonctions, a new electronic density is calculated, and this iterative process is repeated until convergence.

3.3.2. Exchange-correlation energy

The exchange-correlation energy can be approximated using two methods: the local density approximation (LDA), and the generalized gradient approximation (GGA).

The LDA describes an inhomogeneous electronic system as locally homogeneous, which allows the use of the exchange-correlation functional of a homogeneous electron gas, as reported in **equation 3.15**. Electronic density inhomogeneities, non-local exchange and correlation terms, and strong local correlation, cannot be described in this method. However systems with slowly varying density, as bulk metals, are properly described. Comparisons of experimental results with LDA calculations show accuracy on the exchange energy of about 10%, while the correlation energy is overestimated by a factor 2. Energies of atom ionization, dissociation and cohesion of molecules, are estimated at 10-20% of the experimental values, while the error of bond length is below 1%^[14].

$$E_{XC}^{LDA}[n(\vec{r})] = \int \epsilon_{xc}[n(\vec{r})] n(\vec{r}) d^3r \quad (\text{Eq. 3.15})$$

In order to consider density inhomogeneities, the GGA method was introduced, using different order of gradient density besides electronic density itself, as reported in **equation 3.16**.

$$E_{XC} = \int \epsilon_{xc}[n(\vec{r})] F_{XC}[n(\vec{r}), \nabla n(\vec{r}), \nabla^2 n(\vec{r}), \dots] n(\vec{r}) d^3r \quad (\text{Eq. 3.16})$$

At order zero, the exchange-correlation energy is similar at the one from LDA, $E_{XC}^0 = E_{XC}^{LDA}$, for which only the density $n(\vec{r})$ shall be calculated. At first order, the variables $n(\vec{r})$ and $\nabla n(\vec{r})$ shall be calculated independently; the approach is called generalized gradient, with $E_{XC}^1 = E_{XC}^{GGA}$.

To reach better accuracy, hybrid functionals were developed, using non-empirical coefficients as the PBE0 functional, empirical coefficients based on spectroscopic data as the B3LYP functional, or a mix of the Hartree-Fock exchange functional and GGA exchange-correlation functional.

The exchange-correlation functional used in the present work to simulate $\text{Nd}_2\text{NiO}_{4+d}$ is the Perdew, Burke and Ernzerhof (PBE)^[15], a GGA-type functional, which allows to calculate with a good accuracy the bulk properties and critical case, without neglecting weak interactions. The PBE functional is parametrized and depends on the density, the magnetization density when magnetic properties are calculated, and a gradient density.

3.3.3. Direct method for phonon calculations

While the DFT allows one to find the equilibrium structure of the material, which is the position of atoms R_i^0 , lattice dynamic considers however the instantaneous position $R_i = R_i^0 + u_i$, where u_i is the displacement vector. In the harmonic approximation, considering small displacements, electrons are in their fundamental states and the energy of the system depends only of nuclei positions, as described in **equation 3.17**. The classic approach of phonon mode calculation would be to construct the dynamical matrix from masses and force constants C_{ij} , themselves derived from forces on nuclei F_i and from energy $E(R_i)$, reported in **equation 3.18** to **equation 3.20**.

$$E = E(R_i) \cong E_{tot}^{harm}(R_i) = E_{tot}^0 + \frac{1}{2} \sum_{i,j} \left(\frac{d^2 E}{dR_i dR_j} \right) u_i u_j \quad (\text{Eq. 3.17})$$

$$F_i = \frac{dE}{du_i} \quad (\text{Eq. 3.18})$$

$$C_{ij} = \frac{d^2 E}{dR_i dR_j} = \frac{dF_i}{dR_j} \quad (\text{Eq. 3.19})$$

$$D_{ij}(\vec{q}) = \frac{C_{ij}(\vec{q})}{\sqrt{M_i M_j}} \quad (\text{Eq. 3.20})$$

Vibrational states come from the dynamical matrix determinant, reported in **equation 3.21**, where frequencies $\omega(\vec{q})$ shape the dispersion curves of phonons polarized along \vec{q} .

$$\det \left| \frac{1}{D_{ij}(\vec{q})} - \omega^2(\vec{q}) \right| = 0 \quad (\text{Eq. 3.21})$$

Several methods are available to calculate dispersion curves from DFT calculations, the most used being the linear response, implemented in the ABINIT^[16] code or the CASTEP^[17] module of Materials Studio^[18], and the direct method, implemented in the PHONON^[7] software, VASP^[5, 6] or Wien2k^[19] codes. In the present work, only the direct method was used, with the *ab initio* calculation on VASP and the post-treatment on PHONON.

Direct method is similar of classic approach from **equation 3.18** to **equation 3.21**, with Hellmann-Feynman (HF) forces calculated using DFT, on a set of structures with inequivalent atoms shifted away from equilibrium. HF forces are the forces felt by atom i when atom j is shifted by u_j , as reported in **equation 3.22**. If necessary an extended cell – supercell – is used to reach a minimum of 10Å in a, b and c, to limit self-interaction – when an atom interact with its equivalent from Born-von Karman boundary condition. Due to the supercell, **equation 3.22** becomes **equation 3.23**.

$$F_i = -C_{i,j}^p U_j \quad (\text{Eq. 3.22})$$

$$F_i = - \sum_{i \in SC} C_{i,j}^{SC} U_j \quad (\text{Eq. 3.23})$$

In order to reduce the number of parameters, force constants are split into a matrix for crystal symmetry $A_{i,j}$ and a matrix for potential forces $P_{i,j}$, as in **equation 3.24**. As such, the supercell symmetry – which is most of the time a subgroup of the conventional cell symmetry – and the potential forces are independent.

$$C_{i,j} (9 \times 1) = A_{i,j} (9 \times p) \times P_{i,j} (p \times 1) \quad (\text{Eq. 3.24})$$

Moving the atom affected by the force at the center of the supercell, the dynamical matrix becomes (**equation 3.25**):

$$D_j^{SC}(\vec{q}) = \frac{1}{\sqrt{M_i M_j}} \sum_{j \in SC} C_{0,j} e^{2\pi i \vec{q} \cdot \vec{R}_j} \quad (\text{Eq. 3.25})$$

The supercell allows calculating the exact phonon modes when the reach of interactions is smaller than half of the supercell. When interactions are more extended, phonon modes are exact only at specific points \vec{q}_s of high symmetry of the Brillouin zone, when condition **equation 3.26** is fulfilled, where L is the parameter of the supercell.

$$e^{-2\pi i \vec{q}_s \cdot \vec{L}} = 1 \quad (\text{Eq. 3.26})$$

Extending the supercell allows increasing the density of reciprocal space vectors \vec{q}_s , which means more points in between extrapolate dispersion curves. The size of the supercell has the only limit the computing resources, and is conventionally extended enough when force constants loose two or three order of magnitude along half of the supercell parameter.

3.3.4. MD & VACF

While first-principle phonon calculation is a very effective tool to probe the lattice dynamics of well defined systems, as can be the stoichiometric $\text{Nd}_2\text{NiO}_{4.0}$ at low-temperature, it reaches its limits for partially disordered, or partially delocalized systems as can be non-stoichiometric $\text{Nd}_2\text{NiO}_{4+d}$ at room-temperature. The main issue on these cases is that there is no unique most stable structure, due to the experimentally reported incommensurability, easy diffusion events, and shallow potential of apical oxygen atoms. Another approach to describe the dynamics of

these complex systems is through molecular dynamics calculations. Where first-principle calculation aim to find the most stable structure, molecular dynamics are solving the evolving Newton's equations of motion (**equation 3.27**), and thus give access to the microscopic behavior in time of a collection of atoms.

$$\ddot{\mathbf{R}}_I = -\frac{1}{M_I} \frac{\partial V}{\partial \mathbf{R}_I}(\mathbf{R}_1, \dots, \mathbf{R}_N) \quad I = 1, N \quad (\text{Eq. 3.27})$$

For a collection of N atoms with positions (R_1, R_2, \dots, R_N), with masses (M_1, M_2, \dots, M_N) and potential of interaction among them $V(\mathbf{R}_1, \mathbf{R}_2, \dots, \mathbf{R}_N)$. Finding an adequate description of the interatomic potential V on first-principle bases, *i.e.* based on the Schrödinger equation, is the main issue of molecular dynamics simulations when considering computational resources. The same methods and approximations, as described in **section 3.3.1**: the Born-Oppenheimer approximation, the DFT formalism, and pseudopotential to describe atoms, are used to reduce the number of parameters and make *ab initio* molecular dynamics actually computable.

Basically the MD time step is accomplished by: (1) Choosing an initial set of nuclear positions ($\mathbf{R}_1, \dots, \mathbf{R}_N$) (in this work systematically an output of first-principle DFT calculations), (2) Solving the Hamiltonian, *i.e.* determining the ground-state wave function associated to the nuclear configuration, (3) Calculating the forces on the nuclei as the derivative of the potential, (4) Evolving the Newton's equations for all nuclei with a finite time step δt , to determine the new set of nuclear positions corresponding to the step $t+\delta t$, then going back to (2). This procedure is iterated for a large number of time steps, about 10^5 - 10^6 steps, generally considering a time step of about 1-2fs and total length of simulation of about 20-100ps. The main output of molecular dynamics is the nuclear positions at each step of the calculations: the nuclear trajectories.

Most of the calculations presented in **chapter 5** are performed in the canonical ensemble, with constant volume and constant temperature (NVT) through coupling with a thermostat. Only the generation part of molecular dynamics calculation of magnetic $\text{Nd}_2\text{NiO}_{4.0}$ was performed in the microcanonical ensemble, with constant volume and constant energy (NVE), after equilibration in the NVT ensemble.

From the molecular dynamic trajectories, the velocity autocorrelation function (VACF) can be defined as (**equation 3.28**):

$$C_{vv;\alpha\alpha}(t) \doteq \frac{1}{3} \langle v_\alpha(t_0) \cdot v_\alpha(t_0 + t) \rangle_{t_0} \quad (\text{Eq. 3.28})$$

The vibrational density of states can be calculated from the Fourier transform of the VACF (**equation 3.29**), and is comparable to density of states from neutron when weighted by the incoherent atomic structures factors (**equation 3.30**).

$$\tilde{C}_{vv;\alpha\alpha}(\omega) = \frac{1}{2\pi} \int_{-\infty}^{+\infty} dt e^{-i\omega t} C_{vv;\alpha\alpha}(t) \quad (\text{Eq. 3.29})$$

$$G(\omega) = \sum_{\alpha} b_{\alpha,inc}^2 \tilde{C}_{vv;\alpha\alpha}(\omega) \quad (\text{Eq. 3.30})$$

3.4. Positional recurrence maps (PRM)

As shown here before, a lot of useful information concerning atomic motion, diffusion pathway, diffusion constants or at least statistics of diffusion events, and lattice dynamics, can be extracted from molecular dynamic trajectories. However, while the diffusion events are obvious to notice with a global time-summation of the trajectory – as available in most of the post-treatment programs of molecular dynamics, we didn't find any tool to have a visual representation of the on-site motion of the diffusive oxygen, meaning the occupation in space and time of an atom of its site. Thus we wrote a basic code using Matlab^[10] to perform time-summation of specific atoms or atomic displacements, involving symmetries and adapted projections to our case, and providing visual maps – quite similar as density maps. To avoid any confusion with the 'nuclear density map' from diffraction, which usually refers to reverse Fourier transform of the coherent part of a neutron diffusion pattern, we will use the term 'positional recurrence maps' (PRM) for the present representations.

The construction process of a PRM is basically a cumulative sum in time of the nuclear dynamic trajectories, considering atomic displacements instead of atomic positions, as described in **equation 3.31**.

$$n(x, y, z)_{j,T} = \sum_{sym. i} A^i \sum_{atom j} \sum_{t=0}^T (p_j(x_t, y_t, z_t) - p_j(x_{CoM}, y_{CoM}, z_{CoM}) + B_j + C_j) \quad (\text{Eq. 3.31})$$

With $n(x, y, z)_{j,T}$ the positional recurrence map of atoms j limited in time to the simulation step T . The atomic position of atom j at step t is $p_j(x_t, y_t, z_t)$, while its center-of-mass (CoM) position is $p_j(x_{CoM}, y_{CoM}, z_{CoM})$. Here the structure is geometry optimized before the molecular dynamics, hence (**equation 3.32**):

$$p_j(x_{CoM}, y_{CoM}, z_{CoM}) = p_j(x_{t=0}, y_{t=0}, z_{t=0}) \quad (\text{Eq. 3.32})$$

Point group symmetry is added through i operations A^i corresponding to the i symmetry equivalences, while the B_j vectors are used to sum equivalent atoms. The additional vectors C_j can be added to shift the space between the obtained atom-dependent center-of-mass origin – which can be seen as an atomic displacement space, back to the classic Cartesian origin – or Cartesian space. The differences between to two origins will be described hereafter.

Due to structural considerations we are solely interested in c-axis projection of $n(x, y, z)_T$, which greatly simplify the code. While the PRM works on any atoms, we consider only the former apical oxygen atoms, *i.e.* oxygen atoms whose center-of-mass at $t = 0$ were in apical oxygen sites. Since our structural models are linked to room-temperature phases, which mean equilibrium apical oxygen atom positions are shifted away from the usually considered high-temperature high-symmetry sites, we want to stay in the center-of-mass projection to nullify the static shift while applying symmetry. Of course this approximation implies the artificial splitting of neighbor sites, but our interest is on the occupation of an atom of its site, not its

behavior after diffusion. With typical 40ps long molecular dynamics and tetragonal supercell, **equation 3.31** becomes **equation 3.33**:

$$n(x,y)_{o_{ap},40ps} = \sum_{sym. i} A^i \sum_z \sum_{atom j} \sum_{t=0}^{40ps} (p_j(x_t, y_t, z_t) - p_j(x_{t=0}, y_{t=0}, z_{t=0}) + B_j) \quad (\text{Eq. 3.33})$$

With A^i (**equation 3.34**):

$$A^i = \left\{ \begin{array}{l} \left[\begin{array}{cc} 1 & \\ & 1 \end{array} \right], \left[\begin{array}{cc} -1 & \\ & 1 \end{array} \right], \left[\begin{array}{cc} 1 & \\ & -1 \end{array} \right], \left[\begin{array}{cc} -1 & \\ & -1 \end{array} \right], \\ \left[\begin{array}{cc} 1 & \\ & 1 \end{array} \right], \left[\begin{array}{cc} 1 & \\ & -1 \end{array} \right], \left[\begin{array}{cc} -1 & \\ & 1 \end{array} \right], \left[\begin{array}{cc} -1 & \\ & -1 \end{array} \right] \end{array} \right\} \quad (\text{Eq. 3.34})$$

To explicit the difference between the center-of-mass origin and the Cartesian origin, we draw the PRM of the apical oxygen atoms of tetragonal $\text{Nd}_2\text{NiO}_{4.0}$ in the LTT structure in **Figure 3.10**. Considering first the reduced c-axis case with about no freedom of motion of the apical oxygen atoms in **a,b**): since the atomic position of the apical oxygen atom is of the type (x,x,z) , we expect a splitting in four individuals in the $[110]$ direction from $(0,0,z)$ in the Cartesian projection – which is effectively observed in **b**). In the center-of-mass projection, the center-of-mass positions (x,x,z) are shifted to $(0,0,z)$. Thus we expect a single spot – which is observed in **a**). When we add atomic motion – as in the case of the optimal c-axis parameter in **c,d**), we can see in CoM projection **c**) that the atomic motion are clearly along $[100]$ and $[010]$, while the pattern is more ‘blurred’ in the Cartesian projection **d**) due to superimposition of the splitting. In other word, the Cartesian projection would be useful to directly compare the PRM with nuclear density maps, while the CoM projection gives a clearer view of the atomic motion.

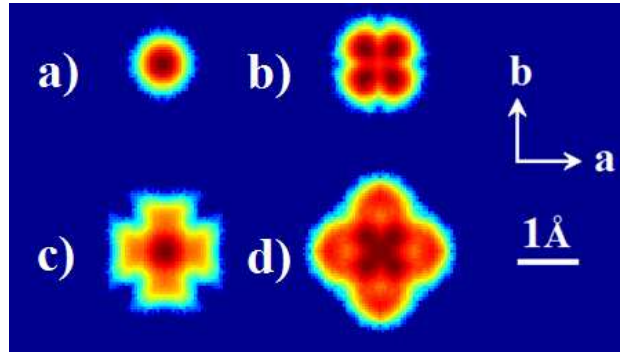


Figure 3.10 – PRM of former apical oxygen atoms of $\text{Nd}_2\text{NiO}_{4.0}$ in the LTT structural model, from 40ps molecular dynamics at $T=310\text{K}$. Structural model has slightly compressed c-axis parameter in **a,b**), and as optimized c-axis parameter in **c,d**). Origins are center-of-mass for **a,c**) and Cartesian for **b,d**). The color scale is logarithmic.

Another point to precise is the effect of simulation time on PRM: in **Figure 3.11** is represented the time-dependent PRM of former apical oxygen atoms of $\text{Nd}_2\text{NiO}_{4.25}$ in the tetragonal structural model. The time label corresponds to the upper limit of the cumulative sum over the former apical oxygen atom trajectories. Superimposed atoms at $t=0$ are vibrating and explore

the different conformations allowed by the structure, which takes an amount of time that depends on the potential stiffness, the complexity of neighboring shells, etc... Here at least 20ps long molecular dynamics are needed to explore the whole core density. Since PRM are strongly dependent on the simulation time, only summations with constant cutoff T are comparable.

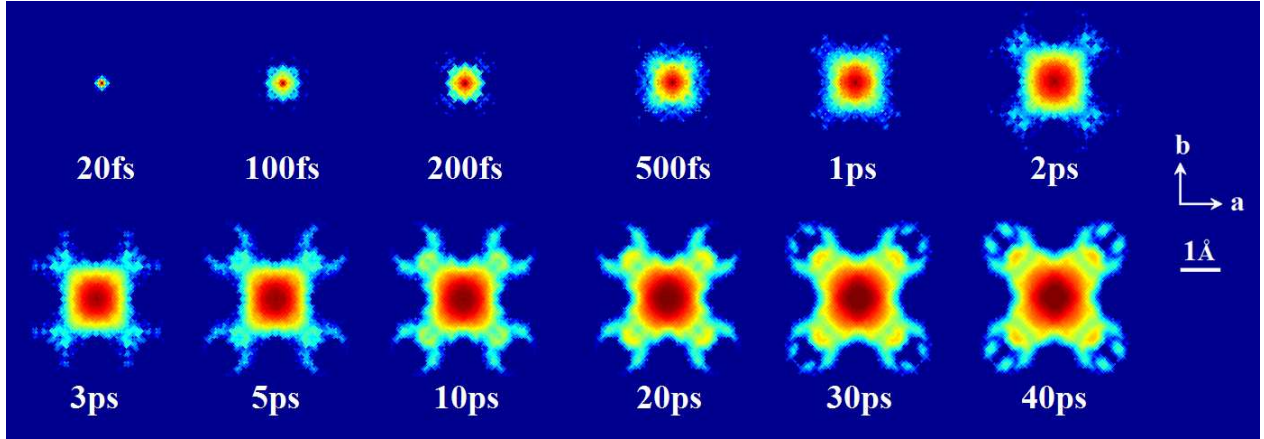


Figure 3.11 – Time-dependent PRM, in CoM projection, of former apical oxygen atoms of $Nd_2NiO_{4.25}$ in the tetragonal structural model, from 40ps molecular dynamics at $T=310K$. The color scale is logarithmic.

Concerning the code itself, its core can be found in **appendix A**.

3.5. Inelastic neutron scattering – Theory

3.5.1. Inelastic scattering cross section

Scattering cross sections are quantities used to characterize the interaction between a neutron beam and the scattering system. The partial differential cross section is defined as (**equation 3.35**):

$$\frac{d^2\sigma}{d\Omega dE} = \left(\begin{array}{l} \text{neutrons per second, per solid angle } d\Omega, \\ \text{whose energy is inbetween } E \text{ and } E + dE \end{array} \right) \quad (\text{Eq. 3.35})$$

The total cross section, which is the number of scattered neutrons per second, is linked to the partial differential cross section by the equation **equation 3.36**:

$$\sigma_{tot} = \int_{\text{all directions}} \int_{E=0}^{\infty} \left(\frac{d^2\sigma}{d\Omega dE} \right) dE d\Omega \quad (\text{Eq. 3.36})$$

In order to quantify the scattering power of a nucleus, the scattering length b is introduced, as reported in **equation 3.37**, from the spherical scattering of the neutron wavefunction at point r , considering a monochromatic neutron beam of wavevector \vec{k} along \vec{z} .

$$\psi_{incident} = e^{i\vec{k}\vec{z}}, \quad \psi_{scattered} = -\frac{b}{r} e^{i\vec{k}\vec{r}} \quad (\text{Eq. 3.37})$$

For a single scattering nucleus (**equation 3.38**):

$$\sigma = 4\pi b^2 \quad (\text{Eq. 3.38})$$

3.5.2. Scattering by nuclei

In the simple case where the magnetic interaction is not considered, the neutron is defined entirely by its momentum, the wavevector \vec{k} . While scattered by a potential V related to the state λ of an atomic system, it induces a transition from the state λ to λ' , and its wavevector is changed to \vec{k}' . Considering a flux ϕ of incident neutrons, the differential cross section in the solid angle $d\Omega$ can be expressed as (**equation 3.39**), where $W_{k,\lambda \rightarrow k',\lambda'}$ is the number of transitions between the states (k,λ) and (k',λ')

$$\left(\frac{d\sigma}{d\Omega}\right)_{\lambda \rightarrow \lambda'} = \frac{1}{\phi} \frac{1}{d\Omega} \sum_{k' \text{ in } d\Omega} W_{k,\lambda \rightarrow k',\lambda'} \quad (\text{Eq. 3.39})$$

The right term of **equation 3.39** can be clarified with Fermi's golden rule, as in **equation 3.40**, where $\rho_{k'}$ is the number of states in the solid angle $d\Omega$ per energy unit, for a neutron of wave vector k' .

$$\sum_{k' \text{ in } d\Omega} W_{k,\lambda \rightarrow k',\lambda'} = \frac{2\pi}{\hbar} \rho_{k'} |\langle k', \lambda' | V | k, \lambda \rangle|^2 \quad (\text{Eq. 3.40})$$

The term of the potential V is deduced from the single nucleus case, considering the very short range interaction between the neutron and the nucleus (**equation 3.41**), with $\delta(\vec{r})$ a tri-dimensional Dirac function. In this hypothesis, we're speaking of "Fermi's pseudopotential".

$$V(\vec{r}) = \frac{2\pi\hbar^2}{m} b \delta(\vec{r}) \quad (\text{Eq. 3.41})$$

Considering now the interaction of a beam of neutrons with the nuclei composing the material, the measured cross-section would be (neglecting terms from magnetism and polarization) equivalent to the average cross-section of all nuclei, as stated in **equation 3.42**; where $R_j(t)$ the position of particle j at time t , and \vec{Q} the momentum transfert, or scattering vector $\vec{Q} = \vec{k} - \vec{k}'$.

$$\frac{d^2\sigma}{d\Omega dE} = \frac{k'}{k} \frac{1}{2\pi\hbar} \sum_{jj'} \overline{b_j' b_j} \int \langle \exp\{-i\vec{Q} \cdot \overline{R_j'(0)}\} \exp\{i\vec{Q} \cdot \overline{R_j(t)}\} \rangle \exp(-i\omega t) dt \quad (\text{Eq. 3.42})$$

The cross-section can be separated in a coherent part (**equation 3.43**) and an incoherent part (**equation 3.44**).

$$\left(\frac{d^2\sigma}{d\Omega dE}\right)_{coh} = \frac{\sigma_{coh} k'}{4\pi k} \frac{1}{2\pi\hbar} \sum_{jj'} \int_{-\infty}^{\infty} \langle \exp\{-i\vec{Q}\cdot\overline{R_{j'}(0)}\} \exp\{i\vec{Q}\cdot\overline{R_j(t)}\} \rangle \exp(-i\omega t) dt \quad (\text{Eq. 3.43})$$

$$\left(\frac{d^2\sigma}{d\Omega dE}\right)_{inc} = \frac{\sigma_{inc} k'}{4\pi k} \frac{1}{2\pi\hbar} \sum_j \int_{-\infty}^{\infty} \langle \exp\{-i\vec{Q}\cdot\overline{R_j(0)}\} \exp\{i\vec{Q}\cdot\overline{R_j(t)}\} \rangle \exp(-i\omega t) dt \quad (\text{Eq. 3.44})$$

With $\sigma_{coh} = 4\pi(\overline{b})^2$ and $\sigma_{inc} = 4\pi\{\overline{b^2} - (\overline{b})^2\}$.

The coherent part of the scattering cross-section represents both the correlation of a single nucleous position with time, and the correlation of several nuclei positions with time – which can lead to interference phenomenon –, while the incoherent part of scattering represents only the correlation of a single nucleous position with time, which cannot produce interference.

If every particles shared the same diffusion coefficient \overline{b} , the total scattering would be equivalent to the coherent scattering; the incoherent part of the cross-section being linked to the distribution of diffusion coefficient around the average value.

The coherent and incoherent cross-sections of oxygen, nickel, and neodymium, are reported in **Tableau 3.2**.

Tableau 3.2 – Coherent and incoherent scattering length b , scattering cross-section σ and absorption considering 2200m/s neutrons^[20].

Element	Coherent b (fm)	Incoherent b (fm)	Coherent σ (barn)	Incoherent σ (barn)	Total σ (barn)	Absorption (barn)
O	5.803	-	4.232	0.0008	4.232	0.00019
Ni	10.3	-	13.3	5.2	18.5	4.49
Nd	7.69	-	7.43	9.2	16.6	50.5(1.2)

3.5.3. Scattering by phonons

In order to integrate the scattering by phonons into the previous equations, the displacements \overline{u}_i of particle from their equilibrium positions, located on a node \vec{l} of the Bravais lattice, shall be considered instead of the instantaneous position $\overline{R}_i = \vec{l} + \overline{u}_i$.

Considering **equations 3.45**,

$$U = -i\vec{Q}\cdot\overline{u_0(0)} \quad \text{and} \quad V = i\vec{Q}\cdot\overline{u_i(t)} \quad (\text{Eq. 3.45})$$

The coherent cross-section can be developed as in **equation 3.46**, where N is the number of atoms.

$$\left(\frac{d^2\sigma}{d\Omega dE}\right)_{coh} = (\overline{b})^2 \frac{k'}{k} \frac{N}{2\pi\hbar} \exp\langle U^2 \rangle \sum_l \exp(i\vec{Q}\cdot\vec{l}) \int_{-\infty}^{\infty} \exp\langle UV \rangle \exp(-i\omega t) dt \quad (\text{Eq. 3.46})$$

Where:

$$\exp\langle UV \rangle = \sum_n \frac{1}{n!} \langle UV \rangle^n \quad (\text{Eq. 3.47})$$

For a system of N atoms, thus with $3N$ phonon modes, going from the state λ , defined by $3N$ quantum numbers n , to the state λ' can change some of the quantum numbers:

- If the quantum numbers do not change ($n=0$), thus $\exp\langle UV \rangle = 1$, which leads to the Bragg's law. The scattering is elastic.
- If only one quantum number does change, we speak of "one phonon scattering" ($\exp\langle UV \rangle = 1 + \langle UV \rangle$).
- If p quantum numbers do change, the scattering is said to be "multi phonon" (order p of $\exp\langle UV \rangle$).

In the one phonon scattering scenario, the coherent cross-section becomes as in **equation 3.48**, with W the Debye-Waller factor, \vec{e}_s the polarisation factor of the mode s , and ω_s its frequency.

$$\left(\frac{d^2\sigma}{d\Omega dE} \right)_{coh\ 1\ ph} = (\bar{b})^2 \frac{k'}{k} \frac{N}{2\pi\hbar} \exp(-2W) \sum_l \exp(i\vec{Q}\vec{l}) \sum_s \frac{(\vec{Q}\vec{e}_s)^2}{\omega_s} \int_{-\infty}^{\infty} [\exp\{-i(\vec{q}\vec{l} - \omega_s t)\} \langle n_s + 1 \rangle + \exp\{i(\vec{q}\vec{l} - \omega_s t)\} \langle n_s \rangle] \exp(-i\omega t) dt \quad (\text{Eq. 3.48})$$

The time integral can be developed as in **equation 3.49**:

$$\int_{-\infty}^{\infty} \exp\{i(\omega_s - \omega)t\} dt = 2\pi \delta(\omega - \omega_s) \quad (\text{Eq. 3.49})$$

The summation over l can be developed as in **equation 3.50**:

$$\sum_l \exp\{i(\vec{Q} - \vec{q})\vec{l}\} \propto \sum_{\vec{\tau}} \delta(\vec{Q} - \vec{q} - \vec{\tau}) \quad (\text{Eq. 3.50})$$

The cross-section contains the factors $\delta(\omega - \omega_s)$ and $\delta(\vec{Q} - \vec{q} - \vec{\tau})$, thus for scattering to occur two conditions must be satisfied (**equations 3.51**), representing energy and momentum transfer conservation. The momentum transfer conservation, or scattering triangle, is represented in **Figure 3.12**.

$$\omega = \omega_s \quad \text{and} \quad \vec{Q} = \vec{q} + \vec{\tau} \quad (\text{Eq. 3.51})$$

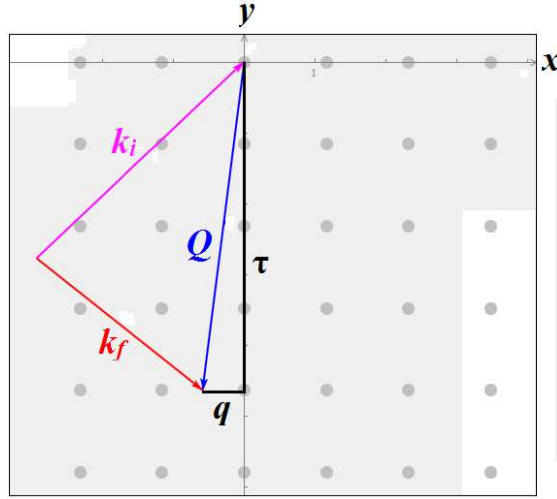


Figure 3.12 – Scattering triangle representing the momentum transfer conservation. The scattering vector \mathbf{Q} is constructed by the neutron incident wavevector \mathbf{k}_i and scattered wavevector \mathbf{k}_f . The reciprocal lattice vector is $\boldsymbol{\tau}$, and the phonon wavevector is \mathbf{q} . Figure drawn using vTAS^[21].

The **equation 3.48** can be differentiated in two terms, respectively in **equation 3.52** and **equation 3.53**:

$$\left(\frac{d^2\sigma}{d\Omega dE} \right)_{coh+1} \propto (\bar{b})^2 \frac{k'}{k} \exp(-2W) \sum_s \sum_{\boldsymbol{\tau}} \frac{(\vec{Q} \cdot \vec{e}_s)^2}{\omega_s} \langle n_s + 1 \rangle \delta(\omega - \omega_s) \delta(\vec{Q} - \vec{q} - \vec{\tau}) \quad (\text{Eq. 3.52})$$

$$\left(\frac{d^2\sigma}{d\Omega dE} \right)_{coh-1} \propto (\bar{b})^2 \frac{k'}{k} \exp(-2W) \sum_s \sum_{\boldsymbol{\tau}} \frac{(\vec{Q} \cdot \vec{e}_s)^2}{\omega_s} \langle n_s \rangle \delta(\omega + \omega_s) \delta(\vec{Q} + \vec{q} - \vec{\tau}) \quad (\text{Eq. 3.53})$$

The first term, as defined in **equation 3.52**, states the scattering conditions $\omega = \omega_s$ and $\vec{Q} = \vec{q} + \vec{\tau}$, meaning that a neutron will lose the kinetic energy $\frac{\hbar^2}{2m}(k^2 - k'^2) = \hbar\omega_s$ and that a phonon with energy $\hbar\omega_s$ will be generated. This process is called phonon creation.

The second term, as defined in **equation 3.53**, states the scattering conditions $\omega = -\omega_s$ and $\vec{Q} = \vec{q} - \vec{\tau}$, meaning that a neutron will gain the kinetic energy $\frac{\hbar^2}{2m}(k'^2 - k^2) = \hbar\omega_s$ and a phonon with energy $\hbar\omega_s$ will be absorbed. This process is called phonon annihilation.

The generalisation of these equations to a crystal with several atoms per cell would be as in **equation 3.54**, where the cross-section represents the intensity measured with the spectrometer.

$$\left(\frac{d^2\sigma}{d\Omega dE} \right)_{coh+1} = \frac{k'}{k} \frac{(2\pi)^3}{2v_0} \sum_s \sum_{\boldsymbol{\tau}} \frac{1}{\omega_s} \left| \sum_d \frac{\bar{b}_d}{\sqrt{M_d}} \exp(-W_d) \exp(i\vec{Q} \cdot \vec{d}) (\vec{Q} \cdot \vec{e}_{ds}) \right|^2 \times \langle n_s + 1 \rangle \delta(\omega - \omega_s) \delta(\vec{Q} - \vec{q} - \vec{\tau}) \quad (\text{Eq. 3.54})$$

Scattering by a phonon can be seen as an elastic scattering for which the atoms are moved from their equilibrium position on a sinusoidal modulation of wave vector \vec{q} , with the phonon wave propagating at the speed ω_s/q in the \vec{q} direction.

Similarly we can define the incoherent one-phonon emission cross-section as in **equation 3.55**.

$$\left(\frac{d^2\sigma}{d\Omega dE}\right)_{inc+1} = \frac{k'}{k} \sum_d \frac{1}{2M_d} \{\overline{b_d^2} - (\overline{b_d})^2\} \exp(-2W_d) \times \sum_s \frac{|\vec{Q} \cdot \vec{e}_{ds}|^2}{\omega_s} \langle n_s + 1 \rangle \delta(\omega - \omega_s) \quad (\text{Eq. 3.55})$$

3.5.4. Calculations of the dynamic structure factor from molecular dynamics

As it will be discussed in **chapter 7**, we have calculated coherent and incoherent structure factor from our molecular dynamics trajectories, using a memory function as implemented in the nMoldyn code^[8, 9].

The double differential cross-section can be expressed in term of the dynamic structure factor (**equation 3.56**). Which itself can be expressed in term of the intermediate scattering function (**equation 3.57**).

$$\frac{d^2\sigma}{d\Omega dE} = N \frac{k'}{k} S(\mathbf{Q}, \omega) \quad (\text{Eq. 3.56})$$

$$S(\mathbf{Q}, \omega) = \frac{1}{2\pi} \int_{-\infty}^{+\infty} dt e^{-i\omega t} F(\mathbf{Q}, t) \quad (\text{Eq. 3.57})$$

The coherent and incoherent intermediate scattering function are calculated using a memory function $\xi(\mathbf{Q}, t)$, shown in **equation 3.58**.

$$\partial_t F(\mathbf{Q}, t) = - \int_0^t d\tau \xi(\mathbf{Q}, t - \tau) F(\mathbf{Q}, \tau) \quad (\text{Eq. 3.58})$$

More informations about the implementation of the numerical algorithm of can be found in literature^[22].

3.6. Inelastic neutron scattering – Instrumentation

3.6.1. The ILL reactor

The high-flux neutron reactor of the Laue-Langevin Institute (ILL), Grenoble, France, is one of the most intense continuous neutron source, with a flux of 1.5×10^{15} neutrons per second per square centimeter, for a thermal power of 58.3 MW. The enriched uranium ^{235}U fuel is located in a 2.5m wide reactor, thermally regulated by an heavy water circuit, also used as moderator for neutrons, and a secondary light water circuit connected to the nearby Drac river through heat exchangers. The biological protection is ensured with dense concrete, and a pool of light water on top of the reactor as pictured in **Figure 3.13**, handy for emergency stops or refuelling.

Neutrons produced by the reactor are in thermal equilibrium with the heavy water at $T=300\text{k}$, and the neutron flux shows a maxwell distribution with a mamimum at $\lambda=1.2\text{\AA}$, wavelength corresponding to ‘thermal neutrons’. Depending on the required neutron wavelength, thermal neutrons may be heated with a $T=2400\text{K}$ graphite source to shift the distribution maximum to $\lambda=0.8\text{\AA}$, or cooled down with a $T=25\text{K}$ liquide deuterium source to shift the distribution maxima to $\lambda=3.0\text{\AA}$. The **Figure 3.13** shows a scheme of the neutron guides.

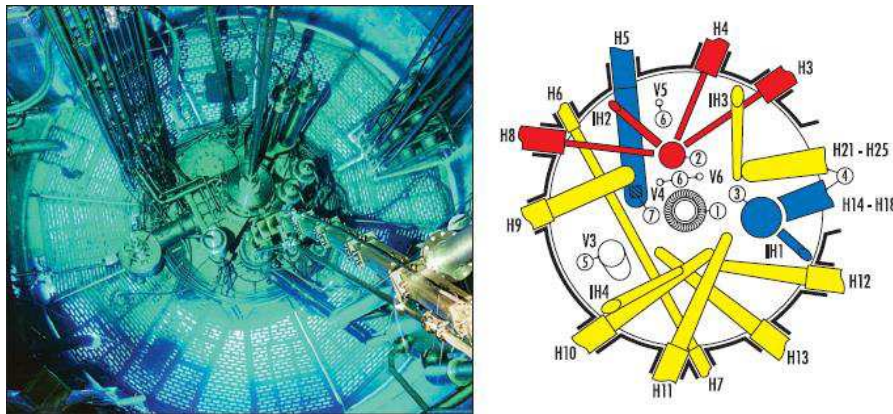


Figure 3.13 – (left) Picture of the pool on top of the reactor showing the blue glow of the Cherenkov effect. (right) Guides noses close to the reactor, thermal neutron guides in yellow, cold neutron guides in blue, and hot neutron guides in red^[4].

3.6.2. Time-of-flight IN6 spectrometer

We performed inelastic neutron scattering experiments on the direct-geometry time-focussing time-of-flight spectrometer IN6 of the ILL, designed for quasielastic and inelastic scattering experiments on powders with cold neutrons ($\lambda=4\text{-}6\text{\AA}$).

The IN6 spectrometer works as follow. The cold neutron beam from the H15 guide is extracted by a vertically focussing monochromator in pyrolytic graphite, which select one of the four wavelength $\lambda=4.1\text{\AA}$, $\lambda=4.6\text{\AA}$, $\lambda=5.1\text{\AA}$, or $\lambda=5.9\text{\AA}$; the second order reflection being removed by a beryllium-filter. The monochromatic beam is then pulsed by a Fermi chopper and, if needed,

the pulses are spaced by a suppressor chopper rotating slower. The pulsed beam then scatter on the sample, and the scattered neutrons are collected on a set of 337 elliptical ^3He detectors. An helium filled box between the sample and the detectors minimises the background, and furnace or cryostat can be adapted on the sample area. With this pseudo-2D detector, with powder samples, and considering the time on which the neutron arrive on the detector – thus the neutron energy, a whole part of the **Q-E** space is measured with each pulse without moving the detectors. The **Figure 3.14** shows a scheme of the IN6 spectrometer.

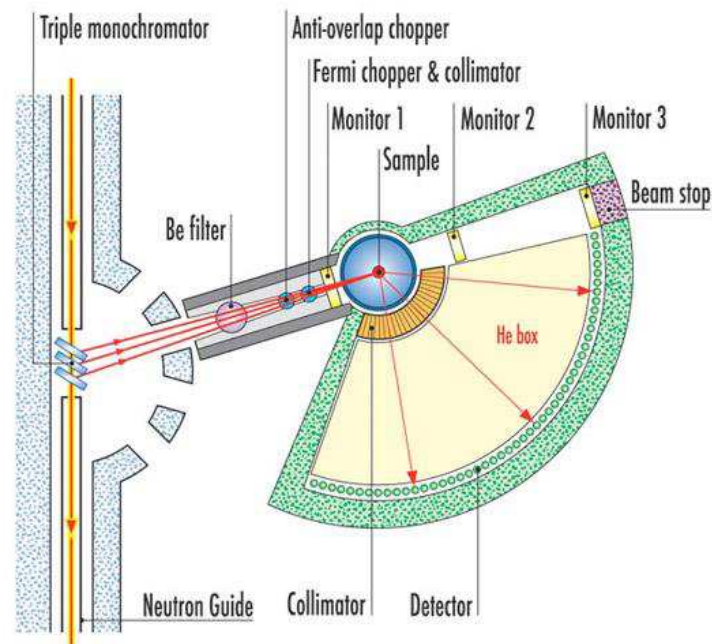


Figure 3.14 – Scheme of the direct-geometry time-focussing time-of-flight spectrometer IN6 at the ILL^[4].

Data were collected at high-temperatures between $T=310\text{-}1073\text{K}$ using a furnace, in the upscattering mode using an incident wavelength of $\lambda=4.14\text{\AA}$, through reflection of the beam on the (002) plan of the pyrolytic graphite monochromator, leading to a resolution of 0.17meV at the elastic line. In this setup the best resolution is reached on the elastic line. However for the low-temperature part of the experiments, using a cryostat to collect data between $T=150\text{-}310\text{K}$, the spectrometer was set in inelastic focusing at about 6.25meV to increase the resolution at the expense of the flux.

Besides the sample, a vanadium standard and the empty sample holders were measured to perform respectively the detector efficiency calibration and the background subtraction. Standard corrections and data analysis were performed using the LAMP software developed by the ILL^[23].

At the neutron wavelength $\lambda=4.14\text{\AA}$, the IN6 angular coverage ($17\text{-}114^\circ$) corresponds to a maximum momentum transfer of $Q\sim 2.6\text{\AA}^{-1}$. As such, for the low-temperature experiments, in order to minimize the contamination of phonon spectra by magnetic scattering, only the high- Q region was considered ($1.8\text{-}2.6\text{\AA}^{-1}$). Therefore, after correction for energy-dependent detector

efficiency, the one-phonon generalised phonon density of states (gDOS) was obtained from the angle-integrated data of the high-Q region of the measured (Q, ω) space, using the incoherent approximation in the same way as in previous works dealing with phonon dynamics^[24-27].

As an example of the output of a TOF experiment, we draw in **Figure 3.15** the raw spectra of the vanadium standard, the empty cane and the $\text{Nd}_2\text{NiO}_{4.25}$ sample at $T=310\text{K}$. The scattering angle – the momentum transfer, is measured by the set of detector and recorded on the y-axis, and the time on which the neutron reaches the detector – depending on the speed on the neutron after scattering, thus the energy transfer, is recorder in x-axis. In order to get a clean measurement, the vanadium standard is used to calibrate the detector efficiency, and the spectra of the sample holder is subtracted from the sample spectra. Summation of the signal in \mathbf{Q} and conversion of the x-axis in energy unit allows to obtain the density of states, which then shall be corrected for multi-phonon scattering to get the one-phonon generalized phonon density of states.

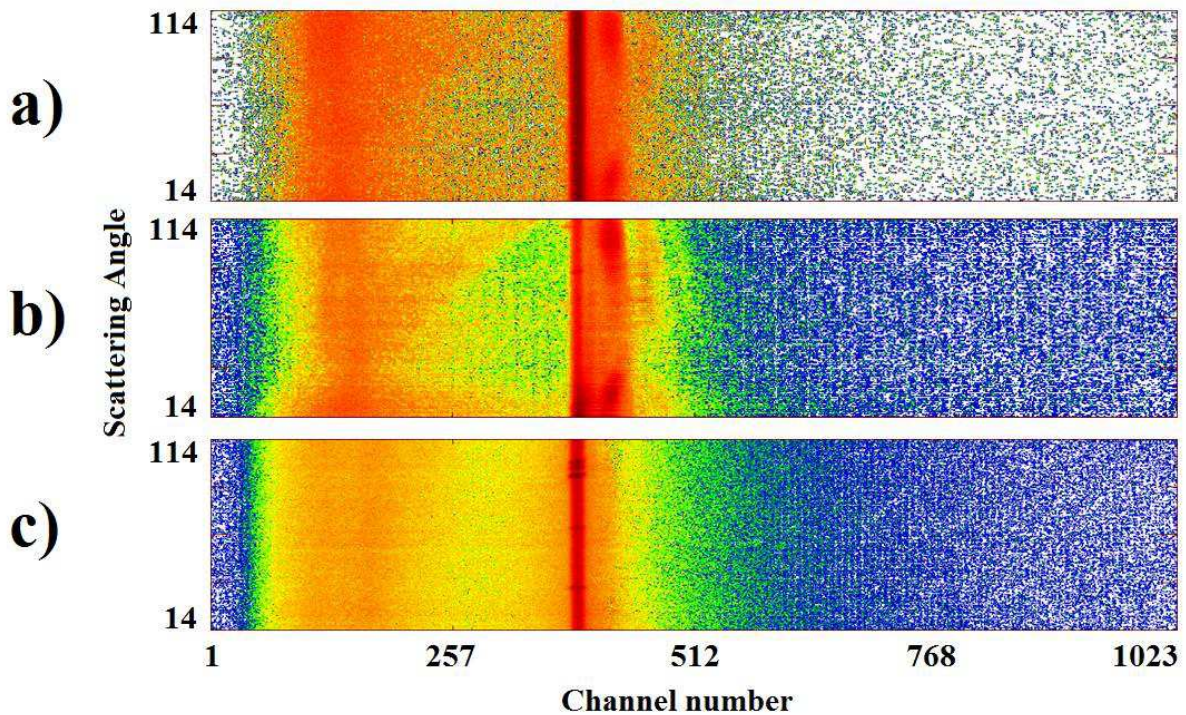


Figure 3.15 – Raw spectra from TOF measurements of a) the Vanadium standard, b) the empty cane, and c) the $\text{Nd}_2\text{NiO}_{4.25}$ sample at $T=310\text{K}$. The space is channel number (time) as a function of scattering angle. The 1024 channels correspond to $5.80\mu\text{s}$, the neutron pulse frequency. The intense line on channels 389-390 corresponds to the elastic line – diffraction peaks are observable for the $\text{Nd}_2\text{NiO}_{4.25}$ samples, allowing to follow changes in the stoichiometry. The color scale is logarithmic.

3.6.3. Three-axis IN8 spectrometer

We performed inelastic neutron spectroscopy experiments on the high-flux thermal neutron three-axis spectrometer IN8 of the ILL, designed for inelastic measurements on single-crystals over a wide range of energy and momentum transfer.

The IN8 spectrometer works as follow. The thermal neutron beam is extracted from the H10 guide, through reflection on a double focusing chromator made of pyrolitic graphite (002), copper (200) or silicum (111) crystals, which allows the selection of the incident neutron wavelength. The horizontal focusing allows to increase the flux at the expense of momentum resolution. The take-off angle of the monochromator can be set between 10-90°. The beam then goes through a set of converging collimators and diaphragms to optimize the beam dimension and definition, before scattering on the single-crystal sample. The scattered beams are then selected by a second monochromator, called analyser, with a take-off angle set between 0-130°, and then measured by a ^3He point detector. The sample environment can adapt furnaces or cryostat for temperature experiments, or vacuum box to reduce the background. The **Figure 3.16** shows a scheme of the IN8 spectrometer.

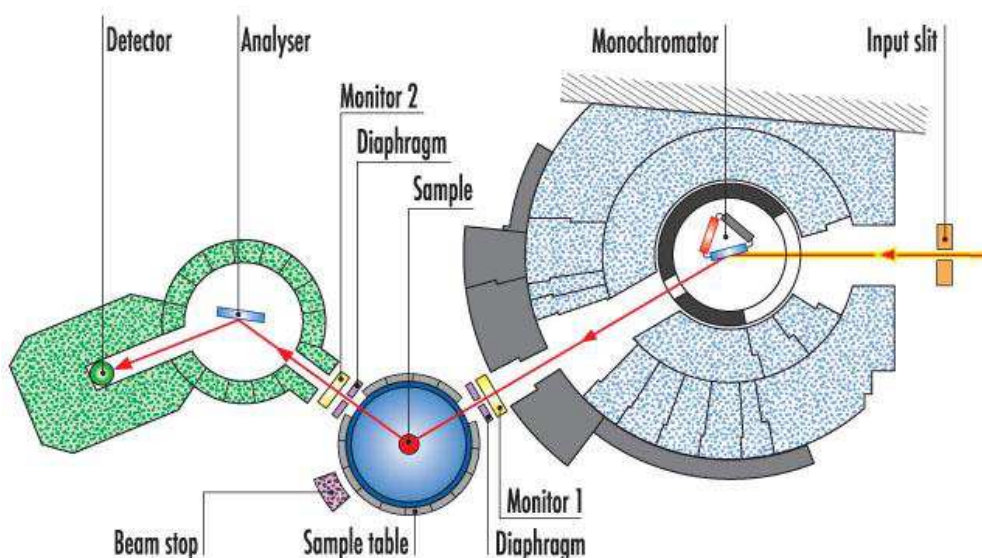


Figure 3.16 – Scheme of the high-flux thermal neutron three-axis spectrometer IN8 at the ILL^[4].

Using both a monochromator and an analyser, each position of the spectrometer corresponds to a single point of the (\mathbf{Q},ω) space, which means that the region of interest must be determined prior to the experiments, as it will be shown in **chapter 5**. As it will be discussed in **chapter 7**, it is possible to differentiate between longitudinal modes, for which associated atomic displacements are parallel to the propagation vector \mathbf{q} , and transverse modes, for which

associated atomic displacements are perpendicular to the propagation vector, depending on the instrument geometry, as shown in **Figure 3.17**.

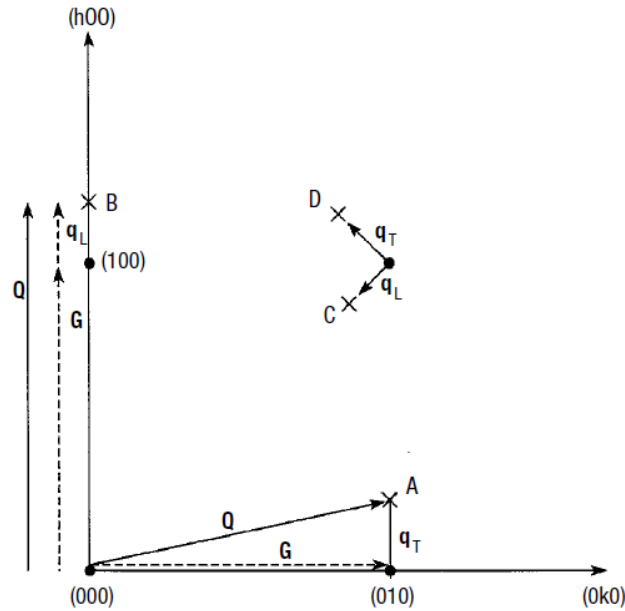


Figure 3.17 – Within an $(hk0)$ zone of reciprocal space, purely transverse acoustic modes, subscript T , can be measured at points A and D , while purely longitudinal acoustic modes, subscript L , are obtained at B and C . Phonon propagation vector is \mathbf{q} , reciprocal lattice vector is \mathbf{G} , and wave vector is \mathbf{Q} . Figure from reference [28].

Most experiments were performed using a pyrolytic graphite filter to suppressing 2nd and 3rd order reflections for the incident wavelength $k_i=2.662\text{\AA}^{-1}$. This natural filtering of higher order reflections comes from the anomalous transmission of the graphite, as shown in **Figure 3.18**.

Besides the standard geometry of a three-axis spectrometer, we also performed measurements using Flatcone, a secondary spectrometer made of 31 silicium analyzers and ^3He detectors, designed to collect up to 31 points of the (Q,ω) space simultaneously. Contrary to the standard setting where only a few points of interest are measured, the Flatcone setting allow to measure whole scattering plane for a set energy transfer. Flatcone and its scheme are shown in **Figure 3.19**

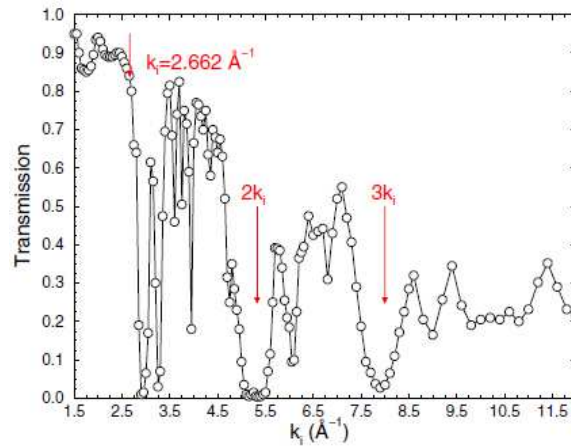


Figure 3.18 – Transmission of a graphite crystal. For a selected incident wavelength of $k_i=2.662\text{\AA}^{-1}$ showing $T\sim 0.85$, the second and third order reflections show a negligible transmission^[29].

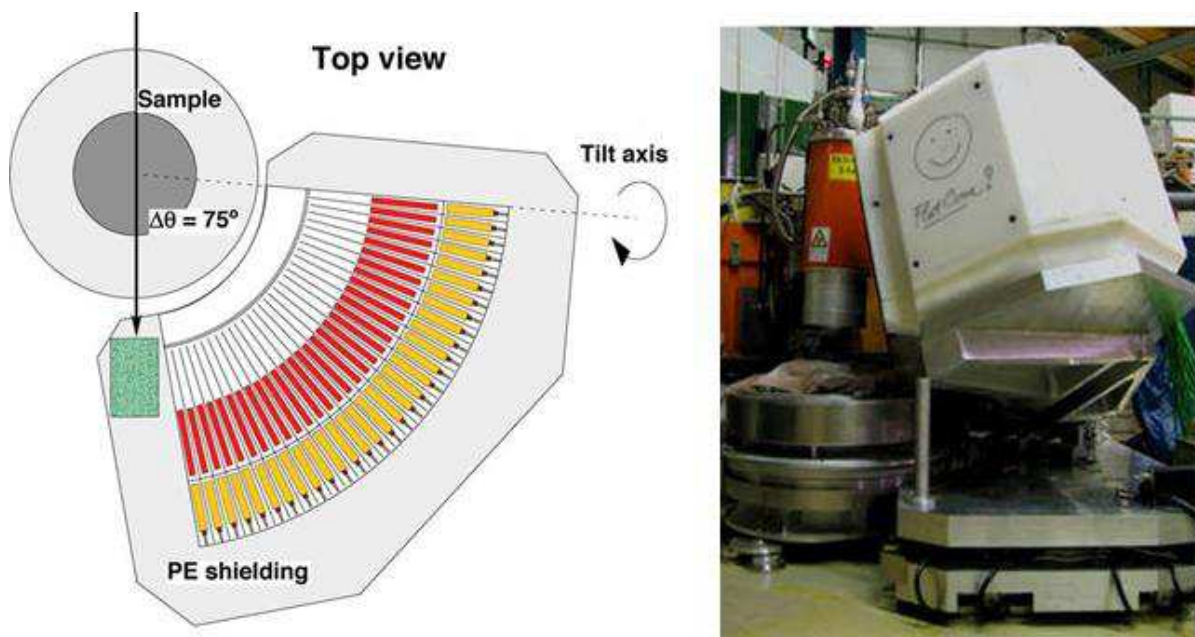


Figure 3.19 – (left) Scheme of the Flatcone secondary spectrometer at the ILL, showing its 31 couple analyzer-detector^[30]. PE refers to polyethylene. (right) Picture of Flatcone.

3.7. Bibliography

1. Wahyudi, O. (2011). *Université de Rennes 1, PhD thesis 4468*.
2. Le Toquin, R., Paulus, W., Cousson, A., Dhahlenne, G., and Revcolevschi, A. (2004). *Physica B: Condensed Matter*, 350(1–3, Supplement), E269-E272.
3. Le Dréau, L., Prestipino, C., Hernandez, O., Schefer, J., Vaughan, G., Paofai, S., Perez-Mato, J.M., Hosoya, S., and Paulus, W. (2012). *Inorganic Chemistry*, 51(18), 9789-9798.
4. The Yellow Book, Guide to Neutron Research Facilities, Institut Laue Langevin. http://www.ill.eu/fileadmin/users_files/Other_Sites/YellowBook2008CDRom/index.htm.
5. Kresse, G. and Furthmüller, J. (1996). *Physical Review B*, 54(16), 11169-11186.
6. Kresse, G. and Hafner, J. (1993). *Physical Review B*, 48(17), 13115-13118.
7. Parlinski, K. (1999). *AIP Conference Proceedings*, 479(1), 121-126.
8. Kneller, G.R., Keiner, V., Kneller, M., and Schiller, M. (1995). *Computer Physics Communications*, 91(1–3), 191-214.
9. Róg, T., Murzyn, K., Hinsien, K., and Kneller, G.R. (2003). *Journal of Computational Chemistry*, 24(5), 657-667.
10. Matlab, version 7.10.0 (R2010a). *The Mathworks Inc., Natick, Massachusetts*.
11. Hohenberg, P. and Kohn, W. (1964). *Physical Review*, 136(3B), B864-B871.
12. Kohn, W. and Sham, L.J. (1965). *Physical Review*, 140(4A), A1133-A1138.
13. Hartree, D.R. (1928). *Proc. Camb. Phil. Soc.*, 24(89).
14. Kohn, W. (1999). *Nobel Lecture*.
15. Perdew, J.P., Burke, K., and Wang, Y. (1996). *Physical Review B*, 54(23), 16533-16539.
16. The ABINIT Project. <http://www.abinit.org/>.
17. Segall, M.D., Lindan, P.J.D., Probert, M.J., Pickard, C.J., Hasnip, P.J., Clark, S.J., and Payne, M.C. (2002). *Journal of Physics: Condensed Matter*, 14(11), 2717.
18. Materials Studio. *Accelrys*.
19. Blaha, P., Schwarz, K., Madsen, G., Kvasnicka, D., and Luitz, J. Wien2k. *Institut for Materials Chemistry, TU Vienna, Autriche*.
20. Sears, V.F. (1992). *Neutron News*, 3(3), 26-37. <https://www.ncnr.nist.gov/resources/n-lengths/>
21. Boehm, M., Filhol, A., Raoul, Y., Kulda, J., Schmidt, W., Schmalzl, K., and Farhi, E. (2013). *Nuclear Instruments and Methods in Physics Research Section A: Accelerators, Spectrometers, Detectors and Associated Equipment*, 697(0), 40-44.
22. Kneller, G.R. and Hinsien, K. (2001). *The Journal of Chemical Physics*, 115(24), 11097-11105.
23. LAMP, the Large Array Manipulation Program. http://www.ill.eu/data_treat/lamp/the-lamp-book/.
24. Zbiri, M., Mittal, R., Rols, S., Su, Y., Xiao, Y., Schober, H., Chaplot, S.L., Johnson, M.R., Chatterji, T., Inoue, Y., Matsuishi, S., Hosono, H., and Brueckel, T. (2010). *Journal of Physics: Condensed Matter*, 22(31), 315701.
25. Zbiri, M., Mutka, H., Johnson, M.R., Schober, H., and Payen, C. (2010). *Physical Review B*, 81(10), 104414.
26. Zbiri, M., Schober, H., Choudhury, N., Mittal, R., Chaplot, S.L., Patwe, S.J., Achary, S.N., and Tyagi, A.K. (2012). *Applied Physics Letters*, 100(14), 142901.
27. Zbiri, M., Schober, H., Johnson, M.R., Rols, S., Mittal, R., Su, Y., Rotter, M., and Johrendt, D. (2009). *Physical Review B*, 79(6), 064511.

28. Shirane, G., Shapiro, S.M., and Tranquada, J.M., eds. *Neutron Scattering with a Triple-Axis Spectrometer - Basic Techniques*. 2006. ISBN: 9780521025898
29. Hennion, B. (2010). *Collection Société Française de la Neutronique (SFN)*, 10, 357.
30. Flatcone, Institut Laue-Langevin. <http://www.ill.eu/?id=10583>.

Chapter 4. Diffraction on the $\text{Nd}_2\text{NiO}_{4.25}$ single-crystal.

As described in **chapter 2**, the $\text{Nd}_2\text{NiO}_{4+d}$ system shows a wide range of structures upon excess oxygen content and temperature. While all of them are subgroups of the high-temperature high-symmetry tetragonal parent phase (HTT), being describe in the $I4/mmm$ space-group, they differ by the long-range arrangement of octahedra tilting scheme, and by the long-range organization of excess oxygen atoms. We have mentioned the three single-phases occurring at room-temperature: the low-temperature orthorhombic (LTO) $\text{Nd}_2\text{NiO}_{4.0}$ stoichiometric structure in space-group $Cmce$, the intermediate tetragonal $\text{Nd}_2\text{NiO}_{4.10}$ structure in space-group $P4_2/nm$, and a complex incommensurate phase of stoichiometry $\text{Nd}_2\text{NiO}_{4.25}$, described in an average orthorhombic $Fmmm$ structure; and the low-temperature tetragonal (LTT) found for the stoichiometric $\text{Nd}_2\text{NiO}_{4.0}$ below $T=130\text{K}^{[1]}$. In **chapter 3** we have also mentioned that, due to the synthesis route, the single-crystal obtained by travelling solvent floating zone method shows pseudo-merohedral twinning, with two or four twin domains and a twinning law based on the loss of $[110]$ mirror symmetry elements. Henceforth, finding the exact extended structure of – in particular – the most oxydized incommensurate $\text{Nd}_2\text{NiO}_{4.25}$ is a task that reach far beyond the aim of the present work. However, in order to understand the extent of the moderate-temperature regime in which the anomalous oxygen mobility is found, we shall at least have a qualitative understanding of the structural evolution of the $\text{Nd}_2\text{NiO}_{4.25}$ phase with temperature. The first inquiry is to determine if the room-temperature incommensurate structure of $\text{Nd}_2\text{NiO}_{4.25}$ shows a lock-in transition to a commensurate structure at low-temperature. To adress this issue, we performed single-crystal neutron diffraction at $T=300\text{K}$ and $T=20\text{K}$ using the thermal neutron single-crystal diffractometer D19 at ILL, along with direct measurement of the $(hk0)$ scattering plane using the Flatcone analyser on the thermal neutron three-axis spectrometer IN8 at ILL. This structural analysis in the low-temperature range is reported in **section 4.1**. A second inquiry concerns the dependence with temperature, in the high-temperature regime, of the structural modulation of $\text{Nd}_2\text{NiO}_{4.25}$. We performed temperature dependent single-crystal X-ray diffraction, up to $T=1270\text{K}$, using synchrotron radiation on the BM01A bending magnet at ESRF, which results are reported in **section 4.2**.

4.1. Neutron single-crystal diffraction at low-temperature on $\text{Nd}_2\text{NiO}_{4.25}$

In order to investigate the low-temperature structure of $\text{Nd}_2\text{NiO}_{4.25}$, we performed neutron diffraction on the thermal neutron single-crystal diffractometer D19 at ILL, using wavelength of $\lambda=1.46\text{\AA}$ and $\lambda=0.95\text{\AA}$, at $T=300\text{K}$ and $T=20\text{K}$. The experimental setup is described in **chapter 3**. We performed the experiment on a $3.0 \times 2.8 \times 2.5\text{mm}$ one-time twinned single-

crystal of Nd₂NiO_{4.25}, cut along the crystal axis and mounted on a vanadium sample holder to minimize the background signal.

Diffraction data at $T=300\text{K}$ and $T=20\text{K}$ with $\lambda=0.95\text{\AA}$ were processed using the SHELX code^[2], as implemented in the WINGX platform^[3], in order to extract the average structure – the $\lambda=1.46\text{\AA}$ data sets being collected to get a better statistics on incommensurate satellite. Unfortunately, the current software of D19 does not allow a proper integration of multi- k incommensurability mixed with merohedral twinning, and the extended crystalline structure cannot yet be determined. The average structures at $T=300\text{K}$ and $T=20\text{K}$, calculated from Bragg peaks only, are reported respectively in **Table 4.1** and **Table 4.2**.

Table 4.1 – Structural data of Nd₂NiO_{4.25} at $T=300\text{K}$ in $I4/mmm$ ($\lambda=0.95\text{\AA}$). Cell parameters: $a=b=3.8235(5)\text{\AA}$, $c=12.3440(25)\text{\AA}$. $R=0.0840$, $R_W=0.0785$, $R_G=0.0804$, $R_M=0.0804$.

ATOM	x	y	z	Occ. factor	U _{eq}	U ₁₁	U ₂₂	U ₃₃	U ₁₂	U ₁₃	U ₂₃
Nd	0	0	0.3585(5)	0.125	-	0.0113(26)	0.0113(26)	0.0057(30)	0	0	0
Ni	0	0	0	0.0625	-	0.0039(26)	0.0039(26)	0.0122(35)	0	0	0
O1	½	0	0	0.1250	-	0.0008(56)	0.0155(65)	0.0615(72)	0	0	0
O2	0	0	0.1716(10)	0.1250	-	0.119(11)	0.119(11)	0.0132(58)	0	0	0
O3	½	0	¼	0.0190(45)	0.049(20)	-	-	-	-	-	-

Table 4.2 – Structural data of Nd₂NiO_{4.25} at $T=20\text{K}$ in $I4/mmm$ ($\lambda=0.95\text{\AA}$). Cell parameters: $a=b=3.8172(5)\text{\AA}$, $c=12.3032(25)\text{\AA}$. $R=0.1103$, $R_W=0.0987$, $R_G=0.1079$, $R_M=0.1079$.

ATOM	x	y	z	Occ. factor	U _{eq}	U ₁₁	U ₂₂	U ₃₃	U ₁₂	U ₁₃	U ₂₃
Nd	0	0	0.3590(3)	0.125	-	0.0078(8)	0.0078(8)	0.0033(12)	0	0	0
Ni	0	0	0	0.0625	-	0.0012(7)	0.0012(7)	0.0072(13)	0	0	0
O1	½	0	0	0.125	-	0.0027(17)	0.0057(18)	0.0617(52)	0	0	0
O2	0	0	0.1717(6)	0.125	-	0.1069(69)	0.1069(69)	0.0020(27)	0	0	0
O3	½	0	¼	0.0161(40)	0.05	-	-	-	-	-	-

Since not much can be extracted from the average structures of Nd₂NiO_{4.25} at $T=300\text{K}$ and $T=20\text{K}$, apart from the strong expected delocalization of apical oxygen atoms O2 in the (ab) plane, we took advantage of the three-axis neutron experiments, described in **chapter 7**, to collect the Bragg scattering plane ($hk0$) with the Flatcone analyser, at $T=300\text{K}$ and $T=1.5\text{K}$. The Flatcone analyser is described in **chapter 3**. The sample used for the three-axis spectroscopy experiments is a two-time twinned single-crystal of Nd₂NiO_{4.25} with the shape of a 20mm long cylinder with 6.5mm diameter. The ($hk0$) scattering plane at $T=300\text{K}$ and $T=1.5\text{K}$ are shown on **Figure 4.1** and **Figure 4.2** respectively. Besides variations of satellite intensity, no major modifications of the diffraction pattern occur between $T=300\text{K}$ and $T=1.5\text{K}$. We can thus conclude that the incommensurate modulation simply freezes with lowering the temperature, and thus the satellite intensities increase from decreasing Debye-Waller factor, and that no lock-in transition to a commensurate structure takes place for incommensurate Nd₂NiO_{4.25}.

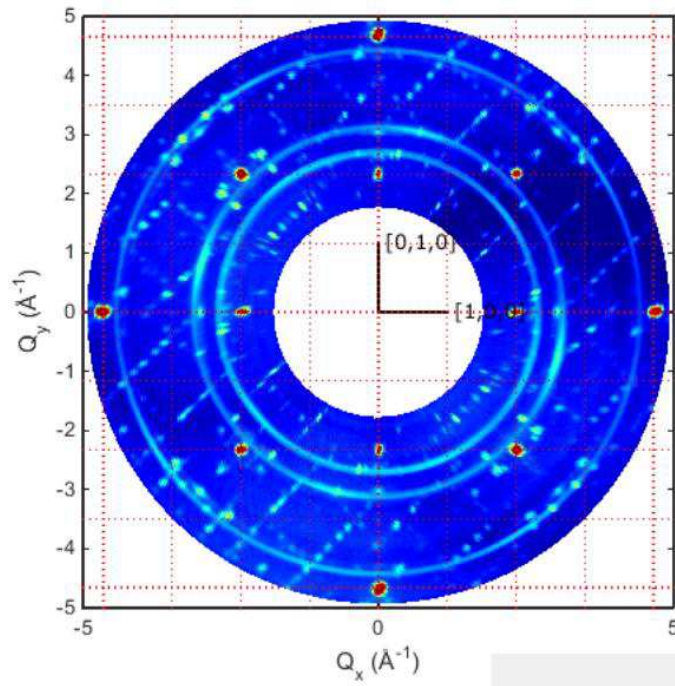


Figure 4.1 – Scattering plan ($hk0$) of $\text{Nd}_2\text{NiO}_{4.25}$ at $T=300\text{K}$ measured with the Flatcone analyzer on IN8. Measurement with constant $k_f=3.0\text{\AA}^{-1}$.

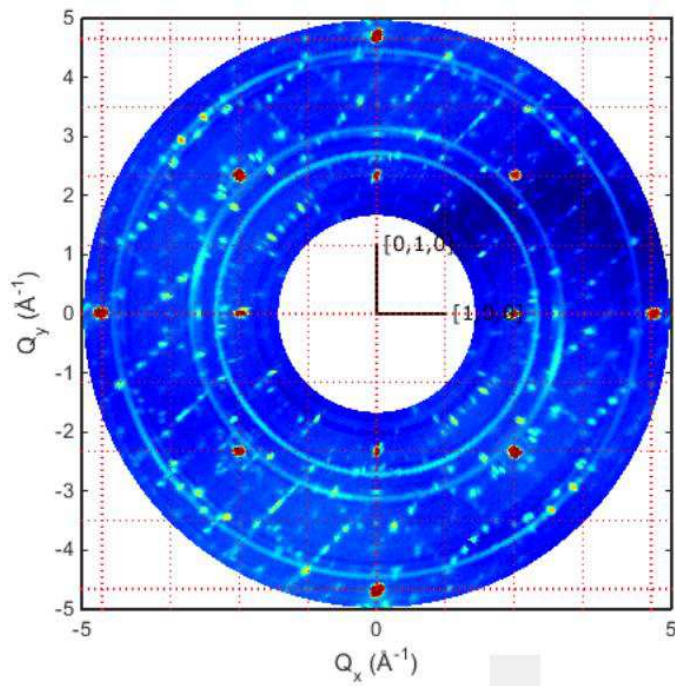


Figure 4.2 – Scattering plan ($hk0$) of $\text{Nd}_2\text{NiO}_{4.25}$ at $T=1.5\text{K}$ measured with the Flatcone analyzer on IN8. Measurement with constant $k_f=3.0\text{\AA}^{-1}$.

4.2. X-ray single-crystal diffraction at high-temperature on Nd₂NiO_{4.25}

In order to investigate the high-temperature structure of Nd₂NiO_{4.25}, we performed X-ray diffraction using the synchrotron radiation at the BM01A bending magnet at ESRF, in the range $T=300-1270\text{K}$, using a wavelength $\lambda=0.663055\text{\AA}$. The experimental setup is described in **chapter 3**. The sample is roughly a sphere of 100nm diameter of Nd₂NiO_{4.25} single-crystal. Diffraction data were processed using the software CrysAlis^[4]. For each temperature, the UB matrix was refined considering an average $F4/mmm$ structure, and the $(hk0)$ scattering plane was unfold as shown in **Figure 4.3**. The evolution of the diffraction pattern with temperature in the region of the $(hk0)$ plane including Bragg's (220) to (440) is reported in **Table 4.3**.

From the observation of the diffraction pattern evolution with temperature, one can identify several behaviors:

(1) From $T=300-420\text{K}$, two distinct orthorhombic phases coexist. The small splitting in d_{hko} values observed between the two phases implies that they have different oxygen hyper-stoichiometry; yet the splitting is only observable with high-resolution synchrotron X-rays, thus the variation in excess oxygen content between the two phases is minimal. Considering the size of the single-crystal, the coexistence of two phases with slight variation of oxygen hyper-stoichiometry can have two origins: a kinetic origin, with the outer layers of the crystal having slightly less excess oxygen atoms than the core of the crystal; or a thermodynamic origin, with a phase separation into oxygen-rich and oxygen-poor regions. The phase separation phenomenon has been observed in isostructural cuprates^[5-7], and is driven by the tendency of doped holes themselves to segregate.

(2) From $T=470-820\text{K}$, the structure is monophasic and orthorhombic, yet still incommensurate.

(3) From $T=870-1270\text{K}$, the structure is monophasic and tetragonal, and all incommensurate satellites disappear. In this high-temperature regime, the material is in the HTT parent phase.

(4) After cooling down, the room-temperature structure is orthorhombic with a minor tetragonal phase (less than a percent), which means the stoichiometry was reduced from $d=0.25$ to $d\approx 0.22$, or that the relative proportion of each twin domains have changed.

(5) Concerning the incommensurate satellites pattern, we observe a disappearance of the reflections at several distinct temperatures, between $T=370-420\text{K}$, between $T=420-470\text{K}$ on the transition from orthorhombic biphasic to monophasic, and between $T=820-870\text{K}$ on the transition from orthorhombic to tetragonal. The remaining incommensurate reflections above $T=870\text{K}$ are most likely to come from an intergrowth phase of Nd₄Ni₃O₁₀. We also remark that, while some satellite 'pairs' are merging with the phases transitions, some of the satellites are unique even at room-temperature, being unaffected by the twinning law.

(6) From the disappearance of the first incommensurate satellites between $T=370-420\text{K}$, and increasingly with temperature, diffuse scattering is observed around the Bragg peaks. After

cooling down, a different incommensurate pattern is observed, with reflections on the contour of the diffuse clouds observed at high-temperature. We interpret this behavior as: structural satellites are a consequence of long-range ordering of octahedra tilting adapting excess oxygen atoms on interstitial sites. Upon heating, due to the increase in mobility of apical and interstitial oxygen atoms, the long-range correlation is lost to single-particle motions producing diffuse scattering. Upon cooling down, the reverse effect occurs, yet the incommensurate satellite pattern is different due to slight changes of stoichiometry and, probably, kinetic effect depending on the cooling speed.

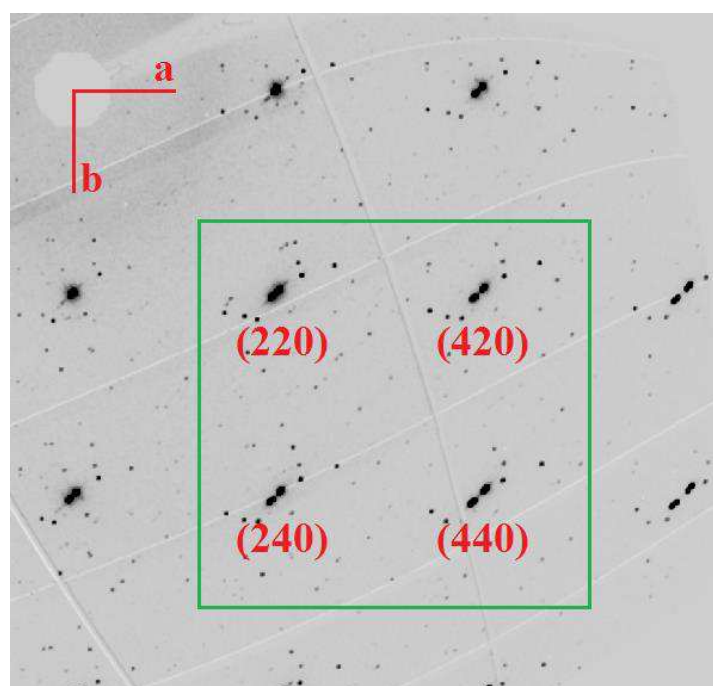
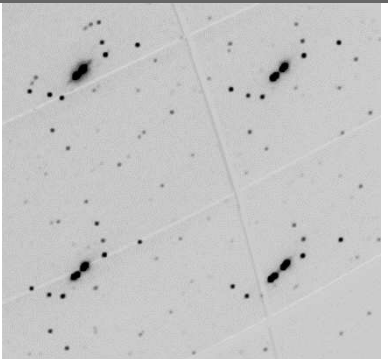
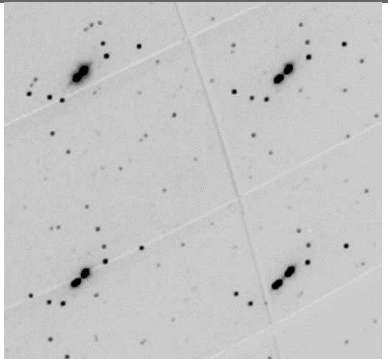
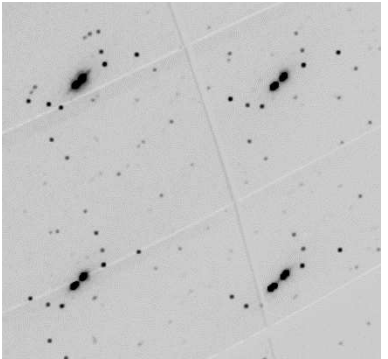
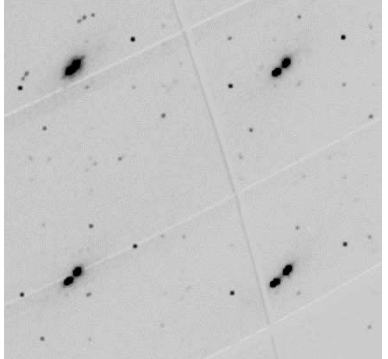
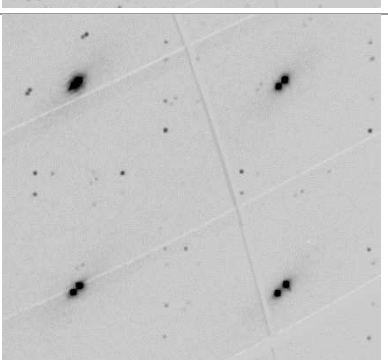
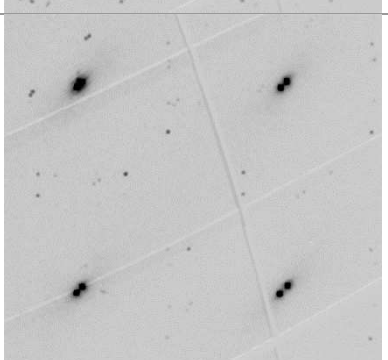
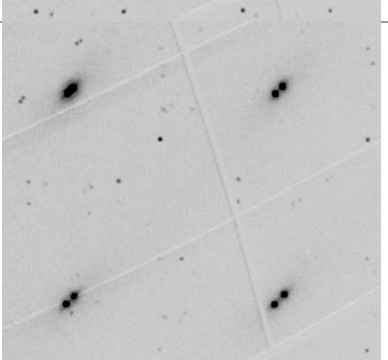
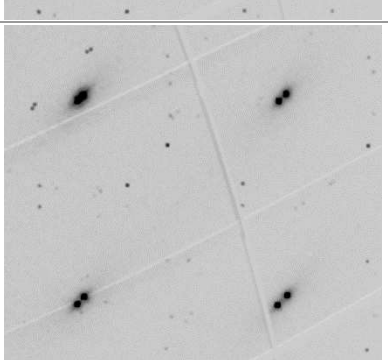
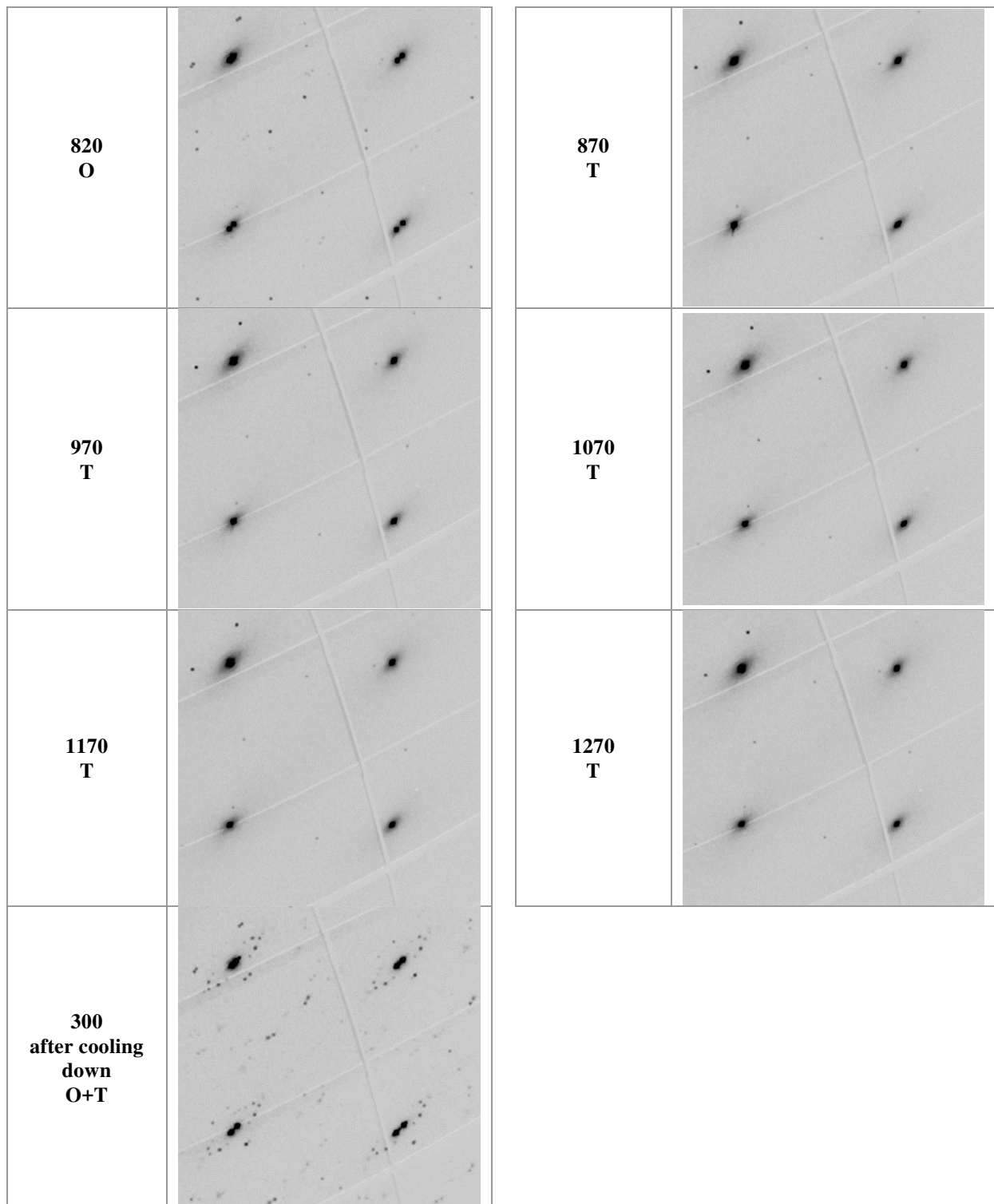


Figure 4.3 – Reconstruction of the scattering plan ($hk0$) of $\text{Nd}_2\text{NiO}_{4.25}$ from diffraction data at $T=300\text{K}$. The shape of the Bragg peak confirms the pseudo-merohedral twinning with two twin domains, and the twinning law from the loss of the (110) mirror. The green box represents the region from which the details of **Table 4.3** are extracted.

Table 4.3 – Evolution between $T=300-1270\text{K}$ of the diffraction pattern of $\text{Nd}_2\text{NiO}_{4.25}$ in the region specified in **Figure 4.3**.

Temperature (K) Phase	Diffraction pattern	Temperature (K) Phase	Diffraction pattern
300 Biphasic O		320 Biphasic O	
370 Biphasic O		420 Biphasic O	
470 O		570 O	
670 O		720 O	



Qualitative information can also be extracted from the scattering plane $(0kl)$, as shown in **Figure 4.4**. We observe that, regardless of temperature, diffuse trails can be observed along the c direction around Bragg peaks – which means there is some disorder along the c direction, most likely stacking faults $n>1$ as commonly observed in Ruddlesden-Popper type materials. We also observe, for the room-temperature phases (up to $T=370\text{K}$), some satellites at $(0\ 1\ 1\pm\frac{1}{6})$, which imply a well-defined organization involving the stacking-axis direction.

Since these satellites are only observed for the room-temperature phases, *i.e.* in the temperature range where the oxygen mobility is low and, thus, with a quasi-static arrangement of excess oxygen atoms, their presence suggests a cell-to-cell favorable arrangement of defective clusters with a periodicity close to the c -axis length, likely in a way to preserve the shape of NiO_6 octahedra.

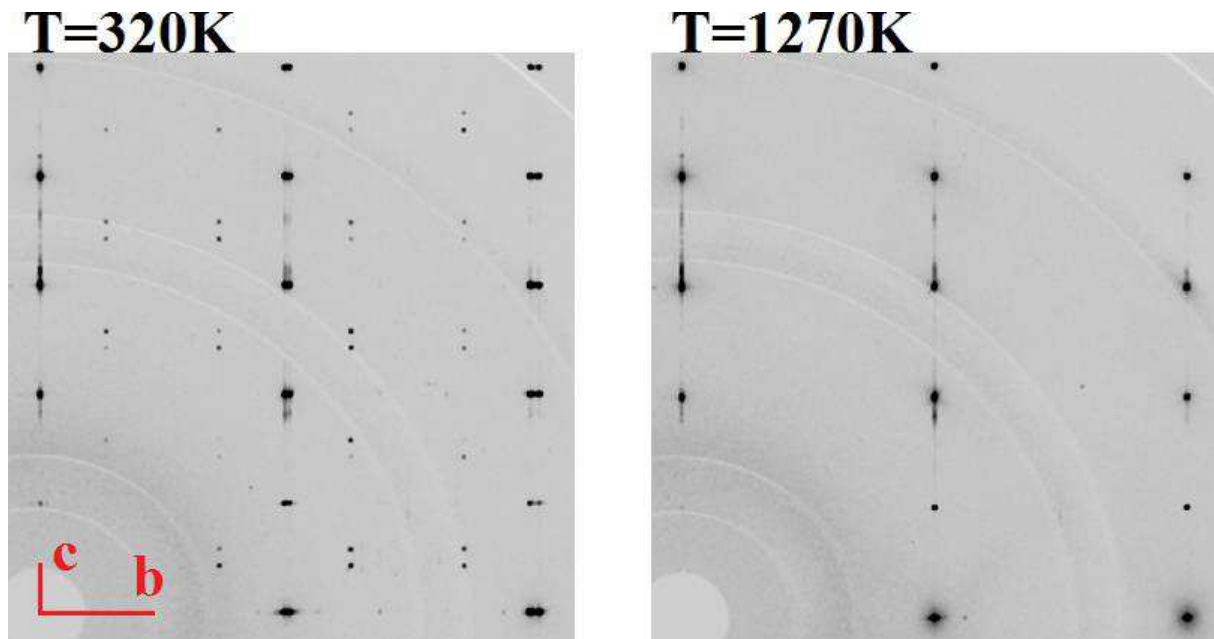


Figure 4.4 – Reconstruction of the scattering plan ($0kl$) of $\text{Nd}_2\text{NiO}_{4.25}$ from diffraction data, at $T=320\text{K}$ (left) and $T=1200\text{K}$ (right). The splitting of Bragg peaks along the b direction at room-temperature confirms the twinning.

4.3. Conclusion

In conclusion, from the joint qualitative studies by neutron and synchrotron X-ray single-crystal diffraction of $\text{Nd}_2\text{NiO}_{4.25}$, we have evidenced three temperature regimes linked to their associated oxygen atom mobility. We note that the complexity of the diffraction pattern is strongly dependent on the excess oxygen content and thermal history of the sample.

In the low-temperature range, from $T=1.5\text{K}$ to $T=370\text{K}$, the oxygen mobility is about null. Besides the long-range arrangement of defective clusters, we observed the presence of two phases with slight variation of excess oxygen content. While the structural modulations may be more pronounced at low-temperature, or better defined, which in both case lead to increasing satellite intensities, we did not find any evidence of lock-in transition or changes in the periodicity of structural modulations.

In the moderate-temperature range, from $T=420\text{K}$ to $T=820\text{K}$, oxygen atoms start to be mobile as suggested by the growing diffuse scattering observed around Bragg peaks. While the long-range ordering of defective clusters is still observed, the presence of two phases is not observed anymore, and we can assume that excess oxygen atoms are now homogeneously distributed in the whole crystal. This is the temperature range we are interested in, where both oxygen mobility and structural correlations coexist, and which will be addressed by studies of lattice dynamics in **chapters 5 to 7**.

In the high-temperature range, above $T=870\text{K}$, the oxygen atoms are mobile and the long-range ordering is lost. This regime, with its associated HTT tetragonal phase, has been extensively studied in terms of oxygen diffusion, as shown in **chapter 2**.

4.4. Bibliography

1. Rodríguez-Carvajal, J., Fernández-Díaz, M.T., Martínez, J.L., Fernández, F., and Saez-Puche, R. (1990). *Europhysics Letters*, 11(3), 261.
2. Sheldrick, G.M. (2008). *Acta Cryst.*, A64, 112-122.
3. Farrugia, L.J. (2012). *J. Appl. Cryst.*, 45, 849-854.
4. CrysAlis CCD, CrysAlis RED. *Oxford Diffraction (2006)*. Oxford Diffraction Ltd, Abingdon, England.
5. Alexandrov, A.S. (2009). *J. Supercond. Novel Magn.*, 22, 95.
6. Di Ciolo, A., Lorenzana, J., Grilli, M., and Seibold, G. (2009). *Physical Review B*, 79(8), 085101.
7. Fine, B.V. and Egami, T. (2008). *Physical Review B*, 77(1), 014519.

Chapter 5. First-principle DFT calculations.

Calculations based on the density functional theory (DFT) are a powerful tool to probe local structural correlations and lattice dynamics of systems, as long as the approximations on the structural models and on the electronic properties allow a proper description of the considered system. Many calculations^[1-9] have been performed on related systems, yet with a focus on the high-temperature oxygen mobility above $T=1070\text{K}$, high-temperature average phases, and generally using classical calculations with core-shell models to describe the systems. Our interest, using *ab initio* methods despite their intrinsic limitations on the number of atoms, and thus the subsequent approximations of structural model, is the impact of excess oxygen on the dynamical properties of the system, and how it may impact the oxygen mobility – thus basically we are looking for the microscopic mechanism of oxygen diffusion at moderate temperature, as it has been done on other materials^[10-12].

In **section 5.1** we will present the structural models of the three-single phases of the $\text{Nd}_2\text{NiO}_{4+d}$ system: the stoichiometric $\text{Nd}_2\text{NiO}_{4.0}$, the intermediate $\text{Nd}_2\text{NiO}_{4.10}$ and the fully-oxidized $\text{Nd}_2\text{NiO}_{4.25}$, and how we approximate the average structures obtained with diffraction experiments into structures with full occupancy of sites, accommodating the local deformations induced by excess oxygen atoms in interstitial sites. The **section 5.2** will describe the DFT phonon calculations performed to calculate the dispersion curves, and the results we draw from analysis of phonon modes and their associated atomic displacements, to show how specific modes can favor the oxygen mobility. In **section 5.3** we will describe the molecular dynamic calculations we performed, and the subsequent informations about the oxygen diffusion pathway and phonon densities of states. At last, we will present in **section 5.4** the analysis of molecular dynamic trajectories using the positional recurrence map (PRM) code, introduced in **chapter 3**, and the conclusions we draw about the effect of temperature and c-axis length on the dynamics of apical oxygen atoms, and how their specific dynamics can be linked to oxygen mobility.

The results drawn from these calculations will be confirmed by the inelastic neutron scattering experiments described in the following chapters, which will retro-actively justify the choices of the DFT-based calculations instead of classical calculations, sets of calculation parameters, and approximations on structural models. Theoretical background on the DFT, along with the description of the positional recurrence map (PRM) code we developed, are available in **chapter 3** and **appendix A**.

5.1. Models and optimized geometries of the $\text{Nd}_2\text{NiO}_{4+d}$ phases

In the following sections are presented the structural models used to describe the three single-phases of $\text{Nd}_2\text{NiO}_{4+d}$: the stoichiometric $\text{Nd}_2\text{NiO}_{4.0}$, the intermediate $\text{Nd}_2\text{NiO}_{4.10}$, and the fully-oxidized $\text{Nd}_2\text{NiO}_{4.25}$. While the real intermediate single-phase has an oxygen excess stoichiometry of about $d=0.10$ ^[13], we used a model containing $d=0.125$ excess oxygen atoms (2 excess oxygen atoms on models with $Z=16$) due to limitations of the number of atoms in the *ab initio* framework. Yet, for the sake of clarity, simulations referring to the intermediate phase will be labelled $\text{Nd}_2\text{NiO}_{4.10}$.

Since our interest is the moderate temperature range in structures showing long-range ordering, thus strong structural correlations, and the effects of local deformations on lattice dynamics, we cannot consider as structural models the commonly used high-temperature high-symmetry average structures^[1-5]. Instead we developed models based on approximations of the room-temperature phases, described in **chapter 2**.

All calculations have been performed with the DFT code implemented in VASP^[14, 15], using PBE exchange-correlation functional, PAW pseudo-potential for ionic core-valence interactions, and the plane wave basis set. More informations about computational parameters are reported in **section 5.2.1**.

5.1.1. Stoichiometric $\text{Nd}_2\text{NiO}_{4.0}$

Even if the stoichiometric phase $\text{Nd}_2\text{NiO}_{4.0}$ seems the easiest system to simulate due to high local symmetry, well defined ordering of NiO_6 octahedra tilting, and lack of interstitial defects, its modeling has been, in fact, challenging. The room-temperature structure we are interested in was found unstable in the $T=0\text{K}$ calculations of the DFT framework, and thus we had to consider the low-temperature structure of $\text{Nd}_2\text{NiO}_{4.0}$ and, in order to obtain cell parameters close to experimental values, we had to include magnetism to our calculations. The steps leading from the structure we initially aimed to model, to the structure we actually modeled, are described hereafter.

As stated in **chapter 2**, the room-temperature phase of $\text{Nd}_2\text{NiO}_{4.0}$, usually referred as low-temperature orthorhombic (LTO) with *Bmcb* space-group, is reported to have the strongest orthorhombicity among the $\text{Nd}_2\text{NiO}_{4+d}$ phases. Experimentally determined cell parameters and atomic positions, as published in literature^[16], are reminded in **Table 5.1**.

Table 5.1 – Cell parameters, space-group and atomic positions of the experimental structure of $\text{Nd}_2\text{NiO}_{4.0}$ at $T=330\text{K}$ ^[16].

Space-group	Atoms	Atomic parameter (r.l.u.)			Cell parameters
		x	y	z	
$Bmcb$ ($n^\circ 64$)	Nd	0	0.985(1)	0.3632(3)	a = 5.3876(5) Å
	Ni	0	0	0	b = 5.5883(5) Å
	O1 (equa.)	¼	¼	0.9821(6)	c = 12.135(1) Å
	O2 (apic.)	0	0.063(1)	0.1794(6)	

Table 5.2 – Cell parameters, space-group and atomic positions of the calculated structure of $\text{Nd}_2\text{NiO}_{4.0}$ in the LTO phase.

Space-group	Atoms	Atomic parameter (r.l.u.)			Cell parameters
		x	y	z	
$Bmcb$ ($n^\circ 64$)	Nd	0	0.9833	0.3629	a = 5.4012 Å
	Ni	0	0	0	b = 5.6434 Å
	O1 (equa.)	¼	¼	0.9799	c = 12.2223 Å
	O2 (apic.)	0	0.0683	0.1788	

Using as a starting point the structure reported in **Table 5.1**, with adapted computational parameters, it is possible to obtain, through geometric optimization, the calculated structure reported in **Table 5.2**. The optimized cell parameters and atomic positions are in good agreement with experimental values, with relative errors lower than a percent.

However, when calculating phonon dispersion from the direct method, several negative phonon modes have been observed. Such negative modes mean that, even if the geometry optimization is properly converged, the structure is not stable against some displacements (typically wrong restoring forces in the calculation of Hellmann-Feynman forces). This instability can be expected since the calculation is performed at $T=0\text{K}$, where the $\text{Nd}_2\text{NiO}_{4.0}$ phase retains the low-temperature tetragonal (LTT) structure. The transition temperature from the LTO to the LTT structure of $\text{Nd}_2\text{NiO}_{4.0}$ has been reported at $T=130\text{K}$ ^[16]: the full description of the phase diagram and associated structures of $\text{Nd}_2\text{NiO}_{4+d}$ are available in **chapter 2**. As previously stated, our main interest is on the dynamics of the room-temperature phase. However, the presence of negative phonon modes in the calculations would invalidate any analysis. In consequence, we performed the calculation on the only stable structure with respect to the $T=0\text{K}$ condition, the LTT phase, using as starting model the experimental structure reported in **Table 5.3**^[16].

Table 5.3 – Cell parameters, space-group and atomic positions of the experimental structure of $\text{Nd}_2\text{NiO}_{4.0}$ at $T=1.5\text{K}$ [16].

Space-group	Atoms	Atomic parameter (r.l.u.)			Cell parameters
		x	y	z	
$P4_2/ncm$ (n°138)	Nd	0.9879(5)	0.9879(5)	0.3641(2)	a = 5.480(1) Å
	Ni	0	0	0	b = 5.480(1) Å
	O1 (equa.)	¼	¼	0.9702(6)	c = 12.057(3) Å
	O2 (equa.)	¾	¼	0	
	O3 (apic.)	0.0508(5)	0.0508(5)	0.1785(5)	

Table 5.4 – Cell parameters, space-group and atomic positions of the calculated structure of $\text{Nd}_2\text{NiO}_{4.0}$ in the LTT phase.

Space-group	Atoms	Atomic parameter (r.l.u.)			Cell parameters
		x	y	z	
$P4_2/ncm$ (n°138)	Nd	0.9882	0.9882	0.3623	a = 5.3734 Å
	Ni	0	0	0	b = 5.3734 Å
	O1 (equa.)	¼	¼	0.9790	c = 12.7357 Å
	O2 (equa.)	¾	¼	0	
	O3 (apic.)	0.0404	0.0404	0.1834	

Geometric optimization on the structure reported in **Table 5.3** leads to the structure reported in **Table 5.4**. One can see that, in the $P4_2/ncm$ space-group, the cell parameters do not match the experimental values, especially the c-axis, which is strongly overestimated with a relative error of about 5% – in general it is important that differences do not exceed 2-3%. However with this structural model the subsequent vibrational analysis gave phonon modes all positive.

Collinear magnetism was added to the calculation to simulate the antiferromagnetism of the nickel ions sublattice. In collinear magnetism, magnetic moments are approximated by a positive or negative magnetic charge carried by the ions. The addition of ponctual charges in antiferromagnetic setting lowers the symmetry of the system, with the loss of the four-fold axis, as schemed in **Figure 5.1**, reducing the Bravais lattice from tetragonal to orthorhombic, and thus the space-group from $P4_2/ncm$ to $Pccn$. However the a-b splitting have been calculated to be very small, in the order of numerical errors, so that its contribution can be neglected. The calculated magnetic structure is reported in **Table 5.5**.

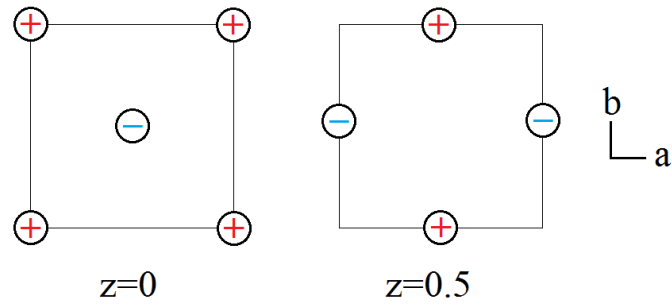


Figure 5.1 – Scheme of the Nickel atoms in the $z=0$ and $z=1/2$ plans, translated by $T=(1/2 \ 0 \ 1/2)$. The addition of positive and negative ponctual charges to simulate magnetism leads to the loss of the 4-fold axis.

Table 5.5 – Cell parameters, space-group and atomic positions of the calculated structure of $Nd_2NiO_{4.0}$ in the quasi-LTT phase, with collinear magnetism.

Space-group	Atoms	Atomic parameter (r.l.u.)			Cell parameters
		x	y	z	
<i>Pccn</i> (n°56)	Nd	0.9844	0.9844	0.3638	a = 5.5146 Å
	Ni	0	0	0	b = 5.5168 Å
	O1 (equa.)	1/4	1/4	0.9756	c = 12.2330 Å
	O2 (equa.)	3/4	1/4	0.0000	
	O3 (apic.)	0.0288	0.0288	0.1793	

As consequence of the inclusion of magnetism, calculated cell parameters and atomic positions are closer to the experimental values, with a relative error on the c-axis of about 1.4%. In this *Pccn* space-group, all phonon modes, even if artificially doubled in (x,y), are positive. This last calculation, in **Table 5.5**, has been used as model for the $Nd_2NiO_{4.0}$ phase for the lattice dynamics calculations described in **section 5.2**.

Concerning the molecular dynamic calculations, and as described in **chapter 3**, the cell shall be designed in a way that the force constants are reduced by 2-3 orders of magnitude for half the cell length to minimize boundary effects – which is in practice realized when using a cell with parameters higher than 10Å. In our case, we build a 2x2x1 supercell, *i.e.* the structure of **Table 5.5**, duplicated along the **a** and **b** directions. Since the **a** and **b** parameters are almost equal, we designed the 2x2x1 supercell to be tetragonal with parameters $a'=b'=(a+b)=11.0314\text{Å}$ and $c'=c=12.2330\text{Å}$. The subsequent supercell is pictured in **Figure 5.2**.

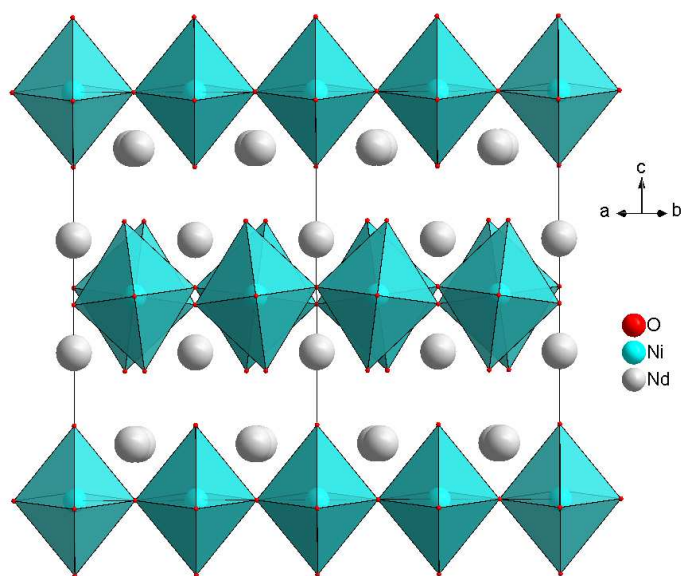


Figure 5.2 – Supercell $2 \times 2 \times 1$ of $\text{Nd}_2\text{NiO}_{4.0}$ ($a=b=11.0314\text{\AA}$, $c=12.2330\text{\AA}$), projected on the (110) plan to evidence the alternate octahedra tilting along $[110]$ and $[-110]$ for octahedral layers stacked along the c -axis.

5.1.2. Intermediate $\text{Nd}_2\text{NiO}_{4.10}$

The experimental structure of the intermediate phase $\text{Nd}_2\text{NiO}_{4.10}$ has been measured by powder diffraction^[13, 17]. The space-group was determined to be $P4_2/nm$, and cell parameters and atomic positions are reported in **Table 5.6**.

Table 5.6 – Cell parameters, space-group and atomic positions of the experimental structure of $\text{Nd}_2\text{NiO}_{4.10}$ at $T=300\text{K}$ ^[13]. O4 has a partial occupancy corresponding to an excess oxygen stoichiometry of $d=0.095(9)$.

Space-group	Atoms	Atomic parameter (r.l.u.)			Cell parameters
		x	y	z	
$P4_2/nm$ (n°138)	Nd	0.9893(4)	0.9893(4)	0.3609(1)	$a = 5.45490(5) \text{\AA}$
	Ni	0	0	0	$b = 5.45490(5) \text{\AA}$
	O1 (equa.)	$\frac{1}{4}$	$\frac{1}{4}$	0.9790(6)	$c = 12.2204(1) \text{\AA}$
	O2 (equa.)	$\frac{3}{4}$	$\frac{1}{4}$	0	
	O3 (apic.)	0.0438(4)	0.0438(4)	0.1766(3)	
	O4 (inter.)	$\frac{1}{4}$	$\frac{1}{4}$	0.250(4)	

While the structural refinement from diffraction allows partial occupancy of sites, our DFT calculations can only handle full occupancy of sites. As such, the structure reported in **Table 5.6** cannot be used as a starting point for DFT calculation: the excess oxygen must be located on a specific interstitial site, which would considerably lower the symmetry.

Considering a typical F-cell of $\text{Nd}_2\text{NiO}_{4.0}$ with $Z=4$, the inclusion of one excess oxygen on one of the eight interstitial sites would give an overstoichiometry of $d=0.25$. Even if the

smallest supercell required to give $d=0.125$ would be with $Z=8$, we preferred a $2 \times 2 \times 1$ supercell ($Z=16$), with two excess oxygen atoms in interstitial sites, in prevision of the molecular dynamic calculations. Concerning the choice of the two interstitial sites occupied by excess oxygen, we avoided positions on cell boundaries in (a,b), and interstitial sites too close from each other. This because we would get unphysical distances and unreasonably deformed octahedra. The localization of multiple excess oxygen atoms is discussed in detailed in **section 5.1.3**.

Geometry optimization leads to supercell parameters $a=b=10.6673\text{\AA}$ and $c=12.6493\text{\AA}$, which means $a'=b'=5.3337\text{\AA}$ and $c'=c$ when projected to the F-cell.

Similarly to the $\text{Nd}_2\text{NiO}_{4.0}$ calculations, cell parameters are underestimated for the a- and b-axis and overestimated for the c-axis. We can imagine that the calculated cell-parameters would be closer to the experimental values if we add collinear magnetism to the calculation. Anyhow no magnetic ordering has been reported for $\text{Nd}_2\text{NiO}_{4.10}$ at any temperature, as shown in **chapter 2**, and thus the magnetic contribution has not been considered. Such supercell is depicted in **Figure 5.3**.

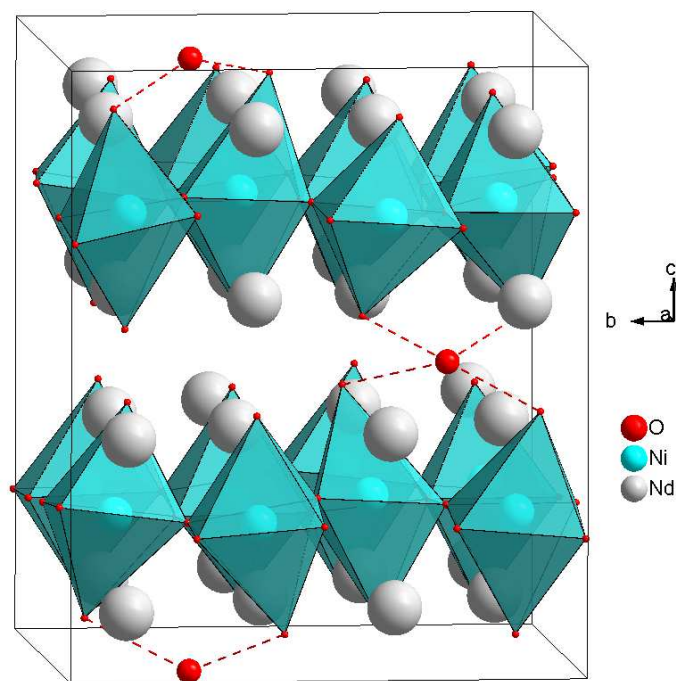


Figure 5.3 – Geometry optimized supercell of $\text{Nd}_2\text{NiO}_{4.10}$ ($2 \times 2 \times 1$, with respect to the F-cell), with cell parameters $a=b=10.6673\text{\AA}$ and $c=12.6493\text{\AA}$. As previously stated, the exact stoichiometry in the calculation is $\text{Nd}_2\text{NiO}_{4.125}$, while for clarity the calculation is labelled as $\text{Nd}_2\text{NiO}_{4.10}$.

5.1.3. Further discussion about the defect localization

As discussed in **chapter 2**, it has been shown that the room-temperature phases of $\text{Nd}_2\text{NiO}_{4+d}$ have long-range ordering of octahedral tilting, or incommensurate superlattice peaks showing long-range structural correlations in between excess oxygen atoms and associated defective clusters. However, due to the limited number of atoms in our DFT calculations, and since we must consider fully-occupied sites, the question of the local arrangement of multiple excess oxygen atoms arises – *i.e.* on which interstitial sites we place the excess oxygen atoms.

To solve this question, we built a structural model as follows: as a starting point, we consider a $2 \times 2 \times 1$ supercell with respect to the F-cell, shifted in a way to have an interstitial site at the center of the supercell (basically the **Figure 5.3** without any excess oxygen). First we fill the central interstitial site with an excess oxygen, and we observe a stabilization of the whole structure. In a second time, we insert a second excess oxygen in the structure: there are actually five distinct sites on which this second excess oxygen can be accommodated. On each site, we did a geometry optimization and calculated the variation of the total energy, to see which of the five configurations is the most stable. A scheme of the structural model is depicted in **Figure 5.4**, and the results are reported in **Table 5.7**. As a result, we see that configurations for which the excess oxygen are too close from each other, or configurations that would imply a strong deformation of the NiO_6 octahedra – or a strongly frustrated tilt, lead to an instability of the structure. In conclusion, multiple excess oxygen shall be localized in a way to minimize the juxtaposition of defective clusters and preserve the shape of NiO_6 octahedra.

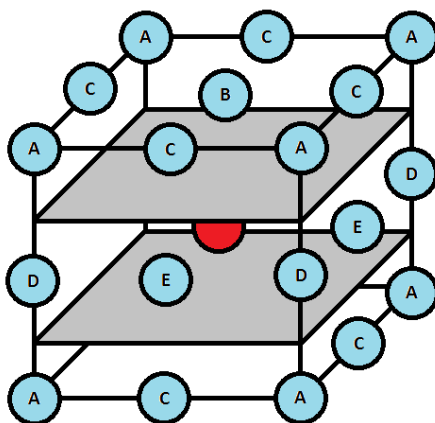


Figure 5.4 – Scheme of the structural model used to estimate the stable local arrangement of multiple excess oxygen on the interstitial sites. The first excess oxygen is located at the center of the supercell, pictured by a red circle. Inequivalent neighboring interstitial sites are labelled from A to E and pictured as blue circles. The grey layers represent the perovskite layers.

Table 5.7 – Summary of energy variation (in kBar), for each of the five configurations (A-E). In the table, a positive variation refers to a stabilization, and a negative to a destabilization. The “-∞” refers to a non-convergence of the calculation, i.e. an unstable structure.

Oxygen site	Energy variation (kBar)
1 st excess oxygen	+ 3.08
2 nd excess oxygen on site A	+ 1.52
2 nd excess oxygen on site B	- ∞
2 nd excess oxygen on site C	+ 2.11
2 nd excess oxygen on site D	+2.31
2 nd excess oxygen on site E	- 21.61

5.1.4. Fully-oxidized Nd₂NiO_{4.25}

The same issue about partial occupancy is encountered for the fully-oxidized Nd₂NiO_{4.25}. The experimental structure is reported in **Table 5.8**. While the diffraction pattern shows incommensurate satellites, the average space-group was determined to be *Fmmm*. We note that, while the *Fmmm* space-group would not allow a tilting scheme of NiO₆ octahedra, the O2 atom is in fact strongly delocalized in (xy) at the (00z) position in site O2a, and some of it shows a position O2b due to the deformation from excess oxygen in interstitial site.

Table 5.8 – Cell parameters, space-group and atomic positions of experimental structure of Nd₂NiO_{4.25} at T=300K^[13]. O3 has a partial occupancy corresponding to an excess oxygen stoichiometry of d=0.19(15). The O2 atoms are shared between an average high-symmetry position O2a and a splitted O2b position.

Space-group	Atoms	Atomic parameter (r.l.u.)			Cell parameters
		x	y	z	
<i>Fmmm</i> (n°69)	Nd	0	0	0.3592(6)	a = 5.3685(80) Å
	Ni	0	0	0	b = 5.4543(10) Å
	O1 (equa.)	¼	¼	0	c = 12.3642(29) Å
	O2a (apic.)	0	0	0.175(87)	
	O2b (apic.)	0.093(14)	0.093(14)	0.245(22)	
	O4 (inter.)	¼	¼	¼	

Here again we used the approximation of a tetragonal supercell with cell parameters a=b=15.4272Å and c=12.2629Å, (2√2, 2√2, 1) with respect to the F-cell, in order to have excess oxygen atoms properly arranged and avoid occupancy of interstitial sites at the cell boundary in (xy) at the beginning of the simulation.

Since the structure is quite complex and many diffusion events happen during the MD, a random step is taken out and pictured in **Figure 5.5**. One expects all excess oxygen atoms in interstitial site (*red*) and all apical oxygen atoms belonging to – more or less – deformed NiO₆ octahedra (*blue polyhedra*) ; however, in this frame, and in most frames of the calculation, several nickel atoms show a square pyramid configuration (*orange polyhedra*), with two oxygen atoms in-between apical and interstitial sites (*orange*). These in-between states are

reported as saddle states for the ‘interstitialcy’ mechanism of diffusion^[10], and as such shall be very instable. However this “square pyramid plus two oxygen” configuration can last up to a picosecond of simulation time (500 steps), *i.e.* is quite stable.

It is open if the saddle state is locally stabilized for sterical reasons due to the strong amount of excess oxygen, or if the potential energy barrier for migration shows a dip, a metastable state, at the saddle point.

Others questions arise from this behavior: Is the diffusion of apical and interstitial atoms actually simultaneous? A one-step two-atom diffusion? And more generally, if this lasting NiO_{5.7} configuration is relevant for the room-temperature diffusion, can a classical rigid-unit model properly describe the Nd₂NiO_{4.25} system? These questions will be adressed in **section 5.3.1**.

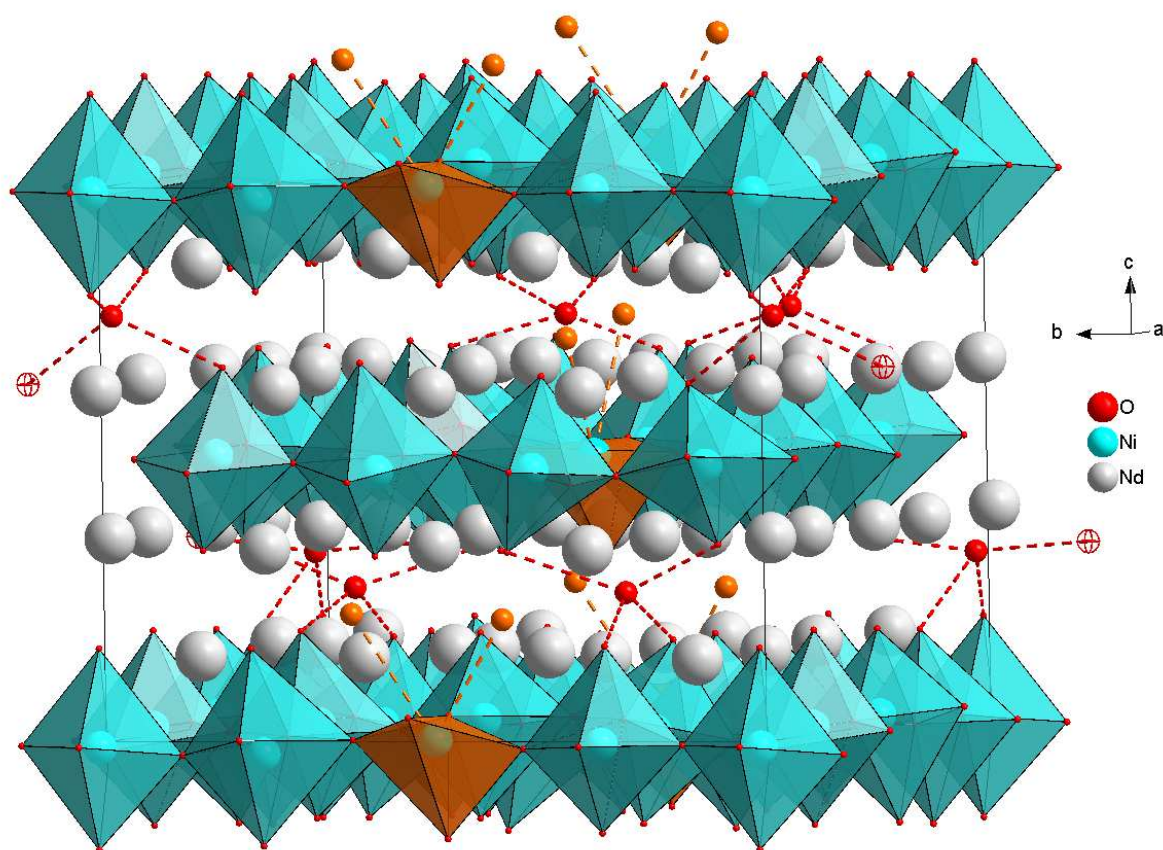


Figure 5.5 – Random step of the MD of a supercell $(2\sqrt{2}, 2\sqrt{2}, 1)$ of Nd₂NiO_{4.25} at T=310K. NiO₆ polyhedra are depicted in blue, while square-pyramide NiO₅ polyhedra are in orange. Excess oxygen atom in an interstitial site is in red and bound to its four apical oxygen neighbors. Apical-interstitial oxygen pair in saddle state is in orange and bound to its first-neighbor nickel atom.

5.2. Phonon calculations

Now that the structural models are built to describe the $\text{Nd}_2\text{NiO}_{4.0}$, $\text{Nd}_2\text{NiO}_{4.10}$ and $\text{Nd}_2\text{NiO}_{4.25}$ phases and adapted to the DFT framework, we can proceed with the calculations of phonon dispersion curves and to the description of displacements associated to these modes. The phonon dispersion curves calculated here will be compared with neutron inelastic three-axis spectroscopy experiments in **chapter 7**.

5.2.1. Parameters for $\text{Nd}_2\text{NiO}_{4.0}$

All our DFT calculations are performed using the VASP code^[14, 15]. For the elements oxygen, nickel and neodymium, PBE pseudo-potentials were used, with frozen 4f orbitals for the neodymium. Trials with neodymium pseudo-potentials including the 4f orbitals were also performed, yet the iterative process of energy minimization did not converge; the approximation of frozen 4f orbitals has no consequences since the neodymium ions stay in the +III oxydation state indepently of the amount of excess oxygen, and its magnetic ordering only happens at $T=8\text{K}$ ^[16], far bellow the temperature range where oxygen mobility occurs. Projected augmented wave (PAW) potentials were chosen for the ionic core-valence interactions, and the generalized gradient approximation (GGA) for the exchange-correlation potential. We performed both magnetic and non-magnetic calculations on the low-temperature tetragonal phase of stoichiometric $\text{Nd}_2\text{NiO}_{4.0}$ considering only the antiferromagnetism of the nickel sublattice, in the setup of collinear magnetism (*i.e.* describing magnetic moments as positive or negatives point charges). Since the $\text{Nd}_2\text{NiO}_{4+d}$ system has been reported as an insulator or semi-conductor depending on the oxygen content at room-temperature, an additional Hubbard corrective term was needed to create an electronic gap at the Fermi level; the parameters $U=7.0$ and $J=0.88$ were used for the nickel, as for the perovskites RNiO_3 ^[18].

A typical INCAR file for the energy calculation to get the electronic density of states on the geometry optimized structure is reported in **Table 5.9**.

Table 5.9 – Input parameters for the INCAR file to perform an energy calculation.

NELMIN = 4	SIGMA = 0.01	LORBIT =11	LDAUU = 0.0 7.0 0.0
EDIFF = 1E-8	ENMAX = 600	NPAR = 1	LDAUJ = 0.0 0.88 0.0
NSW = 0	ISYM = 2	LDAU = .TRUE.	LDAUPRINT = 2
PREC = Accurate	ISPIN = 2	LDAUTYPE = 2	MAGMOM = 16*0.0 2.0 -2.0 -2.0 2.0 8*0.0
ISMEAR = 0	ICHARG = 2	LDAUL = -1 2 -1	

For mode eigenvector analysis, we performed additional phonon calculations on $\text{Nd}_2\text{NiO}_{4.0}$ using the direct method as described in **chapter 3**, with *ab initio* calculated Hellmann-Feynman forces. The dynamical matrix diagonalization and the calculation of phonon dispersion curves and phonon density of states at $T=0\text{K}$ were performed with PHONON^[19]. While phonon calculations were performed on all models reported in **section 5.1.1**, only the most relevant, $\text{Nd}_2\text{NiO}_{4.0}$ in the *Pccn* magnetic space-group (**Table 5.5**), will be described hereafter.

5.2.2. Phonon dispersion curves and DOS of $\text{Nd}_2\text{NiO}_{4.0}$

As stated in **section 5.1.1**, the best description of the $\text{Nd}_2\text{NiO}_{4.0}$ phase is its low-temperature LTT structure. In order to get cell parameters close to experimental ones, the antiferromagnetism of the nickel ions had to be considered, which induce a symmetry breaking from tetragonal to orthorhombic, lowering the space-group from $P4_2/nm$ to *Pccn*. As such, phonon modes become artificially splitted (such as initially degenerate phonon modes along *x* and *y*). A full representation of the dispersion curves of $\text{Nd}_2\text{NiO}_{4.0}$ -*Pccn*, with the related vibrational DOS, is shown if **Figure 5.6**. Three regions of the dynamic spectrum are of interest : the acoustic part ranging from $E=0$ to about $E=12$ meV, a continuum of spaghetti-like optical modes up to $E=50$ meV, and well separated optical modes from $E=50$ to $E=80$ meV. From literature^[6], we expect the low-energy optical modes to be associated with tilting motions, while the high-energy modes to any kind of octahedral and stretching motions.

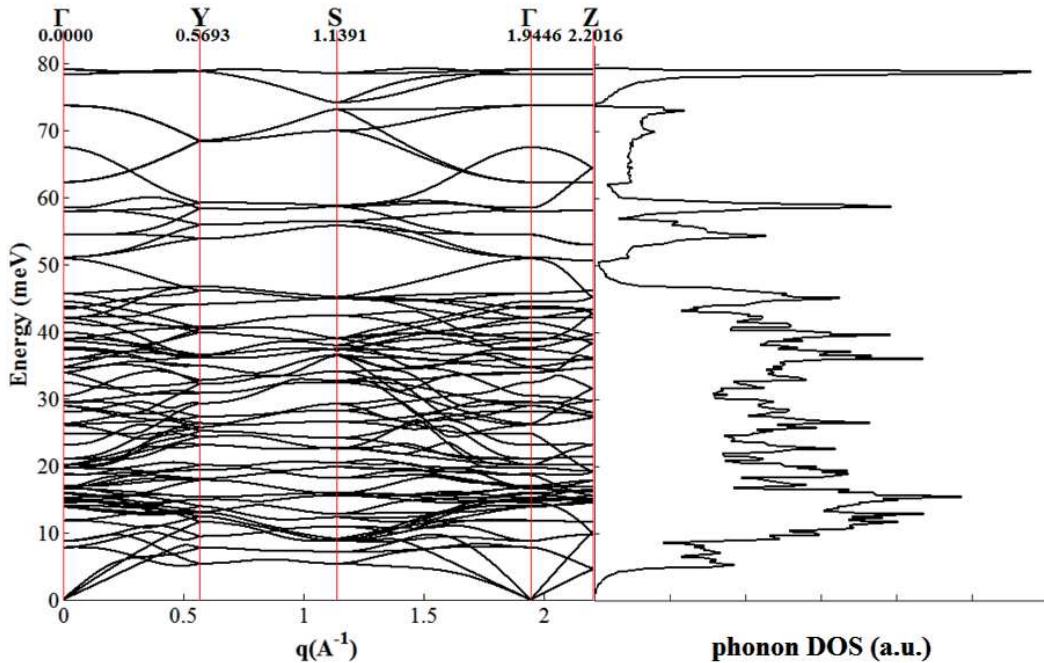


Figure 5.6 – Dispersion curves and vibrational DOS of $\text{Nd}_2\text{NiO}_{4.0}$ in the *Pccn* model, in the full energy range. High-symmetry points are $\Gamma(000)$, $Y(0 \frac{1}{2} 0)$, $S(\frac{1}{2} \frac{1}{2} 0)$, and $Z(00 \frac{1}{2})$. For further considerations the *S* point will be referred as *M* point, as in tetragonal phases.

In order to sort and identify the phonon modes of interest, and considering the spectroscopy experiments performed on three-axis spectrometers, described in **chapter 7**, we calculated the phonon mode intensities $S(\mathbf{q},\omega)$ in the energy and momentum transfer ranges available on the spectrometers. Beyond geometry limitations of the spectrometers, high-intensity acoustic modes have their origin at high-intensity Bragg peaks; as such the regions of interest in \mathbf{Q} are mainly located around (040) and (220). The following figures, as well as those of **chapter 7**, are drawn using the code described in **appendix B**. Phonon intensities are shown in logarithmic scale, and every figure shares the same color scale, meaning that every figure can be compared in term of intensities.

In **Figure 5.7** we draw the longitudinal phonon modes along the $Y(0\xi 0)$ direction, between $Q(030)$ and $Q(050)$. In **Figure 5.8** we draw the transverse phonon modes along the $X(\xi 00)$ direction, between $Q(-140)$ and $Q(140)$. In **Figure 5.9** we draw an hybrid projection (both longitudinal and transverse phonon modes have intensity) of phonon modes along the Y -direction, between $Q(-2-30)$ and $Q(-2-10)$.

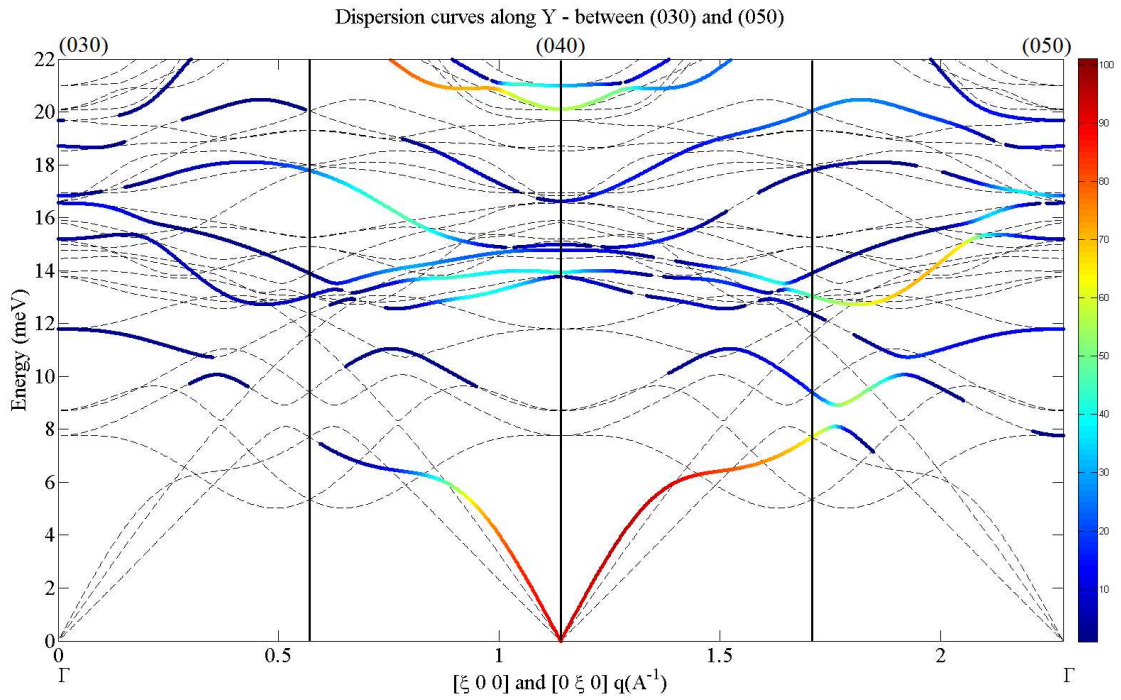


Figure 5.7 – (color) $S(q,\omega)$ of longitudinal phonon modes in the Y -direction between $Q(030)$ and $Q(050)$. The color scale is logarithmic. (dot) Total dispersion curve in the Y -direction. Calculation of $Nd_2NiO_{4.0}$ in the $Pccn$ model. Vertical black lines represent zone boundaries, high symmetry points. The longitudinal acoustic phonon shows an interesting dip close to $Q(0\ 4.4-4.5\ 0)$ for energy transfer of 6-8 meV. Also, instead of cleanly transferring its energy up to $Q(050)$, it somehow shows an hybridization with the 14 meV optical band : instead of an effective acoustic mode, we observe a splitting of the energy, which reach $Q(050)$ in hybrid modes at about $E=12$ meV and a band at $E=16$ meV.

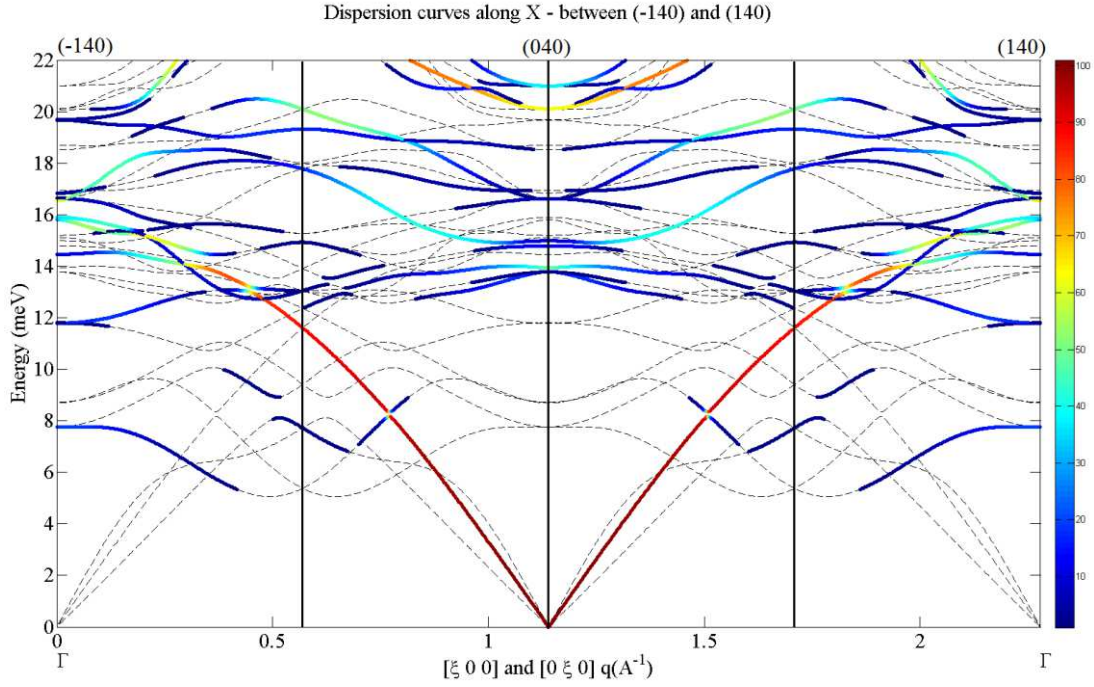


Figure 5.8 – (color) $S(q,\omega)$ of transverse phonon modes in the X-direction between $Q(-140)$ and $Q(140)$. The color scale is logarithmic. (dot) Total dispersion curve in the X-direction. Vertical black lines represent zone boundaries, high symmetry points. Calculation of $Nd_2NiO_{4.0}$ in the Pccn model. Compared to the longitudinal projection, the transverse acoustic mode cleanly propagate as an effective phonon from $Q(040)$ up to $Q(140)$.

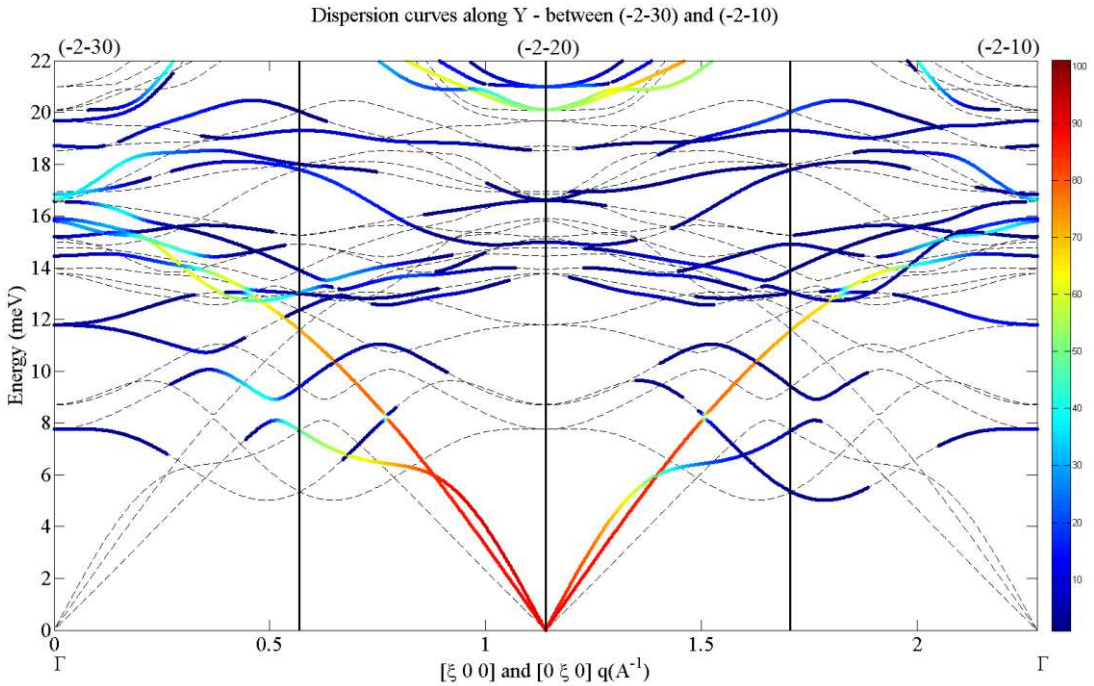


Figure 5.9 – (color) $S(q,\omega)$ of hybrid phonon modes in the Y-direction between $Q(-2-30)$ and $Q(-2-10)$. The color scale is logarithmic. (dot) Total dispersion curve in the Y-direction. Calculation of $Nd_2NiO_{4.0}$ in the Pccn model. Vertical black lines represent zone boundaries, high symmetry points. Considering Y-modes around the $Q(220)$ point, where both longitudinal and transverse projection are observable, we get the same behavior as for pure longitudinal and transverse representations – a clean propagation of the transverse effective acoustic mode, and a somehow broken energy transfer of the longitudinal mode.

In **Figure 5.10** we draw the longitudinal phonon modes along the $\mathbf{M}(\xi\xi 0)$ direction, between $\mathbf{Q}(110)$ and $\mathbf{Q}(330)$. In **Figure 5.11** we draw the hybrid projection of the phonon modes along \mathbf{M} , between $\mathbf{Q}(3-10)$ and $\mathbf{Q}(400)$. In **Figure 5.12** we draw the hybrid projection of the phonon modes along \mathbf{M} , between $\mathbf{Q}(008)$ and $\mathbf{Q}(118)$.

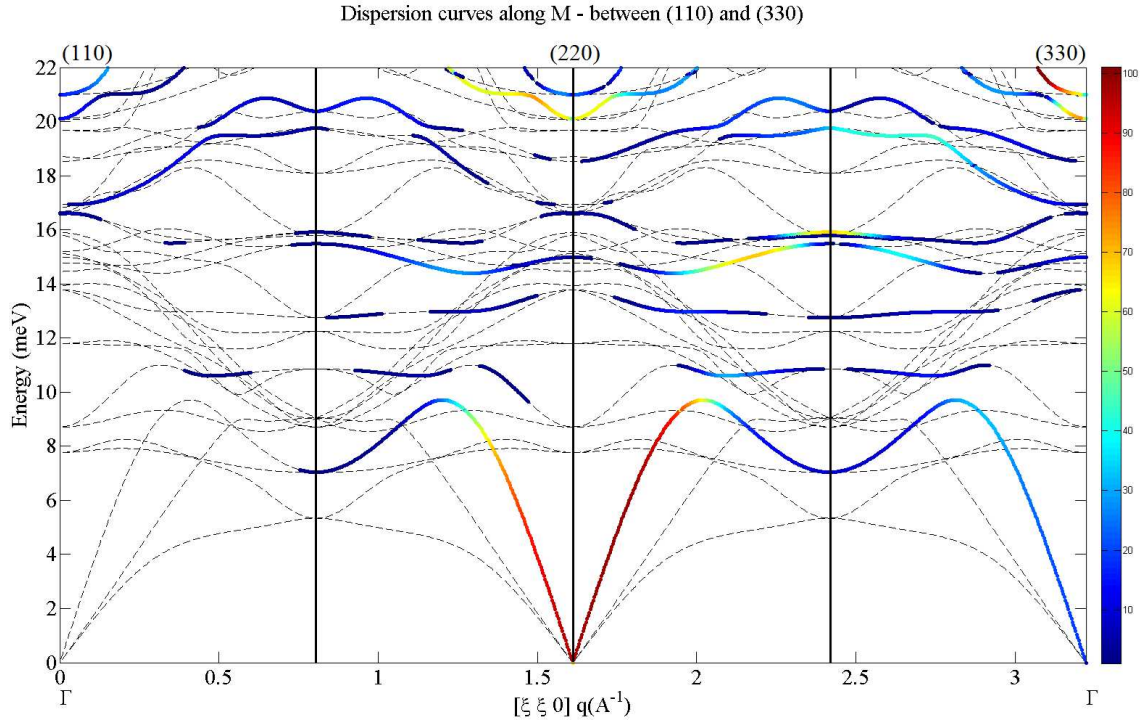


Figure 5.10 – (color) $S(q, \omega)$ of longitudinal phonon modes in the \mathbf{M} -direction between $\mathbf{Q}(110)$ and $\mathbf{Q}(330)$. The color scale is logarithmic. (dot) Total dispersion curve in the \mathbf{M} -direction. Vertical black lines represent zone boundaries, high symmetry points. Calculation of $\text{Nd}_2\text{NiO}_{4.0}$ in the $Pccn$ model. Similarly of the \mathbf{Y} -projected scenario, the acoustic longitudinal phonon along the \mathbf{M} -direction is only cleanly defined up to $E=10$ meV. Above this value, it hybridizes with flat optical modes to transfer its energy.

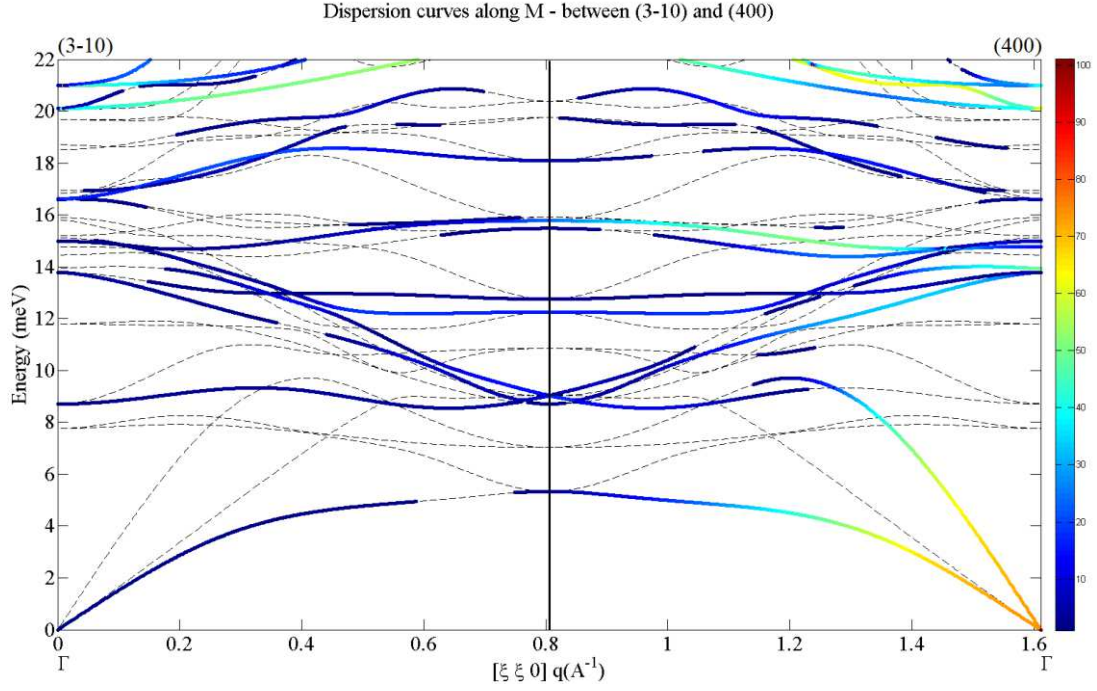


Figure 5.11 – (color) $S(q,w)$ of hybrid phonon modes in the M -direction between $Q(3-10)$ and $Q(400)$. The color scale is logarithmic. (dot) Total dispersion curve in the M -direction. Vertical black line represents zone boundary, high symmetry point. Calculation of $Nd_2NiO_{4.0}$ in the $Pccn$ model. In the (400) Brillouin zone, the phonon energy transfer from the longitudinal acoustic mode to flat optical modes is clearer. We also note that the transverse acoustic mode lays at very low energy at the zone boundary, about $E=4-5$ meV.

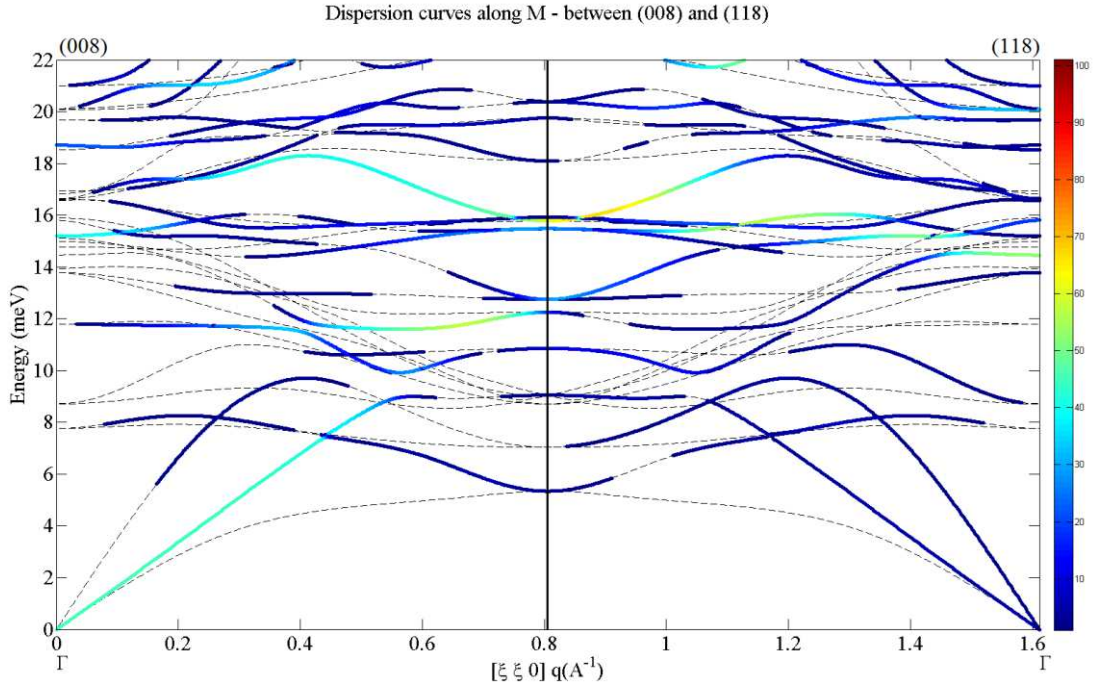


Figure 5.12 – (color) $S(q,w)$ of hybrid phonon modes in the M -direction between $Q(008)$ and $Q(118)$. The color scale is logarithmic. (dot) Total dispersion curve in the M -direction. Vertical black line represents zone boundary, high symmetry point. Calculation of $Nd_2NiO_{4.0}$ in the $Pccn$ model. In the (008) Brillouin zone, the other acoustic transverse mode is activated, though weak, and propagate, through transferring its energy to optical modes, to $E=14-15$ meV at $Q(118)$.

In **Figure 5.13** we draw the longitudinal phonon modes along the $\mathbf{Z}(00\xi)$ direction, between $\mathbf{Q}(00-7)$ and $\mathbf{Q}(00-6)$. In **Figure 5.14** we draw the transverse phonon modes along \mathbf{Z} , between $\mathbf{Q}(220)$ and $\mathbf{Q}(221)$. In **Figure 5.15** we draw the hybrid projection of phonon modes along the \mathbf{Z} -direction, between $\mathbf{Q}(22-7)$ and $\mathbf{Q}(22-6)$.

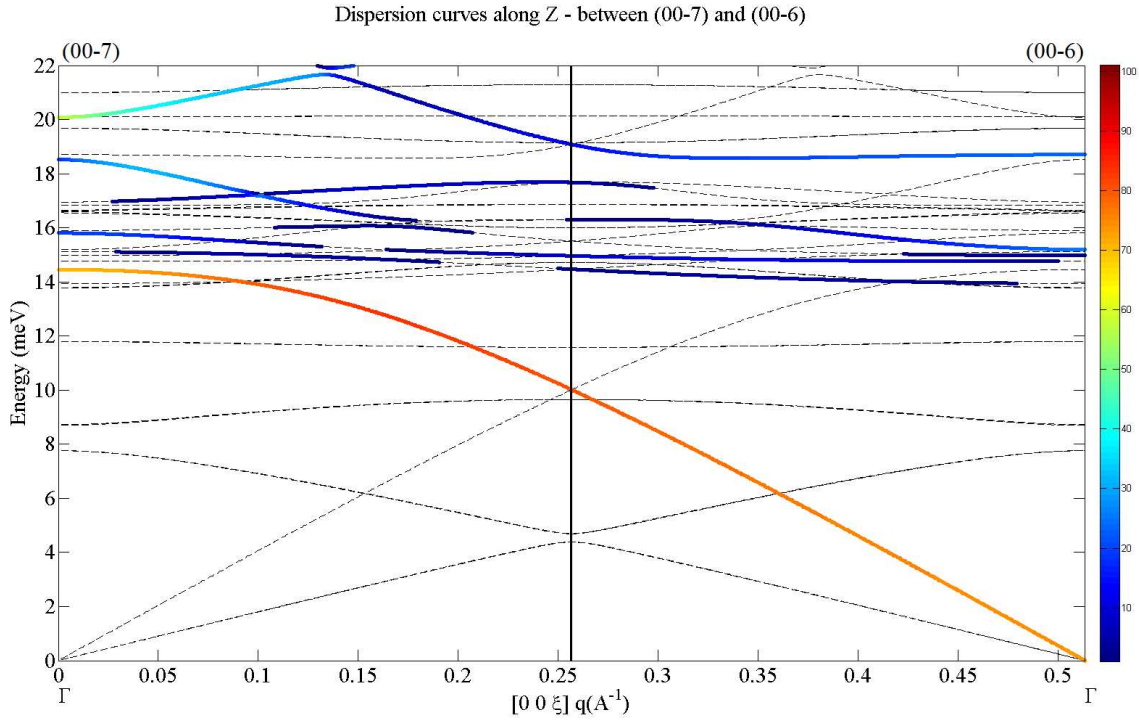


Figure 5.13 – (color) $S(q,w)$ of longitudinal phonon modes in the \mathbf{Z} -direction between $\mathbf{Q}(00-7)$ and $\mathbf{Q}(00-6)$. The color scale is logarithmic. (dot) Total dispersion curve in the \mathbf{Z} -direction. Vertical black line represents zone boundary, high symmetry point. Calculation of $\text{Nd}_2\text{NiO}_{4.0}$ in the $Pccn$ model. Contrary to \mathbf{Y} - and \mathbf{M} -directions, the longitudinal acoustic phonon propagates smoothly along \mathbf{Z} without showing any coupling with optical modes. We note some intensities in the flat optical modes at $E=18$ and 20 meV.

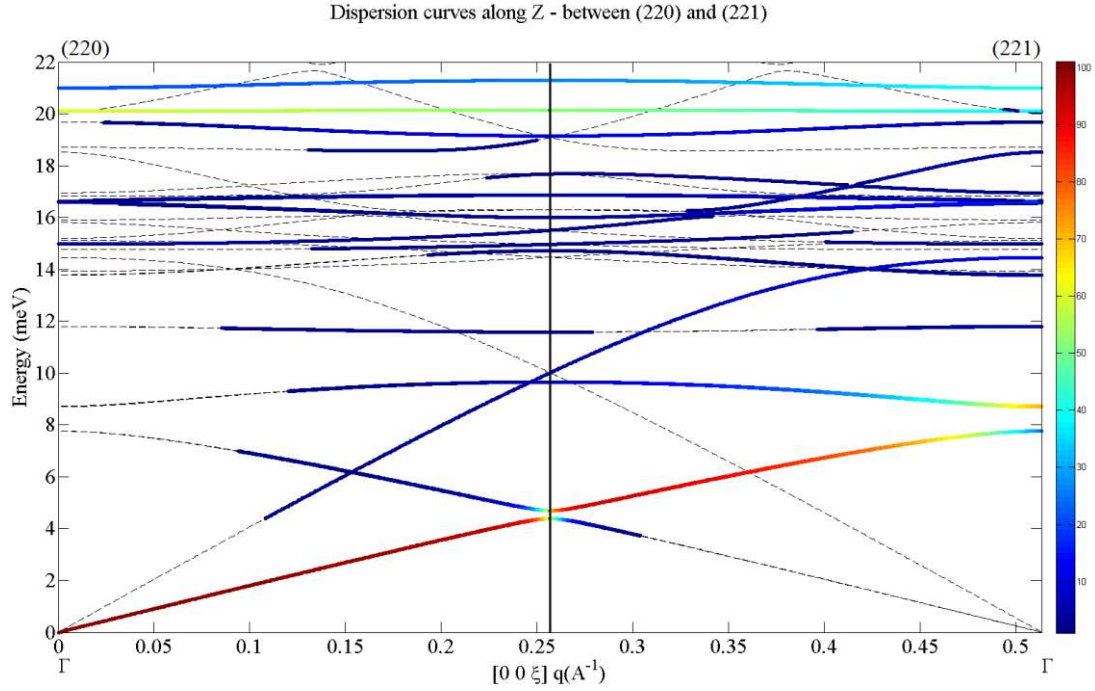


Figure 5.14 – (color) $S(q,w)$ of transverse phonon modes in the Z -direction between $Q(220)$ and $Q(221)$. The color scale is logarithmic. (dot) Total dispersion curve in the Z -direction. Vertical black line represents zone boundary, high symmetry point. Calculation of $Nd_2NiO_{4.0}$ in the $Pccn$ model. Here again, the transverse acoustic phonon propagates smoothly along Z , yet anticrosses with itself at the zone boundary, letting some energy in the folding. Flat optical modes at $E=20$ and $E=21$ meV are showing some intensities.

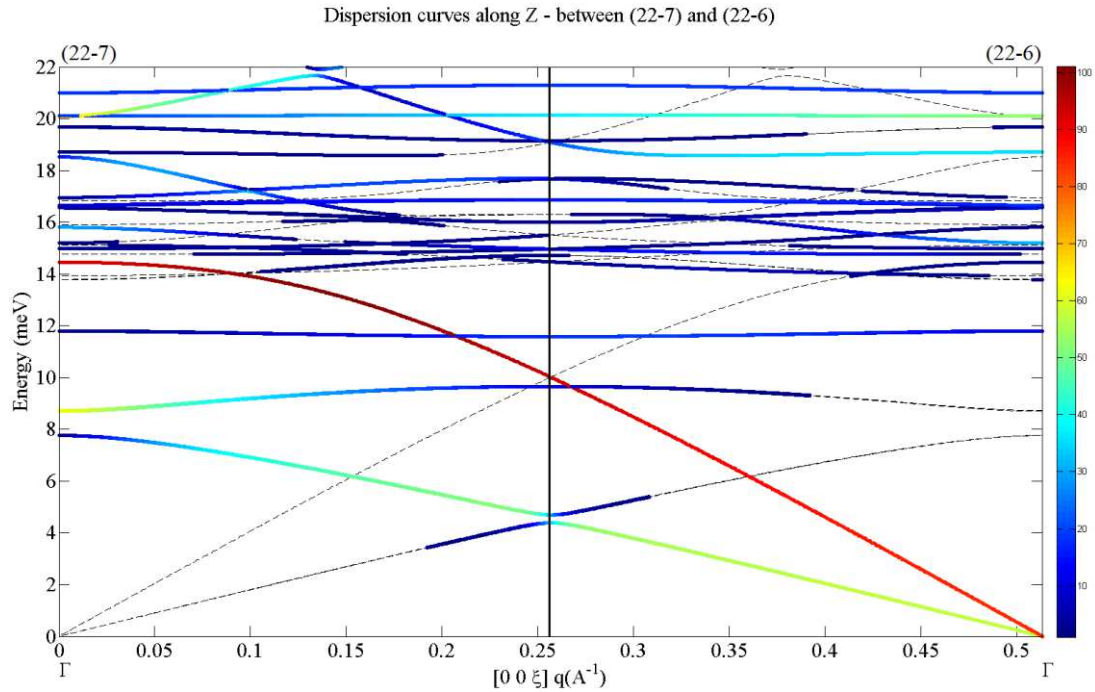


Figure 5.15 – (color) $S(q,w)$ of hybrid phonon modes in the Z -direction between $Q(22-7)$ and $Q(22-6)$. The color scale is logarithmic. (dot) Total dispersion curve in the Z -direction. Vertical black line represents zone boundary, high symmetry point. Calculation of $Nd_2NiO_{4.0}$ in the $Pccn$ model. Similarly as for the pure longitudinal and transverse projections, both acoustic phonon modes propagate cleanly to $Q(22-7)$, and the flat optical bands are showing some intensities.

In summary of this first representation of phonon modes in the low-energy region from $E=0$ to 22 meV, several dynamical behavior are of interest : beside the weak intensity of some optical modes in the flat optical band, we noticed dips in longitudinal acoustic phonons of the X/Y- and M-directions, the low-lying transverse acoustic phonon in the M-direction, and the mode folding of the transverse acoustic phonon in the Z-direction. Most of the times such broad dips in \mathbf{q} are induced by a mismatch of bond lengths – or structural instabilities, and favor small dynamical distortions away from the high-symmetry structure^[20]. These features will be investigated with inelastic scattering on three-axis spectrometers, as described in **chapter 7**.

5.2.3. Eigenvectors for $Nd_2NiO_{4.0}$

In order to get a better understanding of the dispersion curves described previously, and to link atomic displacements to phonon modes, one has to look at the mode eigenvectors. In the following tables are reported, for the high-symmetry points Γ (0 0 0), Y (0 $\frac{1}{2}$ 0), X ($\frac{1}{2}$ 0 0), M ($\frac{1}{2}$ $\frac{1}{2}$ 0) and Z (0 0 $\frac{1}{2}$), a short description of the main atomic displacements associated to modes up to $E=16$ meV. Respectively, **Table 5.10** refers to modes at Γ , **Table 5.11** modes at Y , **Table 5.12** modes at X , **Table 5.13** modes at M , and finally **Table 5.14** modes at Z .

As a reminder, since the symmetry has been reduced from the tetragonal $P4_2/nm$ to the orthorhombic $Pccn$ space-group due to magnetism, most of the modes are split. While their associated atomic displacements can vary slightly, their frequency stays about the same, and they are reported as degenerate in the tables. Another issue from this splitting is the minor variation in energy transfer and atomic displacements between the high-symmetry points X and Y .

We are particularly interested in phonon modes where atomic displacements are relevant to oxygen mobility, *i.e.* atomic displacements which concern out-of-phase motions in the rock-salt layer, and tilting/sliding motions that bring apical oxygen atoms closer to the interstitial sites. As shown in **Table 5.10**, the modes at Γ at $E=14.46$; 15.19 ; 15.80 meV (in bold), belonging to the flat optical band, have displacements involving a strong fluctuation of the Ni- O_{ap} distance, which may be favorable to a diffusion event through weakening of the Ni- O_{ap} bond. The low-energy modes at M , shown in **Table 5.13**, at $E=5.34$ and 7.04 meV, have displacements involving the tilt of NiO_6 octahedron – and the sliding of the apical oxygen – towards the interstitial site in [110]. Furthermore, the optical modes at higher energy, at $E=12.26$ and 12.75 meV, reveal an in-phase breathing of the interstitial site, increasing its volume and opening the pathway, which is favorable to a diffusion event. While the modes in Z , as shown in **Table 5.14**, have displacements which do not directly favor diffusion events (no direct movement of apical oxygen atoms toward [110]), the out-of-phase sliding of whole layers along z implies fluctuations of Ni- O_{ap} distances – or at least variations of the distance between the perovskite and the rock-salt layers, which compress or elongate the oxygen apical sites. Such compression and elongation are a key factor of the apical oxygen instability, and will be described in detail in **section 5.4.1**.

Table 5.10 – Short description of atomic displacements (eigenmodes) associated to phonon modes up to $E=16$ meV at Γ (0 0 0). Artificially splitted modes with similar frequencies and atomic displacements are merged and labelled “degenerate”. Apical oxygen atoms are referred as “ O_{ap} ”, equatorial oxygen atom as “ O_{eq} ”, and distinct motions on different atomic group are separated with a “+”.

Momentum transfer Q (rlu)	Frequency E (meV)	Atomic displacements
Γ (0 0 0)	Degenerate (7.76 ; 7.76)	In-phase [100] tilt + [001] rotation of NiO_6 (clock mechanism)
	Degenerate (8.69 ; 8.72)	Out-of-phase [100]/[010] sliding of the whole perovskite layer
	Degenerate (11.79 ; 11.80)	Half of the O_{ap} : In-phase [100]/[010] tilt + [001] rotation of NiO_6 (clock mechanism)
	Degenerate (13.77 ; 13.79)	Out-of-phase bending of $Ni-O_{eq}$ layers + constant $Ni-O_{ap}$ distance + $Ni-Nd$ distance is fluctuating strongly in z
	13.94	O_{ap} and half of O_{eq} : pure [110]/[-110] tilt
	14.46	Out-of-phase breathing of $Ni-O_{eq}$ layers + rock-salt layer static + $Ni-O_{ap}$ fluctuating strongly in z
	14.78	O_{ap} and half of O_{eq} : pure [110]/[-110] tilt
	14.99	Nd: pure [110]/[-110] sliding
	15.12	O_{ap} and half of O_{eq} : [110]/[-110] tilt + [110]/[-110] sliding of Nd
	15.19	In-phase breathing of $Ni-O_{eq}$ layers + rock-salt layer static + $Ni-O_{ap}$ fluctuating strongly in z
15.80	Out-of-phase breathing of $Ni-O_{eq}$ layers while O_{ap} is static: $Ni-O_{ap}$ strongly fluctuating in z + [110]/[-110] sliding of Nd	

Table 5.11 – Short description of atomic displacements (eigenmodes) associated to phonon modes up to $E=16$ meV at Y (0 $\frac{1}{2}$ 0). Artificially splitted modes with similar frequencies and atomic displacements are merged and labelled “degenerate”. Apical oxygen atoms are referred as “ O_{ap} ”, equatorial oxygen atom as “ O_{eq} ”, and distinct motions on different atomic group are separated with a “+”.

Momentum transfer Q (rlu)	Frequency E (meV)	Atomic displacements
Y (0 $\frac{1}{2}$ 0)	Degenerate (5.34 ; 5.34)	Out-of-phase breathing and ondulation in [010] of $Ni-O_{eq}$ + Nd and half of O_{ap} : [100] tilt
	Degenerate (7.71 ; 7.71)	In-phase bending of $Ni-O_{eq}$ layers + in-phase [100] sliding of rock-salt layers
	Degenerate (9.41 ; 9.41)	In-phase breathing and ondulation in [010] of all atoms
	Degenerate (11.60 ; 11.60)	In-phase [100] sliding, O_{ap} less affected
	Degenerate (12.37 ; 12.37)	[100] sliding of half of Nd
	Degenerate (13.00 ; 13.00)	Out-of-phase [111] elliptic motion of Nd inside the rock-salt layers
	Degenerate (13.04 ; 13.04)	Out-of-phase bending of half of Ni + in-phase [010] sliding of rock-salt layers
	Degenerate (13.90 ; 13.90)	In-phase [100] sliding of all but O_{ap} and half of O_{eq}
	Degenerate (14.91 ; 14.91)	Out-of-phase elliptic motion, mainly in [100], slightly in [010], of Nd and O_{ap}

Table 5.12 – Short description of atomic displacements (eigenmodes) associated to phonon modes up to $E=16$ meV at X ($\frac{1}{2}$ 0 0). Artificially splitted modes with similar frequencies and atomic displacements are merged and labelled “degenerate”. Apical oxygen atoms are referred as “ O_{ap} ”, equatorial oxygen atom as “ O_{eq} ”, and distinct motions on different atomic group are separated with a “+”.

Momentum transfer Q (rlu)	Frequency E (meV)	Atomic displacements
X ($\frac{1}{2}$ 0 0)	Degenerate (5.38 ; 5.38)	Out-of-phase breathing of Ni- O_{eq} layer + ondulation in [100] + [100] sliding of Nd_2O_{ap2}
	Degenerate (7.72 ; 7.72)	Ondulation of Ni- O_{eq} layer in [100] + sliding of half Nd_2O_{ap2} along [100]
	Degenerate (9.42 ; 9.42)	Ondulation of all atoms in [100]
	Degenerate (11.61 ; 11.61)	In-phase [010] sliding of all but half of Nd and O_{ap}
	Degenerate (12.38 ; 12.38)	Out-of-phase [010] sliding of Nd_2O_{ap2} tetrahedron
	Degenerate (13.02 ; 13.02)	Out-of-phase [010] sliding of half of O_{ap} + out-of-phase [110] sliding of half of Nd
	Degenerate (13.05 ; 13.05)	In-phase bending of Ni- O_{eq} + coupled sliding of rock-salt layer along [100], and of Nd_2O_{ap2} along [110]/[-110]
	Degenerate (13.90 ; 13.90)	Slight in-phase [100] ondulation of Ni- O_{eq} + out-of-phase [110] sliding of Nd
	Degenerate (14.93 ; 14.93)	Slight in-phase [100] ondulation of Ni- O_{eq} + half breathing (Nd) of Nd_2O_{ap2} tetrahedron

Table 5.13 – Short description of atomic displacements (eigenmodes) associated to phonon modes up to $E=16$ meV at M ($\frac{1}{2}$ $\frac{1}{2}$ 0). Artificially splitted modes with similar frequencies and atomic displacements are merged and labelled “degenerate”. Apical oxygen atoms are referred as “ O_{ap} ”, equatorial oxygen atom as “ O_{eq} ”, and distinct motions on different atomic group are separated with a “+”.

Momentum transfer Q (rlu)	Frequency E (meV)	Atomic displacements
M ($\frac{1}{2}$ $\frac{1}{2}$ 0)	Degenerate (5.34 ; 5.34)	[110] tilt of half of O_{ap}, O_{eq}, and Nd
	Degenerate (7.04 ; 7.04)	In-phase [110] sliding of Nd and O_{ap}
	Degenerate (8.71 ; 8.71)	z-rotation of Nd- O_{ap}
	Degenerate (9.02 ; 9.02)	z-rotation of Nd- O_{ap}
	Degenerate (9.05 ; 9.05)	In-phase [-110] bending of Ni- O_{eq} layers + Out-of-phase [110] sliding of Nd_2O_{ap2}
	Degenerate (10.86 ; 10.86)	Out-of-phase [-110] bending of Ni- O_{eq} + Out-of-phase [110] sliding of O_{ap}
	Degenerate (12.26 ; 12.26)	Out-of-phase [-110] bending of Ni-O_{eq} layers + tetrahedron mode of Nd_2O_{ap2} (half breathing half sliding: breathing of the diffusion pathway)
	Degenerate (12.75 ; 12.75)	Out-of-phase [-110] bending of Ni-O_{eq} layers + in-phase breathing (volume change) tetrahedron mode of Nd_2O_{ap2}
	Degenerate (15.48 ; 15.48)	Out-of-phase [-110] bending of Ni- O_{eq} layers + tetrahedron mode of Nd_2O_{ap2} : out-of-phase breathing (constant volume)

Table 5.14 – Short description of atomic displacements (eigenmodes) associated to phonon modes up to $E=16$ meV at \mathbf{Z} (0 0 $\frac{1}{2}$). Artificially splitted modes with similar frequencies and atomic displacements are merged and labelled “degenerate”. Apical oxygen atoms are referred as “ O_{ap} ”, equatorial oxygen atom as “ O_{eq} ”, and distinct motions on different atomic group are separated with a “+”.

Momentum transfer \mathbf{Q} (rlu)	Frequency E (meV)	Atomic displacements
\mathbf{Z} (0 0 $\frac{1}{2}$)	Degenerate (4.38 ; 4.38)	[110] sliding of all atoms with a phase [001]
	Degenerate (4.69 ; 4.69)	[110] sliding of all atoms with a phase [002]
	Degenerate (9.65 ; 9.65)	z-rotation of NiO_6 + in-phase [110] sliding of Nd
	Degenerate (10.01 ; 10.01)	Out-of-phase breathing of Ni- O_{eq} layers
	Degenerate (11.58 ; 11.58)	Half of Nd: [110] sliding + half of Nd [001] sliding + [110] sliding of Ni- O_{eq}
	Degenerate (14.47 ; 14.47)	Out-of-phase breathing of Ni- O_{eq} layers + tetrahedron mode of half Nd_2O_{ap2} (dimerization)
	Degenerate (14.72 ; 14.72)	Half of Nd_2O_{ap2} tetrahedron: flattening + half of Nd_2O_{ap2} tetrahedron: [-110] swinging + [110] sliding of Ni- O_{eq}
	Degenerate (14.96 ; 14.96)	Out-of-phase breathing of Ni- O_{eq} layers + Half of Nd_2O_{ap2} tetrahedron: twisting + half of Nd_2O_{ap2} tetrahedron: breathing
	Degenerate (15.50 ; 15.50)	Out-of-phase breathing of Ni- O_{eq} layers with phase [0 0 0.5] + Nd_2O_{ap2} tetrahedron breathing

5.2.4. Overstoichiometric $Nd_2NiO_{4.125}$ & $Nd_2NiO_{4.25}$

As described in **section 5.1.2** and **5.1.3**, a complex issue rises from the conversion of disordered structures, conventionnaly described in average set-up in crystallography, to ‘real’ atomic structures with full occupancy of sites, needed to perform our DFT calculations. While the models described in the previous sections are relevant for molecular dynamic calculations – and are indirectly confirmed with neutron time-of-flight experiments, described in **chapter 6** – or for any kind of simulations where symmetry does not matter, they are not adapted for phonon calculations. Indeed, non-stoichiometric Nd_2NiO_{4+d} can only be modeled in supercell, involving low-symmetry and numerous inequivalent atoms; as the total number of phonon branches is equivalent to $3N$, where N is the number of inequivalent atoms, such supercells lead to an excessive number of phonon branches, usually flat and irrelevant to the dynamics. In order to find a compromise between a reasonable number of phonon branches and a reasonable structural model, models of $Nd_2NiO_{4.125}$ and $Nd_2NiO_{4.25}$ were built from the high-symmetry $P4_2/nm-Nd_2NiO_{4.0}$ model, with occupied interstitial sites chosen to preserve the highest symmetry possible.

As an example, the $Nd_2NiO_{4.125}$ phase is described in a $2 \times 2 \times 1$ supercell with $P4_2cm$ space-group ($n^\circ 101$). This model contains 114 atoms with 23 inequivalent sites, as shown in **Figure 5.16**.

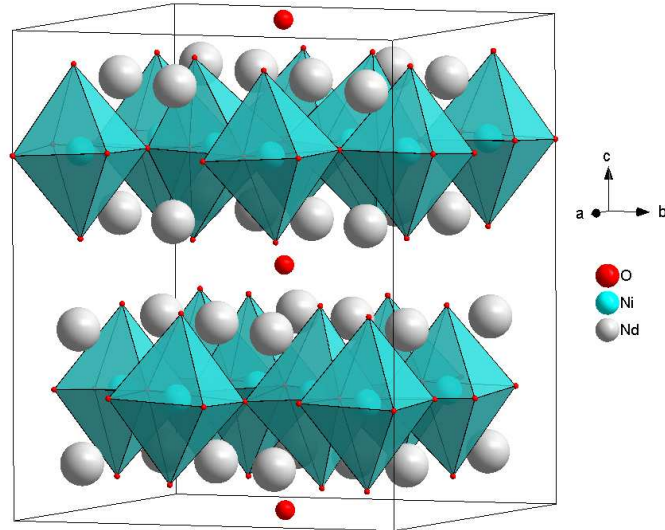


Figure 5.16 – Model of $\text{Nd}_2\text{NiO}_{4.125}$ in the $P4_2\text{cm}$ space-group, with 114 atoms and 23 inequivalent sites. Cell parameters are $a=b=10.747\text{\AA}$ and $c=12.712\text{\AA}$.

However, even though the residual forces on atoms are minor during the geometry optimization, when calculating phonon modes on such a model, negative phonon modes appear, *i.e.* structural instabilities, as drawn in **Figure 5.17**. This means that the restoring forces are calculated incorrectly, and that the diagonalisation of the dynamical matrix, and thus the eigenmodes, is meaningless. Furthermore, calculating the $S(\mathbf{q},\omega)$ is not possible, if even one mode is negative, and the analysis of **section 5.2.2** and **5.2.3** cannot be performed.

In order to stabilize these three negative phonon modes, we reduced the symmetry of the model to the $Pcc2$ space-group ($n^\circ 27$), with 114 atoms and 31 inequivalent sites. The structure looks almost the same as in **Figure 5.16**. After geometry optimization the cell parameters are $a=10.666\text{\AA}$, $b=10.669\text{\AA}$ and $c=12.649\text{\AA}$. The calculated dispersion curve is shown in **Figure 5.18**. While the phonon modes are slightly stabilized, they remain negative, and thus no further analysis can be performed on these simulations.

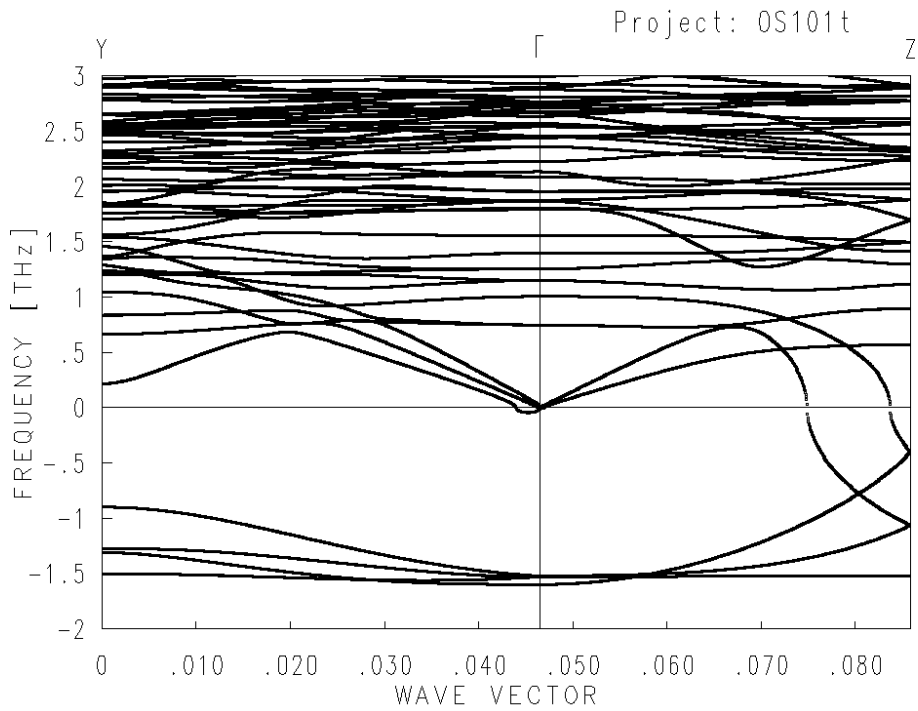


Figure 5.17 – Phonon dispersion in the directions Y and Z for the $P4_2cm\text{-Nd}_2\text{NiO}_{4.125}$ model. The figure is made with the PHONON software. We note that three phonon modes are instable in the z-direction, and flat at about $E=-1.5$ THz \sim -7 meV. We also note some issues with the invariance of the transverse acoustic phonon mode at Γ .

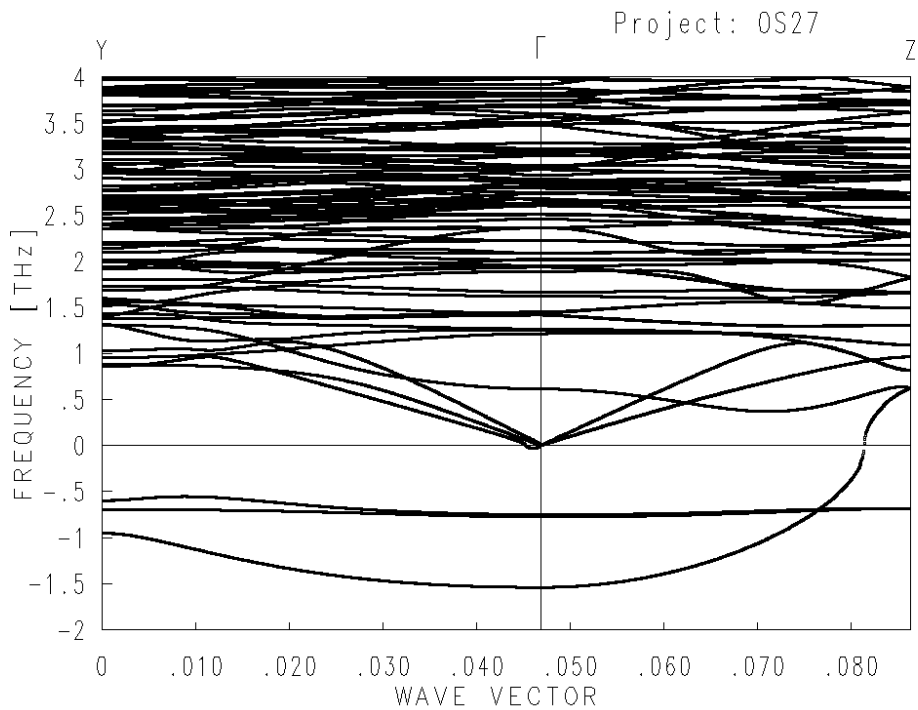


Figure 5.18 – Phonon dispersion in the directions Y and Z for the $Pcc2\text{-Nd}_2\text{NiO}_{4.125}$ model. The figure is made with the PHONON software. We note that the three phonon modes are still instable in the z-direction, and flat at about $E=-1$ THz \sim -4 meV.

Several other space-groups were investigated, and a similar process was followed for the $\text{Nd}_2\text{NiO}_{4.25}$ system, but none of them is free of negative phonon modes. These wrongly calculated eigenvectors are associated with displacements on the first-neighbor shell around the excess oxygen atom in interstitial sites. While no proper solutions were found to calculate phonon dispersion curves in non-stoichiometric $\text{Nd}_2\text{NiO}_{4+d}$, the issue obviously comes from the defective clusters surrounding the excess oxygens: the restoring force cannot be symmetrical nor harmonic on atoms too close to the defect, and thus phonon modes cannot be calculated by the direct method in this specific case.

5.3. Molecular dynamics of the $\text{Nd}_2\text{NiO}_{4+d}$ phases

Molecular dynamic calculations, which are not limited by symmetry, are the perfect complementary tool to probe systems as complex as the non-stoichiometric $\text{Nd}_2\text{NiO}_{4.10}$ and $\text{Nd}_2\text{NiO}_{4.25}$. Furthermore, post-processing of molecular dynamic trajectories allow to calculate the vibrational density of states (vDOS), which will be compared to the experimental DOS from inelastic neutron time-of-flight spectroscopy experiments in **chapter 6**.

5.3.1. Parameters

As stated in **section 5.1**, structural models to describe stoichiometric and over-stoichiometric $\text{Nd}_2\text{NiO}_{4+d}$ involve supercells of about 10\AA sides, and were geometrically optimized prior to the molecular dynamic calculations. As previously mentioned, models are build from the F-cell in supercells $2\times 2\times 1$ for $\text{Nd}_2\text{NiO}_{4.0}$ ($a=b=11.0314\text{\AA}$, $c=12.2330\text{\AA}$), of $2\times 2\times 1$ for $\text{Nd}_2\text{NiO}_{4.10}$ ($a=b=10.6673\text{\AA}$, $c=12.6493\text{\AA}$) and $2\sqrt{2}\times 2\sqrt{2}\times 1$ for $\text{Nd}_2\text{NiO}_{4.25}$ ($a=b=15.4272\text{\AA}$, $c=12.2629\text{\AA}$).

Ab initio molecular dynamics were performed through the VASP code using the Verlet algorithm to integrate Newton's equations of motion. Initial forces on atoms were randomly distributed in direction, while their amplitude is set by the simulation temperature. A canonical ensemble NVT was chosen for the calculations, and the simulation time between each step was set to 2fs. Typically the total simulation length was set to 42ps, considering 2ps for stabilization and 40ps for trajectory generation. The exact input for most of the molecular dynamics performed is reported in **Table 5.15**.

Table 5.15 – Inputs of the INCAR file used for most of the molecular dynamic simulations performed on the $\text{Nd}_2\text{NiO}_{4+d}$ system. The only variable is *TEBEG*, the simulation temperature.

ALGO = V	POTIM = 2	LCHARG = .FALSE.
MAXMIX = 40	TEBEG = 310	PREC = LOW
IBRION = 0	ISYM = 0	ISTART = 0
NSW = 21000	ISIF = 2	ISMEAR = 0
NELMIN = 4	SMASS = 2	SIGMA = 0.05
NBLOCK = 1	LREAL = .TRUE.	

As it will be shown in **chapter 6**, where the experimental and calculated density of states are compared, simulation results obtained with the preceding parameters gave a calculated vibrational density of states close to experiments, validating the structural model and the simulation parameters. The only exception is the low-temperature stoichiometric $\text{Nd}_2\text{NiO}_{4.0}$. Indeed, as shown in **section 5.1.1**, magnetism cannot be disregarded to describe $\text{Nd}_2\text{NiO}_{4.0}$. Using the same set of parameters and adding the control tags relevant to magnetism led to non-convergent results. To stabilize the simulation, the time step and the frequency of coupling with the thermostat were reduced and, more importantly – since no diffusion events are detected at low-temperature in the stoichiometric case – the previously calculated set of plan waves was kept as a starting point from step to step and the precision was increased. Parameters for the magnetic calculation are reported in **Table 5.16**.

Table 5.16 – Inputs of the INCAR file used for the magnetic molecular dynamic simulations performed on the $\text{Nd}_2\text{NiO}_{4.0}$ system.

ALGO = V	ISYM = 0	ISTART = 0
MAXMIX = 40	ISIF = 2	ISMEAR = 0
IBRION = 0	SMASS = 1	SIGMA = 0.05
NSW = 21000	LREAL = .TRUE.	ISPIN = 2
NBLOCK = 1	LCHARG = .TRUE.	ICHARG = 2
POTIM = 1	NELMIN = 4	MAGMOM = 64*0.0 2.0 2.0 2.0
TEBEG = 150	PREC = ACCURATE	2.0 -2.0 -2.0 -2.0 -2.0 -2.0 -2.0 -2.0 -2.0 2.0 2.0 2.0 2.0 32*0.0

While the magnetism is necessary to get density of states close to the experimental ones, in the specific case of the low-temperature $\text{Nd}_2\text{NiO}_{4.0}$ we see no impact of the magnetism when we look at the dynamics of the apical oxygen atoms. This is shown in **Figure 5.19**, using the code described in **chapter 3** and **appendix A**, the positional recurrence maps of apical oxygen atoms from the $\text{Nd}_2\text{NiO}_{4.0}$ system at $T=150\text{K}$ in the magnetic and non-magnetic scenario. No major difference in the shape of the two figures is observed, apart from a slightly more pronounced weight in the outer rings for the magnetic case, easily correlated to the compression of the c-axis.

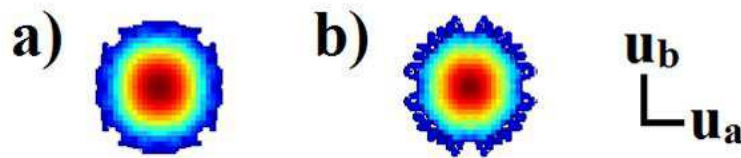


Figure 5.19 – Positional Recurrence Maps of apical oxygen atoms from the $\text{Nd}_2\text{NiO}_{4.0}$ molecular dynamic simulation at $T=150\text{K}$ in a) the non-magnetic case and b) the magnetic case. The projection is (x,y) , perpendicular to the stacking c -axis, and the color scale is logarithmic. A detailed description of these figures is given in **section 5.4**. The shape and the size of the two densities is similar, showing that the magnetism has no effect on the dynamics of apical oxygen atoms.

5.3.2. Diffusion events: pathway & MSD

One of the most obvious observations available from a set of molecular dynamic trajectories is the presence of diffusion events. The **Figure 5.20** and **Figure 5.21**, respectively the full supercell and a zoom of the rock-salt layer, are both obtained from an integration over time of the trajectory using the LAMP software^[21, 22]. One can see that ‘gray clouds’ – representing the 5% occupancy surface of the cumulated trajectory – connect the interstitial sites to the apical sites, on a pathway overlined in yellow (**Figure 5.21**). Such pathway connect apical to interstitial sites along the [110] direction with respect to the F-cell. It is not a straight line between the two-site, more of a tunnel curved in **z**.

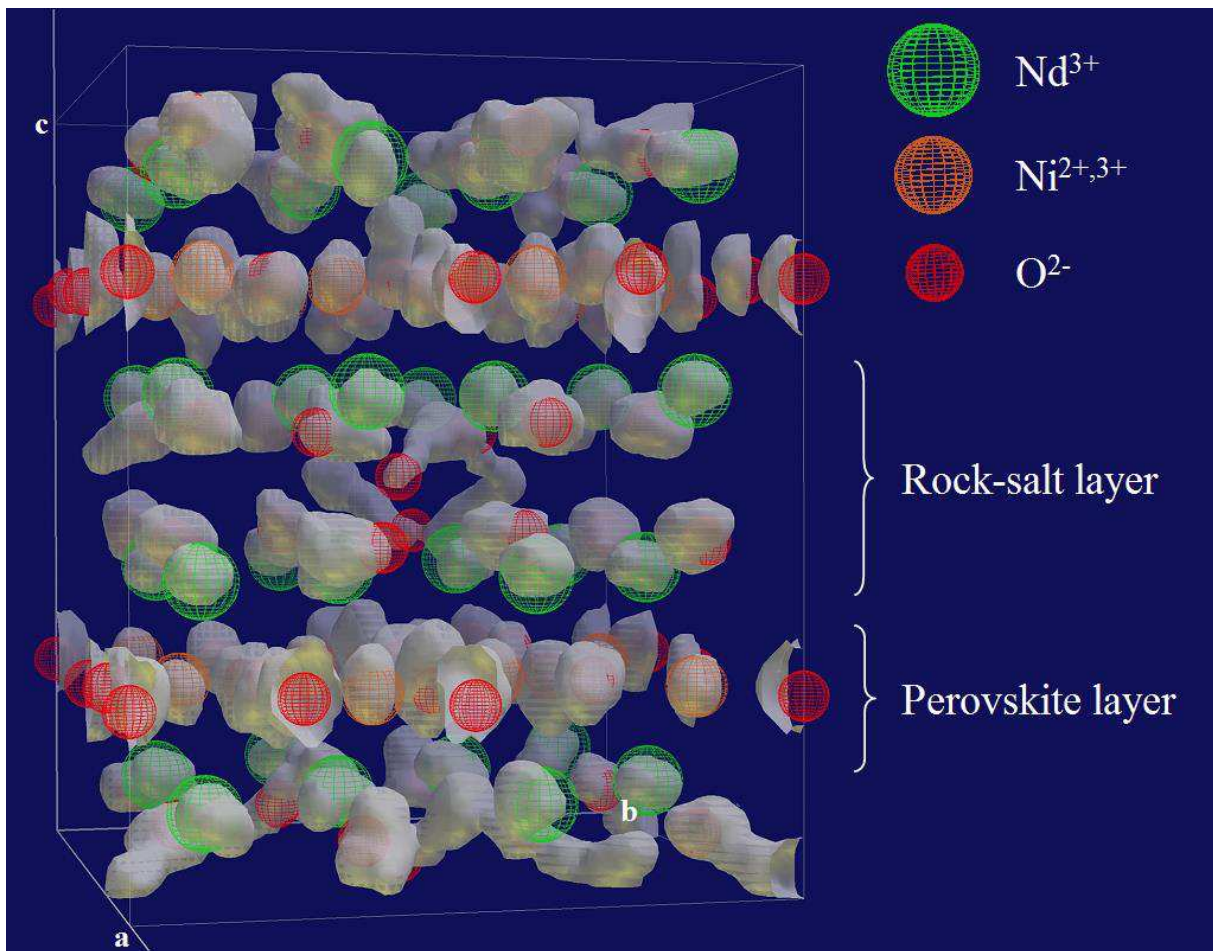


Figure 5.20 – Supercell used to simulate $\text{Nd}_2\text{NiO}_{4.25}$ at moderate temperature. Wired green spheres represent the initial position of Nd atoms ; wired red spheres the initial positions of oxygen atoms. The grey clouds are a 5% occupancy surface, and represent the sum over time of each atom positions along the simulation. Grey clouds connect interstitial sites to apical sites.

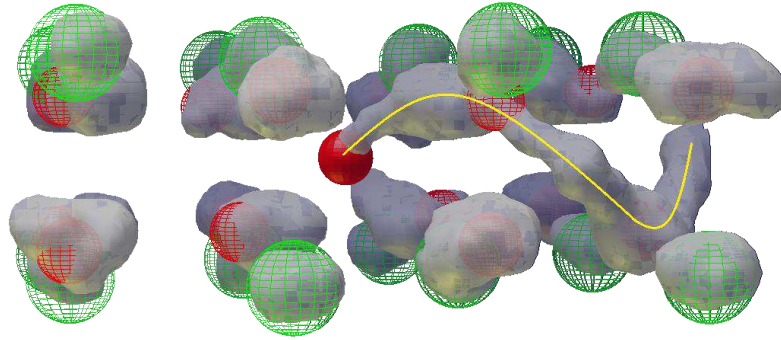


Figure 5.21 – Fragment of the supercell used to simulate $\text{Nd}_2\text{NiO}_{4.25}$ at moderate temperature: zoom on a rock-salt layer containing the interstitial sites. Wired red spheres represent the initial positions of apical oxygen atoms ; and plain red sphere the initial position of an excess oxygen in interstitial site. The grey clouds connecting interstitial sites to apical sites mean the oxygen atoms are mobile on this two-sites pathway, overlined in yellow.

To confirm that this oxygen behavior is a real diffusion and not only a swinging motion of oxygen between apical and interstitial sites, in **Figure 5.22** we plotted only the oxygen atoms initially standing on apical sites. In order to improve statistics and avoid boundary effect, we shifted the initial positions of every apical oxygen atoms to the arbitrary $(\frac{1}{2}, \frac{1}{2}, \frac{1}{2})$ position. Using the same process as in **Figure 5.20**, we draw the 5% occupancy surface, and we see that the oxygen atoms initially standing on apical sites indeed diffuse to the neighboring interstitial sites, and recombine or jump further to other apical oxygen sites.

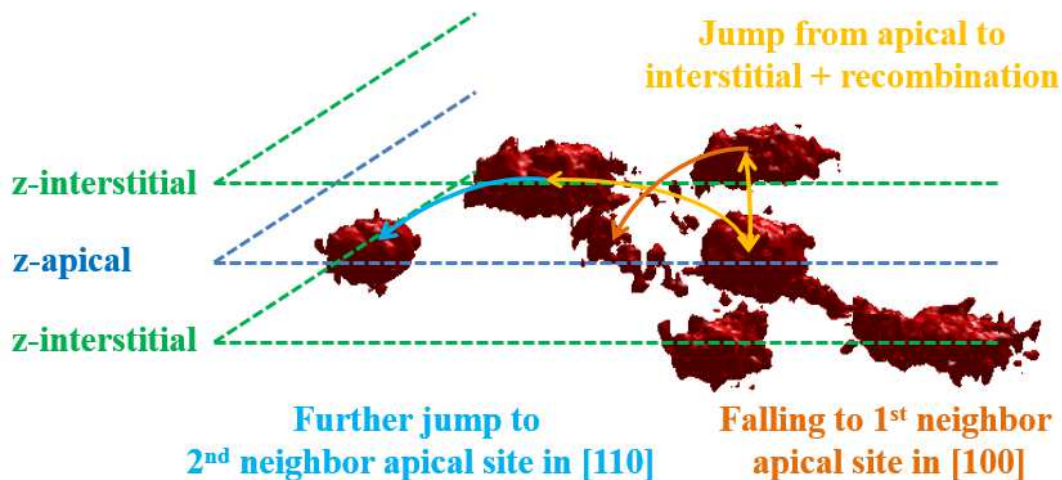


Figure 5.22 – Summation over time of apical oxygen atom trajectories, where the initial apical oxygen atom positions are shifted to an arbitrarily $(\frac{1}{2}, \frac{1}{2}, \frac{1}{2})$ position. Due to this shift, the space is artificially mirrored at z-apical, meaning that in this construction, the apical oxygen atoms lay inbetween two interstitial layers. Since all the apical oxygen atoms are initially stacked, the fact that there are several spots on the figure proves that the motion is, indeed, a diffusion. The yellow arrow represents the first diffusion events, from apical to empty interstitial sites (and the reverse diffusion, from interstitial to empty apical sites) ; the orange arrow represents a second step of diffusion, from the newly occupied interstitial site to a 1st neighbor empty apical site in [100] ; the blue arrow represents a second step of diffusion, from the newly occupied interstitial site to a 2nd neighbor empty apical site in [110].

Both representations, **Figure 5.21** and **Figure 5.22**, evidence the diffusion between apical an interstitial oxygen sites, *i.e.* restrictively in the (ab) plane, as for other related compounds^[1, 8, 23]. We note that, even if at some step the atom initially on apical site diffuses to a neighboring apical site in $[100]$, this diffusion must go through the interstitial site in $[110]$. Such pathway can be described in the Kröger-Vink notation as a two-step process :



This diffusion process has already been observed in other compounds of the $\text{Re}_2\text{MO}_{4+d}$ family and is known as “interstitialcy”^[1, 5, 10, 24]. We remark that it is observed – though in small proportion – down to room-temperature in our simulations, with an increasing amount of diffusion events with increasing temperature and/or excess oxygen stoichiometry. For the stoichiometric $\text{Nd}_2\text{NiO}_{4.0}$, no diffusion events were observed in the temperature range $T=150\text{-}1070\text{K}$, and as such we can assume that at least a small amount of excess oxygen in interstitial site is necessary to promote the diffusion.

A further analysis from molecular dynamic trajectories is a mean square displacement or a root mean square analysis of the atomic motions. However, due to the limited size of the structural models, and the limited computational time available, both linked to the choice of *ab initio* over classical simulations, the number of diffusion events is small even in high-temperature simulations. As such no proper quantitative analysis can be performed and we are restricted to qualitative observations. The **Figure 5.23** shows the mean square displacements (MSD) of oxygen atoms for $\text{Nd}_2\text{NiO}_{4.0}$, $\text{Nd}_2\text{NiO}_{4.10}$ and $\text{Nd}_2\text{NiO}_{4.25}$ calculations at $T=310, 670$ and 1070K . We can only observe that, indeed, the oxygen mobility increases with both temperature and excess oxygen stoichiometry, and that in the absence of oxygen excess there is no oxygen mobility at all. This behavior is similar to the one of the related $\text{Pr}_2\text{NiO}_{4+d}$ ^[5].

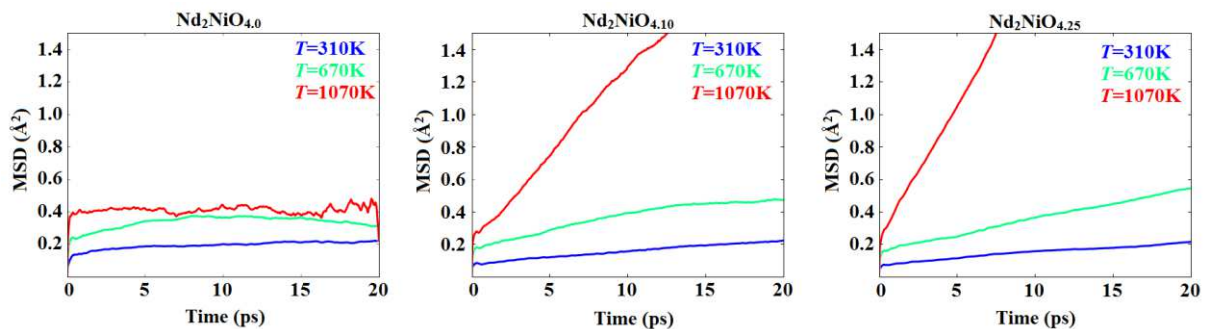


Figure 5.23 – Mean square displacements (MSD) of apical and interstitial oxygen atoms in the $\text{Nd}_2\text{NiO}_{4.0}$, $\text{Nd}_2\text{NiO}_{4.10}$, and $\text{Nd}_2\text{NiO}_{4.25}$ scenario, for temperatures $T=310, 670$ and 1070K . The slopes of the MSD are increasing both with increasing temperature and excess oxygen stoichiometry, and correspond to a better oxygen mobility. In the stoichiometric case, the slope is zero regardless of the temperature, which means at least a few excess oxygen atoms are needed to promote the diffusion.

5.3.3. Phonon density of states

The main argument to validate the molecular dynamic calculations previously described comes from a comparison of the experimental phonon densities of states with the vibrational densities of states calculated from the molecular dynamic trajectories, using the auto-correlation function as described in **chapter 3**. The comparison itself will be discussed in **chapter 6**. Hereafter, only the main qualitative features of the calculated vDOS are described.

In **Figure 5.24** are plotted the total and partial vDOS of $\text{Nd}_2\text{NiO}_{4.0}$, $\text{Nd}_2\text{NiO}_{4.10}$ and $\text{Nd}_2\text{NiO}_{4.25}$ at $T=310$ and 1070K . The vDOS are convoluted with a 1meV wide gaussian function. We observe that, as expected considering the mass of every atom, the main features at low-energy, up to $E=20\text{meV}$, comes from the neodymium and some of the nickel, then from $E=20-50\text{meV}$ from the nickel and some of the oxygen, and finally above $E=50\text{meV}$ mainly from the oxygen atoms. We observe both a broadening and a shift to lower energy of every contribution with increasing temperature and excess oxygen stoichiometry. When looking at the oxygen contribution, we note that the high-energy quadrupolar modes around $E=60\text{meV}$ and $E=80\text{meV}$ are the most affected by the presence of excess oxygen. This is easily understandable since the excess oxygen in interstitial sites, by its sterical effect, will strain its close neighbors, the top and corners of the NiO_6 octahedra, thus strongly disturbing the modes involving displacements of these atoms.

To get a closer look at the low-energy part of the vDOS, we plotted in **Figure 5.25** the total and partial vDOS of $\text{Nd}_2\text{NiO}_{4.10}$ at $T=310\text{K}$, projected on the $[100]$, $[001]$ and $[110]$ directions. Considering the oxygen contribution, we observe that the signal is mostly isotropic, with a small polarization of the peak at $E=18\text{meV}$ in the (ab) plan, and the signal over $E=24\text{meV}$ along **c**. We also note that the lowest contribution of the neodymium is polarized in the (ab) plan, except its $E=10\text{meV}$ peak ; and the lowest contribution of the nickel is mainly polarized along **c**. While much less relevant than the phonon analysis in **section 5.2.3**, these calculations are coherent : the lowest energy modes indeed affect mostly the oxygen and the neodymium atoms, *i.e.* the rock-salt layer, as suggested from the eigenmodes.

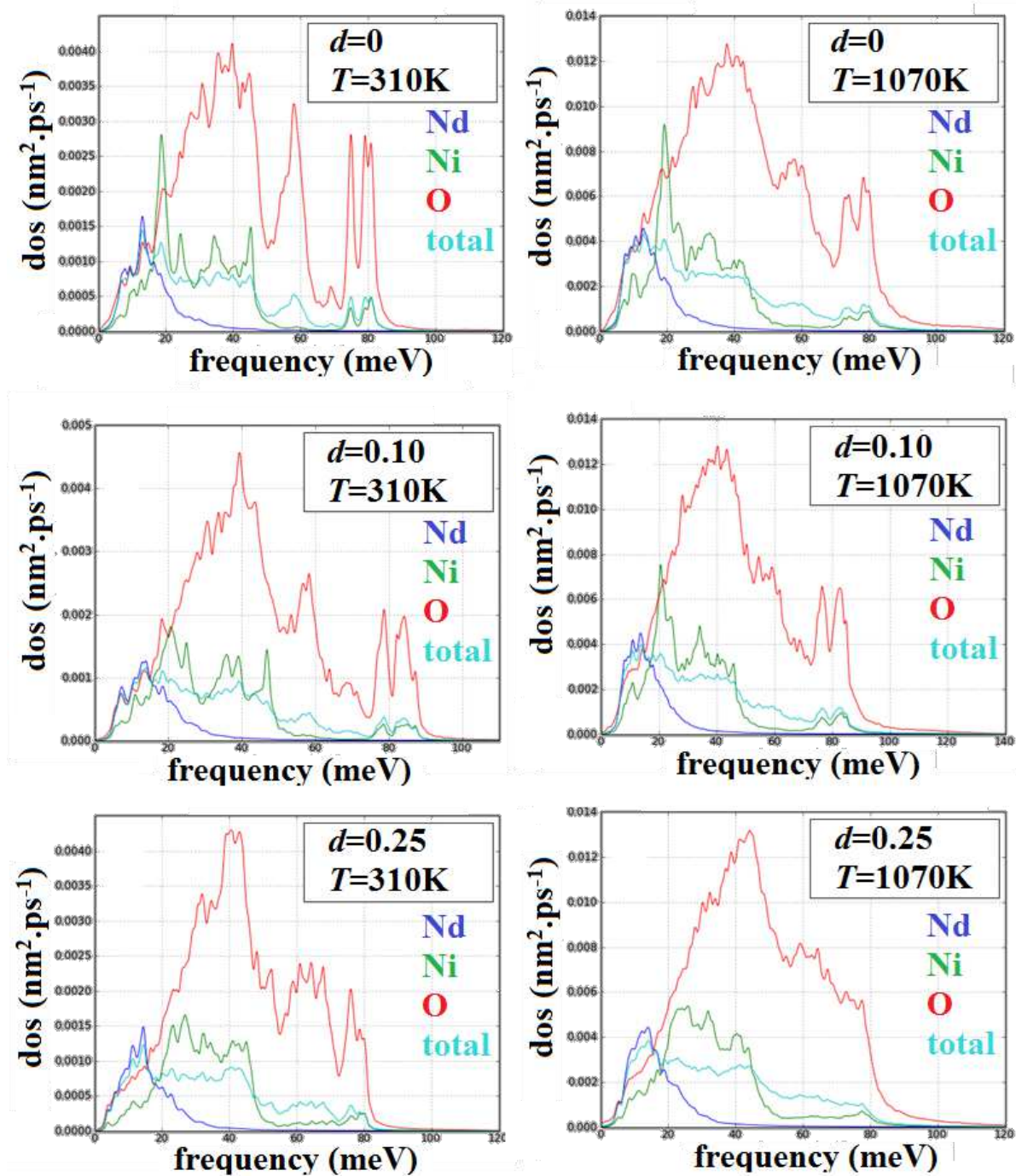


Figure 5.24 – Total and partial vibrational densities of states of $\text{Nd}_2\text{NiO}_{4.0}$, $\text{Nd}_2\text{NiO}_{4.10}$ and $\text{Nd}_2\text{NiO}_{4.25}$, at $T=310\text{K}$ and $T=1070\text{K}$. The vDOS are calculated from the molecular dynamic trajectories using the auto-correlation function. Each curves is convoluted with a 1meV wide gaussian.

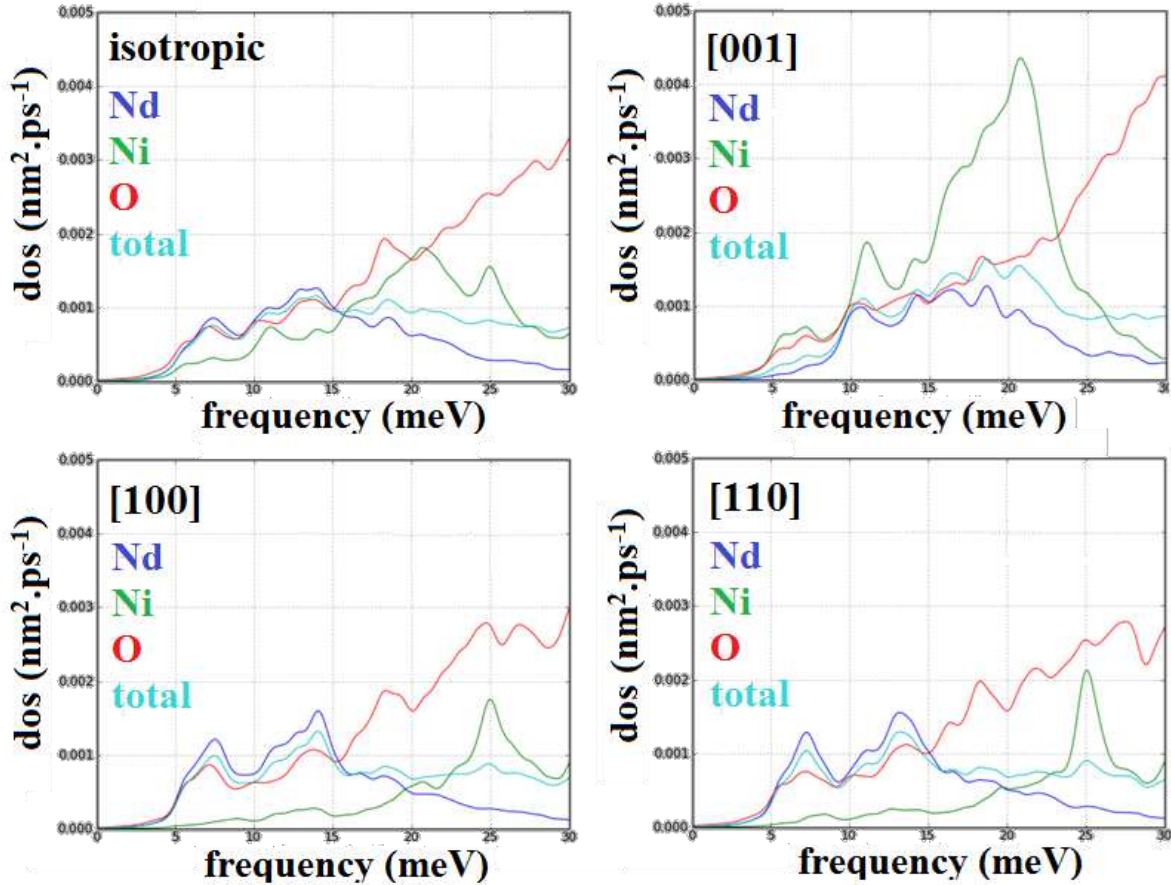


Figure 5.25 – Total and partial vibrational densities of states in the low-energy range $E=0-30\text{meV}$, of $\text{Nd}_2\text{NiO}_{4.10}$ at $T=310\text{K}$, isotropic, and projected on the [100], [001] and [110] axis.

5.4. Positional recurrence maps (PRM)

In order to obtain further informations about the dynamics of apical oxygen and excess oxygen on interstitial sites, especially for the non-stoichiometric models, we designed the positional recurrence map (PRM) code to isolate their contribution. The code itself is described in **chapter 3** and **appendix A**.

5.4.1. *d*-dependent PRM

We have seen in **section 5.3.2** that diffusion events were only observed for non-stoichiometric $\text{Nd}_2\text{NiO}_{4+d}$, and that mobile oxygen are first the apical oxygen – closest to the interstitial one – jumping along [110] to the nearest vacant interstitial site, and then a recombination of one of the interstitial oxygen on the vacant apical site. Furthermore, in **section 5.3.3** – as it will be confirmed from experiments in **chapter 6** – we show that excess oxygen in interstitial sites

tend to damp phonon modes polarized along [010], and populate modes along [110]. How does this switch in dynamics impact on atomic motion?

Hereafter, in **Figure 5.26**, is reported the PRM in CoM projection (atomic displacement space) of former apical oxygen atoms, of $\text{Nd}_2\text{NiO}_{4.0}$, $\text{Nd}_2\text{NiO}_{4.10}$ and $\text{Nd}_2\text{NiO}_{4.25}$ at $T=310\text{K}$, from 40ps molecular dynamic trajectories. The structural models we used are tetragonal and described in **section 5.1**. The optimized structures show a decrease of c-axis parameter with increasing oxygen content – due to the missing paramagnetic contribution – compared to the experimental case where the c-axis is increasing. To go around this limitation, and especially to decorrelate the effects of the c-axis parameter from the local deformations due to excess oxygen in interstitial sites, we considered, for each stoichiometry, cells with optimized, reduced and increased c-axis parameter. An interesting point is, considering 0.5\AA of variation for the c-axis parameter, nickel to apical oxygen bond lengths are changed by about 4%, which is less than half the variation induced by the apical oxygen moving to the saddle point of diffusion. As such, a reduced c-axis parameter would describe the case where the apical oxygen is close to nickel and belongs to the NiO_6 octahedron, an increased c-axis parameter the case of free apical oxygen, and the optimized c-axis parameter an intermediate situation. On the following figures, the small satellites in the outer shell come from diffusion events of oxygen atoms from the apical to the interstitial sites, while the ‘*inner*’ pattern translate on-site atomic motion.

In the stoichiometric $\text{Nd}_2\text{NiO}_{4.0}$ case, the apical oxygen PRM with an optimal stacking-axis parameter (**Figure 5.26.b**) shows a cross shape with preferred displacements in the [010] direction, which is expected since the LTO has its tilt pattern along [010]. When we look at the case with a contracted stacking-axis parameter (**Figure 5.26.a**), we note that the apical oxygen PRM is completely isotropic, which means that the apical oxygen is rigidly held within the NiO_6 octahedron. With an elongated stacking-axis parameter (**Figure 5.26.c**), we observe a shifting of the displacement from the [010] to [110] direction, hence an activation of the [110] tilt mode.

In the most-oxidized $\text{Nd}_2\text{NiO}_{4.25}$ case, the PRM of apical oxygen with reduced stacking-axis parameter (**Figure 5.26.g**) shows [110] delocalization of the core density, which comes from the first neighbor interaction of NiO_6 and interstitial oxygen atoms. A smaller delocalization direction is also observed in the outer shell, and comes from the second neighbor interaction between the apical oxygen and different combinations of the several interstitial oxygen atoms. In this rigid case, most of the freedom of NiO_6 octahedron is pinned by the interstitial oxygen. With an optimal stacking-axis parameter (**Figure 5.26.h**), the second neighbor interaction disappears and the [110] pathway is broadened. With an elongated stacking-axis parameter (**Figure 5.26.i**), the apical oxygen density shows an even broader [110] delocalization.

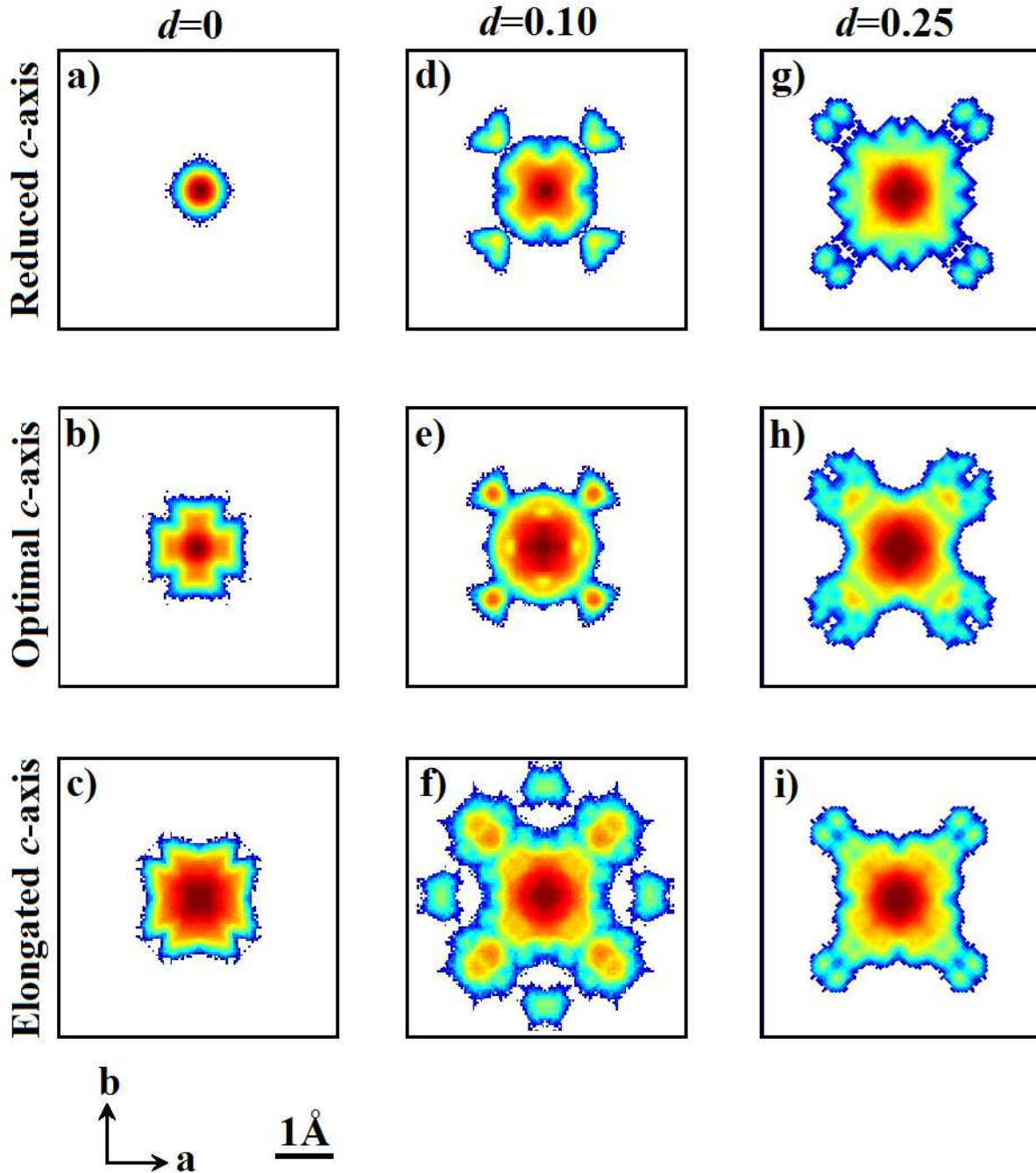


Figure 5.26 – a-i) Positional recurrence maps: displacement vectors from center-of-mass positions projected on unitary vectors (a, b), with respect to the conventional F -cell, of former apical oxygen atoms. PRM are calculated from 40ps *ab initio* molecular dynamics at $T=310\text{K}$, of **a)b)c)** $\text{Nd}_2\text{NiO}_{4.0}$, **d)e)f)** $\text{Nd}_2\text{NiO}_{4.10}$, **g)h)i)** $\text{Nd}_2\text{NiO}_{4.25}$, with **a)d)g)** reduced c -axis parameter by 0.5\AA , **b)e)h)** optimal c -axis parameter, and **c)f)i)** elongated c -axis parameter by 0.5\AA . This value of 0.5\AA of increase or decrease of the cell induces variation of distances along c of about 4%. Each PRM is cut in space to the conventional F -cell (black border). The color scale is logarithmic.

In the intermediate $\text{Nd}_2\text{NiO}_{4.10}$ case, the positional recurrence pattern of the apical oxygen atom with an optimal stacking-axis parameter (**Figure 5.26.e**) shows both [010] and [110] delocalization. This is consistent with the quarter filling of interstitial sites by excess oxygen atoms for $d=0.125$, which means that 75% of apical oxygen atoms have ‘normal’ dynamics and contribute to [010] delocalization, and 25% of them suffer from a [110] deformation, which activates the [110] delocalization. In the case of a reduced stacking-axis parameter (**Figure 5.26.d**), a similar PRM is formed, yet with fewer [010] displacements and pronounced [110] delocalization. In this rigid regime, every NiO_6 octahedron is strongly dependent on its neighbors, which means that the [110] strained apical oxygen drives the free apical oxygen from [010] to [110]. With an elongated stacking-axis parameter (**Figure 5.26.f**), the octahedrons become less dependent, which leads to a renewed [010] delocalization, a strong [110] delocalization from interstitial oxygen, and an easy diffusion between apical and interstitial sites.

Thus the effect of the stacking-axis parameter can be summarized as follows: a short stacking-axis parameter forbids any diffusion event and will freeze the NiO_6 octahedron in its current tilt pattern, with a strong localization of the apical oxygen atom. At the contrary, a long stacking-axis parameter enables the delocalization of the apical oxygen and thus the free rotations of the NiO_6 octahedrons; furthermore, it favors the apical oxygen to be pulled into the rock-salt layer, with a drift of the dynamics from [010] to [110], and to become diffusive.

Considering the effect of d : excess oxygen in interstitial sites activates the [110] dynamics of apical oxygen atoms. When the assumption that the second neighbor interaction is negligible, which is likely to be the case in the $d=[0-0.125]$ regime, we can state that the more d , the lower the stacking-axis parameter has to be to get an activated [110] dynamics. It also implies, considering thermal expansion, the mobility of apical oxygen at lower temperature with increasing excess oxygen content. However, the $d=0.125$ case seems to have a larger delocalization of apical oxygen than the $d=0.25$, for which the second neighbor interaction is important. Unfortunately, the number of atoms – the supercell size – is limited by computing capabilities, and long-range ordering of oxygen cannot be simulated in DFT.

5.4.2. Temperature-dependent PRM

In **section 5.4.1**, the molecular dynamic temperature was fixed to $T=310\text{K}$ for all stacking axis lengths and all stoichiometries, which can be seen as constant filling of the potential energy well around apical oxygen atoms. Hence we evaluated the shape of the potential well in several configurations of the apical oxygen atoms. A similar approach can be made by keeping constant the stacking axis, while varying the simulation temperature: for a fixed configuration, we expect to see the shape of the well at several fillings.

Figure 5.27 sums up the PRM of apical oxygen atoms in center-of-mass projection, from 40ps long molecular dynamics of $\text{Nd}_2\text{NiO}_{4.0}$, $\text{Nd}_2\text{NiO}_{4.10}$ and $\text{Nd}_2\text{NiO}_{4.25}$. Only structural models with optimized cell parameters are considered.

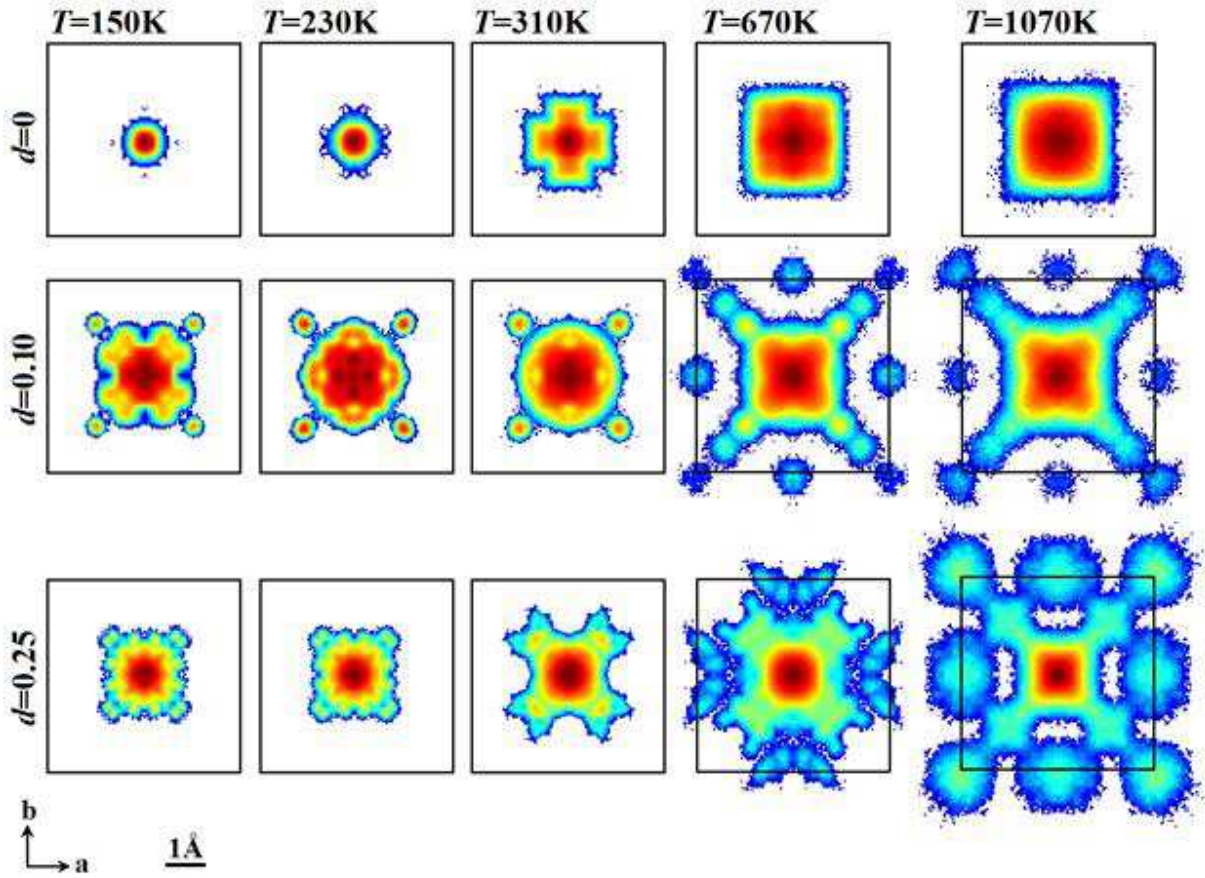


Figure 5.27 – PRM of apical oxygen atoms from 40 ps *ab initio* molecular dynamics at $T=150, 230, 310, 670$ and 1070K , of $\text{Nd}_2\text{NiO}_{4.0}$, $\text{Nd}_2\text{NiO}_{4.10}$ and $\text{Nd}_2\text{NiO}_{4.25}$. Each PRM is cut in space to the conventional F -cell (black border). The color scale is logarithmic.

For the $d=0$ structure, the bottom of the well explored at $T=150, 230\text{K}$ shows the localization of the apical oxygen atoms. As for the case of the reduced stacking axis described in **section 5.4.1**, apical oxygen atoms belong to the NiO_6 octahedron and the tilt scheme remains rigid through the simulation, with respect to the LTT structural model. While increasing the temperature, the transition from LTT to LTO is translated by delocalization in the $[010]$ direction, which is observed in the $T=310\text{K}$ pattern. Reaching the high-temperature limit at $T=670$ then 1070K , delocalization along $[110]$ is growing which makes the pattern almost isotropic. Such behavior means the apical oxygen atoms are freed from the octahedron and independent, which is coherent with the HTT average representation. We note that, even at high temperature, no diffusion events are observed for the $\text{Nd}_2\text{NiO}_{4.0}$ model.

For the $d=0.25$ structure at low temperatures $T=150$ and 230K , even a more complex pattern than the one obtained for the reduced stacking axis in **section 5.4.1** is obtained.

5.4.3. About the interstitial site

A similar approach can be performed on oxygen formerly on interstitial sites (the excess oxygen). The **Figure 5.28** shows the PRM of these oxygen for $\text{Nd}_2\text{NiO}_{4.10}$ and $\text{Nd}_2\text{NiO}_{4.25}$ for three temperatures, $T=310$, 670 and 1070K . While the $\text{Nd}_2\text{NiO}_{4.10}$ case a quite straightforward from the previous analysis: a well defined and stressed interstitial site, and diffusion events to broad and strained apical sites ; the $\text{Nd}_2\text{NiO}_{4.25}$ scenario is more complex, yet similar to description of the apical oxygen PRM. At room temperature we found back the behavior of the complex frozen structure with a swinging of the excess oxygen in interstitial site toward the apical site (**Figure 5.28.d**). At intermediate temperature $T=670\text{K}$ (**Figure 5.28.e**) we find the renewed freedom and diffusion events, as well has weak outer spots in the same directions as those of apical oxygen PRM. And at high-temperatyre (**Figure 5.28.f**) we find again a very similar pattern as the one of the apical oxygen atoms, yet less pronounced in intensity due to the lower statistic (much less excess oxygen than apical oxygen). Even if the PRM is not optimized to describe post-diffusion motions, the evolution of the outer pattern in $\text{Nd}_2\text{NiO}_{4.10}$ with temperature is explicit. At room-temperature (**Figure 5.28.a**), the interstitial oxygen diffuses to a neighboring apical site, yet it stays ‘where it lands’, *i.e.* the newly formed octahedron has a quasi-static tilt. With increasing temperature, we observe that the former interstitial oxygen density is distributed more homogeneously in the apical site, meanin that the tilt of the newly formed octahedron is dynamic.

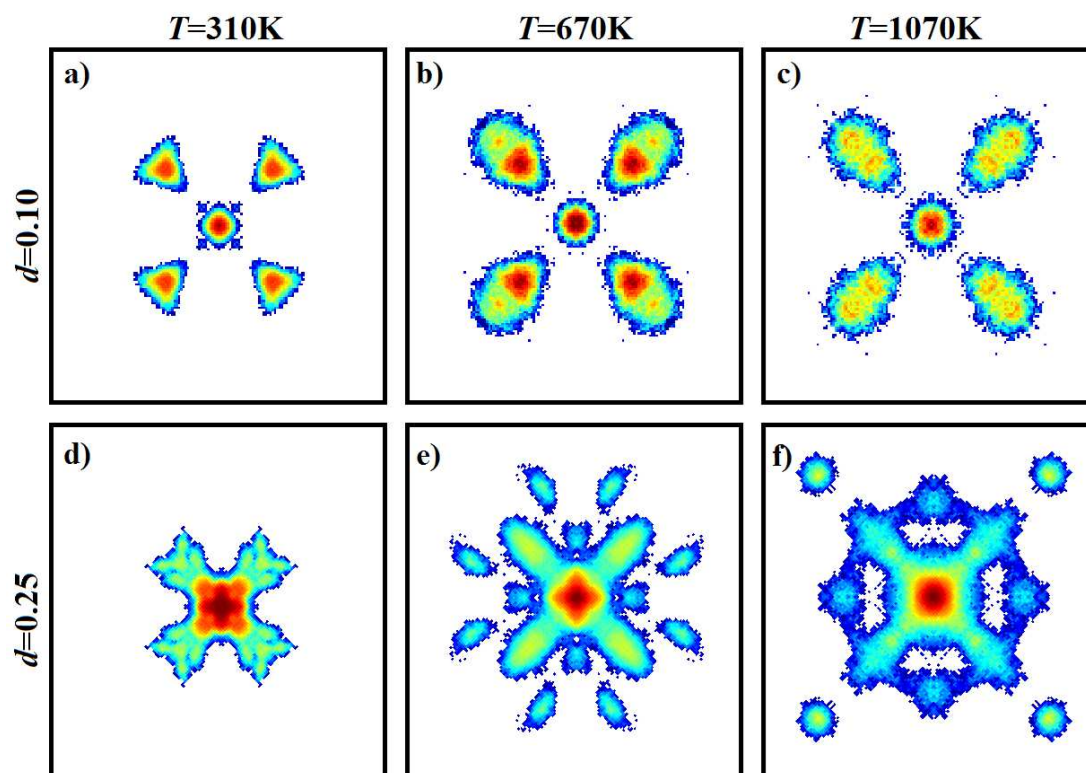


Figure 5.28 – PRM of interstitial oxygen atoms from 40ps *ab initio* molecular dynamics at (a,d) $T=310\text{K}$, (b,e) $T=670\text{K}$, and (c,f) $T=1070\text{K}$, of (a,b,c) $\text{Nd}_2\text{NiO}_{4.10}$, and (d,e,f) $\text{Nd}_2\text{NiO}_{4.25}$. Each PRM is cut in space to the conventional F -cell (black border). The color scale is logarithmic.

In the case of the simulations with a reduced or increased c -axis, as plotted in **Figure 5.29** for $\text{Nd}_2\text{NiO}_{4.10}$ and $\text{Nd}_2\text{NiO}_{4.25}$ at $T=310\text{K}$, here again the behavior is similar as described for the apical oxygen atoms, considering a stiff interstitial site and a loose apical one, and a lower statistic. We note that in the $\text{Nd}_2\text{NiO}_{4.25}$ case, we observe a maxima of delocalization along $[110]$ for the optimal c -axis (**Figure 5.29.e**), and a reduced delocalization while increasing the c -axis (**Figure 5.29.f**). At room-temperature we do not observe diffusion events for $\text{Nd}_2\text{NiO}_{4.25}$, yet a swinging motion of interstitial oxygen atoms toward apical sites; increasing the c -axis, this motion loses amplitude toward $[110]$ and gain amplitude toward $[001]$. When comparing the decreased and increased c -axis (**Figure 5.29.d** and **Figure 5.29.f**), we clearly see the transfer of population from $[100]$ to $[110]$; for the optimal c -axis parameter, due to steric pressure along c , this swinging motion just happen to be more in-plane, thus showing a more extended delocalization on the PRM. Looking at the outer pattern of the PRM of $\text{Nd}_2\text{NiO}_{4.10}$, we observe that the post-diffusion site is well defined when the c -axis is reduced, and strongly broaden with increasing c -axis.

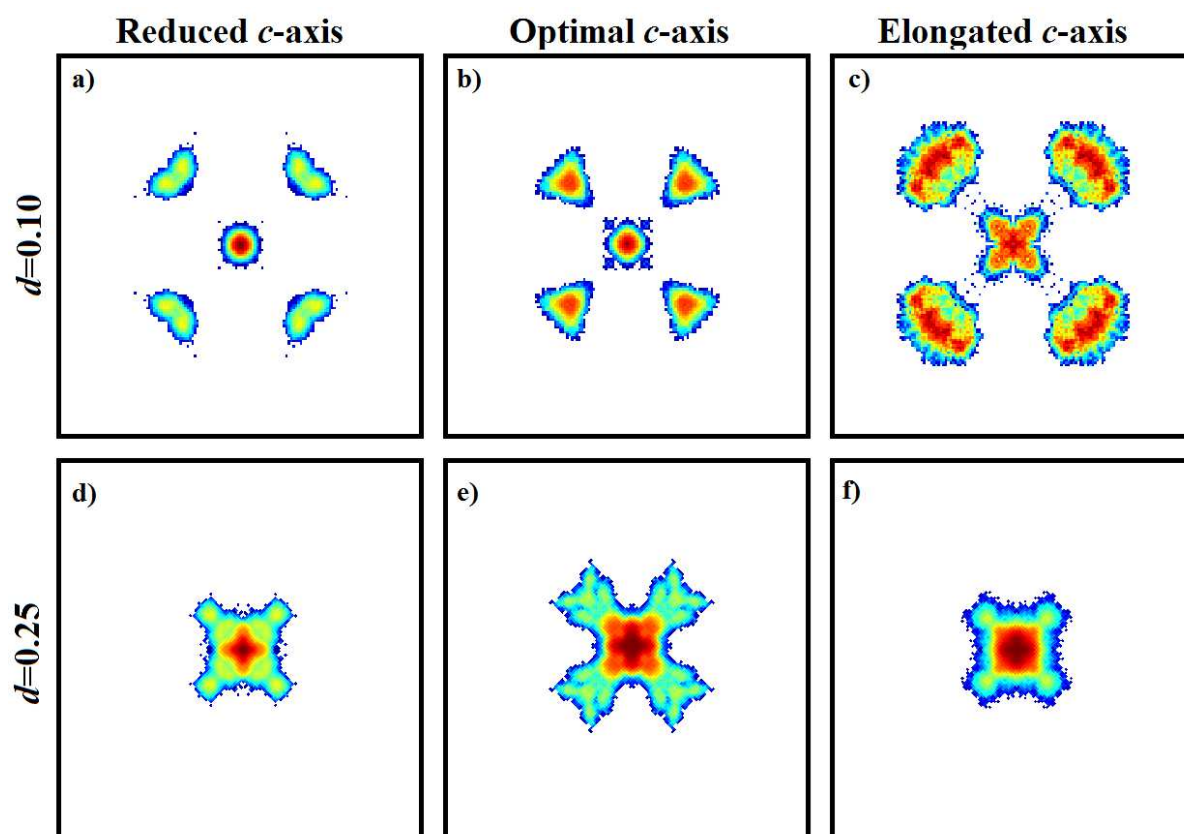


Figure 5.29 – PRM of interstitial oxygen atoms from 40ps *ab initio* molecular dynamics at $T=310\text{K}$ (**a,b,c**) $\text{Nd}_2\text{NiO}_{4.10}$ and (**d,e,f**) $\text{Nd}_2\text{NiO}_{4.25}$, with (**a,d**) a reduced c -axis, (**b,e**) the optimal c -axis, and (**c,f**) an increased c -axis. Each PRM is cut in space to the conventional F -cell (black border). The color scale is logarithmic.

5.4.4. About the nickel, equatorial oxygen, and neodymium sites

As a control experiment we calculated the PRM of nickel atoms, equatorial oxygen atoms and neodymium atoms. We could expect a very low delocalization for all species and, as shown in **Figure 5.30**, we indeed observed it. Comparing with the PRM of apical oxygen atoms or excess oxygen atoms in interstitial sites, we confirm that the delocalization of the mobile species in the rock-salt layer are anomalously large.

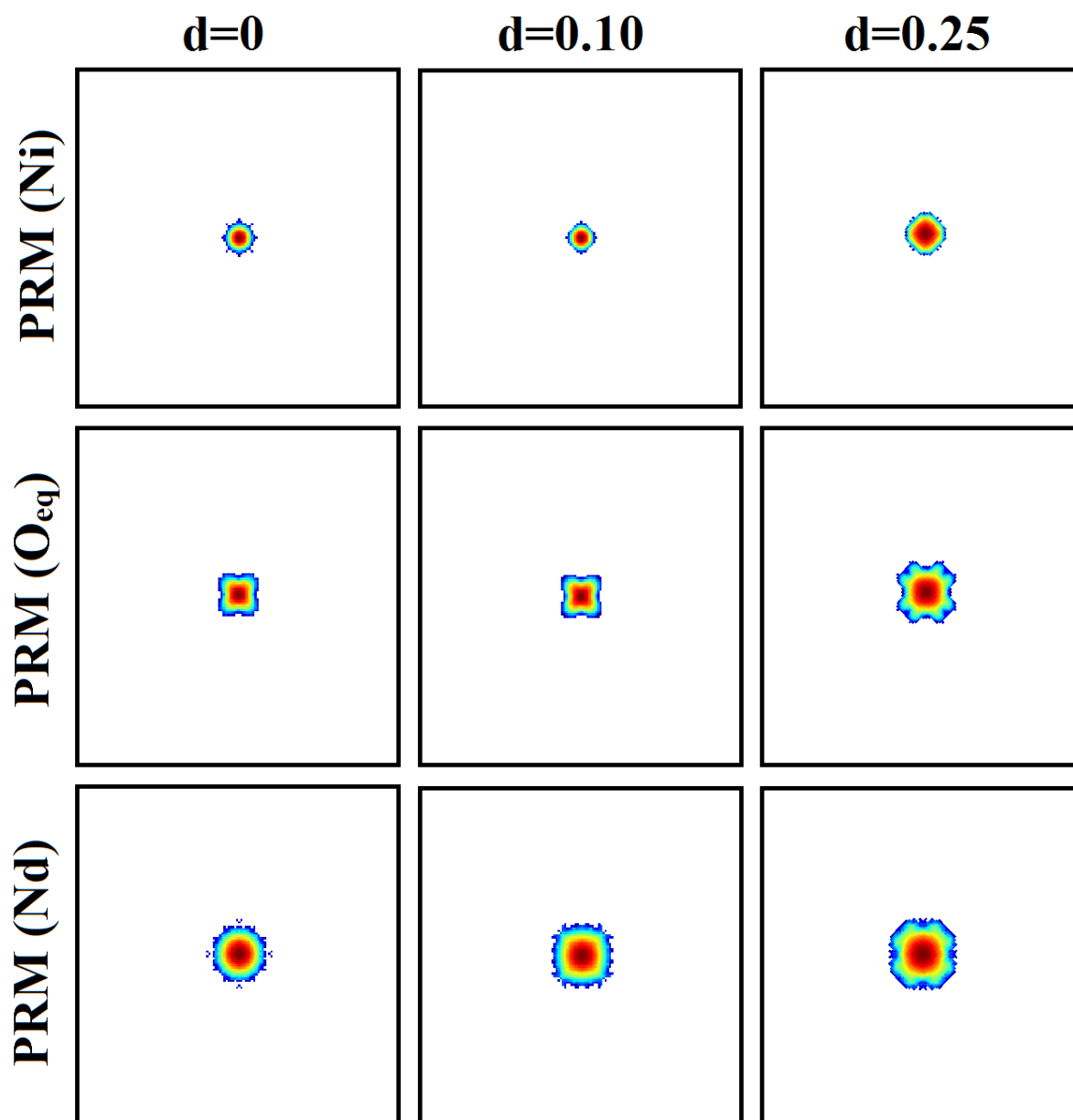


Figure 5.30 – PRM of nickel atoms and equatorial oxygen atoms from 40ps *ab initio* molecular dynamics at $T=310\text{K}$ of $\text{Nd}_2\text{NiO}_{4.0}$, $\text{Nd}_2\text{NiO}_{4.10}$ and $\text{Nd}_2\text{NiO}_{4.25}$. PRM is cut in space to the conventional F -cell (black border). The color scale is logarithmic. These species, which we expected to have well defined sites, show indeed a sharp PRM with low delocalization.

5.5. Conclusion

In this chapter focused on *ab initio* simulations, we have shown structural models and parameters we have used to simulate the $\text{Nd}_2\text{NiO}_{4.0}$, the $\text{Nd}_2\text{NiO}_{4.10}$ and the $\text{Nd}_2\text{NiO}_{4.25}$ single-phases. While the structural complexity of this family of structure have been challenging to model, and some over simplification may make one doubtfull, the results drawn from phonon calculations, molecular dynamics calculation and its post-processing through the PRM code have shown to be coherent and, as it will be proved in the following chapters, in adequation with the measurements.

The phonon calculations led to a precise description of phonon mode through their polarizations, and the calculated dispersion can be directly compared to measurements of three-axis spectrometry. We have shown that modes both at Γ and \mathbf{M} ([110]) may contribute to the easy oxygen mobility, through breathing or tilting motions of the apical oxygen atoms.

The molecular dynamic calculations have unveiled the diffusion pathway in the intermediate temperature range, which is found to be similar to the interstitialcy mechanism described at higher temperature. We also found that the presence of excess oxygen in interstitial sites is a prerequisite to promote the diffusion. The vibrational densities of states drawn from the molecular dynamic trajectories can be directly compared to measurements of time-of-flight spectroscopy.

And lastly, the PRM code we developed was proven particularly usefull to isolate the dynamical contributions of interest, showing that the presence of excess oxygen in interstitial site activates the [110] dynamics of the apical oxygen atoms, which itself promote the diffusion, which is coherent with our vision of lattice activated diffusion.

Thus the oxygen diffusion in $\text{Nd}_2\text{NiO}_{4+d}$ was proven to increase with the amount of excess oxygen atoms, the stacking axis parameter length, and the temperature, which directly impact on the activation of the [110] dynamics of the apical oxygen atoms.

5.6. Bibliography

1. Chroneos, A., Parfitt, D., Kilner, J.A., and Grimes, R.W. (2010). *Journal of Materials Chemistry*, 20(2), 266-270.
2. Cleave, A.R., Kilner, J.A., Skinner, S.J., Murphy, S.T., and Grimes, R.W. (2008). *Solid State Ionics*, 179(21–26), 823-826.
3. Minervini, L., Grimes, R.W., Kilner, J.A., and Sickafus, K.E. (2000). *Journal of Materials Chemistry*, 10(10), 2349-2354.
4. Naumovich, E.N. and Kharton, V.V. (2010). *Journal of Molecular Structure: THEOCHEM*, 946(1-3), 57-64.
5. Parfitt, D., Chroneos, A., Kilner, J.A., and Grimes, R.W. (2010). *Physical Chemistry Chemical Physics*, 12(25), 6834-6836.
6. Pintschovius, L., Bassat, J.M., Odier, P., Gervais, F., Chevrier, G., Reichardt, W., and Gompf, F. (1989). *Physical Review B*, 40(4), 2229-2238.
7. Tealdi, C., Ferrara, C., Mustarelli, P., and Islam, M.S. (2012). *Journal of Materials Chemistry*, 22(18), 8969-8975.
8. Yashima, M., Enoki, M., Wakita, T., Ali, R., Matsushita, Y., Izumi, F., and Ishihara, T. (2008). *Journal of the American Chemical Society*, 130(9), 2762-2763.
9. Yashima, M., Sirikanda, N., and Ishihara, T. (2010). *Journal of the American Chemical Society*, 132(7), 2385-2392.
10. Kushima, A., Parfitt, D., Chroneos, A., Yildiz, B., Kilner, J.A., and Grimes, R.W. (2011). *Physical Chemistry Chemical Physics*, 13(6), 2242-2249.
11. Paulus, W., Schober, H., Eibl, S., Johnson, M., Berthier, T., Hernandez, O., Ceretti, M., Plazanet, M., Conder, K., and Lamberti, C. (2008). *Journal of the American Chemical Society*, 130(47), 16080-16085.
12. Villesuzanne, A., Paulus, W., Cousson, A., Hosoya, S., Le Dréau, L., Hernandez, O., Prestipino, C., Ikbel Houchati, M., and Schefer, J. (2012). *Journal of Solid State Electrochemistry*, 15(2), 357.
13. Wahyudi, O. (2011). *Université de Rennes 1, PhD thesis 4468*.
14. Kresse, G. and Furthmüller, J. (1996). *Physical Review B*, 54(16), 11169-11186.
15. Kresse, G. and Hafner, J. (1993). *Physical Review B*, 48(17), 13115-13118.
16. Rodríguez-Carvajal, J., Fernández-Díaz, M.T., Martínez, J.L., Fernández, F., and Saez-Puche, R. (1990). *Europhysics Letters*, 11(3), 261.
17. Ishikawa, K., Metoki, K., and Miyamoto, H. (2009). *Journal of Solid State Chemistry*, 182(8), 2096-2103.
18. Yamamoto, S. and Fujiwara, T. (2002). *Journal of the Physical Society of Japan*, 71(5), 1226-1229.
19. Parlinski, K. (1999). *AIP Conference Proceedings*, 479(1), 121-126.
20. Reznik, D. (2012). *Physica C: Superconductivity*, 481(0), 75-92.
21. LAMP, the Large Array Manipulation Program. http://www.ill.eu/data_treat/lamp/the-lamp-book/.
22. Richard, D., Ferrand, M., and Kearley, G.J. (1996). *Journal of Neutron Research*, 4(1-4), 33-39.
23. Savvin, S.N., Mazo, G.N., and Ivanov-Schitz, A.K. (2008). *Crystallography Reports*, 53(2), 291-301.
24. Chroneos, A., Vovk, R.V., Goulatis, I.L., and Goulatis, L.I. (2010). *Journal of Alloys and Compounds*, 494(1–2), 190-195.

Chapter 6. INS-TOF.

Lattice dynamics on $\text{Nd}_2\text{NiO}_{4+d}$ powders.

In the previous chapter we have developed theoretical models to describe the lattice dynamics and the microscopic mechanism of oxygen diffusion at moderate temperature in $\text{Nd}_2\text{NiO}_{4+d}$ phases. From now on, we will investigate the real materials $\text{Nd}_2\text{NiO}_{4.0}$, $\text{Nd}_2\text{NiO}_{4.10}$ and $\text{Nd}_2\text{NiO}_{4.25}$ with the purpose of evaluating the adequation of calculations with measurements.

In **section 6.1** we will describe the experiments on the cold-neutron time-focussing time-of-flight spectrometer IN6 – as introduced in **chapter 3** – that we performed in order to measure the phonon generalized densities of states (gDOS). In **section 6.2**, we will show the measured gDOS and propose a basic interpretation from relating the effects of the excess oxygen stoichiometry on the gDOS and the local structure of defective clusters. In **section 6.3**, we will compare the measured gDOS to the calculated vibrational density of states (vDOS) and draw conclusions on the agreement of the simulations with the real material behavior. In **section 6.4**, we will draw the analogy between the spectra measured with neutron TOF spectroscopy and RAMAN spectroscopy. Lastly, in **section 6.5**, we will conclude on the lattice-activated diffusion mechanism from the results of the time-of-flight experiments.

6.1. Experiments on the IN6 spectrometer

The cold-neutron time-focussing time-of-flight spectrometer IN6 at the Laue-Langevin Institute (ILL), Grenoble, France, is a neutron spectrometer designed to perform inelastic neutron scattering experiments to probe densities of states of polycrystalline materials. The description of the instrument, as well as the theoretical basis of inelastic neutron scattering^[1], are described in **chapter 3**.

Our aim, through these experiments, is to measure the effect of excess oxygen stoichiometry and the effect of temperature on the dynamics of the $\text{Nd}_2\text{NiO}_{4+d}$ system. To do so, we performed two experiments: first the high-temperatures from $T=310\text{K}$ to $T=1070\text{K}$, and secondly the low-temperatures from $T=310\text{K}$ to $T=150\text{K}$, through respectively the use of a furnace and a cryostat, on the three single-phases $\text{Nd}_2\text{NiO}_{4.0}$, $\text{Nd}_2\text{NiO}_{4.10}$ and $\text{Nd}_2\text{NiO}_{4.25}$. In the last chapter, the interpretation of the positional recurrence maps (PRM) of the apical oxygen atoms led to the following interpretation: the phases at room-temperature are tough to be an intermediate case between the low-temperature scenario where the oxygen excess is frozen, is a constituent of a well-defined extended super-structure, and the high-temperature

scenario where the oxygen excess can be seen as a mobile defect in an average structure. A study as a function of temperature is thus primordial to evaluate on which proportion the excess oxygen, at room-temperature, belongs to the structure and/or is a mobile defect.

6.1.1. The high-temperature experiment

For the high-temperature experiment, we used an incident wavelength of $\lambda=4.14\text{\AA}$ with a setup in elastic focussing, thus an high-flux and a good resolution around the elastic line. We performed the experiment on about 9 gram samples of $\text{Nd}_2\text{NiO}_{4.0}$ and $\text{Nd}_2\text{NiO}_{4.25}$, prepared by conventional solid state method, as described in **section 3.1** – we remind that the $\text{Nd}_2\text{NiO}_{4.0}$ sample is slightly over-reduced and shows traces of NiO oxide. Since we aim to measure at $T=1070\text{K}$, and since the sample is under dynamic secondary vacuum during the measurement, the $\text{Nd}_2\text{NiO}_{4.10}$ sample was obtained *in situ* from oxygen loss of the $\text{Nd}_2\text{NiO}_{4.25}$ sample upon heating. Laboratory X-ray diffraction performed right-after the experiment confirms that the $\text{Nd}_2\text{NiO}_{4.0}$ and $\text{Nd}_2\text{NiO}_{4.10}$ sample have the right stoichiometry and are pure phases.

Thus we performed the high-temperature experiment as follow:

- Measurement of the $\text{Nd}_2\text{NiO}_{4.25}$ sample at $T=310\text{K}$,
- Heating up then stabilization at $T=570\text{K}$: since the spectrometer has a low resolution in \mathbf{Q} , we cannot know exactly the cell parameters, yet the sample stays monophasic, and the excess oxygen stoichiometry is between $d=0.21$ and $d=0.25$,
- Measurement of the $\text{Nd}_2\text{NiO}_{4.21-25}$ sample at $T=570\text{K}$,
- Heating up and stabilization at $T=1070\text{K}$, till we reach a monophasic $\text{Nd}_2\text{NiO}_{4.10}$ stoichiometry,
- Measurement of the $\text{Nd}_2\text{NiO}_{4.10}$ sample at $T=1070\text{K}$,
- Cooling down and continuous measurements till $T=310\text{K}$.

- Measurement of the $\text{Nd}_2\text{NiO}_{4.0}$ sample at $T=310\text{K}$,
- Heating up then stabilization at $T=570\text{K}$, the sample is still monophasic $\text{Nd}_2\text{NiO}_{4.0}$,
- Measurement of the $\text{Nd}_2\text{NiO}_{4.0}$ sample at $T=570\text{K}$,
- Heating up then stabilization at $T=1070\text{K}$, the sample is still monophasic $\text{Nd}_2\text{NiO}_{4.0}$,
- Measurement of the $\text{Nd}_2\text{NiO}_{4.0}$ sample at $T=1070\text{K}$,
- Cooling down and continuous measurements till $T=310\text{K}$.

We also measured the vanadium standart at $T=310\text{K}$, and the empty canes (sample holder) at $T=310\text{K}$, $T=570\text{K}$ and $T=1070\text{K}$.

6.1.2. The low-temperature experiment

For the low-temperature experiment, we used and incident wavelength of $\lambda=4.14\text{\AA}$ with a setup in elastic focusing at about 6.5meV , thus a lower flux yet gaining a 0.5 to 2meV in resolution in the range $\Delta E=15-60\text{meV}$. We performed the experiment on about 15 gram

samples of $\text{Nd}_2\text{NiO}_{4.0}$, $\text{Nd}_2\text{NiO}_{4.10}$ and $\text{Nd}_2\text{NiO}_{4.25}$, prepared by conventional solid state method, as described in **section 3.1** – similarly to the high-temperature experiment, the $\text{Nd}_2\text{NiO}_{4.0}$ sample shows traces of NiO. Laboratory X-ray diffraction performed after the experiment confirmed the stoichiometries stayed nominal and the sample monophasic.

We performed the low-temperature experiment as follow, for the three-samples:

- Measurement of the sample at $T=310\text{K}$,
- Cooling down and stabilization at $T=230\text{K}$,
- Measurement at $T=230\text{K}$,
- Cooling down and stabilization at $T=150\text{K}$,
- Measurement at $T=150\text{K}$,
- Heating up to $T=310\text{K}$,
- Measurement at $T=310\text{K}$.

We also measured the vanadium standard at $T=310\text{K}$, and the empty canes (sample holder) at $T=310\text{K}$, $T=230\text{K}$ and $T=150\text{K}$.

6.2. Generalized phonon density of states

6.2.1. Measured gDOS

Once processed, one-phonon generalized phonon density of states are calculated from the data of time-of-flight scattering experiments. In **Figure 6.1** is shown the gDOS of $\text{Nd}_2\text{NiO}_{4.0}$, $\text{Nd}_2\text{NiO}_{4.10}$, and $\text{Nd}_2\text{NiO}_{4.21-25}$, respectively labeled $d=0$, $d=0.10$ and $d=0.25$, for temperatures $T=570\text{K}$ and $T=1070\text{K}$. In **Figure 6.2** is shown the gDOS of $\text{Nd}_2\text{NiO}_{4.0}$, $\text{Nd}_2\text{NiO}_{4.10}$ and $\text{Nd}_2\text{NiO}_{4.25}$, respectively labeled $\delta=0$, $\delta=0.10$ and $\delta=0.25$, for temperatures $T=310\text{K}$, $T=230\text{K}$ and $T=150\text{K}$. We note that the low-temperature gDOS are not showing a Debye growth in the range $\Delta E=0-4\text{meV}$, due to magnetic contamination. In order to solve, yet partially, this issue, the summation in momentum transfer \mathbf{Q} was restricted to the high- \mathbf{Q} region ; more informations are available in **chapter 3**.

We can notice at first that the gDOS at high-temperature are similar regardless of the excess oxygen content, while the gDOS at low-temperature are strongly varying with oxygen content. Since there is no doubt about the oxygen content – from diffraction lines –, we can directly confirm that the excess oxygen does not contribute to the phononic spectra in the high-temperature limit, which means it doesn't belong to the lattice and behaves as a defect in an average Nd_2NiO_4 structure. In the low-temperature limit, as it was expectable since the excess oxygen induces incommensurate long-range ordering, the gDOS are strongly varying upon excess oxygen content, which means that the excess oxygen belongs to the lattice and contribute to its dynamic. At room-temperature, the gDOS shows some differences, while weaker than in the low-temperature scenario, which confirms that the excess oxygen shows a mixed behavior, both belonging to the lattice and behaving as a defect.

A second observation, comparing the gDOS of $\text{Nd}_2\text{NiO}_{4.0}$, $\text{Nd}_2\text{NiO}_{4.10}$ and $\text{Nd}_2\text{NiO}_{4.25}$ at $T=150\text{K}$, is that the $\text{Nd}_2\text{NiO}_{4.0}$ shows a strong peak at $\Delta E=6\text{meV}$ and a weak bump at $\Delta E=13\text{meV}$, while the fully-oxidized $\text{Nd}_2\text{NiO}_{4.25}$ as the opposite behavior, a weak bump at $\Delta E=6-8\text{meV}$ and a strong peak at $\Delta E=13\text{meV}$. For the intermediate stoichiometry $\text{Nd}_2\text{NiO}_{4.10}$, we observe an intermediate dynamics with moderate peaks at $\Delta E=6-8\text{meV}$ and $\Delta E=13\text{meV}$. We also note that the strong $\Delta E=20\text{meV}$ peak of $\text{Nd}_2\text{NiO}_{4.0}$ harden – is shifted to higher energy – and broaden.

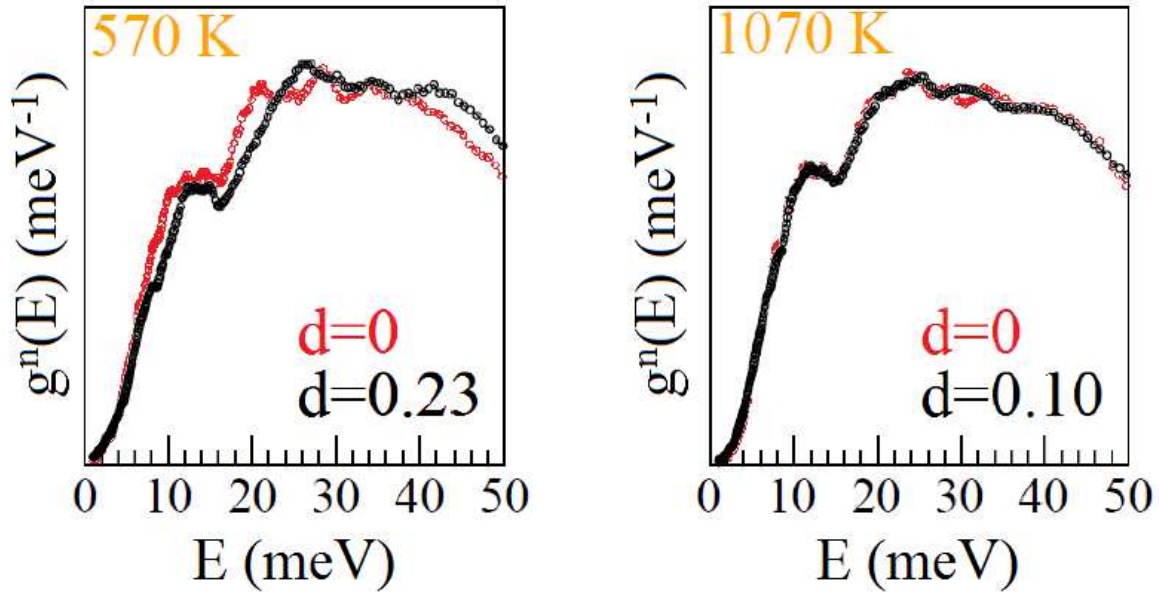


Figure 6.1 – One-phonon generalized phonon densities of states (gDOS) of $\text{Nd}_2\text{NiO}_{4.0}$, $\text{Nd}_2\text{NiO}_{4.10}$ and $\text{Nd}_2\text{NiO}_{4.21-25}$, respectively labeled $d=0$, $d=0.10$ and $d=0.23$, at (left) $T=570\text{K}$ and (right) $T=1070\text{K}$.

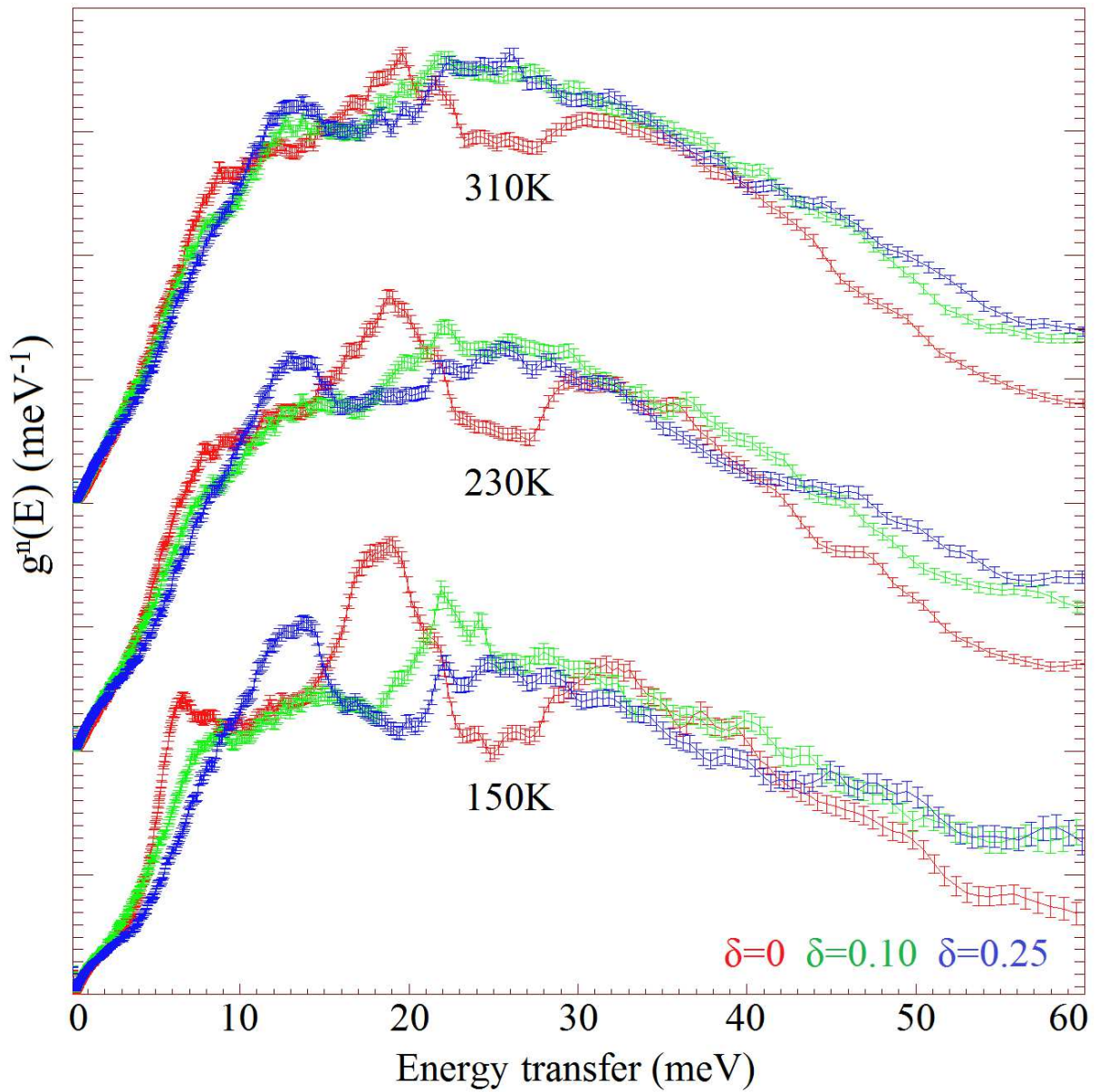


Figure 6.2 – One-phonon generalized phonon densities of states ($gDOS$) of $Nd_2NiO_{4.0}$, $Nd_2NiO_{4.10}$ and $Nd_2NiO_{4.25}$, respectively labeled $\delta=0$, $\delta=0.10$ and $\delta=0.25$, at $T=310K$, $T=230K$ and $T=150K$.

6.2.2. Attribution of modes

In the previous section we noticed variations of the lattice dynamics as a function of excess oxygen content, which the **Figure 6.3** is summing up.

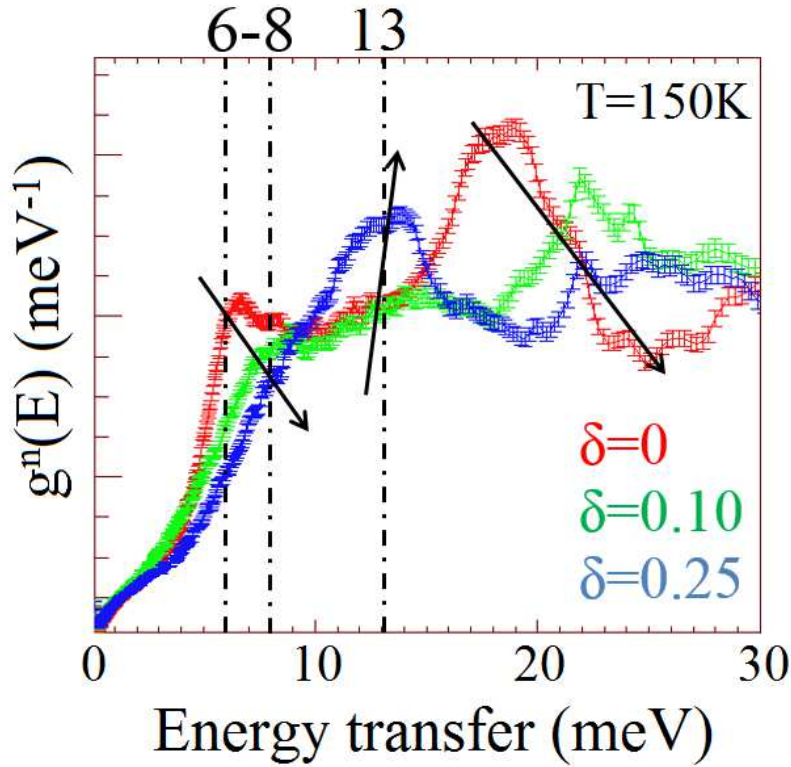


Figure 6.3 – Zoom on the low-lying energy part of the gDOS of $\text{Nd}_2\text{NiO}_{4.0}$, $\text{Nd}_2\text{NiO}_{4.10}$ and $\text{Nd}_2\text{NiO}_{4.25}$, respectively labeled $\delta=0$, $\delta=0.10$ and $\delta=0.25$, at $T=150\text{K}$. The discussed variation are explicated by arrows.

The variations in the lattice dynamics can be directly related to the structural deformations imposed on the host lattice by a simple model containing the inclusion of additional oxygen atoms. In the stoichiometric case the structure is described in the $Bmcb$ space-group, with a tilt pattern of the NiO_6 octahedron along the $[100]$ direction. Upon filling the interstitial tetrahedral sites of the rock-salt layers, the additional oxide ions deform the first shell of neighboring apical oxygen atoms, forcing a tilt from the $[100]$ to the $[110]$ direction. As schematized in **Figure 6.4**, for an oxygen content of $d=0.10$, about one excess oxygen is present for 16 apical oxygen atoms, forcing a quarter of the apical oxygen atoms along $[110]$, while the rest may still follow the $[010]$ tilt direction. Reaching the content $d=0.25$, half of the apical oxygen atoms are affected by this additional tilt. One therefore expects a perturbation of the tilting mode along the $[100]$ directions leading to an hardening and possible damping with increasing excess oxygen content, while the $[110]$ mode should, on the contrary, get softened. Therefore we would expect the $\Delta E=6-8\text{meV}$ contribution to concerns tilting motions along $[100]$, and the $\Delta E=13\text{meV}$ contribution to relates to tilting motions along $[110]$ – which is indeed confirmed by DFT calculation, as described in **chapter 5**.

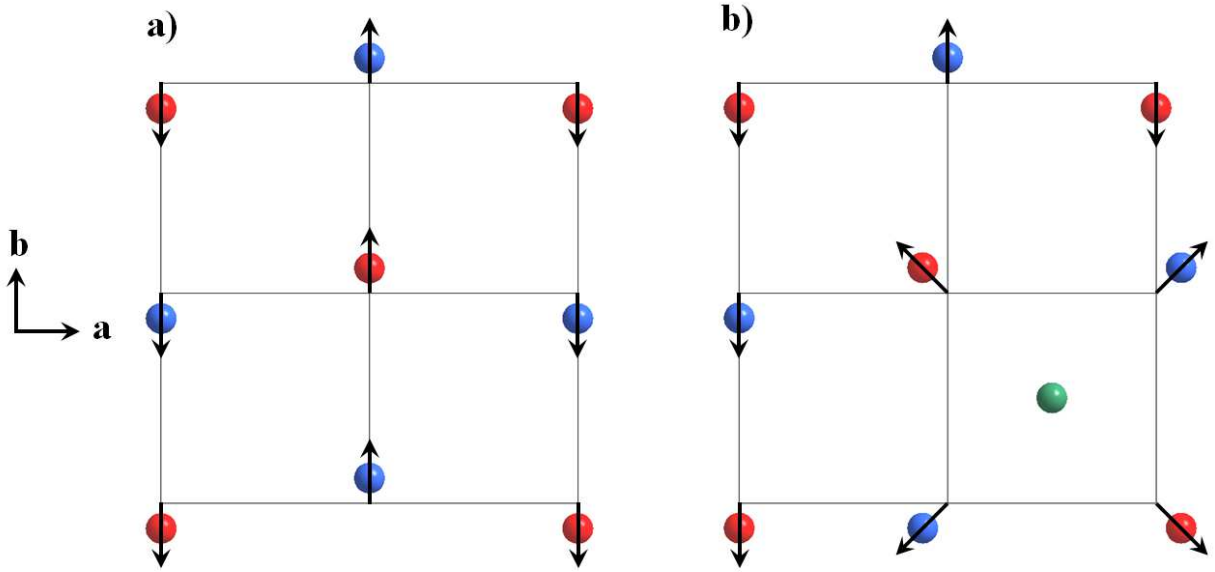


Figure 6.4 – Scheme of the tilt pattern in Bmb space-group of (a) stoichiometric $Nd_2NiO_{4.0}$ and (b) Nd_2NiO_{4+d} with excess oxygen in interstitial site. Apical oxygen atoms in the plane below the interstitial site are represented in red ($z \approx 0.17$) and in the plan above in blue ($z \approx 0.33$). Excess oxygen in the interstitial site is represented in green ($z = 0.25$). The first shell of apical oxygen atoms surrounding the interstitial is deformed from $[100]$ to $[110]$.

6.3. Comparison with calculations

A fundamental step to validate the *ab initio* calculations is to validate the approximations of the structural models and confirm the agreement of the calculated results with experimental measurements. We already confirmed that, as calculated, the excess oxygen in interstitial site lays at room-temperature in a intermediate state, between the low-temperature scenario where it belongs to the lattice and plays on lattice dynamics, and the high-temperature scenario where it behaves as a mobile defect.

Furthermore, the mode attribution based on a simple structural model of defect inclusion, as described in **section 6.2.2**, is coherent with the eigenvector analysis performed in **section 5.2.3**, with a $[100]$ polarized motion measured at $\Delta E = 6-8 \text{ meV}$ and calculated at about $\Delta E = 5.3 \text{ meV}$, and with a $[110]$ polarized motions measured at $\Delta E = 13 \text{ meV}$ and calculated at about $\Delta E = 13-13.9 \text{ meV}$. We note that only the modes at Γ , X , Y and Z are observable during the TOF experiments – the M point of the Brillouin zone being out of reach in momentum transfert due to the limited angular coverage of the TOF spectrometer (the first Bragg peak, where acoustic modes are intense, is at $Q_{(220)} = 3.3 \text{ \AA}^{-1}$ while maximum momentum transfert on IN6 is $Q_{\text{max}} \approx 2.6 \text{ \AA}^{-1}$).

The next step is to confirm that the calculated vibrational densities of states from molecular dynamic simulations are in agreement with the measured one-phonon generalized phonon

densities of states. A comparison of gDOS from calculations and experiments is shown in **Figure 6.6** for $\text{Nd}_2\text{NiO}_{4.0}$, $\text{Nd}_2\text{NiO}_{4.10}$ and $\text{Nd}_2\text{NiO}_{4.25}$. We see that, except for the stoichiometric $\text{Nd}_2\text{NiO}_{4.0}$ case at low-temperature, where two sharp and non-existing peak are calculated, the calculated vDOS match, at least qualitatively, the main features of the measured gDOS. In the low-temperature stoichiometric case – as well as the room-temperature case, we’ve shown in **chapter 5** that the magnetism of the nickel ions cannot be neglected to properly model the $\text{Nd}_2\text{NiO}_{4.0}$ lattice dynamics – yet it can be neglected when looking only on the dynamical motion of the apical oxygen atoms, as proven in **chapter 3**. If we consider the magnetic molecular dynamic calculation of $\text{Nd}_2\text{NiO}_{4.0}$ at $T=150\text{K}$, and calculate the vDOS, the agreement with the measured gDOS is a lot better, as shown in **Figure 6.5**.

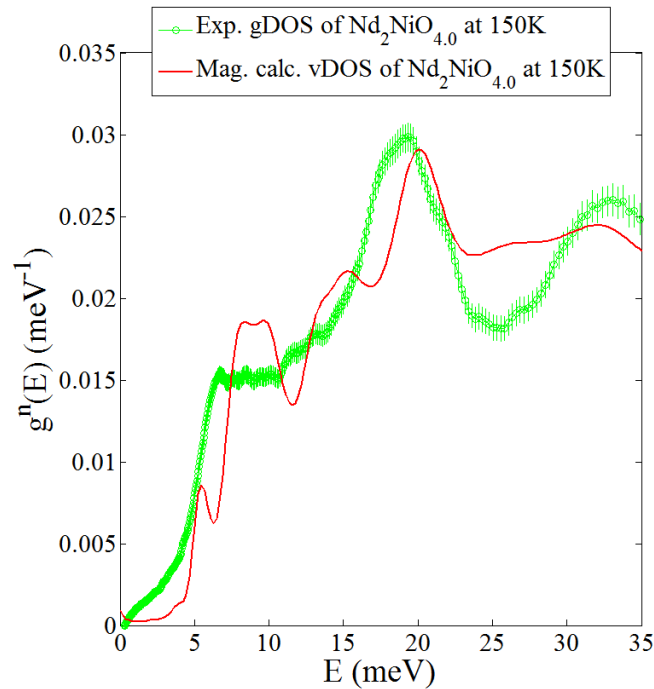


Figure 6.5 – Comparison of the calculated vibrational density of states from magnetic molecular dynamic simulations with the measured one-phonon generalized phonon density of states on the IN6 spectrometer, of $\text{Nd}_2\text{NiO}_{4.0}$ at $T=150\text{K}$. Using the magnetic molecular dynamics, we are able to simulate properly the dynamical features experimentally measured.

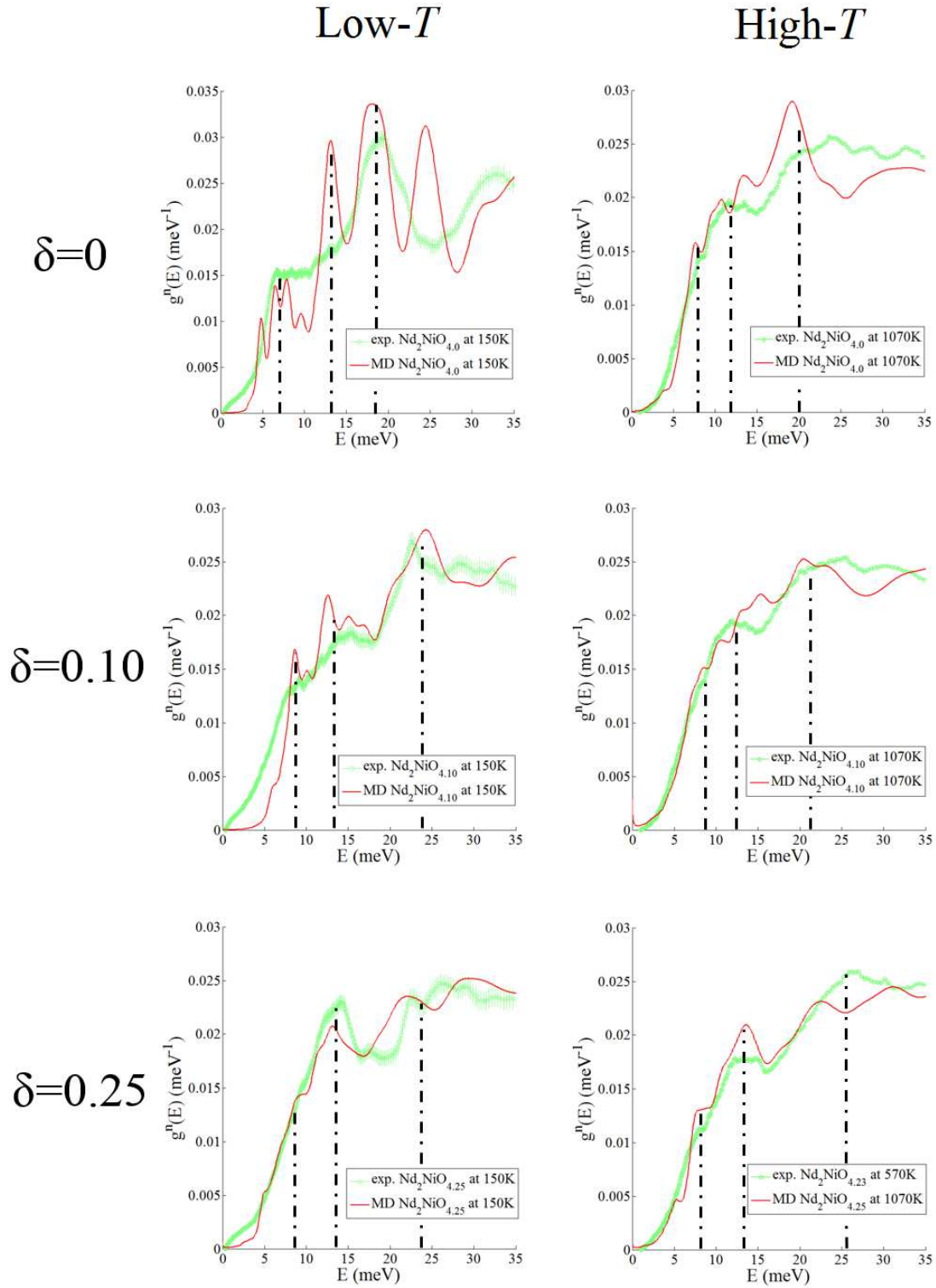


Figure 6.6 – Comparison of calculated vibrational densities of states from non-magnetic molecular dynamic simulations with measured one-phonon generalized phonon densities of states on the IN6 spectrometer, for $\text{Nd}_2\text{NiO}_{4.0}$, $\text{Nd}_2\text{NiO}_{4.10}$ and $\text{Nd}_2\text{NiO}_{4.25}$, at $T=150\text{K}$ and $T=1070\text{K}$. The overall agreement is good and experimentally measured dynamic features are well reproduced in the calculations, except for the low-temperature stoichiometric $\text{Nd}_2\text{NiO}_{4.0}$ for which the non-magnetic calculation cannot properly simulate the lattice dynamics.

Since the calculated vDOS from molecular dynamics were able to properly simulate the main dynamical features observable on the measured gDOS for both limit case at $T=150\text{K}$ and $T=1070\text{K}$, it isn't surprising that the agreement between experiments and calculations is also good for the intermediate case at room-temperature, as shown in **Figure 6.7**. The variations of the dynamical features as a function of excess oxygen content are properly reproduced :

- the decreasing $\Delta E=8\text{meV}$ peak, corresponding to $[100]$ polarized tilting motion, labeled as **A**,
- the increasing $\Delta E=13\text{meV}$ peak, corresponding to $[110]$ polarized tilting motion, labeled as **B**,
- the broadening and hardening of the $\Delta E=20\text{meV}$ peak, labeled as **C**.

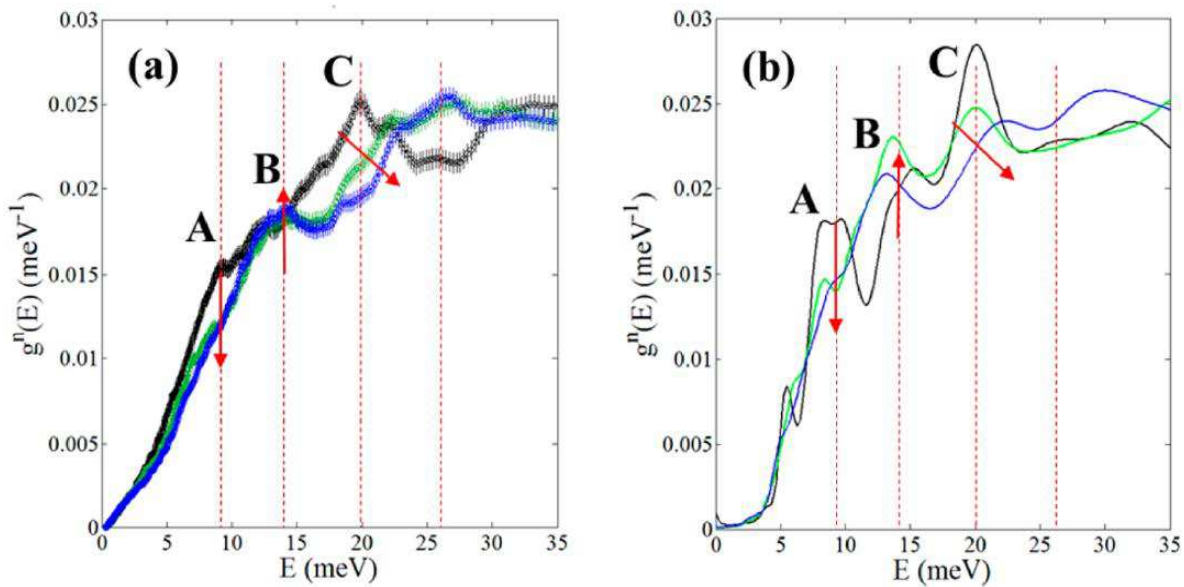


Figure 6.7 – (a) Generalized phonon density of states collected on the IN6 spectrometer of $\text{Nd}_2\text{NiO}_{4.0}$ (black), $\text{Nd}_2\text{NiO}_{4.10}$ (green), and $\text{Nd}_2\text{NiO}_{4.25}$ (blue) at $T=310\text{K}$. (b) Vibrational density of states calculated from *ab initio* molecular dynamics; same color legend as (a). As a guide for the eyes, the increase, decrease and shift of the main features are marked with red arrows.

Through this section we have shown that both the *ab initio* DFT calculations and molecular dynamic calculations we performed lead to results in good agreement with experimental data, matching measured densities of states for all temperatures and stoichiometries and reproducing temperature-dependant features.

6.4. Analogy with RAMAN spectra

We have shown in the previous sections that vibrational densities of states calculated from the molecular dynamics simulations of $\text{Nd}_2\text{NiO}_{4.0}$, $\text{Nd}_2\text{NiO}_{4.10}$ and $\text{Nd}_2\text{NiO}_{4.25}$ are in good agreement with experimental data. We have also shown in **chapter 5** that the phonon modes contributing to the mobility of the apical oxygen atoms toward interstitial sites, and thus enhancing the diffusion, have an energy below $E=15\text{meV}$, and are located at the Γ point and along the $\mathbf{M}(\frac{1}{2} \frac{1}{2} 0)$ direction.

To provide further proof of the validity of our calculations, we performed RAMAN spectroscopy experiments on powders of $\text{Nd}_2\text{NiO}_{4.0}$ and $\text{Nd}_2\text{NiO}_{4.25}$. While the neutron inelastic spectroscopy is the most powerful method to probe the low-lying phonon modes standing away from the Γ point, the RAMAN spectroscopy allows measuring accurately the inelastic spectra at the Γ point. Furthermore, due to the selection rules inherent to RAMAN spectroscopy, only a few phonon modes are observable, which make the analysis easier than of neutron data. We used a Microspectrometer LabRAM ARAMIS, with a HeNe laser of wavelength $\lambda=633\text{nm}$.

The RAMAN spectra of $\text{Nd}_2\text{NiO}_{4.0}$ and $\text{Nd}_2\text{NiO}_{4.25}$ powders, measured at room-temperature, are shown in **Figure 6.8**. We clearly observe that the spectrum of $\text{Nd}_2\text{NiO}_{4.25}$ shows broader and less intense peaks than the $\text{Nd}_2\text{NiO}_{4.0}$ spectra, which is due to structural disorder at a local range. This observation is consistent with the simple analysis performed in **section 6.2.2**: the presence of excess oxygen atoms in interstitial sites strain its surroundings.

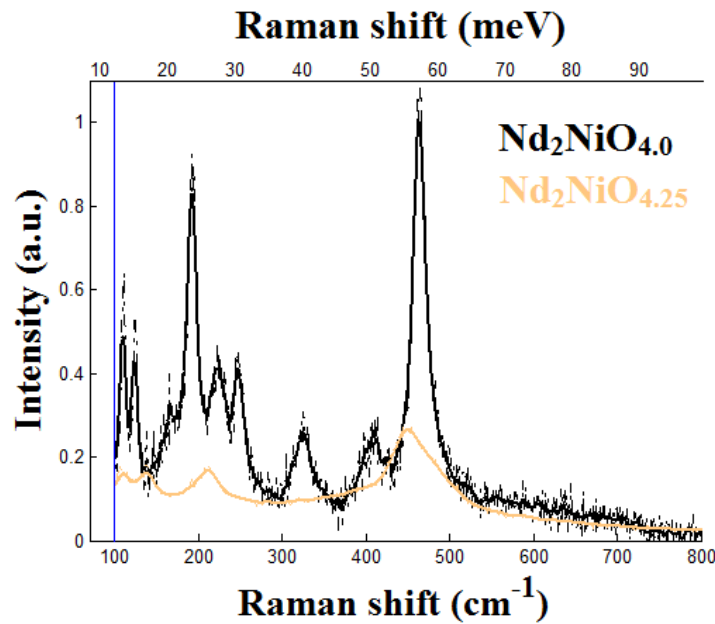


Figure 6.8 – RAMAN spectra of $\text{Nd}_2\text{NiO}_{4.0}$ (black) and $\text{Nd}_2\text{NiO}_{4.25}$ (red). Spectra at lower energy than the blue line are contaminated by the filter and removed.

In **Figure 6.9** we follow the dependance with temperature of the RAMAN spectra of the $\text{Nd}_2\text{NiO}_{4.0}$ powder. The experimental setup being restricted to a closed furnace in air atmosphere, the surface of the powder is quickly oxydizing, and after cooling down the spectrum is similar to the $\text{Nd}_2\text{NiO}_{4.25}$ spectrum shown in **Figure 6.8**.

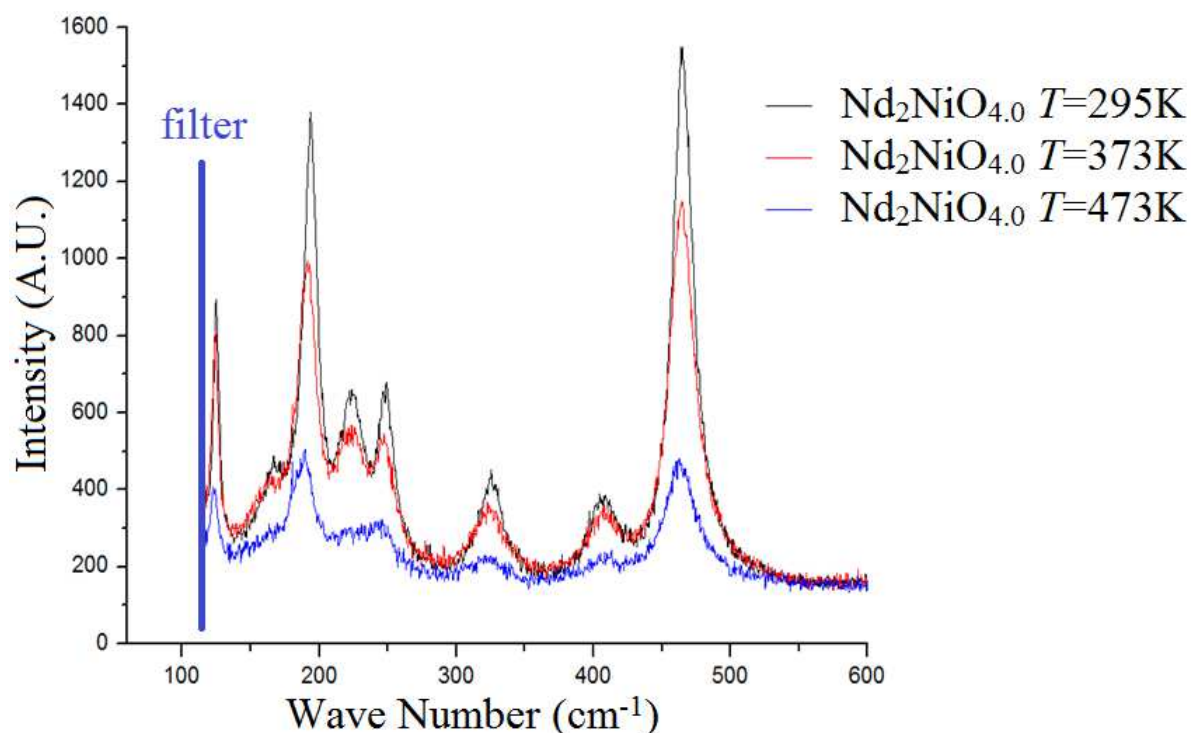


Figure 6.9 – RAMAN spectra of $\text{Nd}_2\text{NiO}_{4.0}$ at $T=295\text{K}$ (black), $T=373\text{K}$ (red) and $T=473\text{K}$ (blue). After cooling, the spectrum is similar to the $\text{Nd}_2\text{NiO}_{4.25}$ spectra: the surface of the powder is quickly oxidizing with temperature.

While the informations available from our RAMAN spectroscopy experiments are restricted compared to those from neutron inelastic scattering – the spectrum is restricted to the surface of the sample, the sample environnement was not fully controllable, the spectrum is limited to the Γ point and, due to the filter, only modes above $E \approx 120\text{cm}^{-1} \approx 15\text{meV}$ can be measured – yet all the RAMAN peaks can be identified and are matched by our DFT calculations.

6.5. Conclusion

We performed neutron time-of-flight spectroscopy experiments on powder of $\text{Nd}_2\text{NiO}_{4.0}$, $\text{Nd}_2\text{NiO}_{4.10}$ and $\text{Nd}_2\text{NiO}_{4.25}$.

We observed two distinct behavior of excess oxygen atoms depending on the temperature range. At high-temperature, the generalized densities of states do not depend on the excess oxygen content, meaning that the excess oxygen atoms behave as point defect of the Nd_2NiO_4 lattice. Meanwhile, at low-temperature, gDOS are showing differences depending the excess oxygen content, meaning that the excess oxygen atoms contribute to the coherent dynamics of the system. We also confirmed that increasing the amount of excess oxygen will shift the dynamics of modes polarized along [100] to [110], while the modes along [001] remains unaffected, as predicted in our calculations.

Comparing the measured and calculated gDOS, we confirmed the accuracy of our molecular dynamics calculations and the approximations of the structural models of $\text{Nd}_2\text{NiO}_{4.0}$, $\text{Nd}_2\text{NiO}_{4.10}$ and $\text{Nd}_2\text{NiO}_{4.25}$. Analogy with spectra from RAMAN scattering further confirmed the results from neutron TOF spectroscopy and DFT simulations.

6.6. Bibliography

1. Squires, G.L. *Introduction to the Theory of Thermal Neutron Scattering*.

Chapter 7. INS-TAS.

Lattice dynamics on Nd₂NiO_{4.25} single-crystal.

We have seen in **chapter 6** the lattice dynamics of the Nd₂NiO_{4.0}, Nd₂NiO_{4.10} and Nd₂NiO_{4.25} powders, and shown the effects of excess oxygen content and temperature. In **chapter 7**, we will investigate the lattice dynamics of an as-grown Nd₂NiO_{4.25} single-crystal, which allows the measurement of phonon modes at specific high-symmetry **Q** value of the Brillouin zone, evaluate their longitudinal or transverse polarization, and estimate dispersion curves. As described in **chapter 5**, we performed phonon calculations on the Nd₂NiO_{4.0} system and highlighted the phonon modes involved with the easy mobility of oxygen oxide ions. While we were unable to perform phonon calculations on non-stoichiometric Nd₂NiO_{4+d}, we have seen the effects of excess oxygen through analysis of molecular dynamics trajectories, which have been confirmed by time-of-flight inelastic neutron experiments. In **section 7.1**, we are thus comparing experimental dispersion curves of twinned Nd₂NiO_{4.25} single-crystal, with phonon calculations on the Nd₂NiO_{4.0} model, showing the agreements and limits of the approach. Since we have shown that the lattice dynamics calculated from molecular dynamics simulations show a good agreement with experimental measurements, even for non-stoichiometric models, in **section 7.2** we will further process the molecular dynamics to calculate the dynamic structure factors at specific **Q**-values in function of energy and compare them with their experimental counterparts. At last, in **section 7.3**, we will conclude on the lattice dynamics of the Nd₂NiO_{4.25} system.

7.1. Dispersion curves of Nd₂NiO_{4.25} measured on the IN8 spectrometer

The thermal neutron three-axis spectrometer (TAS) IN8, as well as the Flatcone analyser, have been presented in **chapter 3**. As described in **chapter 3** and precised in **chapter 4**, single-crystals of Nd₂NiO_{4.25}, other than the incommensurability, show pseudo-merohedral twinning. Due to the size of a crystal suitable for TAS experiments – the one we use is a 20mm long cylinder with 6.5mm diameter – and the huge ellipsoid resolution of a three-axis spectrometer compared to diffractometer, we cannot differentiate the dynamics of a twin domain from another. Thus instead of using the cell parameters of a twin, we used average cell parameters with $a=b=5.42\text{\AA}$ and $c=12.36\text{\AA}$, with respect to the average F-cell. This also means that, except from slight intensity differences due to weighting from the twin distribution, the **X**($\xi 0 0$) and **Y**($0 \xi 0$) directions are equivalent. We investigated two orientations of the crystal : the first with the [110] and [001] axis in the scattering plane, and the second with the [100] and [010] axis in the scattering plane. This gave access to the **X**($\xi 0 0$)=**Y**($0 \xi 0$), **M**($\xi \xi 0$) and **Z**($0 0 \xi$) directions in both longitudinal and transverse setup.

Many three-axis spectroscopy experiments have been performed on related $\text{Re}_2\text{MO}_{4+d}$ systems^[1-8]. The majority of them dealt with superconductors and magnetism, and these experiments investigate the high energy transfer ΔE or the low momentum transfer $\Delta \mathbf{q}$ regions. On the contrary, as shown in **chapter 5** and **chapter 6**, we are investigating the phonon dynamics which contribute to oxygen mobility and, as such, we are focused on the low energy transfer ΔE and high momentum transfer $\Delta \mathbf{q}$ region.

Experimental points of the dispersion curves of the $\text{Nd}_2\text{NiO}_{4.25}$ crystal, from fit of spectra measured on IN8, are shown in **Figure 7.1**, along with theoretical dispersion curves calculated for the $\text{Nd}_2\text{NiO}_{4.0}$ system (black lines). On this superimposed representation, we only consider the \mathbf{q} vector (disregarding for now the \mathbf{Q} value) – with in red data points measured in a longitudinal setup, in blue in transverse setup, and in green with an hybrid setup where both longitudinal and transverse phonon are measurable. Spectrometer geometries to measure longitudinal and transverse contributions are shown in **chapter 3**.

We observe that, in the $\mathbf{Z}(00\xi)$ direction, the data points measured on the $\text{Nd}_2\text{NiO}_{4.25}$ crystal follow the calculated dispersion curve of $\text{Nd}_2\text{NiO}_{4.0}$, and that the phonon width is limited by the instrumental resolution. We can thus conclude that the excess oxygen content has only minor or negligible effects on the low-energy lattice dynamics along the stacking-axis direction. However, when considering the $\mathbf{X}(\xi 00)=\mathbf{Y}(0\xi 0)$ and $\mathbf{M}(\xi\xi 0)$ directions, phonon calculations do not properly describe experimental dispersion curves: too many phonon modes are calculated due to the reduce symmetry of the $\text{Nd}_2\text{NiO}_{4.0}$ structural model compared to the average lattice of $\text{Nd}_2\text{NiO}_{4.25}$ and, as shown in **chapter 6**, excess oxygen atoms are strongly impacting the dynamics in the (ab) plane. Yet, the experimental acoustic modes are steeper than calculated – which means that the excess oxygen in interstitial sites stiffen the lattice. Moreover phonon modes at zone boundaries, and low-energy optical phonons in general, show a width much larger than the instrumental resolution. Such increase of phonon widths may have two explanations, both linked to the effects of excess oxygen on the lattice: (1) the width may be of dynamical origin, coming from a short lifetime of associated phonons due to the presence of excess oxygen atoms, seen as defects by the lattice; (2) the width may be of statistic origin, and represent a distribution of many splitted phonon modes due to heterogeneous local environments constituted by the distribution of excess oxygen atoms on the lattice. While these two explanations are both experimentally supported, we have shown in **chapter 5** that calculated potential wells of atoms close to excess oxygen are anharmonic, which support the dynamical (1) explanation of the origin of phonon width.

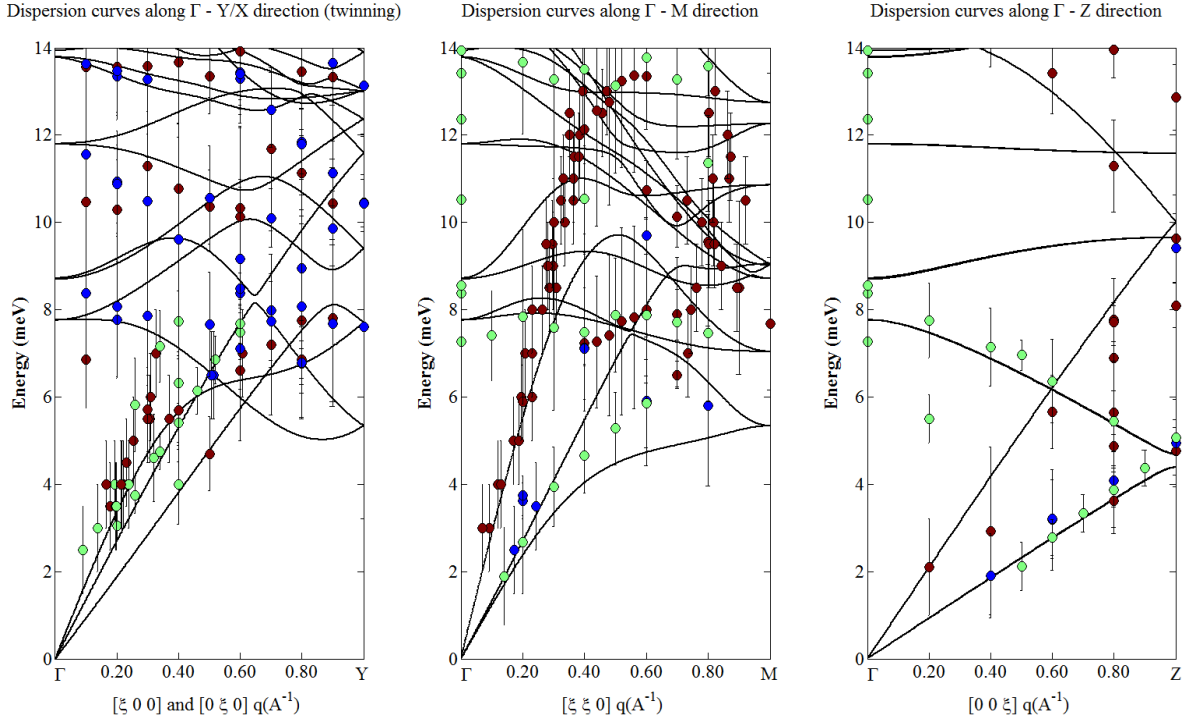


Figure 7.1 – Superimposed dispersion curves measured on IN8 of the $\text{Nd}_2\text{NiO}_{4.25}$ crystal, in the $\mathbf{X}(\xi 0 0)=\mathbf{Y}(0 \xi 0)$, $\mathbf{M}(\xi \xi 0)$ and $\mathbf{Z}(0 0 \xi)$ directions. In this figure only the relative position \mathbf{q} in the Brillouin zone is considered, not the absolute position $\mathbf{Q}+\mathbf{q}$. Data points are fitted from the IN8 spectra, with in red data collected in longitudinal setup, in blue in transverse setup, and in green in hybrid setup where both the longitudinal and the transverse contribution is measurable. Error bars represent the fitted width of phonons. Black lines represent the theoretical dispersion curves of $\text{Nd}_2\text{NiO}_{4.0}$, as calculated in **chapter 5**.

In order to get a more explicit representation of the experimental data, they can be plot directly as intensity colormaps of the IN8 spectra, as shown in **Figure 7.2** for measurements in transverse configuration of the $\mathbf{X}(\xi 0 0)$ direction at the (140) Brillouin zone, along with fitted points and calculated $S(\mathbf{q}, \omega)$. At $\mathbf{X}(0.5 \ 0 \ 0)$, the intense mode at $\Delta E=10\text{meV}$ is the acoustic mode coming from the (040) Brillouin zone center, while the mode at $\Delta E=13\text{meV}$ is an optic mode. Other than these two modes and the $\Delta E=12\text{meV}$ mode at Γ , we observed weak flat optic phonon modes at $\Delta E=7\text{-}8\text{meV}$. Their behavior will be discussed in detail in **section 7.2**. We also observed some weak intensity below $\Delta E=2\text{meV}$ and some constant background up to $\Delta E=15\text{meV}$. These weak contributions are observed for $\mathbf{X}(\xi 0 0)=\mathbf{Y}(0 \xi 0)$ and $\mathbf{M}(\xi \xi 0)$ directions in every measured Brillouin zone, as shown for scans around Brillouin zones (400) and (220) in **Figure 7.3**.

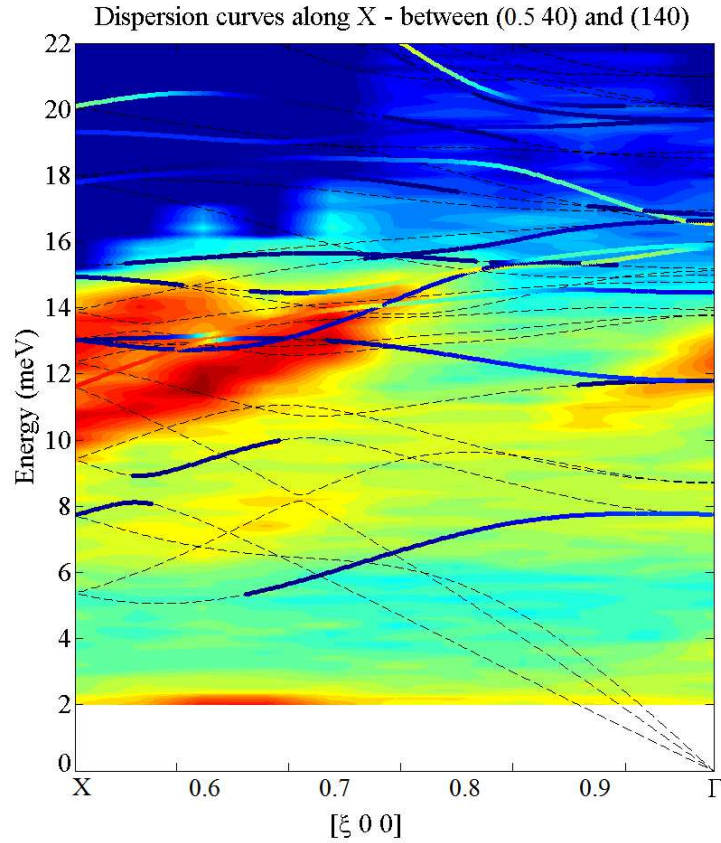


Figure 7.2 – Colormap in logarithmic scale from a composition of IN8 spectra: measurement of the $X(\xi 00)$ direction in transverse configuration of the (140) Brillouin zone at $T=50K$. Dotted lines correspond to calculated dispersion curve; full colored lines correspond to calculated $S(\mathbf{Q}, \omega)$.

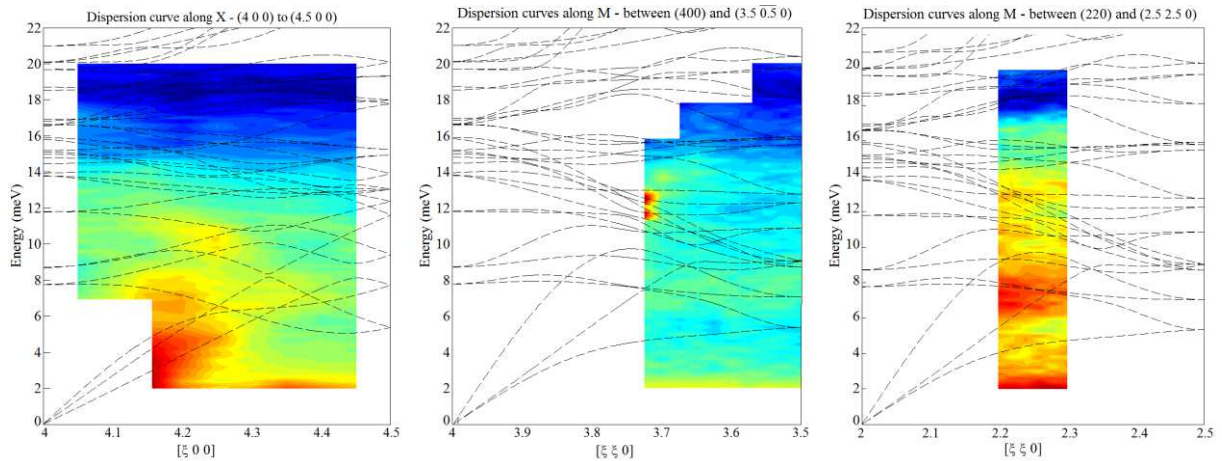


Figure 7.3 – Colormap in logarithmic scale from a composition of IN8 spectra: measurement of the $X(\xi 00)$ direction in longitudinal configuration of the (400) Brillouin zone (left); measurement of the $M(\xi \xi 0)$ direction in hybrid configuration of the (400) Brillouin zone (center); measurement of the $M(\xi \xi 0)$ direction in longitudinal configuration of the (220) Brillouin zone (right). Dotted lines correspond to calculated dispersion curves.

Incommensurate phases are predicted to have specific dynamics associated with the loss of translational symmetry. In the case of small incommensurable distortions with respect to the high-symmetry phase, the extra dynamics can be described in terms of phase mode (often called phason) and amplitude mode^[9, 10]. In particular, the phase mode has an acoustic-like dispersion, centered on the \mathbf{q} -values associated with the incommensurate modulation: as acoustic phonons emerges from Bragg peaks, phasons emerges from satellites. We have measured inelastic signal along a satellite line, as shown in **Figure 7.4**. High-intensity lines in the range $\Delta E=0.5-1\text{meV}$ are due to the resolution ellipsoid touching the elastic satellites. We found no evidences of the presence of phase modes.

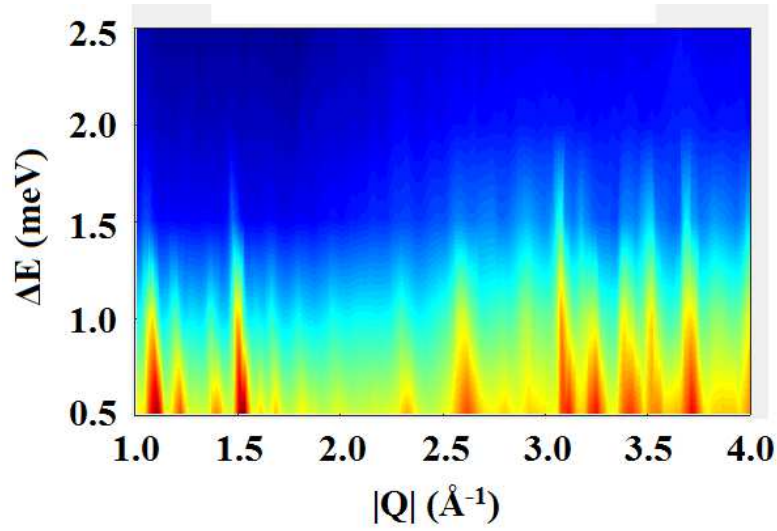


Figure 7.4 – Colormap in logarithmic scale of inelastic spectra measured along a satellite line using IN8 with Flatcone. High-intensity lines are due to the resolution ellipsoid touching the elastic satellites.

7.2. Comparison of phonon modes with dynamic structure factors from MD

As seen in **section 7.1**, except for the $\mathbf{Z}(00\xi)$ direction, the low part of acoustic modes and a few optic modes, theoretical dispersion curves calculated on the $\text{Nd}_2\text{NiO}_{4.0}$ system do not accurately match the phonon modes measured experimentally on a single-crystal of $\text{Nd}_2\text{NiO}_{4.25}$. This was also the outcome of the time-of-flight spectroscopy experiments, showing that the excess oxygen atoms in interstitial sites strongly impact the low-energy part of the lattice dynamics at low- and room-temperature. However, even if the agreement is not perfect, and since the calculations do match the most intense phonon modes – *i.e.* phonon modes from the average lattice – and the $\mathbf{Z}(00\xi)$ direction, we can ascertain the validity of the phonon analysis performed in **chapter 5**, and state that the excess oxygen atoms impact mainly the lattice dynamics in the $\mathbf{X}(\xi 00)=\mathbf{Y}(0\xi 0)$ and $\mathbf{M}(\xi\xi 0)$ directions. Furthermore, while the phonon modes may be shifted in energy, broaden or damped, we do know from the eigenvector analysis that, for example, the low-energy optic modes around $\Delta E=8\text{meV}$ are mostly sliding motions in the (ab) plane, and concern the neodymium and apical oxygen atoms.

In order to perform a more precise analysis of the IN8 spectra, and since we have shown in **chapter 6** the good agreement of molecular dynamic calculations with experimental results from time-of-flight spectroscopy, we further processed the molecular dynamics to calculate the dynamic structure factors $S(\mathbf{q},\omega)$ for the available \mathbf{q} -values, as detailed in **chapter 3**. The number of available \mathbf{q} -value is limited by the size of the supercell – and for a $2 \times 2 \times 1$ supercell of the F-cell we used, only the Γ points and the zone boundaries $\mathbf{X}(\frac{1}{2} 0 0)=\mathbf{Y}(0 \frac{1}{2} 0)$ and $\mathbf{M}(\frac{1}{2} \frac{1}{2} 0)$ can be calculated. The dynamic structure factors from molecular dynamics have the advantage of being independent of any approximation on the shape of the potential. Indeed, the potential of an atom does not have to be harmonic since the dynamic structure factor is calculated directly from the velocity auto-correlation function.

As shown in **Figure 7.5** (left) for an energy scan at $\mathbf{Q}(0.5 \ 4 \ 0)$, and for most of the measurements on the $\text{Nd}_2\text{NiO}_{4.25}$ single-crystal, the spectrum can be fitted with a pseudo-voigt function for the incoherent, simple gaussian functions for phonon modes and a wide gaussian function – almost overdamped – for the flat optic band centered at $\Delta E=8\text{meV}$. On the right side on **Figure 7.5** are presented the coherent and incoherent dynamic structure factors calculated from the molecular dynamics. We remark that reciprocal lattices of the crystal and of the structural model used in molecular dynamics have different size and orientation, and that we performed an averaging of calculated $S(\mathbf{Q},\omega)$ for symmetry equivalent \mathbf{Q} vectors. Looking at the coherent dynamic structure factor (blue line), we can see that a strong phonon mode is calculated at $\Delta E=12\text{meV}$ instead of the two modes measured experimentally at $\Delta E=11\text{meV}$ and $\Delta E=13\text{meV}$. Interestingly, the incoherent dynamic structure factor (orange line), besides the expected contribution at $\Delta E=0$, shows a broad inelastic signal centered at about $\Delta E=8\text{meV}$. Comparing spectral weights, we observe that the coherent contribution is overestimated in the calculation. Effects associated with the incoherent are thus more pronounced in the real crystal than in our structural model. Now, apart the lack of ‘splitting’ of the $\Delta E=12\text{meV}$ phonon, we can see that the sum of the calculated coherent and incoherent dynamic structure factor (gray line) is similar to the experimental spectra.

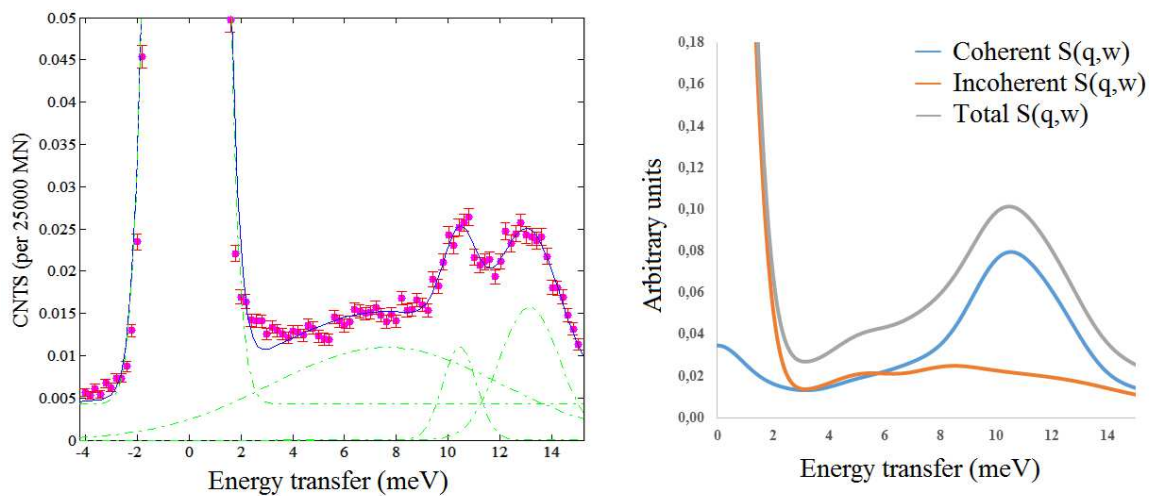


Figure 7.5 – (left) Energy scan at $\mathbf{Q}(0.5 \ 4 \ 0)$ of $\text{Nd}_2\text{NiO}_{4.25}$, measured at $T=50\text{K}$ on IN8. (right) Coherent, incoherent and total dynamic structure factors calculated from molecular dynamics simulation of $\text{Nd}_2\text{NiO}_{4.25}$ at $\mathbf{Q}(0.5 \ 4 \ 0)$ at $T=310\text{K}$. $S(\mathbf{Q},\omega)$ are convoluted with a 2meV wide gaussian function to take account of the experimental resolution.

While using a wide single gaussian function is the most simple approximation to fit the flat optic band for most scans, and especially at zone boundaries, the exception is the Γ point where the use of multiple gaussian functions is necessary, as shown in **Figure 7.6** for an energy scan at $\mathbf{Q}(4\ 0\ 0)$. Looking at the dynamic structure factors, we observe that we indeed find the strong $\Delta E=0$ coherent contribution corresponding to the elastic Bragg peak, yet only weak coherent inelastic signal. The incoherent inelastic contribution is preponderant in the $\Delta E=4-15\text{meV}$ region. We note that, besides discrepancy of intensities, the total dynamic structure factor is in good agreement with the experimental spectrum.

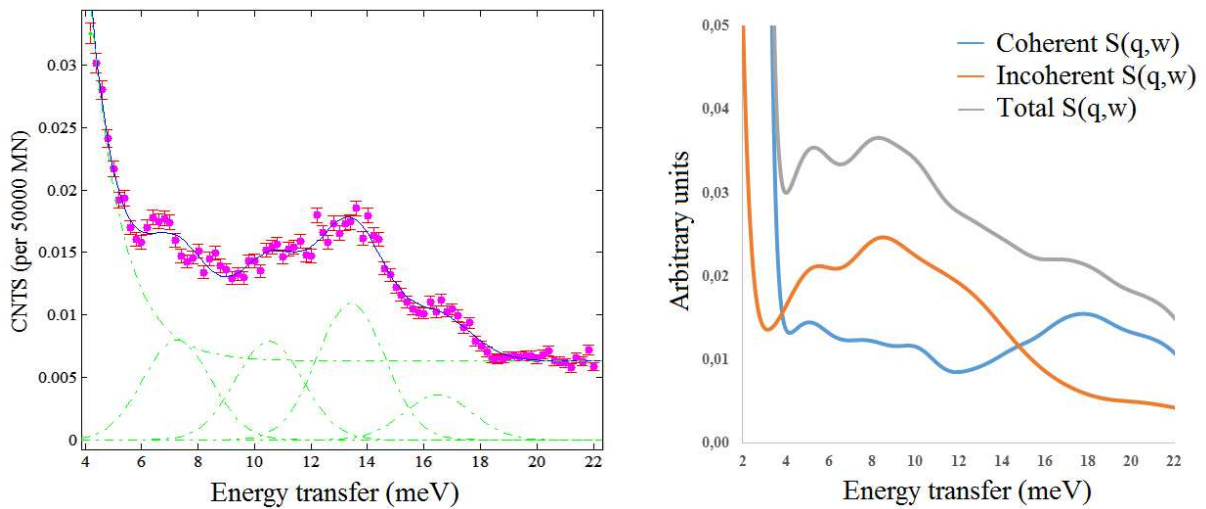


Figure 7.6 – (left) Energy scan at $\mathbf{Q}(4\ 0\ 0)$ of $\text{Nd}_2\text{NiO}_{4.25}$, measured at $T=50\text{K}$ on IN8. (right) Coherent, incoherent and total dynamic structure factor calculated from molecular dynamics simulation of $\text{Nd}_2\text{NiO}_{4.25}$ at $\mathbf{Q}(4\ 0\ 0)$ at $T=310\text{K}$. $S(\mathbf{Q},\omega)$ are convoluted with a 2meV wide gaussian function to take account of the experimental resolution. We note that, due to the Bragg peak at (400) and the resolution effect, the coherent contribution appears larger than the incoherent one below $\Delta E=4\text{meV}$.

These two comparisons of experimental spectra with calculated dynamic structure factors have shown that, apart small discrepancies of the shape and intensity of the calculated spectral weights, calculations are in good qualitative agreement with the measurements. It also shows that the inelastic incoherent contribution is far from neglectible in the high- \mathbf{q} low-energy region. Physically, the incoherent inelastic contribution represents the correlation of a single nucleus position with time, *i.e.* time-correlation of single-particle-like motions. In **Figure 7.7** are shown the partial incoherent dynamic structure factors of the oxygen, nickel and neodymium atoms, without the weighting by the incoherent cross-section and the mass. We remark that the partial incoherent structure of the oxygen, without the weighting, is significant. However, the inelastic cross-section of the oxygen is $\sigma_{\text{inc}}=0.000(8)$ barn, which means that once weighted, its contribution to the total incoherent dynamic structure factor is null. As such, the incoherent dynamic structure factor is dominated by the neodymium contribution.

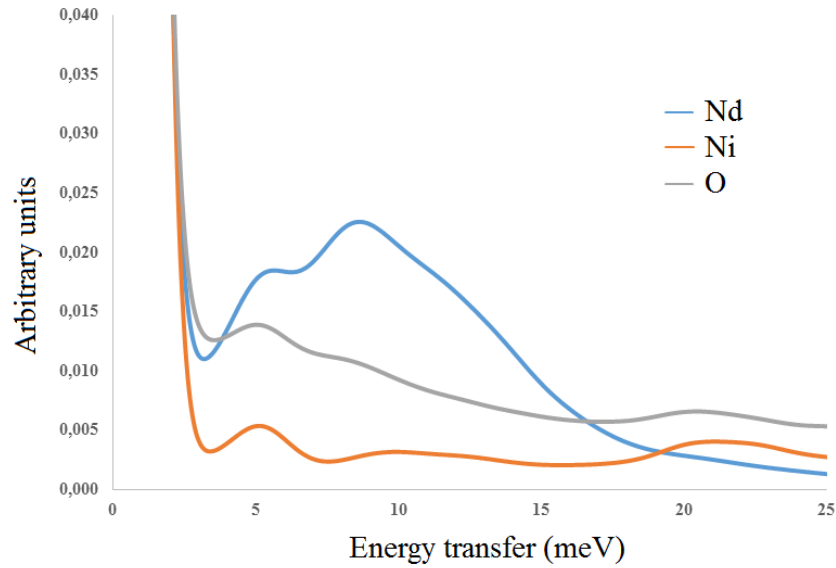


Figure 7.7 – Partial incoherent dynamic structure factor at $\mathbf{Q}(2.5\ 2\ 0)$ of the neodymium, nickel and oxygen atoms, without weighting by the incoherent cross-section and the mass, calculated from a molecular dynamics simulations of $\text{Nd}_2\text{NiO}_{4.25}$ at $T=310\text{K}$. $S_{inc}(\mathbf{Q},\omega)$ are convoluted with a 2meV wide gaussian function to take account of the experimental resolution.

If we look at the incoherent dynamic structure factor of the $\text{Nd}_2\text{NiO}_{4.0}$ molecular dynamics, as shown in **Figure 7.8**, we do not observe any incoherent inelastic contribution. The presence of excess oxygen is thus necessary to promote the single-particle incoherent motion.

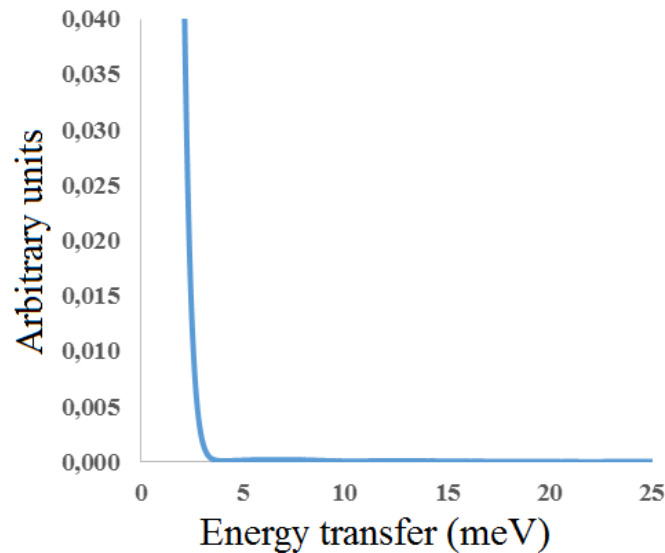


Figure 7.8 - Incoherent dynamic structure factor at $\mathbf{Q}(1.5\ 1.5\ 0)$ with respect to the F -cell for $\text{Nd}_2\text{NiO}_{4.0}$, calculated from molecular dynamics simulation at $T=310\text{K}$. $S_{inc}(\mathbf{Q},\omega)$ is convoluted with a 2meV wide gaussian function to take account of the experimental resolution.

Since the incoherent scattering physically represents the time-correlation of a single nucleus, which cannot generate interference phenomenon, its inelastic structure is independent of \mathbf{q} . If the calculated incoherent dynamic structure factor is valid, it would appear on every energy scan as a broad signal centered at $\Delta E=8\text{meV}$ with tails going up to $\Delta E=14\text{-}17\text{meV}$ depending on the background value. This is indeed what experimentally has been observed.

We do know from the eigenvector analysis that the $\Delta E=8\text{meV}$ phonon modes, at zone boundaries, are sliding motions involving mainly the neodymium and apical oxygen atoms in the rock-salt layer. We have shown that the low-energy optic phonon modes have a finite width, and thus a limited lifetime, or are a statistic distribution of nearly degenerate modes. We have also shown from the incoherent dynamic structure factor that the neodymium atoms – and the apical oxygen atoms, yet with no incoherent contribution with neutron due to their incoherent cross-section – have a single-particle motion in the (ab) plan which require an energy of about $\Delta E=8\text{meV}$, at the \mathbf{Q} values where the coherent optic phonon mode is active. We have two types of motions, a coherent sliding and an incoherent single-particle motion, with similar energy requirements, with similar momentum transfer, and involving the same atomic species, thus with similar amplitude of atomic displacements. This has a direct impact on the $\Delta E=8\text{meV}$ phonon mode, which propagates in a slightly disordered environment: waves forming the phonon wave-packet are quickly dephased, hence the limited lifetime of the phonon and its associated finite width. Furthermore, the effective atomic displacement induced by the phonon mode is modulated by the instantaneous deviation in atomic position induced by the single-particle motion. On an atomic site, if displacement vectors of the phonon and of the single-particle motion are opposed, the effective displacement of the atom would be about null. *A contrario*, if displacement vectors are in the same direction, the effective displacement would be about doubled. This effect is of fundamental importance to understand oxygen diffusion at moderate-temperature. Conceptually, if the single-particle motion could be described as an oscillator with a phase, there would be localized ‘addition’ between the phonon displacement vector and the single-particle motion amplitude, with ‘in-phase’ states that would locally strongly enhance the sliding motion, and ‘out-of-phase’ states that would nullify it.

Another interesting point of discussion comes from the comparison of calculated coherent dynamic structure factor from $\text{Nd}_2\text{NiO}_{4.25}$ and $\text{Nd}_2\text{NiO}_{4.0}$ molecular dynamics. As we discussed the incoherent part of scattering, the coherent part represents the time-correlation of several nuclei positions. As an example, the comparison at $\mathbf{Q}(-1.5\ 2.5\ 0)$ with respect to the F-cell is shown in **Figure 7.9**. We observe that, other than the shift in energy transfer and width, thus intensities, of the phonon modes, some of the spectral weight initially in the $\Delta E=8\text{meV}$ mode for $\text{Nd}_2\text{NiO}_{4.0}$ shifted to the elastic line for $\text{Nd}_2\text{NiO}_{4.25}$. This coherent quasi-elastic signal can be seen as a frozen phonon, *i.e.* a phonon which does not require energy to propagate, thus a structural modulation with an infinite lifetime, thus displacements with no recoil. This is another signature of the modification of the shape of potential energy wells induced by the excess oxygen atoms, from harmonic to anharmonic and shallow. We remark that such a weak coherent quasi-elastic contribution cannot be measured experimentally due to the strong incoherent elastic contribution.

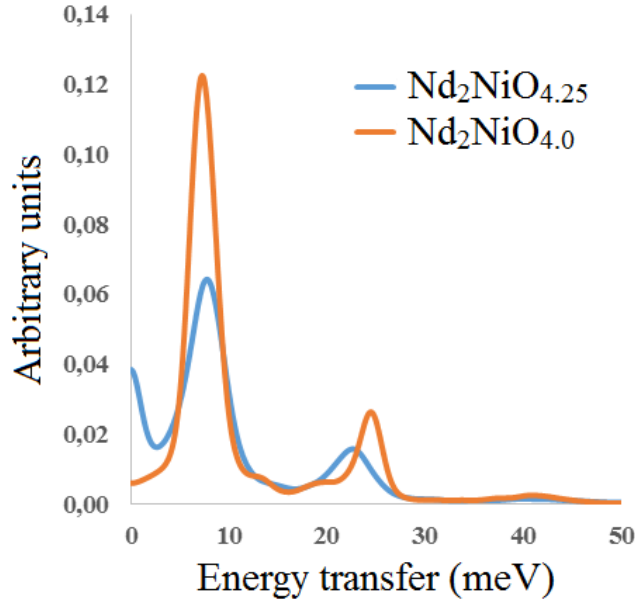


Figure 7.9 – Coherent dynamic structure factor at $\mathbf{Q}(-1.5 \ 2.5 \ 0)$ with respect to the F -cell for $\text{Nd}_2\text{NiO}_{4.25}$ (blue) and $\text{Nd}_2\text{NiO}_{4.0}$ (orange), calculated from molecular dynamics simulations at $T=310\text{K}$. $S_{\text{coh}}(\mathbf{Q},\omega)$ are convoluted with a 2meV wide gaussian function to take account of the experimental resolution.

7.3. Conclusion

In this chapter, we have shown the results of three-axis inelastic neutron scattering experiments on a single-crystal of $\text{Nd}_2\text{NiO}_{4.25}$. Comparing the experimental dispersion curves of $\text{Nd}_2\text{NiO}_{4.25}$ with phonon calculation of $\text{Nd}_2\text{NiO}_{4.0}$, we first observed that the calculations can only properly describe the $\mathbf{Z}(00\xi)$ direction and the acoustic regime in the $\mathbf{X}(\xi 00)$ and $\mathbf{M}(\xi\xi 0)$ directions of the Brillouin zone, *i.e.* where excess oxygen atoms have the least impact on the lattice dynamics of Nd_2NiO_4 .

We observed an overall stiffening of the lattice dynamics of $\text{Nd}_2\text{NiO}_{4.25}$ compared to $\text{Nd}_2\text{NiO}_{4.0}$. We also found low-lying optic phonon modes to be broader than the experimental resolution, which suggest a limited lifetime of the excitation or a distribution of quasi-degenerate modes. Furthermore, an unexpected non-dispersive signature was observed, for energy transfer $\Delta E=6-8\text{meV}$, with no dependence in momentum transfer, that we attributed to inelastic incoherent scattering.

We calculated neutron structure factors $S(\mathbf{Q},\omega)$ at high-symmetry points of the Brillouin zone from molecular dynamics trajectories, which shown a good agreement with experimental spectra. In particular, a non-trivial incoherent inelastic contribution was predicted, associated with single-particle motions of neodymium and apical oxygen atoms. This incoherent

contribution is found at similar frequencies than the measured broad optic phonon modes, which are themselves associated with coherent sliding motions of neodymium and apical oxygen atoms in phonon calculation. We also calculated that this incoherent contribution is several order of magnitude lower for stoichiometric $\text{Nd}_2\text{NiO}_{4.0}$, thus that associated single-particle motions are dependent on the presence of excess oxygen atoms.

Such results suggest that overall sliding motions, in particular of apical oxygen atoms, can be dissociated into a lattice-correlated coherent contribution and a single-particle incoherent contribution; a favorable combination of the two would locally enhance the amplitude of the atomic motion, thus eventually promoting an apical oxygen atom towards a vacant interstitial site.

7.4. Bibliography

1. McQueeney, R.J., Petrov, Y., Egami, T., Yethiraj, M., Shirane, G., and Endoh, Y. (1999). *Physical Review Letters*, 82(3), 628-631.
2. Park, S.R., Hamann, A., Pintschovius, L., Lamago, D., Khaliullin, G., Fujita, M., Yamada, K., Gu, G.D., Tranquada, J.M., and Reznik, D. (2011). *Physical Review B*, 84(21), 214516.
3. Pintschovius, L. and Braden, M. (1999). *Physical Review B*, 60(22), R15039-R15042.
4. Reznik, D., Pintschovius, L., Fujita, M., Yamada, K., Gu, G.D., and Tranquada, J.M. (2007). *Journal of Low Temperature Physics*, 147(3-4), 353-364.
5. Reznik, D., Pintschovius, L., Ito, M., Iikubo, S., Sato, M., Goka, H., Fujita, M., Yamada, K., Gu, G.D., and Tranquada, J.M. (2006). *Nature*, 440(7088), 1170-1173.
6. Tranquada, J.M., Nakajima, K., Braden, M., Pintschovius, L., and McQueeney, R.J. (2002). *Physical Review Letters*, 88(7), 075505.
7. Pintschovius, L., Bassat, J.M., Odier, P., Gervais, F., Chevrier, G., Reichardt, W., and Gompf, F. (1989). *Physical Review B*, 40(4), 2229-2238.
8. Pintschovius, L., Reichardt, W., Braden, M., Dhalenne, G., and Revcolevschi, A. (2001). *Physical Review B*, 64(9), 094510.
9. Axe, J.D. (1980). *Phil. Trans. R. Soc. Lond. B*, 290(1043), 593-603.
10. Dorner, B. (1981). Investigation of Structural Phase Transformations by Inelastic Neutron Scattering. In K.A. Müller & H. Thomas (Eds.), *Structural Phase Transitions I* (pp. 118-130): Springer-Verlag.

Chapter 8. General conclusion.

The focus of this thesis have been the characterization of the effect of excess oxygen content on structures and, primarily, lattice dynamics of $\text{Nd}_2\text{NiO}_{4+d}$ phases, with the aim of finding correlations between specific low-lying dynamics and the non-classical oxygen mobility observed in the room- and moderate-temperature regimes. To do so, we have performed a synergetic study involving neutron and synchrotron X-rays single-crystal diffraction, first-principle phonon calculations and molecular dynamics, and inelastic neutron scattering on time-of-flight and three-axis spectrometers, on the three single-phases $\text{Nd}_2\text{NiO}_{4.0}$, $\text{Nd}_2\text{NiO}_{4.10}$ and $\text{Nd}_2\text{NiO}_{4.25}$ chosen as model structures for the $\text{Nd}_2\text{NiO}_{4+d}$ phases at room-temperature.

The structural characterization of $\text{Nd}_2\text{NiO}_{4.25}$ using neutron and synchrotron X-rays single-crystal diffraction, performed in **chapter 4**, yet remaining qualitative, provided evidences of three temperature regimes with respect to oxygen mobility. Below $T=370\text{K}$, in the low-temperature range, defective clusters surrounding excess oxygen atoms in interstitial sites are long-range ordered, which leads to a complex pattern of incommensurate satellites. The slight splitting of Bragg peaks in terms of θ and d_{hkl} value, only observed thanks to high-resolution synchrotron X-rays, suggests the presence of two phases with minor differences in oxygen hyper-stoichiometry. In the moderate-temperature range, from $T=420\text{K}$ to $T=820\text{K}$, while the main incommensurate modulation remains, Bragg peaks splitting and some satellites are disappearing, which suggest that excess oxygen atoms are homogeneously distributed in the crystal, and thus imply an increase in oxygen mobility. The incommensurate modulation lasts up to $T=820\text{--}870\text{K}$, at which temperature a phase transition from average orthorhombic $Fmmm$ to high-temperature tetragonal $F4/mmm$ is observed. In the high-temperature regime, above $T=870\text{K}$, and to a lesser extent in the moderate-temperature range, diffuse scattering is observed around Bragg peaks in the $(hh0)$ -type directions, and is a direct signature of oxygen diffusion along the $(hh0)$ channels in the rock-salt layer, which is in agreement with the interstitialcy mechanism of oxygen diffusion proposed for high-temperature phases of $\text{RE}_2\text{MO}_{4+d}$. Concerning the moderate-temperature regime, the main result is the coexistence of long-range ordering of interstitial oxygen atoms and associated defective clusters, and noticeable oxygen mobility: two behaviors that are intuitively antagonist.

As described in **chapter 5**, we have performed extensive *ab initio* phonon calculations and molecular dynamics on $\text{Nd}_2\text{NiO}_{4.0}$, $\text{Nd}_2\text{NiO}_{4.125}$ as an approximation of $\text{Nd}_2\text{NiO}_{4.10}$, and $\text{Nd}_2\text{NiO}_{4.25}$. We calculated lattice dynamics and phonon eigenvectors, *i.e.* atomic displacements associated with phonon modes, on the low-temperature phase of $\text{Nd}_2\text{NiO}_{4.0}$, and evidenced several low-energy modes involving displacements of apical oxygen atoms towards the diffusion pathway. While this calculation does not accurately describe the room-temperature dynamics of non-stoichiometric $\text{Nd}_2\text{NiO}_{4+d}$ phases, it allowed us to identify the low-energy dynamic signatures observed in the inelastic neutron scattering experiments, especially modes involving tilting motions of NiO_6 octahedra and sliding motions of apical

oxygen atoms. In order to attain a better description of the room-temperature dynamics of $\text{Nd}_2\text{NiO}_{4+d}$ phases, we performed *ab initio* molecular dynamics for temperatures ranging from $T=150\text{K}$ to $T=1070\text{K}$, on structural models based on low-temperature structures of $\text{Nd}_2\text{NiO}_{4.0}$, $\text{Nd}_2\text{NiO}_{4.125}$ and $\text{Nd}_2\text{NiO}_{4.25}$. We evidenced that the presence of excess oxygen atoms in interstitial sites is necessary to observe diffusion events, and that the moderate-temperature diffusion pathway is similar to the one described by the interstitialcy mechanism for $\text{RE}_2\text{MO}_{4+d}$ phases at high-temperature: a two-step push-pull diffusion process involving both apical and interstitial oxygen atoms, on a [110] oriented pathway bridging apical and interstitial oxygen sites. Besides the diffusing behavior of oxygen atoms, we calculated vibrational densities of states and neutron structure factors $S(\mathbf{Q},\omega)$ from molecular dynamics trajectories, that have shown good agreement with measures of inelastic neutron experiments. At last, we developed the ‘positional recurrence maps’ (PRM) code to post-process molecular dynamics trajectories, which allows to directly visualize the dynamical part of the nuclear densities of selected atoms. Through the PRM analysis, we have evidenced that the presence of interstitial oxygen atoms significantly modify the dynamics of apical oxygen atoms, shifting their main motion from the [100] to [110] direction, *i.e.* towards the diffusion pathway. Furthermore, the apical oxygen atoms have been found to be strongly delocalized, which means that even if our *ab initio* molecular dynamics calculations do not take into account the long-range structural correlations evidenced in diffraction, the shallow potential the apical oxygen atom sits in have been properly reproduced.

In order to provide experimental data of the lattice dynamics of $\text{Nd}_2\text{NiO}_{4+d}$ phases – and validate our calculations – we have performed time-of-flight neutron inelastic experiments to obtain generalized phonon densities of states of powders of $\text{Nd}_2\text{NiO}_{4.0}$, $\text{Nd}_2\text{NiO}_{4.10}$ and $\text{Nd}_2\text{NiO}_{4.25}$, for temperatures ranging from $T=150\text{K}$ to $T=1070\text{K}$, as described in **chapter 6**. We observed two distinct behavior related to excess oxygen atoms depending on the temperature range. At high-temperature, the generalized phonon densities of states (gDOS) do not depend on the excess oxygen content, which imply that excess oxygen atoms behave as point defect in the Nd_2NiO_4 lattice. Meanwhile, at low-temperature, gDOS are showing significant differences depending on the excess oxygen content, thus excess oxygen atoms contribute to the coherent dynamics of the system. The room-temperature scenario is basically an intermediate case between the high-temperature and the low-temperature behaviors: the excess oxygen content is still impacting the gDOS, yet to a lesser extent than at low-temperature. From comparison with calculated vibrational densities of states from molecular dynamics, and identification of modes with phonon calculation, we also confirmed that increasing the amount of excess oxygen atoms will shift the dynamics of modes polarized along [100] to [110]. Through the analysis of the dependence of generalized phonon densities of states with temperature and excess oxygen content, we have provided direct experimental evidences of the impact of excess oxygen atoms on lattice dynamics. We have shown that oxygen atoms involved in the diffusion process at moderate-temperature cannot be considered as point defects with single-particle dynamics, thus that the oxygen diffusion cannot be simply described by independent stochastic hopping events.

Taking a step further in the characterization of the lattice dynamics of $\text{Nd}_2\text{NiO}_{4+d}$ phases, we performed three-axis inelastic neutron scattering on a single-crystal of $\text{Nd}_2\text{NiO}_{4.25}$, in order to estimate dispersion curves and measure inelastic spectra at selected high-symmetry points of the Brillouin zone, as described in **chapter 7**. Comparing the experimental dispersion curves of $\text{Nd}_2\text{NiO}_{4.25}$ with phonon calculation of $\text{Nd}_2\text{NiO}_{4.0}$, we first observed that the calculations can only properly describe the $\mathbf{Z}(00\xi)$ direction and the acoustic regime in the $\mathbf{X}(\xi 00)$ and $\mathbf{M}(\xi\xi 0)$ directions of the Brillouin zone, *i.e.* where excess oxygen atoms have the least impact on the lattice dynamics of Nd_2NiO_4 . Yet we observed an overall stiffening of the lattice dynamics of $\text{Nd}_2\text{NiO}_{4.25}$ compared to $\text{Nd}_2\text{NiO}_{4.0}$. We also found low-lying optic phonon modes to be broader than the experimental resolution, which suggest a limited lifetime of the excitation or a distribution of quasi-degenerate modes. Furthermore, an unexpected non-dispersive signature was observed, for energy transfer $\Delta E=6-8\text{meV}$, with no dependence in momentum transfer, that we attributed to inelastic incoherent scattering. We calculated neutron structure factors $S(\mathbf{Q},\omega)$ at high-symmetry points of the Brillouin zone from molecular dynamics trajectories, which shown a good agreement with experimental spectra. In particular, a non-trivial incoherent inelastic contribution was predicted, associated with single-particle motions of neodymium and apical oxygen atoms. This incoherent contribution is found at similar frequencies than the measured broad optic phonon modes, which are themselves associated with coherent sliding motions of neodymium and apical oxygen atoms in phonon calculation. We also calculated that this incoherent contribution is several order of magnitude lower for stoichiometric $\text{Nd}_2\text{NiO}_{4.0}$, thus that associated single-particle motions are dependent on the presence of excess oxygen atoms. Such results suggest that overall sliding motions, in particular of apical oxygen atoms, can be dissociated into a lattice-correlated coherent contribution and a single-particle incoherent contribution; a favorable combination of the two would locally enhance the amplitude of the atomic motion, thus eventually promoting an apical oxygen atom towards a vacant interstitial site.

In summary, oxygen mobility in the $\text{Nd}_2\text{NiO}_{4+d}$ phases, in the moderate-temperature regime can be depicted as follow. Excess oxygen atoms in interstitial sites are inducing a shift of lattice dynamics from modes with associated displacement towards $[100]$ to modes with associated displacements towards $[110]$, *i.e.* towards the diffusion pathway. Furthermore, interstitial oxygen atoms are promoting single-particle behavior of apical oxygen atoms by increasing their delocalization – flattening the potential they sit in – and shifting their incoherent motions towards the $[110]$ direction. The random favorable combination of local single-particle motion and lattice-activated coherent motion eventually promote the apical oxygen atom along the diffusion pathway. Such a mechanism can only be effective in a temperature regime where diffusive ions show both single-particle behavior and correlation with the lattice, and can be described as lattice-activated diffusion, or phonon-assisted diffusion.

Throughout this thesis, we have investigated the effect of excess oxygen atoms on structures and, primarily, lattice dynamics of the $\text{Nd}_2\text{NiO}_{4+d}$ phases, and provided evidences to support a model of phonon-assisted diffusion to describe the non-classical oxygen diffusion observed in the moderate-temperature regime. Furthermore, we have used and shown the effectiveness of

innovative methods, based in particular on molecular dynamics simulations, to investigate the dynamics of defective materials that conventional approaches fail to describe. While further experiments and calculations are required to confirm the suggested mechanism, with in particular extensive characterization with three-axis inelastic neutron scattering of the $\text{Nd}_2\text{NiO}_{4.0}$ and $\text{Nd}_2\text{NiO}_{4.10}$ phases, the current description may serve as a conceptual framework to approach the issue of non-classical oxygen diffusion in highly-correlated systems.

Appendix A. PRM code for Matlab®.

Here after can be found the core of the PRM code with explanations. The code is written in Matlab R2013a language, and large room remains for time consumption optimization, redundancy, etc. The following is the core on which several calculations are based, not reported here, which is why some parts of the code seems pointless. PRM code is structure dependent yet easily adaptable to any structure with 2D behavior, as layered structure, since they do not require complex coding for symmetry or projections. Here the data importation is defined for 3 types of atoms, O, Ni, Nd, but can be easily adapted for other structures. The following .m script needs only the XDATCAR file from VASP molecular dynamics.

```
% Extract atomic positions from XDATCAR (VASP output for molecular
dynamics) and calculate and plot positional recurrence maps
    % extra=0 without further corrections
    % extra=1 added tetragonal symmetry
    % cd_plot(1) 3D isosurface of 1% density
    % cd_plot(2) surface with z-normal and view(0,90)
    % space
        % 'real' for real Cartesian origin / position projection
        % 'com' for center-of-mass origin / atomic displacement projection
    % !!!! Prepare data for PRM job is structure dependent!!!! Check it
out!!!!

%%%%%%%%%%%%%%%%%%%%%%%%%%%%%%%%%%%%%%%%%%%%%%%%%%%%%%%%%%%%%%%%%%%%%%%%
% Initialization
%%%%%%%%%%%%%%%%%%%%%%%%%%%%%%%%%%%%%%%%%%%%%%%%%%%%%%%%%%%%%%%%%%%%%%%%
close all;
clear; clc;

%%
%%%%%%%%%%%%%%%%%%%%%%%%%%%%%%%%%%%%%%%%%%%%%%%%%%%%%%%%%%%%%%%%%%%%%%%%
% Input/control parameters
%%%%%%%%%%%%%%%%%%%%%%%%%%%%%%%%%%%%%%%%%%%%%%%%%%%%%%%%%%%%%%%%%%%%%%%%
xdatpath='dat\XDATCAR'; % path to XDATCAR file
new=1; % 0/1 % XDATCAR different from last run?
at=num2cell(41:72); % lines corresponding to atoms of interest (equivalent
by symmetry) in XDATCAR
extra=1; % 0/1 % see header
space='com'; % real/com % see header
space_tag='[]'; % apical/interstitial/[] % not needed if 'com' % specific
to structural model
tstep=2; % time step of the molecular dynamics in fs
nstep=0; % number of steps to remove at the beginning of the simulation
%0/1000
nstop=20000; % [] % number of steps to stop at
cd_plot=[0,1]; % see header

%%
%%%%%%%%%%%%%%%%%%%%%%%%%%%%%%%%%%%%%%%%%%%%%%%%%%%%%%%%%%%%%%%%%%%%%%%%
% Import data
%%%%%%%%%%%%%%%%%%%%%%%%%%%%%%%%%%%%%%%%%%%%%%%%%%%%%%%%%%%%%%%%%%%%%%%%
disp('Data importation and conversion: started'); tic;
if new==1
```

```

% read data
fid=fopen(xdatpath);
S_temp=textscan(fid, '%s %s %s');
fclose(fid);
len_temp=length(S_temp{1,1});
S_head=[S_temp{1,1}(1:7,1),S_temp{1,2}(1:7,1),S_temp{1,3}(1:7,1)]; %
first 7 lines of XDATCAR are headers

S=str2double([S_temp{1,1}(8:len_temp,1),S_temp{1,2}(8:len_temp,1),S_temp{1,
3}(8:len_temp,1)]);
lat=str2double(S_head(3:5,1:3));
% loop to remove all non-numerical values
S_flag=1;
while S_flag==1
    [S_nan,~]=find(isnan(S));
    if isempty(S_nan)
        S_flag=0;
    else
        S_nan=S_nan(1);
        S=S([1:S_nan-1,S_nan+1:end],:);
    end
end;
% read simulation length

n_to=str2double(S_head{7,1})+str2double(S_head{7,2})+str2double(S_head{7,3}
); % depends on the number of different atoms
len=length(S);
clear S_temp len_temp S_head S_flag S_nan ans fid;
save ovDATA S len lat n_to;
else
    load('ovDATA.mat');
end
disp('Data importation and conversion: done'); toc; disp(' ');

%%
%%%%%%%%%%%%%%%%%%%%%%%%%%%%%%%%%%%%%%%%%%%%%%%%%%%%%%%%%%%%%%%%%%%%%%%%
% Extract data for selected atoms
%%%%%%%%%%%%%%%%%%%%%%%%%%%%%%%%%%%%%%%%%%%%%%%%%%%%%%%%%%%%%%%%%%%%%%%%
disp('Data extraction for selected atoms and time frame: started'); tic;
if isempty(nstop); nstop=len/n_to; else end
if nstop>(len/n_to); nstop=len/n_to; else end
S=S([1,(n_to*nstop)+2:(n_to*nstop)],:); % the first step is needed to get
the CoM positions
len=len-n_to*nstop-(len-nstop*n_to);
pos_x=zeros(len/n_to,3,length(at)); t=zeros(len/n_to,1);
for h=1:length(at)
    for k=1:len/n_to
        pos_x(k,:,h)=S(at{1,h}-8+(k-1)*n_to,:);
        t(k,1)=k*tstep/1000;
    end; clear k;
end; clear h;
disp('Data extraction for selected atoms and time frame: done'); toc;
disp(' ');

%%%%%%%%%%%%%%%%%%%%%%%%%%%%%%%%%%%%%%%%%%%%%%%%%%%%%%%%%%%%%%%%%%%%%%%%
% Correct data from periodic boundaries
%%%%%%%%%%%%%%%%%%%%%%%%%%%%%%%%%%%%%%%%%%%%%%%%%%%%%%%%%%%%%%%%%%%%%%%%
disp('Data correction from periodic boundaries: started'); tic;
mea_x=pos_x;
for h=1:length(at)
    for v=1:3

```

```

        for k=2:len/n_to
            % if displacement from a frame to another is |d|>0.8 then shift
back
            if mea_x(k,v,h)-mea_x(k-1,v,h)<-0.8==1
                mea_x(k,v,h)=mea_x(k,v,h)+1;
            elseif mea_x(k,v,h)-mea_x(k-1,v,h)>0.8==1
                mea_x(k,v,h)=mea_x(k,v,h)-1;
            else
                end
            end; clear k;
        end; clear v;
    end; clear h;
clear pos_x;
disp('Data correction from periodic boundaries: done'); toc; disp(' ');

%%
%%%%%%%%%%%%%%%%%%%%%%%%%%%%%%%%%%%%%%%%%%%%%%%%%%%%%%%%%%%%%%%%%%%%%%%%
% Prepare data for PRM job
%%%%%%%%%%%%%%%%%%%%%%%%%%%%%%%%%%%%%%%%%%%%%%%%%%%%%%%%%%%%%%%%%%%%%%%%
if strcmp(space,'real')
    disp('Find site label: started'); tic;
    % find grid type: yet only for 2D x-y
    tag=textscan(xdatapath,'%s %s %s %s %s %s','delimiter','MDT'); %
personal delimiter for XDATCAR_MD400T150 labels
    if strcmp(tag{5},'400'); space_ap=[0 0 1/4 1/4]; space_int=[]; else
end; % specific to structural model, [x y z step]
    if strcmp(tag{5},'410'); space_ap=[1/8 1/8 1/4 1/4]; space_int=[1/2 1/2
1/4 1/4]; else end; % specific to structural model
    if strcmp(tag{5},'425'); space_ap=[0 0 1/8 1/8]; space_int=[0 1/8 1/8
1/8]; else end; % specific to structural model
    grid_apx=[space_ap(1):-
space_ap(3):0,space_ap(1)+space_ap(3):space_ap(3):1];
    grid_apy=[space_ap(2):-
space_ap(4):0,space_ap(2)+space_ap(4):space_ap(4):1];
    grid_intx=[space_int(1):-
space_int(3):0,space_int(1)+space_int(3):space_int(3):1];
    grid_inty=[space_int(2):-
space_int(4):0,space_int(2)+space_int(4):space_int(4):1];
    dlap=zeros(length(grid_apx),length(grid_apy));
    dlint=zeros(length(grid_intx),length(grid_inty));
    rea_x=zeros(1,3,length(at)); rea_lb=zeros(1,1,length(at));
    % separate apical from interstitial atoms for jobs not reported here
    for h=1:length(at)
        for xap=1:length(grid_apx)
            for yap=1:length(grid_apy)
                dtap=mea_x(1,:,h)-
[grid_apx(xap),grid_apy(yap),mea_x(1,3,h)];
                dlap(xap,yap)=sqrt(dtap(1)*dtap(1)+dtap(2)*dtap(2));
            end;
        end;
        for xint=1:length(grid_intx)
            for yint=1:length(grid_inty)
                dtint=mea_x(1,:,h)-
[grid_intx(xint),grid_inty(yint),mea_x(1,3,h)];
                dlint(xint,yint)=sqrt(dtint(1)*dtint(1)+dtint(2)*dtint(2));
            end;
        end;
        % label 0 for apical, label 1 for interstitial
        [vap,tmap]=min(dlap(:)); [vint,tmint]=min(dlint(:));
        if vint>vap
            [dx,dy]=ind2sub(size(dlap),tmap); rea_lb(1,1,h)=0;

```

```

        rea_x(1, :, h)=[grid_apx(dx), grid_apy(dy), mea_x(1, 3, h)]-
mea_x(1, :, h);
        else
            [dx, dy]=ind2sub(size(dlint), tmint); rea_lb(1, 1, h)=1;
            rea_x(1, :, h)=[grid_intx(dx), grid_inty(dy), mea_x(1, 3, h)]-
mea_x(1, :, h);
        end
    end; clear tag h xap xint yap yint dtap dtint dlap dlint dx dy tmap
tmint...
        vap vint;
        disp('Find site label: done'); toc; disp(' ');
else
    if strcmp(space, 'real')==0
        rea_x=zeros(1, 3, length(at));
        for h=1:length(at)
            rea_x(1, :, h)=[0, 0, 0];
        end; clear h;
    else
        end
end

%%
%%%%%%%%%%%%%%%%%%%%%%%%%%%%%%%%%%%%%%%%%%%%%%%%%%%%%%%%%%%%%%%%%%%%%%%%
% Processing job (positional recurrence maps)
%%%%%%%%%%%%%%%%%%%%%%%%%%%%%%%%%%%%%%%%%%%%%%%%%%%%%%%%%%%%%%%%%%%%%%%%
disp('PRM for selected atoms: started'); tic;
% shift all selected atoms to (0.5,0.5,0.5)
shi=zeros(1, 3, length(at));
shi(1, :, :)=0.5-mea_x(1, :, :);
map_x=zeros(len/n_to, 3, length(at));
for k=1:len/n_to
    map_x(k, :, :)=mea_x(k, :, :)+shi(1, :, :)+rea_x(1, :, :);
end; clear k;
% set box size, i.e. the plot resolution (careful scales hard)
bs_xstep=300; bs_xsize_min=0; bs_xsize_max=1; % in r.l.u.: from 0 to 1
bs_ystep=300; bs_ysize_min=0; bs_ysize_max=1;
bs_zstep=150; bs_zsize_min=0; bs_zsize_max=1;
bs_xvec=(bs_xsize_min:(bs_xsize_max-bs_xsize_min)/bs_xstep:bs_xsize_max);
bs_xvec=bs_xvec(:);
bs_yvec=(bs_ysize_min:(bs_ysize_max-bs_ysize_min)/bs_ystep:bs_ysize_max);
bs_yvec=bs_yvec(:);
bs_zvec=(bs_zsize_min:(bs_zsize_max-bs_zsize_min)/bs_zstep:bs_zsize_max);
bs_zvec=bs_zvec(:);
% for each atom, for each frame of MD, locate in which box is the atom
bs_void=zeros(bs_xstep+1, bs_ystep+1, bs_zstep+1);
for h=1:length(at)
    for k=2:len/n_to
        [~, bs_cd_x]=min(abs(map_x(k, 1, h)-bs_xvec)); % find x-y-z position
        [~, bs_cd_y]=min(abs(map_x(k, 2, h)-bs_yvec));
        [~, bs_cd_z]=min(abs(map_x(k, 3, h)-bs_zvec));

        bs_void(bs_cd_x, bs_cd_y, bs_cd_z)=bs_void(bs_cd_x, bs_cd_y, bs_cd_z)+1; %
count
    end; clear k;
end; clear h bs_cd_x bs_cd_y bs_cd_z;
% smooth, project on z, log scale
bs_smo=smooth3(bs_void, 'gaussian', [3, 3, 3]);
bs_plan=sum(bs_void, 3); % choice of projection, here along z
bs_log=log(bs_plan); bs_log(bs_log== -Inf)=0;
clear bs_xstep bs_ystep bs_zstep bs_xsize_min bs_ysize_min bs_zsize_min ...
bs_xsize_max bs_ysize_max bs_zsize_max shi map_x

```

```

disp('PRM for selected atoms: done'); toc; disp(' ');

if extra==1
    disp('Symmetry expansion'); tic;
    % set fwd and bcwd axis, set transpose matrix (i.e. "4" operation)
    sym_fwd=1:1:length(bs_void); sym_bcwd=length(bs_void):-1:1;
bs_plan_rev=bs_plan';
    % sym. equivalents

bs_sym=(bs_plan(sym_fwd,sym_fwd)+bs_plan(sym_fwd,sym_bcwd)+bs_plan(sym_bcwd
,sym_fwd)+...

bs_plan(sym_bcwd,sym_bcwd)+bs_plan_rev(sym_fwd,sym_fwd)+bs_plan_rev(sym_fwd
,sym_bcwd)+...
    bs_plan_rev(sym_bcwd,sym_fwd)+bs_plan_rev(sym_bcwd,sym_bcwd))./8;
    % log scale
    clear bs_log; bs_log=log(bs_sym); bs_log(bs_log==-Inf)=0;
bs_log(bs_log<0)=0; % due to non-integer value from averaging
    disp('Symmetry expansion'); toc; disp(' ');
else
end

%%
%%%%%%%%%%%%%%%%%%%%%%%%%%%%%%%%%%%%%%%%%%%%%%%%%%%%%%%%%%%%%%%%%%%%%%%%
% Plot job (positional recurrence maps)
%%%%%%%%%%%%%%%%%%%%%%%%%%%%%%%%%%%%%%%%%%%%%%%%%%%%%%%%%%%%%%%%%%%%%%%%
flag_plot=1;

if cd_plot(1)==1
    d=figure(flag_plot);
    set(d,'Position',[1,1,801,801]);
    [ps_xvec,ps_yvec,ps_zvec]=meshgrid(bs_xvec,bs_yvec,bs_zvec);
    is=patch(isosurface(ps_xvec,ps_yvec,ps_zvec,bs_smo,1));
    set(is,'FaceColor','red','EdgeColor','none');
    camlight; lighting gouraud;
    xlim([0 1]); ylim([0 1]); zlim([0 1]);
    xlabel('x','FontName','Times New Roman','FontSize',14);
    ylabel('y','FontName','Times New Roman','FontSize',14);
    zlabel('z','FontName','Times New Roman','FontSize',14);
    view(0,90);
    flag_plot=flag_plot+1;
else
end

if cd_plot(2)==1
    e=figure(flag_plot);
    set(e,'Position',[80,15,480,480]);
    ep=surf(bs_xvec,bs_yvec,bs_log,'lines','none');
    xlim([0.15 0.85]); ylim([0.15 0.85]);
    axis off; view(0,90);
    flag_plot=flag_plot+1;
else
end

```


Appendix B. dispth code for Matlab®.

Here after can be found the code used to generate the figures in **chapter 5**. Basically it's a compiler of theoretical data calculated using VASP and PHONON (specifically the .d14 and .d51 output files from PHONON), and of experimental data collected on TAS spectrometers. For convenience it uses already formatted data, yet it would be easily adapted to import other format from other software equivalent to PHONON. Basically the dispth code plot the shape of $S(\mathbf{q},\omega)$ from the .d14 file, its intensities from .d51 file on high-symmetry region of $S(\mathbf{q},\omega)$ if specified, and the relevant measured experimental point of $S(\mathbf{q},\omega)$. The code is built as follow: the dispth.m script which overview the four functions, f_dispinth_i.m, f_dispinth_p.m, f_dispex_i.m, and f_dispex_p.m, respectively used to import and plot theoretical and experimental data.

B.1. dispin.m script

```
% Extract calculated dispersion curves from phonon .d14 files or .d51
% files, plot experimental points from .xls, plot fit from .xls
% v1.0 May, 2011 (dispin, dispin2)
% v1.1 October, 2011 (dispin3)
% v2.0 April, 2012 (dispth, dispex*, dispcev)
% v3.0 December, 2012 (inclusion of 'Condition*')

%%%%%%%%%%%%%%%%%%%%%%%%%%%%%%%%%%%%%%%%%%%%%%%%%%%%%%%%%%%%%%%%%%%%%%%%
% Initialisation
%%%%%%%%%%%%%%%%%%%%%%%%%%%%%%%%%%%%%%%%%%%%%%%%%%%%%%%%%%%%%%%%%%%%%%%%
clc
clear
close all

%%%%%%%%%%%%%%%%%%%%%%%%%%%%%%%%%%%%%%%%%%%%%%%%%%%%%%%%%%%%%%%%%%%%%%%%
% Prerequisite: available directions in simulations, available BZs +
DEFAULT
%%%%%%%%%%%%%%%%%%%%%%%%%%%%%%%%%%%%%%%%%%%%%%%%%%%%%%%%%%%%%%%%%%%%%%%%
cd_138_av={'Y','M','Z'};
cd_138_bz={'030_050','400_500','-140_140','-2-30_-2-10','3-
10_400','130_310',...
'-220_-130','110_330','008_118','008_009','00-7_00-
6','220_221','22-7_22-6'};

cd_138m_av={'Y','M','Z'};
cd_138m_bz={'030_050','400_500','-140_140','-2-30_-2-10','3-
10_400','130_310',...
'-220_-130','110_330','008_118','008_009','00-7_00-
6','220_221','22-7_22-6'};

cd_64_av={'Y','M'};
cd_64_bz={};

cd_27_av={'Y','Z'};
cd_27_bz={'030_050'};
```

```

def_mode='true'; % true/ % manual/automatic run
cd_sim_def='138m'; % 138/138m/64/27
cd_lc_def='local'; % superimposed/extended/local
cd_sq_def='y'; % y/n % plot calculated Sqw
cd_ex_def='n'; % y/n % plot experimental data
cd_un_def='AA'; % AA/rlu % x-axis unit
lbz_lb_def='22-7_22-6'; % q range
cd_mp_def='0 0 0 0 0 1'; % data set
cd_cr_def='0 0 1'; % crystal set
cd_dir_def='M'; % X/Y/M/Z % direction, unused if local

%%%%%%%%%%%%%%%%%%%%%%%%%%%%%%%%%%%%%%%%%%%%%%%%%%%%%%%%%%%%%%%%%%%%%%%%
% Input Condition*
%%%%%%%%%%%%%%%%%%%%%%%%%%%%%%%%%%%%%%%%%%%%%%%%%%%%%%%%%%%%%%%%%%%%%%%%

if strcmp(def_mode, 'true')==0
    % Condition1. Choice of simulation.
    disp('Simulation "138": P42/ncm with d=0 ');
    disp('Simulation "138m": same with Ni AF (default)');
    disp('Simulation "64": Cmce with d=0');
    disp('Simulation "27": Pcc2 with d=0.25');
    cd_sim=input('Which sim? [138/138m/64/27] ', 's');
    if strcmp(cd_sim, '')==1
        cd_sim=cd_sim_def;
    else
    end
    fprintf('          A: %s \n', cd_sim);

    % Condition2. Local or global.
    disp(' ');
    disp('"superimposed" Brillouin zones, all high-sym directions
(default)');
    disp('"extended" single high-sym direction');
    disp('"local", define two q-vector');
    cd_lc=input('Where in q-space? [superimposed/extended/local] ', 's');
    if strcmp(cd_lc, '')==1
        cd_lc=cd_lc_def;
    else
    end
    fprintf('          A: %s \n', cd_lc);

    % Condition3. Compare Sqw.
    disp(' ');
    disp('"y" compare Sqw, need .d51 files (need "local" for th. Sqw)
(default)');
    disp('"n" compare only frequencies, need .d14 files');
    cd_sq=input('Compare phonon intensities? [y/n] ', 's');
    if strcmp(cd_sq, '')==1
        cd_sq=cd_sq_def;
    else
    end
    fprintf('          A: %s \n', cd_sq);

    % Condition4. Experimental points.
    disp(' ');
    cd_ex=input('Plot experimental points? [y,n] (default y) ', 's');
    if strcmp(cd_ex, '')==1
        cd_ex=cd_ex_def;
    else

```



```

lbz_lb=input('Which pair? ','s');
if strcmp(lbz_lb,'')==1
    lbz_lb=lbz_lb_def;
else
end
fprintf('          A: %s \n',lbz_lb);
else
clear lbz_lb
lbz_lb=lbz_lb_def;
end

% Converting from (hkl_hkl) to (h k l h k l)
[~,lbz_loc_us]=find(lbz_lb=='_'); [~,lbz_loc_h]=find(lbz_lb=='-'); v=1;
w=1; lbz_flag=0; lbz_qs=zeros(1,6); % new matlab
% [o,lbz_loc_us]=find(lbz_lb=='_'); [o,lbz_loc_h]=find(lbz_lb=='-');
clear o; v=1; w=1; lbz_flag=0; lbz_qs=zeros(1,6); % old matlab
while lbz_flag==0
    if sum(v==lbz_loc_us)==1
        z=v+1;
    elseif sum(v==lbz_loc_h)==1
        lbz_qs(1,w)=str2double(lbz_lb(1,v:v+1));%str2num
        z=v+2; w=w+1;
    else
        lbz_qs(1,w)=str2double(lbz_lb(1,v));%str2num
        z=v+1; w=w+1;
    end
    v=z;
    if v>length(lbz_lb)
        lbz_flag=1;
    else
    end
end
clear v w z lbz_flag

% Setting direction
lbz_qm=lbz_qs(1,4:6)-lbz_qs(1,1:3);
clear cd_dir
if lbz_qm(2)==0 && lbz_qm(3)==0
    cd_dir='X';
elseif lbz_qm(1)==0 && lbz_qm(3)==0
    cd_dir='Y';
elseif lbz_qm(1)==0 && lbz_qm(2)==0
    cd_dir='Z';
elseif abs(lbz_qm(1))==abs(lbz_qm(2)) && lbz_qm(3)==0
    cd_dir='M';
else
end
else
end

% Develop Condition4+
if strcmp(cd_ex,'y')==1
    if strcmp(def_mode,'true')==0
        % Instruments
        disp(' ');
        disp('Format: X X X X X X with X=[0,1] (default 0 0 0 0 0 1)');
        disp('"1" 2011, May, IN3 (PG/PG)');
        disp('"2" 2011, Nov, IN3 (PG/PG)');
        disp('"3" 2011, Nov, IN8 (Cu/Cu)');
        disp('"4" 2011, Nov, Flatcone@IN8 (Si/Si)');
        disp('"5" 2012, Oct, IN3 (PG/PG)');
    end
end

```

```

disp('"6" 2012, Dec, IN8 (Si/Si)');
cd_mp=input('Which experiment? [0,1] ','s');
if strcmp(cd_mp,'')==1
    cd_mp=cd_mp_def;
else
end
fprintf('          A: %s \n',cd_mp);
cd_mp=str2num(cd_mp);

% Crystals
disp(' ');
disp('Format: X X X with X=[0,1] (default 0 0 1)');
disp('"1" crystal NNO MC2 (I, 1-time twinned but minor phase)');
disp('"2" crystal NNO MC5 8A (II, 1-time twinned but biphasic)');
disp('"3" crystal NNO july 2011 (2-time twinned)');
cd_cr=input('Which crystal? [0,1] ','s');
if strcmp(cd_cr,'')==1
    cd_cr=cd_cr_def;
else
end
fprintf('          A: %s \n',cd_cr);
cd_cr=str2num(cd_cr);
else
    cd_mp=cd_mp_def; cd_mp=str2num(cd_mp);
    cd_cr=cd_cr_def; cd_cr=str2num(cd_cr);
end
else
end

%%%%%%%%%%%%%%%%%%%%%%%%%%%%%%%%%%%%%%%%%%%%%%%%%%%%%%%%%%%%%%%%%%%%%%%%
% Import calculated dispersion curves from Conditions*
%%%%%%%%%%%%%%%%%%%%%%%%%%%%%%%%%%%%%%%%%%%%%%%%%%%%%%%%%%%%%%%%%%%%%%%%
[dir_data,dir_kmin,dir_kmax,dir_len,dir_BZsname,dir_BZename,dir_wid,ovW_dim
]=...
    f_dispinth_i(cd_sim,cd_lc,cd_dir,lbz_lb);

%%%%%%%%%%%%%%%%%%%%%%%%%%%%%%%%%%%%%%%%%%%%%%%%%%%%%%%%%%%%%%%%%%%%%%%%
% Plot calculated dispersion curves from Conditions*
%%%%%%%%%%%%%%%%%%%%%%%%%%%%%%%%%%%%%%%%%%%%%%%%%%%%%%%%%%%%%%%%%%%%%%%%
[N_un]=f_dispinth_p(cd_lc,cd_dir,dir_data,dir_kmax,dir_wid,dir_BZsname,dir_
BZename,lbz_lb,cd_un);

if strcmp(cd_ex,'y')==1
%%%%%%%%%%%%%%%%%%%%%%%%%%%%%%%%%%%%%%%%%%%%%%%%%%%%%%%%%%%%%%%%%%%%%%%%
% Import experimental points from Conditions*
%%%%%%%%%%%%%%%%%%%%%%%%%%%%%%%%%%%%%%%%%%%%%%%%%%%%%%%%%%%%%%%%%%%%%%%%

[Xl_data,Xt_data,Xx_data,Yl_data,Yt_data,Yx_data,Ml_data,Mt_data,Mx_data,..
.

Zl_data,Zt_data,Zx_data,C_data,color_step]=f_dispex_i(cd_mp,cd_cr,cd_dir,ov
W_dim);

%%%%%%%%%%%%%%%%%%%%%%%%%%%%%%%%%%%%%%%%%%%%%%%%%%%%%%%%%%%%%%%%%%%%%%%%
% Plot experimental points from Conditions*
%%%%%%%%%%%%%%%%%%%%%%%%%%%%%%%%%%%%%%%%%%%%%%%%%%%%%%%%%%%%%%%%%%%%%%%%

f_dispex_p(cd_sim,cd_lc,cd_sq,cd_dir,N_un,dir_kmax,Xl_data,Xt_data,Xx_data,
Yl_data,Yt_data,...

```

```

Yx_data,Ml_data,Mt_data,Mx_data,Zl_data,Zt_data,Zx_data,C_data,lbz_qs,color
_step,ovW_dim);
else
end

```

B.2. f_dispinth_i.m function

```

function
[dir_data,dir_kmin,dir_kmax,dir_len,dir_BZsname,dir_BZename,dir_wid,ovW_dim
] =...
    f_dispinth_i(cd_sim, cd_lc, cd_dir,lbz_lb)

Norm=2*pi;

% superimposed
if strcmp(cd_lc, 'superimposed')==1
    dir_data={1:length(cd_dir)};
    for v=1:length(cd_dir)

M_name=sprintf('%s%s%s%s%s', ['d14\NNO', cd_sim, '_', cd_dir{1,v}, '.d14']);
    M_rd=struct2cell(importdata(M_name, ' ', 4));
    [lenM_rd, widM_rd]=size(M_rd{1,1});
    dir_data{1,v}=M_rd{1,1};
    dir_kmin{1,v}=str2double(M_rd{2,1}{3,1}(1:10))*Norm;
    dir_kmax{1,v}=str2double(M_rd{2,1}{4,1}(1:10))*Norm;
    dir_len{1,v}=lenM_rd;
    dir_BZsname{1,v}='\Gamma';
    dir_BZename{1,v}=cd_dir{1,v};
    dir_wid{1,v}=widM_rd;
    clear M_name M_rd M_sdata M_rd_kmin M_rd_kmax lenM_rd widM_rd
    end
    clear v

% extended
elseif strcmp(cd_lc, 'extended')==1
    E_name=sprintf('%s%s%s%s%s', ['d14\OS', cd_sim, '_', cd_dir, '.d14']);
    M_E=struct2cell(importdata(E_name, ' ', 4));
    [lenM_E, widM_E]=size(M_E{1,1});
    dir_data={M_E{1,1}};
    dir_kmin={str2double(M_E{2,1}{3,1}(1:10))*Norm};
    dir_kmax={str2double(M_E{2,1}{4,1}(1:10))*Norm};
    dir_len={lenM_E};
    dir_BZsname={'\Gamma'};
    dir_BZename={cd_dir};
    dir_wid={widM_E};

% local
elseif strcmp(cd_lc, 'local')==1
    L_name=sprintf('%s%s%s%s%s', ['d51\OS', cd_sim, '_', lbz_lb, '.d51']);
    Lc_name=sprintf('%s%s%s%s%s', ['d51\OS', cd_sim, '_', lbz_lb, '.d14']);
    M_L=struct2cell(importdata(L_name, ' ', 3));
    M_Lc=struct2cell(importdata(Lc_name, ' ', 4));
    [lenM_ovL, ~]=size(M_L{1,1}); % new matlab
    [lenM_ovLc, widM_Lc]=size(M_Lc{1,1}); % new matlab
%     [lenM_ovL, o]=size(M_L{1,1}); clear o; % old matlab
%     [lenM_ovLc, widM_Lc]=size(M_Lc{1,1}); % old matlab
    dir_data={M_L{1,1}, M_Lc{1,1}};

```

```

dir_kmin={min(M_L{1,1}(:,1))*Norm,str2double(M_Lc{2,1}{3,1}(1:10))*Norm};

dir_kmax={max(M_L{1,1}(:,1))*Norm,str2double(M_Lc{2,1}{4,1}(1:10))*Norm};
dir_len={lenM_ovL/str2double(M_L{2,1}{2,1}(8:9)),lenM_ovLc};
dir_BZsname={'\Gamma', '\Gamma'};
dir_BZename={'\Gamma', '\Gamma'};
dir_wid={str2double(M_L{2,1}{2,1}(8:9)),widM_Lc};
else
end

ovW_dim=length(dir_kmax);

end % of function

```

B.3. f_dispinth_p.m function

```

function [N_un] = f_dispinth_p(cd_lc,cd_dir,dir_data,dir_kmax,...
    dir_wid,dir_BZsname,dir_BZename,lbz_lb,cd_un)

THz_to_meV=4.135702;
Norm=2*pi;
scrsz=get(0, 'ScreenSize');

if strcmp(cd_un, 'AA')
    for v=1:length(cd_dir)
        N_un{1,v}=1;
    end
else
    for v=1:length(cd_dir)
        N_un{1,v}=1./dir_kmax{1,v};
    end
    clear v
end

if strcmp(cd_lc, 'superimposed')==1
    fl=figure(1);
    set(fl, 'Position', [scrsz(1),scrsz(2),scrsz(3),scrsz(4)]);
    for v=1:length(cd_dir)
        figure(1); subplot(1,length(cd_dir),v);
        hold on
        q_Y=dir_data{1,v}(:,1)*Norm*N_un{1,v};
        for w=1:dir_wid{1,v}-1
            n_Y=dir_data{1,v}(:,w+1).*THz_to_meV;
            plot(q_Y,n_Y, '-k', 'LineWidth', 2);
        end
        clear w
        ylabel('Energy (meV)');
        text(0,-0.25,dir_BZsname{1,1});
        if strcmp(cd_un, 'AA')==1
            text(dir_kmax{1,v}+0.005,-0.17,dir_BZename{1,v});
            axis([min(q_Y) max(q_Y) 0 22]);
            if strcmp(cd_dir{1,v}, 'X')==1 || strcmp(cd_dir{1,v}, 'Y')==1
                set(gca, 'XTick', [0.10:0.10:0.50
dir_kmax{1,v}], 'XTickLabel', '0.10|0.20|0.30|0.40|0.50|');
                xlabel(['\xi 0 0] and [0 \xi 0] q(A^{-1})']);
                title(sprintf('Dispersion curves along %s - Y/X direction
(twinning)', dir_BZsname{1,1}));
            elseif strcmp(cd_dir{1,v}, 'M')==1

```

```

        set(gca, 'XTick', [0.10:0.10:0.80
dir_kmax{1,v}], 'XTickLabel', '0.10|0.20|0.30|0.40|0.50|0.60|0.70| |');
        xlabel('\xi \xi_0 q(A^{-1})');
        title(sprintf('Dispersion curves along %s - M
direction', dir_BZsname{1,1}));
        elseif strcmp(cd_dir{1,v}, 'Z')==1
        set(gca, 'XTick', [0.05:0.05:0.25
dir_kmax{1,v}], 'XTickLabel', '0.05|0.10|0.15|0.20|0.25|');
        xlabel('[0 0 \xi] q(A^{-1})');
        title(sprintf('Dispersion curves along %s - Z
direction', dir_BZsname{1,1}));
        else
        end
        else

set(gca, 'XTick', (0.20:0.20:0.8), 'XTickLabel', '0.20|0.40|0.60|0.80|');
text(1, -0.25, dir_BZename{1,1});
axis([0 1 0 22]);
if strcmp(cd_dir{1,v}, 'X')==1 || strcmp(cd_dir{1,v}, 'Y')==1
    xlabel('\xi_0 0] and [0 \xi_0] q(r.l.u.)');
    title(sprintf('Dispersion curves along %s - Y/X direction
(twinning)', dir_BZsname{1,1})); %get set
elseif strcmp(cd_dir{1,v}, 'M')==1
    xlabel('\xi \xi_0] q(r.l.u.)');
    title(sprintf('Dispersion curves along %s - M
direction', dir_BZsname{1,1})); %get set
elseif strcmp(cd_dir{1,v}, 'Z')==1
    xlabel('[0 0 \xi] q(r.l.u.)');
    title(sprintf('Dispersion curves along %s - Z
direction', dir_BZsname{1,1})); %get set
else
end
end
hold off
end
clear v

elseif strcmp(cd_lc, 'extended')==1

elseif strcmp(cd_lc, 'local')==1
    f1=figure(1);
    set(f1, 'Position', [scrsz(1), scrsz(2), scrsz(3), scrsz(4)]);
    hold on
    q_Y=dir_data{1,2}(:,1)*Norm*N_un{1,1};
    for w=1:dir_wid{1,2}-1
        n_Y=dir_data{1,2}(:,w+1).*THz_to_meV;
        plot(q_Y, n_Y, '--k', 'LineWidth', 1);
    end
    clear w
    len_temp=length(dir_data{1,1});
    q_L=zeros(len_temp/dir_wid{1,1}, 1);
    n_L=zeros(len_temp/dir_wid{1,1}, dir_wid{1,1});
    c_L=zeros(len_temp/dir_wid{1,1}, dir_wid{1,1});
    for v=1:(len_temp/dir_wid{1,1})
        q_L(v,1)=dir_data{1,1}(v*dir_wid{1,1}-
dir_wid{1,1}+1,1)*Norm*N_un{1,1};
        for w=1:dir_wid{1,1}
            n_L(v,w)=dir_data{1,1}(v*dir_wid{1,1}-
dir_wid{1,1}+w,5).*THz_to_meV;
            c_L(v,w)=dir_data{1,1}(v*dir_wid{1,1}-dir_wid{1,1}+w,6);
        end
    end

```

```

end
clear v w
c_L_step=100;
c_L_log(:,:)=log10(c_L(:,:)+1);
c_L_max=max(max(c_L_log));
c_L_norm(:,:)=c_L_log(:,:)./c_L_max.*c_L_step;
c_L_round(:,:)=round(c_L_norm(:,:));
c_L_map=colormap(jet(c_L_step));
for v7=1:(len_temp/dir_wid{1,1})
    for v8=1:dir_wid{1,1}
        if c_L_round(v7,v8)~=0

plot(q_L(v7,1),n_L(v7,v8), 'o', 'MarkerEdgeColor',c_L_map(c_L_round(v7,v8),:)
, ...
'MarkerFaceColor',c_L_map(c_L_round(v7,v8),:), 'MarkerSize',3);
        else
            end
        end
    end

ylabel('Energy (meV)', 'FontName', 'Times New Roman', 'FontSize',22);
if strcmp(cd_un, 'AA')==1
    axis([min(q_L) max(q_L) 0 22]);
else
    axis([0 1 0 22]);
end
text(0,-1.25,dir_BZsname{1,1}, 'FontName', 'Times New
Roman', 'FontSize',22);
text(dir_kmax{1,1},-1.25,dir_BZsname{1,1}, 'FontName', 'Times New
Roman', 'FontSize',22);
lbz_bd=floor(length(lbz_lb)/2);
qm_ini_s=lbz_lb(1:lbz_bd);
qm_end_s=lbz_lb(lbz_bd+2:length(lbz_lb));
title(sprintf('Dispersion curves along %s - between (%s) and
(%s)',cd_dir,qm_ini_s,qm_end_s), 'FontName', 'Times New
Roman', 'FontSize',22);
if strcmp(cd_dir, 'X')==1 || strcmp(cd_dir, 'Y')==1
    xlabel(['\xi 0 0] and [0 \xi 0] q(A^{-1})', 'FontName', 'Times New
Roman', 'FontSize',22);
elseif strcmp(cd_dir, 'M')==1
    xlabel(['\xi \xi 0] q(A^{-1})', 'FontName', 'Times New
Roman', 'FontSize',22);
elseif strcmp(cd_dir, 'Z')==1
    xlabel(['[0 0 \xi] q(A^{-1})', 'FontName', 'Times New
Roman', 'FontSize',22);
else
    end
end
hold off
else
end

set(gca, 'FontName', 'Times New Roman', 'FontSize',22);
set(gca, 'box', 'off');
set(gcf, 'color', 'w');

end % of function

```

B.4. f_dispex_i.m function

```
function
[Xl_data,Xt_data,Xx_data,Yl_data,Yt_data,Yx_data,Ml_data,Mt_data,Mx_data,..
.
    Zl_data,Zt_data,Zx_data,C_data,color_step] =
f_dispex_i(cd_mp,cd_cr,cd_dir,ovW_dim)

% Format of the *fits*.xls file
% Exp name (s) / Crystal name (s) / Scan number (s) / Dir(proj) (s) / Qh
(d) / Qk (d)
% / Ql (d) / q (d) / dq (d) / E (d) / dE (d) / w (d) / dw (d) / I (d) / dI
(d)
% Comments in 'crystal name' field used to subtract scans:
% 'ct' for 'close to', 'spurion', 'bs' for '... bad statistic ;)'

E=importdata('fits\ov_fits.xls');
[lenE,~]=size(E.textdata.Feuil1); % new matlab
% [lenE,o]=size(E.textdata.Feuil1); clear o; % old matlab
cd_Xl=strcmp(E.textdata.Feuil1(2:lenE,4),'X(1)');
cd_Xt=strcmp(E.textdata.Feuil1(2:lenE,4),'X(t)');
cd_Xx=strcmp(E.textdata.Feuil1(2:lenE,4),'X(x)');
cd_Yl=strcmp(E.textdata.Feuil1(2:lenE,4),'Y(1)');
cd_Yt=strcmp(E.textdata.Feuil1(2:lenE,4),'Y(t)');
cd_Yx=strcmp(E.textdata.Feuil1(2:lenE,4),'Y(x)');
cd_Ml=strcmp(E.textdata.Feuil1(2:lenE,4),'M(1)');
cd_Mt=strcmp(E.textdata.Feuil1(2:lenE,4),'M(t)');
cd_Mx=strcmp(E.textdata.Feuil1(2:lenE,4),'M(x)');
cd_Zl=strcmp(E.textdata.Feuil1(2:lenE,4),'Z(1)');
cd_Zt=strcmp(E.textdata.Feuil1(2:lenE,4),'Z(t)');
cd_Zx=strcmp(E.textdata.Feuil1(2:lenE,4),'Z(x)');
cd_C=strcmp(E.textdata.Feuil1(2:lenE,4),'C()');

% Convert cd_mp to logical
cd_mpl(:,1)=strcmp(E.textdata.Feuil1(2:lenE,1),'2011 May IN3');
cd_mpl(:,2)=strcmp(E.textdata.Feuil1(2:lenE,1),'2011 Nov IN3');
cd_mpl(:,3)=strcmp(E.textdata.Feuil1(2:lenE,1),'2011 Nov IN8');
cd_mpl(:,4)=strcmp(E.textdata.Feuil1(2:lenE,1),'2011 Nov Flatcone');
cd_mpl(:,5)=strcmp(E.textdata.Feuil1(2:lenE,1),'2012 Oct IN3');
cd_mpl(:,6)=strcmp(E.textdata.Feuil1(2:lenE,1),'2012 Dec IN8');
[~,cd_mpl_temp]=find(cd_mp(1,:)==1); % new matlab
% [o,cd_mpl_temp]=find(cd_mp(1,:)==1); clear o; % old matlab
cd_mpl_sum=sum(cd_mpl(:,cd_mpl_temp),2);
cd_mpl_sum(cd_mpl_sum>1)=1;

% Convert cd_cr to logical
cd_crl(:,1)=strcmp(E.textdata.Feuil1(2:lenE,2),'V1');
cd_crl(:,2)=strcmp(E.textdata.Feuil1(2:lenE,2),'V2');
cd_crl(:,3)=strcmp(E.textdata.Feuil1(2:lenE,2),'V3');
cd_crl_ghost(:,1)=strcmp(E.textdata.Feuil1(2:lenE,2),'Vg'); % ghost points,
bypass Condition* cd_cr
[~,cd_crl_temp]=find(cd_cr(1,:)==1); % new matlab
% [o,cd_crl_temp]=find(cd_cr(1,:)==1); clear o; % old matlab
cd_crl_sum=sum(cd_crl(:,cd_crl_temp),2);
cd_crl_sum(cd_crl_sum>1)=1;
cd_crl_sum=or(cd_crl_sum,cd_crl_ghost);

% Summing up condition and import
cd_gl=and(cd_mpl_sum,cd_crl_sum);
Xl_data=E.data.Feuil1(and(cd_Xl,cd_gl),:);
```

```

Xt_data=E.data.Feuil1(and(cd_Xt,cd_gl),:);
Xx_data=E.data.Feuil1(and(cd_Xx,cd_gl),:);
Yl_data=E.data.Feuil1(and(cd_Yl,cd_gl),:);
Yt_data=E.data.Feuil1(and(cd_Yt,cd_gl),:);
Yx_data=E.data.Feuil1(and(cd_Yx,cd_gl),:);
Ml_data=E.data.Feuil1(and(cd_Ml,cd_gl),:);
Mt_data=E.data.Feuil1(and(cd_Mt,cd_gl),:);
Mx_data=E.data.Feuil1(and(cd_Mx,cd_gl),:);
Zl_data=E.data.Feuil1(and(cd_Zl,cd_gl),:);
Zt_data=E.data.Feuil1(and(cd_Zt,cd_gl),:);
Zx_data=E.data.Feuil1(and(cd_Zx,cd_gl),:);
C_data=E.data.Feuil1(and(cd_C,cd_gl),:);

% Find intensity maxima
int_M_Xl=max(Xl_data(:,10)); int_M_Xl(isempty(int_M_Xl)==1)=0;
int_M_Xt=max(Xt_data(:,10)); int_M_Xt(isempty(int_M_Xt)==1)=0;
int_M_Xx=max(Xx_data(:,10)); int_M_Xx(isempty(int_M_Xx)==1)=0;
int_M_Yl=max(Yl_data(:,10)); int_M_Yl(isempty(int_M_Yl)==1)=0;
int_M_Yt=max(Yt_data(:,10)); int_M_Yt(isempty(int_M_Yt)==1)=0;
int_M_Yx=max(Yx_data(:,10)); int_M_Yx(isempty(int_M_Yx)==1)=0;
int_M_Ml=max(Ml_data(:,10)); int_M_Ml(isempty(int_M_Ml)==1)=0;
int_M_Mt=max(Mt_data(:,10)); int_M_Mt(isempty(int_M_Mt)==1)=0;
int_M_Mx=max(Mx_data(:,10)); int_M_Mx(isempty(int_M_Mx)==1)=0;
int_M_Zl=max(Zl_data(:,10)); int_M_Zl(isempty(int_M_Zl)==1)=0;
int_M_Zt=max(Zt_data(:,10)); int_M_Zt(isempty(int_M_Zt)==1)=0;
int_M_Zx=max(Zx_data(:,10)); int_M_Zx(isempty(int_M_Zx)==1)=0;
int_M_C=max(C_data(:,10)); int_M_C(isempty(int_M_C)==1)=0;
int_M_gl=int_M_C;
if sum(strcmp(cd_dir,'X'))==1 || sum(strcmp(cd_dir,'Y'))==1

int_M_gl=[int_M_gl,int_M_Xl,int_M_Xt,int_M_Xx,int_M_Yl,int_M_Yt,int_M_Yx];
else
end
if sum(strcmp(cd_dir,'M'))==1
    int_M_gl=[int_M_gl,int_M_Ml,int_M_Mt,int_M_Mx];
else
end
if sum(strcmp(cd_dir,'Z'))==1
    int_M_gl=[int_M_gl,int_M_Zl,int_M_Zt,int_M_Zx];
else
end
int_M=max(int_M_gl);

% Set color integer for cd_sq='y' & double log scale
color_step=8;
Xl_data(:,12)=round((((log10((Xl_data(:,10)/int_M)+1))/(log10(2))))*(color_s
tep-1))+1);
Xt_data(:,12)=round((((log10((Xt_data(:,10)/int_M)+1))/(log10(2))))*(color_s
tep-1))+1);
Xx_data(:,12)=round((((log10((Xx_data(:,10)/int_M)+1))/(log10(2))))*(color_s
tep-1))+1);
Yl_data(:,12)=round((((log10((Yl_data(:,10)/int_M)+1))/(log10(2))))*(color_s
tep-1))+1);
Yt_data(:,12)=round((((log10((Yt_data(:,10)/int_M)+1))/(log10(2))))*(color_s
tep-1))+1);
Yx_data(:,12)=round((((log10((Yx_data(:,10)/int_M)+1))/(log10(2))))*(color_s
tep-1))+1);
Ml_data(:,12)=round((((log10((Ml_data(:,10)/int_M)+1))/(log10(2))))*(color_s
tep-1))+1);
Mt_data(:,12)=round((((log10((Mt_data(:,10)/int_M)+1))/(log10(2))))*(color_s
tep-1))+1);

```

```

Mx_data(:,12)=round((((log10((Mx_data(:,10)/int_M)+1))/(log10(2))))*(color_s
tep-1))+1);
Zl_data(:,12)=round((((log10((Zl_data(:,10)/int_M)+1))/(log10(2))))*(color_s
tep-1))+1);
Zt_data(:,12)=round((((log10((Zt_data(:,10)/int_M)+1))/(log10(2))))*(color_s
tep-1))+1);
Zx_data(:,12)=round((((log10((Zx_data(:,10)/int_M)+1))/(log10(2))))*(color_s
tep-1))+1);
C_data(:,12)=round((((log10((C_data(:,10)/int_M)+1))/(log10(2))))*(color_ste
p-1))+1);

% Set color integer for cd_sq='n'
Xl_data(:,13)=color_step;
Xt_data(:,13)=1;
Xx_data(:,13)=round(color_step/2);
Yl_data(:,13)=color_step;
Yt_data(:,13)=1;
Yx_data(:,13)=round(color_step/2);
Ml_data(:,13)=color_step;
Mt_data(:,13)=1;
Mx_data(:,13)=round(color_step/2);
Zl_data(:,13)=color_step;
Zt_data(:,13)=1;
Zx_data(:,13)=round(color_step/2);
C_data(:,13)=round(color_step/2);

% Confirm direction for f_dispex_p loops while scaling dimensions
dim_flag=1;
log_dir_X=isempty(Xl_data) && isempty(Xt_data) && isempty(Xx_data);
log_dir_Y=isempty(Yl_data) && isempty(Yt_data) && isempty(Yx_data);
log_dir_M=isempty(Ml_data) && isempty(Mt_data) && isempty(Mx_data);
log_dir_Z=isempty(Zl_data) && isempty(Zt_data) && isempty(Zx_data);
if log_dir_X==0 || log_dir_Y==0
    Xl_data(:,14)=dim_flag;
    Xt_data(:,14)=dim_flag;
    Xx_data(:,14)=dim_flag;
    Yl_data(:,14)=dim_flag;
    Yt_data(:,14)=dim_flag;
    Yx_data(:,14)=dim_flag;
    dim_flag=dim_flag+1;
else
end
if log_dir_M==0
    Ml_data(:,14)=dim_flag;
    Mt_data(:,14)=dim_flag;
    Mx_data(:,14)=dim_flag;
    dim_flag=dim_flag+1;
else
end
if log_dir_Z==0
    Zl_data(:,14)=dim_flag;
    Zt_data(:,14)=dim_flag;
    Zx_data(:,14)=dim_flag;
else
end
C_data(:,14)=ovW_dim+1;

end % of function

```

B.5. f_dispex_p.m function

```
function [] =
f_dispex_p(cd_sim,cd_lc,cd_sq,cd_dir,N_un,dir_kmax,Xl_data,Xt_data,Xx_data,
Yl_data,Yt_data,...

Yx_data,Ml_data,Mt_data,Mx_data,Zl_data,Zt_data,Zx_data,C_data,lbz_qs,color
_step,ovW_dim)

% Scaling color to intensity
cc=colormap(jet(color_step));
if strcmp(cd_sq,'y')==1
    cd_cc=12;
else
    cd_cc=13;
end

% Plot experimental points
if strcmp(cd_sim,'138')==1 || strcmp(cd_sim,'138m')==1
    if strcmp(cd_lc,'superimposed')==1

ovW_data=[C_data;Yl_data;Yt_data;Yx_data;Xl_data;Xt_data;Xx_data;Ml_data;Mt
_data;...
        Mx_data;Zl_data;Zt_data;Zx_data];
[im,~]=size(ovW_data); % new matlab
% [im,o]=size(ovW_data); clear o; % old matlab
for i=1:im
    if ovW_data(i,14)==4 % loop initiation
        dir_flag=3; % loop iteration
        dir_loop=1; % increment condition
    else
        dir_flag=1;
        dir_loop=0;
    end
    while dir_flag>0
        if dir_loop==1
            ovW_data(i,14)=ovW_data(i,14)-1;
        else
            end
            figure(1); subplot(1,ovW_dim,ovW_data(i,14)); % set ovW_14
to scale linearly with dim
            hold on
            errorbar(ovW_data(i,4)*dir_kmax{1,ovW_data(i,14)}.*N_un{1,ovW_data(i,14)},o
vW_data(i,6),ovW_data(i,8),'marker','O','color','k','MarkerEdgeColor',...
'k','MarkerFaceColor',cc(ovW_data(i,cd_cc),:),'markersize',10,'LineStyle','
none');%for width i,8, for standard errors i,7
            hold off
            dir_flag=dir_flag-1;
        end
    end
    clear im i
elseif strcmp(cd_lc,'extended')==1
    if strcmp(cd_dir,'X')==1 || strcmp(cd_dir,'Y')==1
        %%%
    elseif strcmp(cd_dir,'M')==1
        %%%
    elseif strcmp(cd_dir,'Z')==1
        %%%
    end
end
```

```

else
end
elseif strcmp(cd_lc, 'local')==1
qm_ini=lbz_qs(1,1:3);
qm_end=lbz_qs(1,4:6);

ovW_data=[C_data;Yl_data;Yt_data;Yx_data;Xl_data;Xt_data;Xx_data;Ml_data;Mt_data;...
Mx_data;Zl_data;Zt_data;Zx_data];
figure(1);
hold on
[im,~]=size(ovW_data); % new matlab
% [im,o]=size(ovW_data); clear o; % old matlab
for i=1:im
qm_exp=[ovW_data(i,1),ovW_data(i,2),ovW_data(i,3)];
log_mat=[qm_ini(1)-qm_end(1) qm_ini(2)-qm_end(2) qm_ini(3)-
qm_end(3) ;...
qm_exp(1)-qm_end(1) qm_exp(2)-qm_end(2) qm_exp(3)-qm_end(3)
; 1 1 1]; % determinant method
log_dis=norm(cross((qm_exp-qm_ini),(qm_exp-
qm_end)))/norm(qm_end-qm_ini); % point-line method
if det(log_mat)==0 && log_dis==0
% if roundn(det(log_mat),-8)==0 && roundn(log_dis,-8)==0
qm_exp=[ovW_data(i,1),ovW_data(i,2),ovW_data(i,3)];
qm_pro=(qm_exp-qm_ini)/(qm_end-qm_ini);

errorbar(qm_pro*dir_kmax{1,1},ovW_data(i,6),ovW_data(i,8),'marker','O','col
or','k','MarkerEdgeColor',...

'k','MarkerFaceColor',cc(ovW_data(i,cd_cc),:),'markersize',10,'LineStyle','
none');
else
end
end
hold off
print('-dpsc2','-r1200','test');
else
end

elseif strcmp(cd_sim, '64')==1
if strcmp(cd_lc, 'superimposed')==1
% X,Y
ovXY_data=[C_data;Yl_data;Yt_data;Yx_data;Xl_data;Xt_data;Xx_data];
figure(1); subplot(1,2,1);
hold on
[im,~]=size(ovXY_data); % new matlab
% [im,o]=size(ovXY_data); clear o; % old matlab
for i=1:im

errorbar(ovXY_data(i,4)*dir_kmax{1,1},ovXY_data(i,6),ovXY_data(i,7),'marker
','O','color','k','MarkerEdgeColor',...

'k','MarkerFaceColor',cc(ovXY_data(i,cd_cc),:),'markersize',10,'LineStyle',
'none');
end
clear im i
hold off
% M
ovM_data=[C_data;Ml_data;Mt_data;Mx_data];
figure(1); subplot(1,2,2);
hold on

```

```

        [im,~]=size(ovM_data); % new matlab
%       [im,o]=size(ovM_data); clear o% old matlab
        for i=1:im

errorbar(ovM_data(i,4)*dir_kmax{1,2},ovM_data(i,6),ovM_data(i,7),'marker','
O','color','k','MarkerEdgeColor',...

'k','MarkerFaceColor',cc(ovM_data(i,cd_cc),:),'markersize',10,'LineStyle','
none');
        end
        clear im i
        hold off
    elseif strcmp(cd_lc,'extended')==1
        if strcmp(cd_dir,'X')==1 || strcmp(cd_dir,'Y')==1
            %%%
        elseif strcmp(cd_dir,'M')==1
            %%%
        else
            end
        elseif strcmp(cd_lc,'local')==1
            %%%
        else
            end

elseif strcmp(cd_sim,'27')==1
    if strcmp(cd_lc,'superimposed')==1
        % X,Y
        ovXY_data=[C_data;Yl_data;Yt_data;Yx_data;Xl_data;Xt_data;Xx_data];
        figure(1); subplot(1,3,1);
        hold on
        [im,~]=size(ovXY_data); % new matlab
%       [im,o]=size(ovXY_data); clear o; % old matlab
        for i=1:im

errorbar(ovXY_data(i,4)*dir_kmax{1,1},ovXY_data(i,6),ovXY_data(i,7),'marker
','O','color','k','MarkerEdgeColor',...

'k','MarkerFaceColor',cc(ovXY_data(i,cd_cc),:),'markersize',10,'LineStyle',
'none');
            end
            clear im i
            hold off
            % Z
            ovZ_data=[C_data;Zl_data;Zt_data;Zx_data];
            figure(1); subplot(1,3,3);
            hold on
            [im,~]=size(ovZ_data); % new matlab
%       [im,o]=size(ovZ_data); clear o; % old matlab
            for i=1:im

errorbar(ovZ_data(i,4)*dir_kmax{1,3},ovZ_data(i,6),ovZ_data(i,7),'marker','
O','color','k','MarkerEdgeColor',...

'k','MarkerFaceColor',cc(ovZ_data(i,cd_cc),:),'markersize',10,'LineStyle','
none');
            end
            clear im i
            hold off
    elseif strcmp(cd_lc,'extended')==1
        if strcmp(cd_dir,'X')==1 || strcmp(cd_dir,'Y')==1
            %%%

```

```
elseif strcmp(cd_dir, 'Z')==1
    %%%
else
end
elseif strcmp(cd_lc, 'local')==1
    %%%
else
end
else
end

end % of function
```

Appendix C. Abbreviations used.

CoM	Center-of-Mass
DFT	Density Functional Theory
DOS	Density Of States
gDOS	generalized Density Of States
GGA	Generalized Gradient Approximation
HT	High-Temperature
HTT	High-Temperature Tetragonal phase
INS	Inelastic Neutron Scattering
LT	Low-Temperature
LTO	Low-Temperature Ortorhombic phase
LTT	Low-Temperature Tetragonal phase
MD	Molecular Dynamics
MEM	Maximum Entropy Method
MSD	Mean Square Displacements
PAW	Projected Augmented Wave
PBE	Perdrew Burke Ernzerhof exchange-correlation functional
PRM	Positional Reccurence Maps
RP	Ruddlesden-Popper phase
RT	Room-Temperature
SOFC	Solid Oxide Fuel Cell
TAS	Three-Axis Spectrometer
TOF	Time-Of-Flight
VACF	Velocity AutoCorrelation Function
vDOS	vibrational Density Of States